Solid Mechanics and Its Applications

Wolfgang Brocks

Plasticity and Fracture

Springer

Solid Mechanics and Its Applications

Volume 244

Aims and Scope of the Series

The fundamental questions arising in mechanics are: *Why*?, *How*?, and *How much*? The aim of this series is to provide lucid accounts written by authoritative researchers giving vision and insight in answering these questions on the subject of mechanics as it relates to solids.

The scope of the series covers the entire spectrum of solid mechanics. Thus it includes the foundation of mechanics; variational formulations; computational mechanics; statics, kinematics and dynamics of rigid and elastic bodies: vibrations of solids and structures; dynamical systems and chaos; the theories of elasticity, plasticity and viscoelasticity; composite materials; rods, beams, shells and membranes; structural control and stability; soils, rocks and geomechanics; fracture; tribology; experimental mechanics; biomechanics and machine design.

The median level of presentation is to the first year graduate student. Some texts are monographs defining the current state of the field; others are accessible to final year undergraduates; but essentially the emphasis is on readability and clarity.

More information about this series at http://www.springer.com/series/6557

Wolfgang Brocks

Plasticity and Fracture

Springer

Wolfgang Brocks
Technical Faculty
Christian Albrecht University Kiel
Geesthacht
Germany

ISSN 0925-0042 ISSN 2214-7764 (electronic)
Solid Mechanics and Its Applications
ISBN 978-3-319-62751-9 ISBN 978-3-319-62752-6 (eBook)
DOI 10.1007/978-3-319-62752-6

Library of Congress Control Number: 2017945266

Printed on acid-free paper

This Springer imprint is published by Springer Nature
The registered company is Springer International Publishing AG
The registered company address is: Gewerbestrasse 11, 6330 Cham, Switzerland

Preface

The present book is the outcome of some decades of research and teaching in plasticity and fracture mechanics at various places and institutions. Both subjects have been graduate courses for engineering students over four semesters of four hours per week at the Technical University of Berlin in the 1980s and 1990s. The correspondent lecture notes, jointly written with my former colleagues Knut Burth and Jürgen Olschwski, who both passed away much too early, comprised 200–250 pages per semester. With the European Bologna reform of university education starting in 2000, the curriculum had to be reduced to one course "Plasticity and Fracture", and since a second course on "Elasticity and Fracture" was no compulsory precognition, a short survey on linear elastic fracture mechanics appeared necessary before plasticity could start. This forced the author to compress the substance of teaching by 75% and restrict it to what he considered to be the absolute minimum of knowledge which a student has to learn in order to be able to educate himself in later years, when working in industry or science. The purpose could not be giving a comprehensive presentation of plasticity and fracture mechanics, any more, but providing a general and science-based impression of basic concepts which should be useful for both industrial practice and science.

This has become the design principle of the present book which relies on respective lecture notes, again. Combining both, plasticity and fracture, in one course and in one book means curtailing any encyclopaedic pretence but opens the chance for an interdisciplinary view on both subjects with regular cross references in the context of a unified nomenclature. This relieves the reader from switching between different books and different terminologies. Links to corresponding standards help clarifying the scientific foundation of engineering applications and rating their potentials and limits.

Beyond that, the book wants to make students familiar with relevant original literature in a time when the number of journals and publications expands exponentially and is overgrowing seminal and fundamental papers of the past. Research politics enforces publishing, and hence writing own papers has gained priority to studying other people's publications. The consequences for research and science are obvious. The total number of papers increases but the number of really significant

publications does not, making it difficult to separate the wheat from the chaff, particularly for students, young engineers and scientists.

Not least, the motivation for compiling this book results from experiences with reading and reviewing manuscripts submitted to scientific journals, in which similar misconceptions of established concepts reappear regularly and identical problems are solved again and again by young scientists who are not thoroughly advised by senior scientists. It is alarming which weird opinions about the *J*-integral and its path dependence in incremental plasticity can still be found in the literature and in computer manuals 50 years after its introduction into fracture mechanics. Manuscripts on correction terms of *J* for multiphase materials are submitted periodically. If the present book could help bringing some light into obscurity, the author would be delighted.

On the background of its history, the present book could not have been written without the valuable help, cooperation and assistance of many colleagues along my professional career, starting with Georgia Künecke and Dieter Noack at BAM Berlin, Knut Burth and Jürgen Olschewski jointly lecturing plasticity and fracture mechanics at the TU in Berlin, and ending with Ingo Scheider, Dirk Steglich and Manfred Schödel at GKSS (now Helmholtz Centre) Geesthacht, just to mention the most outstanding. I acknowledge their contributions whose merit and value are greater than references of their publications in the bibliography can express.

Geesthacht, Germany Wolfgang Brocks
June 2017

Contents

Nomenclature

Capital Latin Symbols

A	Area
$\tilde{A}$	Effective area in CDM
A_c	Crack area
B	Specimen thickness
$\mathcal{B}$	Body, material domain
$\partial\mathcal{B}$	Boundary of $\mathcal{B}$
$\{B\} = \{B_{\alpha\beta}\}$	Matrix of elastic moduli (α, β = I, II, III) relating energy release rate and SIFs, Eq. (7.6)
C	Compliance
D	Scalar damage parameter
D_n	Parameter of CTOD in HRR solution, Eq. (5.70)
E	Young's modulus
E'	Modified Young's modulus depending on lateral constraint, Eq. (2.2)
$E(k)$	2nd kind elliptical integral, Eq. (2.37)
F	Force
$\mathbf{F}(\mathbf{x},t)$	(column matrix of) Mechanical impact data (forces, temperature, …), Sect. 8.5
G	Shear modulus
$\mathcal{G} = -\partial U/B\,\partial a$	Energy release rate (Griffith)
$\mathcal{G}_I$, $\mathcal{G}_{II}$, $\mathcal{G}_{III}$	Energy release rates for modes I, II, III
$\mathcal{G}_\theta$	Energy release rate for a (virtual) crack extension under an angle θ
I_n	Parameter in HRR stress equations, Eq. (5.66)
J	J integral of Cherepanov and Rice, Eq. (5.20)
ΔJ	"Cyclic" J-integral, Eq. (5.79)
J_i	J value at initiation of crack extension
J_1, J_2, J_3	Components of the J vector, Eq. (5.15)

$\mathbb{J}_2\left(\sigma'_{ij}\right)$, $\mathbb{J}_3\left(\sigma'_{ij}\right)$	Invariants of deviatoric stress tensor, Eq. (3.19)
K	Bulk modulus (Table 3.1)
$K_\mathrm{r} = K/K_\mathrm{c}$	Normalised SIF in FAD
K_I, K_II, K_III	Stress-intensity factors for modes I, II, III
$K^{\mathrm{aux}}_{\mathrm{I,II,III}}$	Auxiliary SIFs in the interaction integral method
K_Ic	(plane strain) Fracture toughness
$K_\mathrm{I}^{\mathrm{eff}}$	Effective SIF in mode I according to Irwin, Eq. (4.6)
K_σ	Intensity parameter of HRR stress field in EPFM
$\{\mathrm{K}\} = \{K_\alpha\}$	Column matrix of stress-intensity factors (α = I, II, III)
L	Length
L_0	Initial length
L_pl	Plastic constraint factor
$L_\mathrm{r} = F/F_\mathrm{pl}$	Normalised force in FAD
M_b	Bending coefficient for semi-elliptical surface cracks, ASTM BPVC
M_m	Membrane coefficient for semi-elliptical surface cracks, ASTM BPVC
N	Number of cycles in Eq. (2.19), power-law exponent in Eq. (5.83)
P_f	Failure probability
P_{ij}	Energy momentum tensor
Q	Q-stress, Eq. (5.73)
$Q(k)$	Elliptical shape factor, Eq. (4.10)
$\mathbf{R}(\mathbf{x},t)$	(column matrix of) Structural response data, Sect. 8.5
$R_0 = R_\mathrm{F}(0)$	(uniaxial) Yield strength
R'_0	Modified yield strength depending on lateral constraint, Eq. (4.8)
$R_\mathrm{eff} = 0.5(R_0+R_\mathrm{m})$	"Effective" yield strength
R_eL	Lower yield point
$R_\mathrm{F}(\varepsilon_\mathrm{p})$	(uniaxial) Flow curve
R_f	Parameter in Rousselier's model, Eq. (8.27)
R_m	Tensile strength (nominal stress at maximum force)
R_p	Proof stress
S	Surface
$S_\mathrm{p} = R_\mathrm{F}/\varepsilon_\mathrm{p}$	Plastic secant modulus
T	T-stress, Eq. (2.22)
$T_\mathrm{p} = dR_\mathrm{F}/d\varepsilon_\mathrm{p}$	Plastic tangent modulus
U	Potential energy
$U^\mathrm{e} = \int\int \sigma_{ij}\dot{\varepsilon}^\mathrm{e}_{ij}\, dt\, dV$	Elastic strain energy
U_dis	Dissipated energy
U_rel	Released potential energy due to cracking
U_sep	Work of separation, separation energy

V	Volume
∂V	Boundary (surface) of V
W	Width of edge-cracked specimens, half width for centre-cracked specimens
$Y(a/W,\ldots)$	Geometry function of SIF, Eq. (2.25)
Y	Energy release rate density, internal state variable work-conjugate to damage D

Small Latin Symbols

a	Crack length for edge cracks, half crack length for centre cracks, crack depth of surface flaws
a_{eff}	Effective crack length for SSY, Eq. (4.5)
$b = W-a$	Ligament width
$\mathbf{c}$	(column matrix of) Material parameters (Sect. 8.5)
c	Half crack length of surface flaws, half fictitious crack length in Dugdale's model
d	Diameter
d_n	Proportionality factor between J and δ_{t}, Eq. (5.69)
$d_{\text{p}} = 2x_{\text{p}}$	Size of plastic zone in the ligament according to SSY
$\mathbf{e}_i$	Unit vectors along coordinates
f_i	Volume (or body) forces
$f_{ij}(\theta)$	Angular functions of asymptotic stress fields in LEFM
f_{v}	Void volume fraction or porosity, Eq. (8.18)
f_{v}^{c}	Critical void volume fraction at the onset of void coalescence
f_{v}^{f}	Void volume fraction at final failure
f_{v}^{0}	Initial void volume fraction
f_{u}^{*}	Ultimate value of modified damage parameter in GTN model
f_{v}^{*}	Modified damage parameter of the GTN model, Eq. (8.21)
f_{ϕ}	Elliptical shape function
$g_i(\theta)$	Angular functions of asymptotic displacement fields in LEFM
h	(element) Height
$h_j(\phi)$	Geometry functions for semi-elliptical surface cracks
$k = a/c$	Aspect ratio
m	Weibull exponent
n	Exponent in Paris law, Eq. (2.19), hardening exponent in Ramberg–Osgood power law, Eq. (3.48)
$\mathbf{n} = n_i\ \mathbf{e}_i$	Unit normal vector
$\mathbf{n}_{\text{I}}$, $\mathbf{n}_{\text{II}}$, $\mathbf{n}_{\text{III}}$	Unit vectors along principal coordinates

p	Pressure
q_1, q_2, q_3	Adjustable parameters of the GTN model, Eq. (8.20)
r_i, r_o	Inner, outer radius of a cylinder
r, θ, z	Cylindrical coordinates at crack-tip
r, φ, z	Cylindrical coordinates
s	Exponent of singularity in HRR field, Eq. (5.53)
s_c	Arc length of crack front
$s_{ij} = \sigma_{ij} - \xi_{ij}$	(components of) Effective stress tensor, Eq. (3.17)
$\bar{s} = \sqrt{\frac{3}{2}\bar{\Phi}\left(s'_{ij}\right)}$	Equivalent uniaxial effective stress
t	Time, scalar loading parameter in incremental plasticity
$t = r_\mathrm{o} - r\mathrm{i}$	Wall thickness of cylinders
t_i	Surface forces, tractions
$\mathbf{u} = u_i\,\mathbf{e}_i$	Displacement vector (field)
$\tilde{u}_i(\theta)$	Dimensionless angular functions of asymptotic displacement fields in EPFM
v_L	Load point displacement
v_LL	Load line displacement, C(T) specimen
$\bar{w} = \int \sigma_{ij}\dot{\varepsilon}_{ij}dt$	Strain energy density
$\dot{\bar{w}}^\mathrm{p} = \sigma_{ij}\dot{\varepsilon}^\mathrm{p}_{ij}$	Plastic dissipation rate density
$\mathbf{x}$	Spatial coordinates of material points in a body
x, y, z	Cartesian coordinates
x_c	Characteristic distance from crack-tip in RKR model
x_p	Half size of plastic zone in the ligament in SSY

Greek Symbols

α	Parameter of Ramberg–Osgood power law, Eq. (3.48)
α_{ij}	Internal state variables conjugate to back stresses ξ_{ij}
α_th	Coefficient of thermal expansion
Γ	Contour of J-integral
$\Gamma_\mathrm{c} = 2\gamma = \partial U_\mathrm{sep}/\partial A_\mathrm{c}$	Separation energy per cracked area
γ	Surface energy
Δ	Increment
δ	Crack opening displacement (COD), separation in TSL
$\boldsymbol{\delta}$	Separation vector (cohesive model)
δ_{ij}	Kronecker symbol, identity tensor
δ_n, δ_t, δ_s	Normal and shear separations in cohesive model
δ_t	Crack-tip opening displacement (CTOD)
δ_5	CTOD according to Schwalbe, Fig. 5.17
$\varepsilon = \Delta L/L_0$	Normal strain, elongation
E_{ij}	Mesoscopic strains

$\varepsilon_{ij} = \partial u_i / \partial x_j$	Strains, (components of) linear strain tensor
$\varepsilon'_{ij} = \varepsilon_{ij} - \varepsilon_{kk}\delta_{ij}$	Deviatoric strains
$\bar{\varepsilon}^{\mathrm{p}}$	Accumulated (equivalent) plastic strain
$\dot{\bar{\varepsilon}}^{\mathrm{p}}_{\mathrm{vM}} = \sqrt{\frac{2}{3}\dot{\varepsilon}^{\mathrm{p}}_{ij}\dot{\varepsilon}^{\mathrm{p}}_{ij}}$	Equivalent plastic strain rate, work-conjugate to von Mises equivalent stress
ε_0	Normalising parameter of Ramberg–Osgood power law, Eq. (3.47), strain at onset of yielding
ε_{f}	Failure or fracture strain
$\widehat{\varepsilon}_{ij}(\theta)$	Dimensionless angular functions of asymptotic strain fields in EPFM (HRR field)
ζ	(dimensionless) Load factor
$\eta = \sigma_{\mathrm{h}}/\bar{\sigma}$	Triaxiality of stress state
η_J	η-factor for plastic J of bend specimens
Θ	Temperature
θ	Angular coordinate at crack-tip
κ	Factor characterising elastic in-plane deformation in dependence on lateral constraint, Eq. (2.3)
κ_{f}	Parameter of modified damage in GTN model, Eq. (8.22)
$\bar{\kappa}$	Radius of flow cylinder
$\lambda = \sigma^{\infty}_{xx} / \sigma^{\infty}_{yy}$	Biaxiality factor
λ, μ	Lamé's coefficients (Table 3.1)
λ_{p}	Plastic multiplier (finite plasticity)
$\dot{\lambda}_{\mathrm{p}}$	Plastic multiplier (incremental plasticity)
$\lambda_{\mathrm{s}} = a/\sqrt{r_{\mathrm{i}}t}$	Shell parameter
ν	Poisson's ratio
Φ	Yield function, Eq. (3.10), plastic potential, dissipation potential in CDM
Φ_{coh}	Potential of cohesive law (TSL), Eq. (9.19)
φ	Angular coordinate
ϕ	Parametric angle for semi-elliptical surface crack, orientation of maximum shear stress in slip-line theory
$\sigma = F/A$	Uniaxial, tensile stress
$\boldsymbol{\sigma}$	Traction vector (cohesive model)
σ^{∞}, σ_{∞}	Remote nominal tensile stress
$\bar{\sigma}$	Equivalent uniaxial stress
$\bar{\sigma}_{\mathrm{T}}$	Equivalent stress according to Tresca
$\bar{\sigma}_{\mathrm{vM}} = \sqrt{3J_2}$	Equivalent von Mises stress
σ_0	Normalising parameter of Ramberg–Osgood power law
σ_{b}	Bending part of stress distribution, ASME BPVC
σ_{c}	Cleavage fracture stress in RKR model
$\sigma_{\mathrm{h}} = \frac{1}{3}\sigma_{kk}$	Hydrostatic stress
Σ_{ij}	Mesoscopic stresses

σ_{ij}	(true) Stresses, (components of) Cauchy stress tensor
$\sigma'_{ij} = \sigma_{ij} - \sigma_h \delta_{ij}$	Deviatoric stresses
$\widehat{\sigma}_{ij}(\theta)$	Dimensionless angular functions of asymptotic stress fields in EPFM (HRR field)
$\tilde{\sigma}_{ij}$	Effective stresses in CDM (Sect. 8.4)
σ_m	Membrane part of stress distribution, ASME BPVC
σ_n, σ_t, σ_s	Normal and shear tractions in cohesive model
σ_u	Reference stress in Weibull distribution of failure probability, Eq. (8.6)
σ_W	Weibull stress, Eqs. (8.7), (8.8)
σ_I, σ_{II}, σ_{III}	Principal stresses
τ	Shear stress
τ^∞, τ_∞	Remote nominal shear stress
$\tau_0 = \tau_F(0)$	Shear strength
$\tau_F(\varepsilon_p)$	Shear flow curve
ξ_{ij}	(components of) back stress tensor
Ψ	Airy's stress function
ψ	Crack-tip opening angle (CTOA)

Subscripts and Superscripts

c	Critical, characteristic (material parameter), crack
coh	Cohesive
dis	Dissipation, dissipated
e	Elastic
eff	Effective
el	Elastic limit
f	Fracture, failure
i	Initiation of crack extension
i, j, k	Indices of coordinates or components of vectors or tensors
k	Kinematically possible mechanism (Chap. 6)
L	Load point
LL	Load line
max	Maximum
min	Minimum
mod	Model
n	Normal
net	Net section
p	Plastic
pc	Plastic collapse (Chap. 6)
pl	Plastic limit
rel	Released

s	Safe state (Chap. 6), tangential (out of plane)
sa	Statically admissible stress field (Chap. 6)
sep	Separation
t	Tangential (in-plane), (crack) tip
T	Tresca
vM	Von Mises
0	Initial, reference
∞	"Infinite", far-field, remote
I, II, III	Fracture modes I, II, III, principal directions of tensors

Acronyms

ASME	American Society of Mechanical Engineers
ASTM	American Society for Testing and Materials
bcc	Body-centred cubic
BPVC	Boiler and Pressure Vessel Code
BS	British Standards
BSI	British Standards Institution
COD	Crack opening displacement
CMOD	Crack-mouth opening displacement
CTOA	Crack-tip opening angle
CTOD	Crack-tip opening displacement
C(T)	Compact specimen
DE(T)	Double edge crack in tension
ESIS	European Structural Integrity Society
EPFM	Elastic–plastic fracture mechanics
EPRI	Electrical Power Research Institute
ETM	Engineering treatment model
FAD	Failure assessment diagram
fcc	Face-centred cubic
FE	Finite element
FEM	Finite element method
FITNET	Fitness-for-Service Network
HRR	Hutchinson, Rice, Rosengren
ISO	International Standards Organization
LEFM	Linear elastic fracture mechanics
LBB	Leak before break
LCF	Low-cycle fatigue
M(T)	Middle crack in tension
PS(T)	Part-through surface crack in tension
RKR	Ritchie, Knott, Rice
RVE	Representative volume element
SE(B)	Single edge crack in bending

SE(T)	Single edge crack in tension
SIF	Stress-intensity factor
SSY	Small-scale yielding
TSL	Traction–separation law (cohesive model)
TWI	The Welding Institute
VCE	Virtual crack extension

Chapter 1
Introduction

Abstract The general concept of the present book is outlined. A survey of its contents and background are given. The motivation for selecting its topics and their practical relevance for structural assessment are specified. Some references for supplementing textbooks are presented.

There could be no better introductory statement to a book concerned with strength of materials than that of Timshenko [10]: "*From the earliest times when people started to build, it was found necessary to have information regarding the strength of structural materials so that rules for determining safe dimensions of members could be drawn up*." Modern concepts of structural assessment and stress analysis date back to the conceptual inspiration of Navier and Cauchy who established the notion of stresses and strains in the beginning 19th century. With the emerging theory of elasticity, structural components of different shapes under various loading conditions could now be mathematically analysed with respect to the resulting deformations based on Young's modulus of elasticity, which was obtained in a simple test. Two serious limitations were encountered, however: deformation beyond the elastic limit and fracture. The concept of "admissible" stresses governing structural design until the mid 20th century, at least, limited the maximum stresses in a structure which were calculated by the theory of elasticity to either the "yield strength" or the "tensile strength". While the latter is dubious because the respective value is no material constant, the former may result in undesirable conservatism of the design. Brittle fracture is not captured by either of these limits, anyway.

Two new areas transcending these limits arose in the 20th century, namely plasticity and fracture mechanics. The latter began as a special subject within the theory of elasticity analysing stress fields at singularities by means of advanced mathematical techniques like series expansions, complex stress functions or integral transforms. Engineering applications of "linear elastic fracture mechanics" (LEFM) emerged after World War II particular with the upcoming nuclear industry. The theory of plasticity developed in parallel and found industrial applications as limit design concept primarily for steel constructions in civil engineering after 1970,

W. Brocks, *Plasticity and Fracture*, Solid Mechanics and Its Applications 244,
DOI 10.1007/978-3-319-62752-6_1

but only rather recent developments of numerical methods and computer capacities promoted more general implementations.

It was inevitable that both subjects met and merged together in the last quarter of the 20th century when the limits of LEFM where encountered, partly because structural materials became more and more ductile and hence LEFM based toughness values obsolete, and partly because new demands with respect to light-weight design appeared. Last not least, the progress in numerical methods and computer science laid the cornerstone for tackling the new task.

This is the motive and starting point of the present book. It is no text book on plasticity and does not claim to be one. There are others more detailed, extensive, and substantial like Kachanov [5], Chakrabarty [4] or Khan and Huang [6]. It provides an introduction into fundamental concepts of the classical rate and time independent theory of plasticity as deep as necessary to understand non-linear fracture mechanics. Neither is it a comprehensive book on fracture mechanics like the monographs of Broek [3], Andersson [1], Saxena [9] or Broberg [2], which is just due to its rather small volume which enforces restrictions. Instead, it exceeds the common frontiers of classical fracture mechanics by advancing into damage mechanics and cohesive models to illuminate present-day developments and approaches.

Lemaitre and Chaboche [7] and Maugin [8] elaborated the thermodynamics of material behaviour in general and plasticity and fracture in particular. Apart from the advancements during the last 25 years, particularly in numerical modelling, becoming manifest in the ever increasing literature, engineers might miss practical aspects of structural assessment and standardisation. Some sections of the present book are hence particularly concerned with the background of present-day assessment procedures and ASTM standards for fracture testing.

Putting this spectrum into one book of less than 200 pages requires serious restrictions. The presentation focuses on quasi-static loading and failure by either plastic collapse or static fracture. Neither high-cycle fatigue nor creep fracture are addressed, and just some remarks on alternating plasticity (low-cycle fatigue) are included.

Finally, the author would be happy if he had helped students and engineers to an interdisciplinary view of plasticity and fracture and motivated them to have a look into some of the books listed below or read the original and historic papers in the detailed bibliography of the respective chapters. There is more of present relevance to be found there than some people seem to believe.

References

1. Andersson TL (1991) Fracture mechanics—fundamentals and applications. CRC Press, Florida
2. Broberg KB (1999) Ctracks and fracture. Acad Press, London
3. Broek D (1988) The practical use of fracture mechanics. Kluwer Acad Publ, Dordrecht

4. Chakrabarty J (1987) Theory of plasticity. McGraw-Hill, New York
5. Kachanov LM (1971) Foundations of the theory of plasticity. North Holland Publ Comp, Amsterdam
6. Khan A, Huang SJ (1995) Continuum theory of plasticity. Wiley, New York
7. Lemaitre J, Chaboche JL (1990) Mechanics of solid materials. Cambridge University Press, Cambridge
8. Maugin GA (1992) The thermomechanics of plasticity and fracture. Cambridge University Press, Cambridge
9. Saxena A (1997) Nonlinear fracture mechanics for engineers. CRC Press, Florida
10. Timoshenko SP (1983) History of strength of materials. Dover Publ, New York

Chapter 2
Concepts of Fracture Mechanics

Abstract To begin with, linear elastic behaviour is assumed to explicate the basic concepts of fracture mechanics, namely energy and stress intensity approaches. The respective terminology is introduced and the physical quantities of energy release rate and stress intensity factor are defined. Criteria for unstable "brittle" fracture based on the energy release rate and the stress intensity factor are established. Some analytical expressions for stress intensity factors of real structures are given and the problem of a cracked cylinder under internal pressure is addressed, in particular.

Classical fracture mechanics is based on the theory of continuum mechanics and constitutive equations for stable material behaviour (see Sect. 6.1.1 on stability postulates) like elasticity, plasticity or viscoplasticity. It does not account for any damage of the material preceding crack growth or any kind of material separation. It postulates the existence of a defect or crack in a body or structure and either analyses stress and strain fields at the "crack tip", which is a singular point, or considers the energy balance of cracked and uncracked media to derive "crack driving forces" and respective criteria of crack extension. For actually modelling crack growth, the topology of the body has to be modified.

Generally, two basic concepts of classical fracture mechanics have been established, the energy and the stress intensity approach, which are outlined in the following for linear-elastic material behaviour, first, and extended to elasto-plasticity later (see Chap. 5 on elastic-plastic fracture mechanics).

Linear-elastic fracture mechanics (LEFM) is based on Hooke's equation postulating a linear relationship between stresses, σ_{ij}, and strains, ε_{ij},

$$\varepsilon_{ij} = \frac{1}{E}\left[(1+\nu)\sigma_{ij} - \nu\sigma_{kk}\delta_{ij}\right] \tag{2.1}$$

with E being Young's modulus and ν Poisson's ratio, under the assumption of small deformations. The latter is actually not consistent with strain singularities occurring at a crack tip but it is essential for closed form solutions which represent a model of the conditions governing the physical state in some process zone of material degradation where the requirements of continuum mechanics are not met, anyway.

W. Brocks, *Plasticity and Fracture*, Solid Mechanics and Its Applications 244,
DOI 10.1007/978-3-319-62752-6_2

Table 2.1 Fundamental modes of crack displacements

Mode	Local appearance	Types of loading
Mode I	Opening of crack faces under tensile stresses normal to the crack plane	Loading by normal forces or bending, wedging of crack faces
Mode II	Slipping of crack faces along ligament	Pure shear forces, Inclined crack by 45° under biaxial tension-compression forces, Cutting and stamping processes
Mode III	Out-of-plane shearing	Torsion, anti-plane tearing

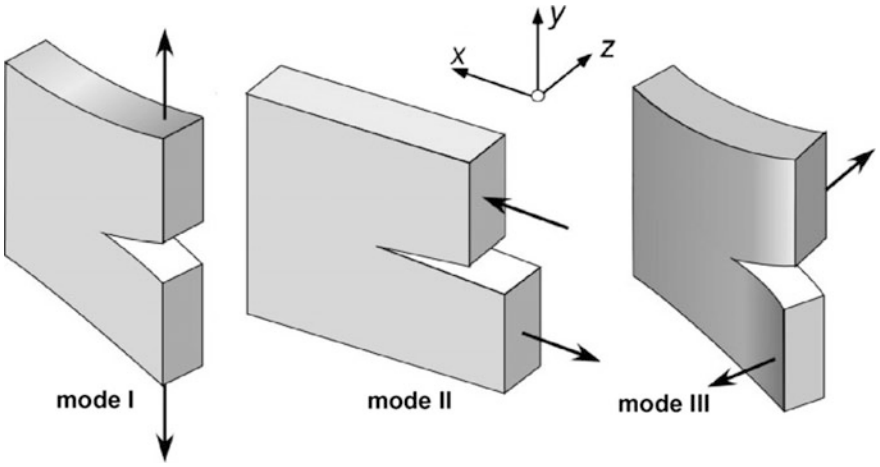

Fig. 2.1 Fundamental modes of crack displacements according to Irwin [17]

Aside from inner circular (penny shaped) or elliptical cracks investigated by Sneddon [35] and Irwin [18], respectively, most analytical models of cracked bodies are two-dimensional. They represent panels of arbitrary in-plane shape but constant thickness, B, with through-thickness cracks. Irwin [17] identified three fundamental modes of crack displacements, Table 2.1 and Fig. 2.1. Loading in mode I and mode II is in-plane, and in mode III is out-of-plane. Mode I configurations are particularly important in engineering practice (pressure vessels, bending of beams) and hence most frequently investigated.

The out-of-plane boundary conditions for panels in mode I or II is either plane strain (zero lateral strain, $\varepsilon_{zz} = 0$) or plane stress (zero lateral stress, $\sigma_{zz} = 0$), respectively, which are the limiting cases for very thick or very thin panels. The out-of-plane condition affects the in-plane deformation owing to Poisson's ratio, ν, which is captured by a modified Young's modulus,

$$E' = \begin{cases} \frac{E}{1-\nu^2} & \text{for plane strain, } \varepsilon_{zz} = 0 \\ E & \text{for plane stress, } \sigma_{zz} = 0 \end{cases}. \tag{2.2}$$

and a factor κ, defined as

$$\kappa = \begin{cases} 3 - 4\nu & \text{for plane strain, } \varepsilon_{zz} = 0 \\ \frac{3-\nu}{1+\nu} & \text{for plane stress, } \sigma_{zz} = 0 \end{cases}. \tag{2.3}$$

Extensions to "real" three-dimensional configurations will be addressed as required.

2.1 The Energy Approach of Griffith

The first one ever studying a cracked structure as an engineering problem was Griffith [11, 12], who treated the occurrence of fracture by the theorem of minimum energy and applied this theory to an "infinite" panel with a centre crack of length $2a$ under biaxial tension, see Fig. 2.2, where "infinite" indicates that the panel width, $2\ W$, is very large compared to the crack size, $a/W \ll 1$. This configuration is known as Griffith crack, since.

The elastic strain energy which is stored in a circular region of radius W of a panel without a crack is

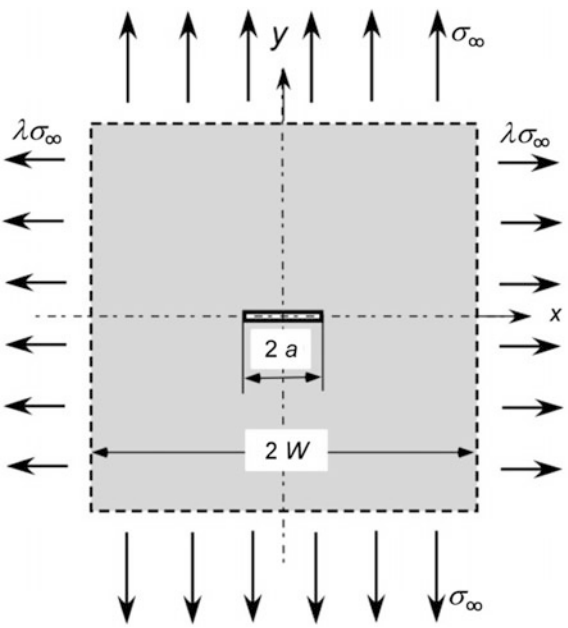

Fig. 2.2 The Griffith crack: centre crack of length 2a in an "infinite" panel ($W \gg a$) under biaxial tension

$$U_0^{\mathrm{e}} = \frac{\pi B W^2 \sigma_\infty^2}{16G}\left[(\kappa-1)(1+\lambda)^2 + 2(1-\lambda)^2\right], \tag{2.4}$$

where B is the panel thickness, σ_∞ the applied uniform far-field stress, $G = E/2(1+\nu)$ the shear modulus and λ the biaxiality factor.

The strain energy depends on the size of the panel and becomes infinite for $W \to \infty$. If a hole is cut into the panel, stress and strain fields change and so does the strain energy. It increases or decreases depending on the boundary conditions. Assuming a constant far-field displacement, that is fixed grip, energy is released,

$$U^{\mathrm{e}} = U_0^{\mathrm{e}} - U_{\mathrm{rel}}^{\mathrm{e}}. \tag{2.5}$$

The decrease of strain energy due to an elliptical hole with principal axes $2a$ and $2c$ can be calculated with the equations of Inglis [16] as

$$U_{\mathrm{rel}}^{\mathrm{e}} = \frac{\pi B \sigma_\infty^2}{32G}(1+\kappa)\left[(1-\lambda)^2(a+c)^2 + 2\left(1-\lambda^2\right)\left(a^2-c^2\right) + (1+\lambda)^2\left(a^2+c^2\right)\right]. \tag{2.6}$$

It depends only on the dimensions of the hole and is always finite. The Griffith crack of length $2a$ is obtained for $c \to 0$,

$$U_{\mathrm{rel}}^{\mathrm{e}} = \frac{\pi a^2 B \sigma_\infty^2}{8G}(1+\kappa). \tag{2.7}$$

Stresses $\lambda\sigma_\infty$ parallel to the crack do not affect the released energy.

Now Griffith established a condition for the crack to grow, which balances the released energy and the material resistance to crack extension,

$$\frac{\partial}{B\,\partial(2a)}\left(U_{\mathrm{rel}}^{\mathrm{e}} - U_{\mathrm{sep}}\right) \geq 0. \tag{2.8}$$

Note that the Griffith crack has a length of $2a$ with two crack tips. The second term, U_{sep}, the work of separation, equals the surface energy per unit thickness of the four crack faces,

$$U_{\mathrm{sep}} = 4Ba\gamma. \tag{2.9}$$

Griffith [11] offered the following argument for his quite unconventional idea of the specific surface energy, γ: "*Just as in a liquid, so in a solid the bounding surfaces possess a surface tension which implies the existence of a corresponding amount of potential energy. If owing to the action of a stress a crack is formed, or a pre-existing crack is caused to extend, therefore, a quantity of energy proportional to the area of the new surface must be added*".

An existing crack will start to extend in an unstable manner if the equality sign in Eq. (2.8) holds, i.e. if the energy release rate,

$$\mathcal{G} = -\frac{\partial U^{\mathrm{e}}}{B\,\partial(2a)} = \frac{\partial U^{\mathrm{e}}_{\mathrm{rel}}}{B\,\partial(2a)} = \frac{\pi a \sigma_{\infty}^2}{8G}(1+\kappa), \tag{2.10}$$

equals the work of separation (sometimes also called separation energy) per increment of crack area,

$$\frac{\partial U_{\mathrm{sep}}}{B\,\partial(2a)} = 2\gamma = \Gamma_{\mathrm{c}}, \tag{2.11}$$

which is necessary to create two new crack surfaces (at each crack tip),

$$\mathcal{G}(a) = \Gamma_{\mathrm{c}}. \tag{2.12}$$

This is Griffith's criterion for the onset of unstable crack extension. It balances an "applied" quantity, $\mathcal{G}$, which depends on the geometry of the structure and the crack as well as external loading with a characteristic material parameter, Γ_{c}. For $\mathcal{G} < \Gamma_{\mathrm{c}}$, the structure is "safe", i.e. the crack will not grow. Note that crack extension under linear elastic (brittle) conditions occurs in an unstable manner, always, since different from plastic behaviour there is no other dissipative term in the energy balance.

Equation (2.12) yields the macroscopic fracture stress of the centre-cracked panel in plane strain as

$$\sigma_{\mathrm{f}}^{\infty} = \sqrt{\frac{2E'\gamma}{\pi a}}. \tag{2.13}$$

2.2 The Stress-Intensity Approach of Irwin

The stress field at the crack tip is commonly described in dependence on the polar coordinates r, θ, Fig. 2.3.

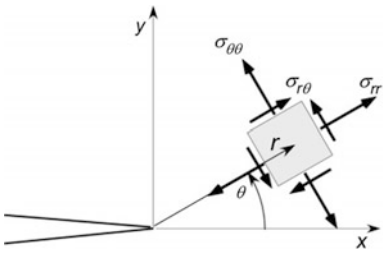

Fig. 2.3 Cartesian (x, y) and cylindrical (r, θ) coordinates and stresses at the crack tip

Though fundamental solutions of stress fields at singularities in elastic media were published in the early and mid 20th century, already, [16, 35, 38], this knowledge did not find its way into the design of engineering structures. It was Irwin [17] who first realised the essential resemblance of all asymptotic singular stress fields at crack tips and concluded to use the intensities of these fields for fracture mechanics based assessments of structural integrity. Actually, the asymptotic stress fields exhibit a $1/\sqrt{r}$ singularity for all crack opening modes which is governed by a stress intensity factor (SIF). Due to the assumption of linear elastic material behaviour and small deformations, the respective fields of all three modes can be superimposed,

$$\lim_{r\to 0}\sigma_{ij}(r,\theta)=\frac{1}{\sqrt{2\pi r}}\left[K_{\mathrm{I}}f_{ij}^{\mathrm{I}}(\theta)+K_{\mathrm{II}}f_{ij}^{\mathrm{II}}(\theta)+K_{\mathrm{III}}f_{ij}^{\mathrm{III}}(\theta)\right]. \tag{2.14}$$

The subscripts i, j indicate Cartesian or cylindrical coordinates.

- K_{I}, K_{II}, K_{III} are the SIFs of the three crack opening modes depending on the geometry of the structure and the crack as well as on the external forces.
- $f_{ij}^{\mathrm{I}}, f_{ij}^{\mathrm{II}}, f_{ij}^{\mathrm{III}}$, are dimensionless angular functions of θ; the first two are graphically displayed in Fig. 2.4. The distribution of normal stresses, σ_{xx}, σ_{yy}, is symmetric to the ligament, $\theta = 0$, that of shear stresses, σ_{xy}, antisymmetric in mode I; for mode II it is the other way round. Note that the maximum of stresses, σ_{yy}, in opening direction is not in the ligament but at $\pm 60°$.

The associated displacement field is given as

$$u_i(r,\theta)=\frac{1}{2G}\sqrt{\frac{r}{2\pi}}\left[K_{\mathrm{I}}g_i^{\mathrm{I}}(\theta)+K_{\mathrm{II}}g_i^{\mathrm{II}}(\theta)+K_{\mathrm{III}}g_i^{\mathrm{III}}(\theta)\right], \tag{2.15}$$

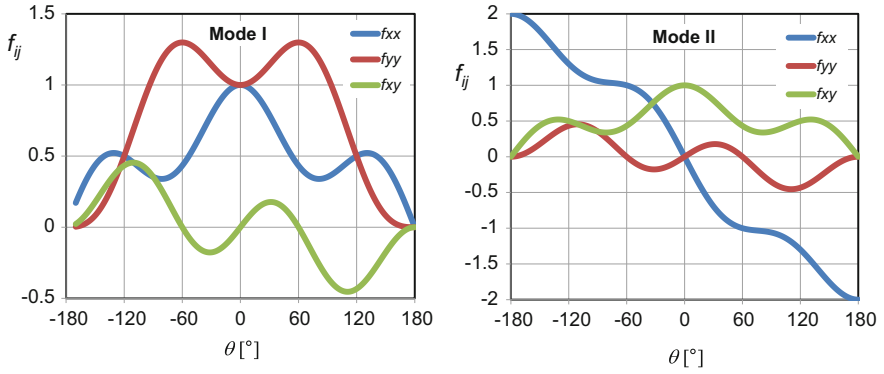

Fig. 2.4 Angular functions of stress fields in Cartesian coordinates at the crack tip in LEFM for mode I and II

Table 2.2 Angular functions of stress and displacement fields in Cartesian coordinates at the crack tip in LEFM

	Mode I	Mode II	Mode III
f_{xx}	$\cos\frac{\theta}{2}\left(1-\sin\frac{\theta}{2}\sin\frac{3\theta}{2}\right)$	$-\sin\frac{\theta}{2}\left(2-\cos\frac{\theta}{2}\cos\frac{3\theta}{2}\right)$	0
f_{yy}	$\cos\frac{\theta}{2}\left(1+\sin\frac{\theta}{2}\sin\frac{3\theta}{2}\right)$	$\sin\frac{\theta}{2}\cos\frac{\theta}{2}\cos\frac{3\theta}{2}$	0
f_{zz}	$\begin{matrix}0 & \text{plane stress}\\ 2\nu\cos\frac{\theta}{2} & \text{plane strain}\end{matrix}$	$\begin{matrix}0 & \text{plane stress}\\ -2\nu\sin\frac{\theta}{2} & \text{plane strain}\end{matrix}$	0
f_{xy}	$\sin\frac{\theta}{2}\cos\frac{\theta}{2}\cos\frac{3\theta}{2}$	$\cos\frac{\theta}{2}\left(1-\sin\frac{\theta}{2}\sin\frac{3\theta}{2}\right)$	0
f_{xz}	0	0	$-\sin\frac{\theta}{2}$
f_{yz}	0	0	$\cos\frac{\theta}{2}$
g_x	$\cos\frac{\theta}{2}\left[\kappa-1+2\sin^2\frac{\theta}{2}\right]$	$\sin\frac{\theta}{2}\left[\kappa+1+2\cos^2\frac{\theta}{2}\right]$	0
g_y	$\sin\frac{\theta}{2}\left[\kappa+1-2\cos^2\frac{\theta}{2}\right]$	$-\cos\frac{\theta}{2}\left[\kappa-1-2\sin^2\frac{\theta}{2}\right]$	0
g_z	0 for plane strain	0 for plane strain	$4\sin\frac{\theta}{2}$

where G is the shear modulus and g_i^{I}, g_i^{II}, g_i^{III} are respective angular functions again. Displacements are not singular at the crack tip, of course, but vanish for $r \to 0$.

Table 2.2 summarises all angular functions for the three modes.

Irwin also depicted the relationship between the stress intensity and the energy approach by deriving that

$$\mathcal{G} = \frac{K_{\mathrm{I}}^2}{E'}. \tag{2.16}$$

Corresponding to Griffith's Eq. (2.12), a criterion for unstable "brittle" fracture in LEFM can be established based on the SIF,

$$K_{\mathrm{I}}(a) = K_{\mathrm{Ic}}, \tag{2.17}$$

which balances an "applied" quantity, K_{I}, depending on the geometry of the structure and the crack as well as external loading with a characteristic material parameter, the "fracture toughness", K_{Ic}. For $K_{\mathrm{I}} < K_{\mathrm{Ic}}$, the structure is "safe", i.e. the crack will not grow. The fracture toughness has to be experimentally determined according to standards like ASTM E399 [4]. For further details see Sect. 7.2.2 on linear-elastic plane-strain fracture toughness.

More generally, the energy release rate in mixed mode results from the SIFs by

$$\mathcal{G} = \mathcal{G}_{\mathrm{I}} + \mathcal{G}_{\mathrm{II}} + \mathcal{G}_{\mathrm{III}} = \frac{K_{\mathrm{I}}^2}{E'} + \frac{K_{\mathrm{II}}^2}{E'} + \frac{K_{\mathrm{III}}^2}{2G}. \tag{2.18}$$

Together with Eq. (2.12), this relation suggests a simple fracture criterion for mixed mode [14, 15], which is not always confirmed by experiments, however. Other criteria have been proposed by Erdogan and Sih [9], Sih [34] or Richard and Kuna [31], for instance. An extensive literature exists on mixed mode problems which are still a matter of research. Further details would overshoot the purpose of the present book.

Likewise, any up-to-date overview on fatigue crack growth would exceed the self-established limits and this issue is solely mentioned to demonstrate the wide application range of the *K*-concept. Paris and Erdogan [26] correlated the rate of crack extension, *da/dN*, where *N* is the number of loading cycles, with the cyclic stress intensity factor, $\Delta K = K_{\max} - K_{\min}$, and found a power law relationship

$$\frac{da}{dN} \sim \Delta K^n, \tag{2.19}$$

where the exponent, n, for many metallic materials is typically between 2 and 4. Enhancements of this "Paris-equation" include effects of the mean stress, crack closure effects etc.

A final remark appears necessary on so-called "higher-order" approaches. For simplicity and because the singular terms of the stress fields, Eq. (2.14), appeared to be dominant, Irwin and his successors restricted to the SIFs (or the energy release rate, $\mathcal{G}$) as crack driving forces. Irwin, however, was aware that the asymptotic stress field included a second non-vanishing parameter for $r \to 0$: "*The influence of the test configuration, loads and crack length upon the stresses near an end of the crack may be expressed in terms of two parameters. One of these is an adjustable uniform stress parallel to the direction of a crack extension…. The other parameter, called the stress intensity factor, is proportional to the square root of the force tending to cause crack extension*". Williams [39] presented a series expansion of the stress field for the biaxially loaded Griffith crack, in which

$$\sigma_{xx} = \frac{A_{-1}}{\sqrt{r}} \cos\frac{\theta}{2}\left(1 - \sin\frac{\theta}{2}\sin\frac{3\theta}{2}\right) - \frac{C_{-1}}{\sqrt{r}} \sin\frac{\theta}{2}\left(2 + \cos\frac{\theta}{2}\cos\frac{3\theta}{2}\right) + A_0 \tag{2.20}$$

contains a constant stress

$$A_0 = \frac{1}{2}\sigma_\infty(\lambda - 1). \tag{2.21}$$

depending on the biaxiality factor, λ, for the Griffith crack and more generally on the specimen geometry. This issue of a second parameter in fracture mechanics became topical many years later in discussions on "geometry effects" on the fracture toughness, see historical overview by Brocks and Schwalbe [7], leading Rice [30] to come up with the *T*-stress approach,

$$\sigma_{ij}(r,\theta) = \frac{K_{\mathrm{I}}}{\sqrt{2\pi r}} f_{ij}(\theta) + T\,\delta_{1i}\delta_{1j}. \tag{2.22}$$

Understanding the effect of the T-stress requires the investigation of plastic zones at the crack tip and will be discussed in Chap. 4 on extension of LEFM for small-scale yielding.

2.3 Determination of SIFs

Stress intensity factors have attained an important role in the assessment of engineering structures against brittle fracture. They are a measure of the "powerfulness" of the $1/\sqrt{\mathrm{r}}$-singularity of stresses,

$$\begin{Bmatrix} K_{\mathrm{I}} \\ K_{\mathrm{II}} \\ K_{\mathrm{III}} \end{Bmatrix} = \lim_{r\to 0} \sqrt{2\pi r} \begin{Bmatrix} \sigma_{yy}(r,\theta=0) \\ \sigma_{xy}(r,\theta=0) \\ \sigma_{yz}(r,\theta=0) \end{Bmatrix}. \tag{2.23}$$

Correspondingly,

$$\begin{Bmatrix} K_{\mathrm{I}} \\ K_{\mathrm{II}} \\ K_{\mathrm{III}} \end{Bmatrix} = \lim_{r\to 0} \sqrt{\frac{2\pi}{r}} \begin{Bmatrix} \frac{1}{\kappa+2} u_y(r,\theta=\pi) \\ \frac{1}{\kappa+1} u_x(r,\theta=\pi) \\ \frac{1}{4} u_z(r,\theta=\pi) \end{Bmatrix} \tag{2.24}$$

holds for the crack edge displacements. From Eq. (2.23), the dimension of K can be read as [force $\times$ length$^{-3/2}$]. Typical units are $\mathrm{MPa}\sqrt{\mathrm{m}} = 10\sqrt{10}\ \mathrm{N\ mm^{-3/2}}$.

If the asymptotic stress fields, $\sigma_{ij}(r,\theta)$, or the crack edge displacements are known from analytical or numerical solutions, the associated K-factors can be immediately calculated by comparisons with Eqs. (2.23) or (2.24). Calculations based on the displacements require an assumption on plane stress or plane strain

Table 2.3 SIFs for some basic loading cases

(a) Griffith crack	K_{I}	K_{II}	K_{III}
Uniaxial tension, σ_{yy}^{∞}	$\sigma_{yy}^{\infty}\sqrt{\pi a}$	0	0
In-plane shear, $\sigma_{yx}^{\infty} = \sigma_{xy}^{\infty}$	0	$\sigma_{xy}^{\infty}\sqrt{\pi a}$	0
Anti-plane shear, σ_{yz}^{∞}	0	0	$\sigma_{yz}^{\infty}\sqrt{\pi a}$
Crack face pressure, p_0	$p_0\sqrt{\pi a}$	0	0
Two pin-forces, F, wedging problem	$\frac{F}{\pi B a}\sqrt{\pi a}$	0	0
(b) circular crack	K_{I}	K_{II}	K_{III}
Uniaxial tension, σ_{yy}^{∞}	$\sigma_{yy}^{\infty}\frac{2}{\pi}\sqrt{\pi a}$	0	0
Crack face pressure, p_0	$p_0\frac{2}{\pi}\sqrt{\pi a}$	0	0

conditions, neither of which is actually realised in a real three-dimensional structure. It is hence approximately assumed, frequently, that the free surface of a specimen is in plane stress and its mid section in plane strain.

SIFs depend on the geometry of the structure, the type of loading (tension or bending, for instance), the crack configuration and (linearly) on the external forces. K-factors of some elementary loading cases of the Griffith crack and a circular ("penny-shaped") centre crack of radius a in an "infinite cylinder [36] are listed in Table 2.3.

The SIF of an arbitrary plane crack problem can be written as a generalisation of the expressions in Table 2.3,

$$K = \sigma_\infty \sqrt{\pi a}\, Y(a/W, \ldots), \tag{2.25}$$

where σ_∞ is an appropriately defined "nominal stress" in the far-field of the crack and Y a dimensionless function of geometry parameters like a/W, which can be determined from analytical or numerical solutions. Classical handbooks like

- "Compendium of Stress Intensity Factors", Rooke and Cartwright [32],
- "The Stress Analysis of Cracks Handbook", Tada et al. [37],
- "Stress Intensity Factors Handbook", Murakami et al. [23]

provide numerous solutions and respective fit functions. It is subject to the engineers' experience with modelling to attribute real structures to these compilations of problems and approximate solutions. The principle of superposition supplies a universal methodology to generate geometry functions of complex structures and loading cases from fundamental solutions. Due to the linear-elastic constitutive equations and the assumption of small deformations, the boundary value problem is linear so that K-factors of the same mode may be added,

$$K_\alpha = \sum_n K_\alpha^{(n)}, \quad \alpha = \mathrm{I}, \mathrm{II}, \mathrm{III}, \quad n = \text{loading cases} \tag{2.26}$$

For instance, the mode I and II SIFs of an infinite panel with a centre crack of length $2a$ which is inclined by an angle, β, to the x-axis under tensile and shear stresses, σ_∞, τ_∞, are obtained by superposition from equations given in Table 2.3 as

$$\begin{aligned} K_\mathrm{I} &= (\sigma_\infty \sin\beta - \tau_\infty \cos\beta) \sin\beta \sqrt{\pi a} \\ K_\mathrm{II} &= (\sigma_\infty \cos\beta + \tau_\infty \sin\beta) \sin\beta \sqrt{\pi a}. \end{aligned} \tag{2.27}$$

SIFs for test specimens which are used to determine fracture parameters like K_Ic, Eq. (2.17), can be found in ASTM E399 [4], see Sect. 7.2.2.

The calculation of SIFs for real structures and practically relevant loading cases requires complex mathematical methods. In the past, analytical solutions have been obtained by complex stress functions [24], series expansions [39] or integral

transforms [36]. They do not necessitate complete solutions of the boundary value problem but just the stress field at the crack tip. Stress fields without the characteristic $1/\sqrt{r}$ singularity do not affect the SIF. If numerical solutions of stress or displacement fields are available, K-factors can be determined with Eqs. (2.23) or (2.24).

With the emerging power of soft- and hardware numerical methods like boundary element or finite element methods, e.g. [21], became increasingly important and popular also for the determination of K-factors. Respective analyses can be done for 3D configurations with straight or curved crack fronts, when the stress field and the SIF depend on the crack-front coordinate, z, or an arc length, s_c, respectively, $K(z)$ or $K(s_c)$, see example of a railway axle in Sect. 7.1.3. In the beginning, numerically calculated courses of stresses or displacements were extrapolated to calculate SIFs according to Eqs. (2.23) and (2.24), but this did not yield sufficiently accurate results, particularly if they are based on stresses. More advanced methods exploit the relation to the energy release rate, Eqs. (2.16) and (2.18) where the latter is commonly evaluated by a domain integral [1], which was first suggested by Parks [27, 28] and became an established technique in FEM [33]. More details will be presented in Sect. 7.1.2 on the numerical determination of energy release rate and J-integral and Sect. 7.1.3 on the numerical determination of SIFs.

2.3.1 Cracked Cylinders

An axial through-crack of length $2a$ in a long pressurised cylinder or pipe, Fig. 2.5, can be considered as a Griffith crack ($W \Rightarrow L$), as the condition of $a/L \ll 1$ is fulfilled. The remote stresses result from the well-known formula

$$\sigma_\infty = \sigma_t = p\frac{r_\mathrm{i}}{t} \tag{2.28}$$

for circumferential (tangential) stresses, $\sigma_\mathrm{t} = \sigma_{\varphi\varphi}$, in a thin walled cylinder, $t/r_\mathrm{o} \ll 1$, where r_i and $t = r_\mathrm{o} - r_\mathrm{i}$ are the (inner) radius and the wall-thickness,

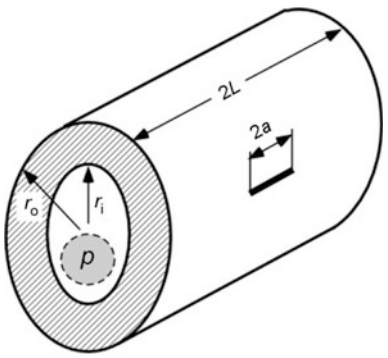

Fig. 2.5 Thick-walled cylinder of length, $2L$, under internal pressure, p, with axial through-crack, $2a$, inner radius r_i, outer radius r_o, Young's modulus E, Poisson's ratio ν

respectively, of the tube and p is the internal pressure. A cylinder is not plane as a panel, however, but bent. Thus, the geometry function depends on the curvature and the wall thickness, $Y(a/\sqrt{r_i t})$. In the following, the shell parameter $\lambda_s = a/\sqrt{r_i t}$ is introduced. As the stress intensity in a cylindrical tube was first analysed by Folias [10], this function is addressed as Folias factor in the literature, e.g. Kiefner et al. [20]. Misleadingly, it is sometimes associated with bulging of the cylinder wall in the vicinity of the crack (BS 7910, [8]).

Murakami et al. [23] present diagrams and tables of $Y(\lambda_s)$ in the range $0 \le \lambda_s \le 4.4$, and British Standard 7910 tabulated values for $0 \le \lambda_s \le 6.7$ and $5 \le r_o/t \le 100$. In his solution of the boundary value problem, Folias [10] derived

$$\frac{\sigma_{\text{shell}}}{\sigma_{\text{panel}}} = Y(\lambda_s) \approx 1 + (c_1 + c_2 \ln \lambda_s)\lambda_s^2 + \mathcal{O}\left(\frac{1}{r_o^2}\right), \tag{2.29}$$

which represents a good approximations of the tabulated values of BS 7910 [8] for $\lambda_s = a/\sqrt{r_o t} \le 6.5$, taking $c_1 = 0.4612$, $c_2 = -0.1806$.

Equation (2.28) holds approximately for thin-walled cylinders, $t/r_o \ll 1$, only. Stresses in thick-walled cylinders (without any crack) can be derived from the axisymmetric boundary value problem in cylindrical coordinates (r, φ, z), $\partial(.)/\partial\varphi = 0$, described by the balance equations,

$$\frac{\partial \sigma_{rr}}{\partial r} + \frac{1}{r}\left(\sigma_{rr} - \sigma_{\varphi\varphi}\right) = 0, \quad \frac{\partial \sigma_{zz}}{\partial z} = 0, \tag{2.30}$$

and Hooke's law, Eq. (2.1), together with the boundary conditions $\sigma_{rr}(r_o) = 0$, $\sigma_{rr}(r_i) = -p$. The equivalence condition for axial forces in a capped cylinder,

$$N_z = 2\pi \int_{r_i}^{r_a} \sigma_{zz} r \, dr = \pi \int_{r_i}^{r_a} \left(\sigma_{rr} + \sigma_{\varphi\varphi}\right) r \, dr = \pi r_i^2 p, \tag{2.31}$$

results in

$$\sigma_{zz} = 1/2\left(\sigma_{rr} + \sigma_{\varphi\varphi}\right). \tag{2.32}$$

Finally, Lamé's equations, are obtained,

$$\begin{aligned} \sigma_{rr} &= \tfrac{r_i^2}{r_o^2 - r_i^2}\left[1 - \left(\tfrac{r_o}{r}\right)^2\right] p \le 0, \\ \sigma_t = \sigma_{\varphi\varphi} &= \tfrac{r_i^2}{r_o^2 - r_i^2}\left[1 + \left(\tfrac{r_o}{r}\right)^2\right] p, \\ \sigma_{zz} &= \tfrac{r_i^2}{r_o^2 - r_i^2} p \end{aligned} \tag{2.33}$$

which are graphically displayed in Fig. 2.6. Maximum circumferential stresses occur at the inner surface.

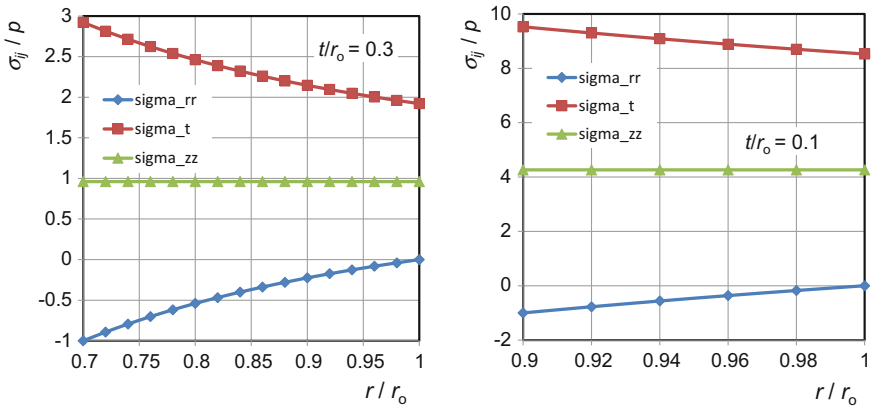

Fig. 2.6 Radial, circumferential (tangential) and axial stresses, σ_{rr}, $\sigma_t \equiv \sigma_{\varphi\varphi}$, σ_{zz}, in an uncracked thick-walled cylinder, $t/r_o = 0.3$ and 0.1, under internal pressure, p

2.3.2 *Semi-elliptical Surface Crack*

Cracks originating from the surface of a component without penetrating the whole wall thickness are of great practical relevance. They may initiate from notches or surface roughness under cyclic loading, thermal stresses or corrosion and grow under service loads to a critical size when failure of the structure occurs. A simplified model for the variety of crack shapes is the semi-elliptical surface flaw, see Fig. 2.7, which is characterised by its depth a, the small principal axis, and its length $2c$, twice the large principal axis, with the aspect ratio,

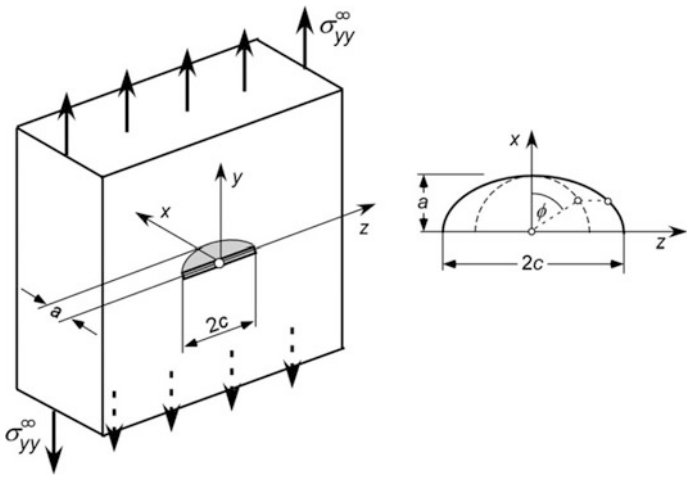

Fig. 2.7 PS(T) specimen (ASTM E1823 [5]) with semi-elliptical surface crack

$$0 \leq k = a/c \leq 1. \tag{2.34}$$

An arbitrary point on the crack front may be identified by a parametric angle, ϕ, which is defined by the projection of an ellipse point to a circle of radius a. The deepest point of the crack in the centre is characterised by $\phi = 0$, and the penetrations points of the crack front with the surface by $\phi = \pm\pi/2$. Irwin [18] presented the solution for an elliptical inner crack under uniaxial tension

$$K_{\mathrm{I}}(\phi) = \sigma_\infty \sqrt{\pi a} \frac{f_\phi(\phi)}{E(k)}, \tag{2.35}$$

with the elliptical shape function,

$$f_\phi(\phi) = \left(\cos^2\phi + k^2 \sin^2\phi\right)^{1/4}, \tag{2.36}$$

which becomes $f_\phi = 1$ for the penny-shaped crack ($k = 1$), and the 2nd kind elliptical integral,

$$E(k) = \int_0^{\pi/2} \sqrt{1 - (1 - k^2)\sin^2\phi}\, d\phi, \tag{2.37}$$

which becomes $E(k) = 1$ for the Griffith crack ($2c \to \infty$, $k = 0$) and $E(k) = \pi/2$ for the penny-shaped crack ($k = 1$), see Fig. 2.8. The extrema of $K_{\mathrm{I}}(\phi)$ are

$$\begin{aligned} K_{\mathrm{I}}^{\max} &= K_{\mathrm{I}}(0) = \tfrac{\sigma_\infty \sqrt{\pi a}}{E(k)} \\ K_{\mathrm{I}}^{\min} &= K_{\mathrm{I}}\left(\pm\tfrac{\pi}{2}\right) = \tfrac{\sigma_\infty \sqrt{\pi a}\sqrt{k}}{E(k)} \end{aligned}. \tag{2.38}$$

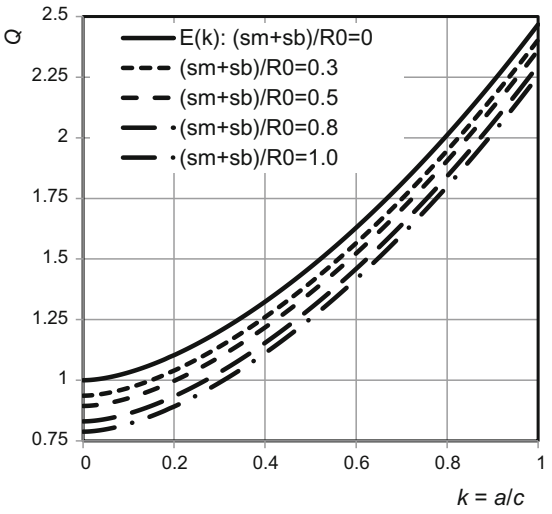

Fig. 2.8 Shape factor of semi-elliptical surface flaws: 2nd kind elliptical integral $E(k)$ and SSY modifications, Eq. (4.10), according to ASME BPVC

Analogous to Eq. (2.25), arbitrary structures with semi-elliptical surface cracks are described by geometry functions, $h_j(\phi)$, which have been calculated numerically and can be found in the literature, for instance Heliot et al. [13], Isida et al. [19], McGowan and Raymund [22], Newman and Raju [25], Raju and Newman [29] among others. General inhomogeneous stress fields are captured by superposition. The problem of a semi-elliptical surface crack in an arbitrary tensile stress field is thus treated as a crack with pressure, $\bar{p}(x)$, on the crack faces which equals the nominal stress distribution in the uncracked component at the position of the crack, $\sigma^0_{yy}(x)$, and the latter is fitted by a polynomial,

$$\sigma^0_{yy}(x) = \sum_j \sigma^0_j \left(\frac{x}{t}\right)^j. \tag{2.39}$$

For $j = 0$ the part of homogeneous tension is obtained, for $j = 1$ pure bending, etc. The resulting stress intensity factor is

$$K_\mathrm{I}(\phi) = \sum_j \sigma^0_j \sqrt{\pi a} \frac{f_\phi(\phi)}{E(k)} h_j(\phi). \tag{2.40}$$

In the following, a surface crack in a pressure vessel is considered. According to Eq. (2.33), $\sigma_{\varphi\varphi}(r)$ in the uncracked cylinder is maximum at the inner surface, $r = r_\mathrm{i}$, and hence a crack at the inner surface is most hazardous. According to Eq. (2.39), $\sigma^0_{yy}(x) = \sigma_{\varphi\varphi}(r - r_\mathrm{i})$ is expanded in a series. The ASME Boiler and Pressure Vessel Code [3] suggests a linear fit, namely a constant fraction, the membrane stresses, σ_m, and the bending stresses, σ_b,

$$\sigma_{\varphi\varphi}(x) = (\sigma_\mathrm{m} + \sigma_\mathrm{b}) - 2\sigma_\mathrm{b}\left(\frac{x}{t}\right), \tag{2.41}$$

with

$$\begin{aligned} \sigma_\mathrm{m} &= p_0 \left[1 - \frac{r_\mathrm{o}^2}{2\left(r_\mathrm{o}^2 + r_\mathrm{i}^2\right)} \left(1 - \frac{r_\mathrm{i}^2}{(r_\mathrm{i} + a)^2}\right) \frac{t}{a}\right], \\ \sigma_\mathrm{b} &= p_0 \frac{r_\mathrm{o}^2}{2\left(r_\mathrm{o}^2 + r_\mathrm{i}^2\right)} \left(1 - \frac{r_\mathrm{i}^2}{(r_\mathrm{i} + a)^2}\right) \frac{t}{a} \end{aligned}, \tag{2.42}$$

and $p_0 = p \frac{r_\mathrm{o}^2 - r_\mathrm{i}^2}{r_\mathrm{o}^2 + r_\mathrm{i}^2}$ as abbreviation. The SIF is

$$K_\mathrm{I}(\phi) = \left[\sigma_\mathrm{m} h_0(\phi) + \sigma_\mathrm{b}\left(h_0(\phi) - 2\frac{a}{t} h_1(\phi)\right)\right] \sqrt{\pi a} \frac{f_\phi(\phi)}{E(k)}. \tag{2.43}$$

Considering its maximum at $\phi = 0$ and the condition for brittle fracture, Eq. (2.17),

$$K_{\mathrm{I}}^{\max} = (M_{\mathrm{m}}\sigma_{\mathrm{m}} + M_{\mathrm{b}}\sigma_{\mathrm{b}})\frac{\sqrt{\pi a}}{E(k)} \leq K_{\mathrm{Ic}}, \tag{2.44}$$

the critical pressure, p_{c}, for an assumed or detected crack depth, a, or a critical crack depth, a_{c}, for the service pressure can be determined accounting for an additional safety factor. The coefficients $M_{\mathrm{m}} = h_0(0)$ and $M_{\mathrm{b}} = h_0(0) - 2(a/t)h_1(0)$ for membrane and bending stresses can be found in the ASME BPVC [3], which also introduces a modified shape factor, Q, instead of $E(k)$ accounting for small plastic zones at the crack tip, see Sect. 4.1 on the equivalent elastic crack.

ASTM E2899 [6] defines test methods and nomenclature for surface cracks under tension and bending. Recent applications can be found in Arafah et al. [2].

References

1. Abaqus (2014) User's manual, Version 6.12. Dassault Systèmes Simulia Corp, Providence, RI, USA
2. Arafah D, Madia M, Zerbst U, Beretta S, Cristea ME (2015) Instability analysis of pressurized pipes with longitudinal surface cracks. Int J Press Vessels Pip 126–127:48–57
3. ASME BPVC (2015) Boiler and pressure vessel code. The American Society of Mechanical Engineers
4. ASTM E399 (2012) Standard test method for linear-elastic plane-strain fracture toughness K_{Ic} of metallic materials. Annual Book of ASTM Standards, vol 03.01, American Society for Testing and Materials, West Conshohocken (PA), USA
5. ASTM E1823 (2013) Standard Terminology Relating to Fatigue and Fracture Testing. Annual Book of ASTM Standards, vol 03.01, American Society for Testing and Materials, West Conshohocken (PA), USA
6. ASTM E2899 (2015) Standard test method for measurement of initiation toughness in surface cracks under tension and bending. Annual Book of ASTM Standards, vol 03.01, American Society for Testing and Materials, West Conshohocken (PA), USA
7. Brocks W, Schwalbe KH (2015) Experimental and numerical fracture mechanics—an individually dyed history. In: Hütter G, Zybell L (eds) Recent trends in fracture and damage mechanics. Springer, Heidelberg, pp 23–57
8. BS 7910 (2005) Guide to methods for assessing the acceptability of flaws in metallic structures, British Standards
9. Erdogan F, Sih GE (1963) On the crack extension in shells and plates under plane loading and transverse shear. J Basic Eng 85:527–529
10. Folias ES (1965) An axial crack in a pressurized cylindrical shell. Int J Fract Mech 1:104–113
11. Griffith AA (1920) The phenomena of rupture and flow in solids. Phil Trans Roy Soc London A211:163–198
12. Griffith AA (1924) Theory of rupture. In: Biezeno B, Burgers JM (eds) Proceedings 1st International Congress for Applied Mechanics. Waltman Uitgevery, Delft, pp 55–63
13. Heliot J, Labbens RC, Pelissier-Tanon A (1978) Semi-elliptical cracks in a cylinder subjected to stress gradients. In: Smith CW (ed) Proceedings of 11th National Symposium on Fracture Mechanics, ASTM STP, vol 677, pp 341–364
14. Hussain MA, Pu SI, Underwood J (1974) Strain energy release rate for a crack under combined Mode I and Mode II. ASTM STP 560:2–28
15. Ichikawa M, Tanaka S (1982) A critical analysis of the relationship between the energy release rate and the stress intensity factors under combined mode loading. Int J Fract 18:19–28

16. Inglis CE (1913) Stresses in a plate due to the presence of cracks and sharp corners. Trans Inst Naval Arch 60:219–230
17. Irwin GR (1957) Analysis of stresses and strains near the end of a crack traversing a plate. J Appl Mech 24:361–364
18. Irwin GR (1962) Crack extension force for a part-through crack in a plate. Trans ASME, Series E, J Appl Mech 29:615–634
19. Isida M, Noguchi H, Yoshida T (1984) Tension and bending of finite thickness plates with a semi-elliptical surface crack. Int J Fract 26:157–188
20. Kiefner JF, Maxey WA, Eiber RJ, Duffy AR (1973) Failure stress levels of flaws in pressurized cylinders. In: Progress in flaw growth and fracture toughness testing. ASTM STP 536:461–481
21. Kuna M (2013) Finite elements in fracture mechanics. Springer, Dordrecht
22. McGowan JJ, Raymund M (1978) Stress intensity factor solutions for internal longitudinal semi-elliptical surface flaws in a cylinder under arbitrary loadings. In: Smith CW (ed) Proceedings of 11th National Symposium Fracture Mechanics, ASTM STP, vol 677, pp 365–3680
23. Muarakami Y (ed) (1987) Stress intensity factors handbook, 3rd edn. Pergamon, New York
24. Muskhelishvili NI (1977) Some basic problems of the mathematical theory of elasticity. Springer, Dordrecht
25. Newman JN, Raju IS (1981) An empirical stress-intensity-factor equation for the surface crack. J Eng Fract Mech 15:185–192
26. Paris PC, Erdogan F (1963) A critical analysis of crack propagation laws. J Basic Eng Trans Am Soc Mech Eng D85:528–534
27. Parks DM (1974) A stiffness derivative finite element technique for determination of crack tip stress intensity factors. Int J Fract 10:487–502
28. Parks DM (1977) The virtual crack extension method for nonlinear material behavior. Comput Meth Appl Mech Eng 12:353–364
29. Raju IS, Newman JN (1979) Stress-intensity-factors for a wide range of semi-elliptical surface cracks in finite thickness plates. J Eng Fract Mech 11:817–829
30. Rice JR (1974) Limitations to the small scale yielding approximation for crack tip plasticity. J Mech Phys Solids 17–26
31. Richard HA, Kuna M (1990) Theoretical and experimental study of superimposed fracture modes I, II, III. Eng Fract Mech 35:949–960
32. Rooke DP, Cartwright DP (1976) Compendium of stress intensity factors. Stationary Office, GB
33. Shih CF, Moran B, Nakamura T (1986) Energy release rate along a three-dimensional crack front in a thermally stressed body. Int J Fracture 30:79–102
34. Sih GE (1974) Strain energy density factor applied to mixed mode crack problems. Int J Fracture 10:305–321
35. Sneddon IN (1946) The distribution of stress in the neighbourhood of a crack in an elastic solid. Proc Roy Soc A187:229–260
36. Sneddon IN (1973): Integral transform methods—circular cracks. In: Shih GC (ed) Mechanics of fracture, vol 1. Methods of analysis und solution of crack problems, pp 350–363
37. Tada H, Paris PC, Irwin GR (2000) The stress analysis of cracks handbook, 3rd edn. ASME, doi:10.1115/1.801535
38. Westergaard HM (1939) Bearing pressures und cracks. J Appl Mech 6:49–53
39. Williams ML (1957) On the stress distribution at the base of a stationary crack. J Appl Mech 24:109–114

Chapter 3
Phenomenological Theory of Time- and Rate-Independent Plasticity

Abstract The phenomenological framework for describing the inelastic deformation of metals at low temperatures and quasistatic loading is explained and the respective equations are presented. The theories of Tresca, von Mises, Prandtl and Reuss are introduced. Stresses in a pressurised cylinder are analysed assuming perfect plasticity, continuing the respective stress analysis for elastic material behaviour in Chap. 2. Incremental plasticity takes the main part of the present chapter but is complemented by the finite (or "deformation") theory of plasticity which provides the constitutive background for elasto-plastic fracture mechanics.

This theory describes the inelastic deformation behaviour of metals at "low" temperatures under "slow" (quasi-static) loading, i.e. excluding time dependence (creep, relaxation) and rate dependence (high-speed impact). The deformation is due to motion of dislocations at the microscale (crystal lattice). However, only the macroscopically observable phenomena are described in the framework of continuum mechanics.

As plastic deformations occur nonlinearly and depend on the loading history, the constitutive equations are established "incrementally", namely for small changes of stresses and strains,

$$\Delta\sigma_{ij} = \dot{\sigma}_{ij}\Delta t, \quad \Delta\varepsilon_{ij} = \dot{\varepsilon}_{ij}\Delta t, \tag{3.1}$$

where the parameter $t > 0$ is some monotonically increasing scalar variable characterising the load history. It is not a physical time, so that stress and strain rates, $\dot{\sigma}_{ij}$, $\dot{\varepsilon}_{ij}$, are no (physical) velocities. That is why the theory presented in Sects. 3.2 and 3.3 is called "incremental plasticity" unlike the "finite plasticity" of Hencky [14], see Sect. 3.4 on deformation plasticity.

W. Brocks, *Plasticity and Fracture*, Solid Mechanics and Its Applications 244,
DOI 10.1007/978-3-319-62752-6_3

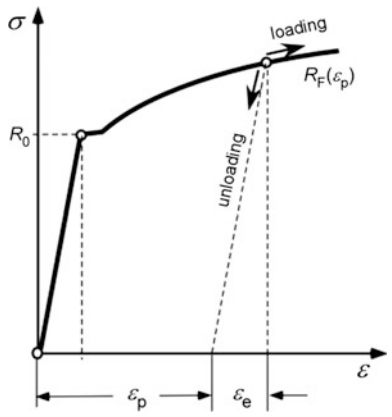

Fig. 3.1 Uniaxial true stress-strain curve

3.1 Uniaxial Tensile Test

A uniaxial stress, $\sigma = F/A$, below the elastic limit, R_0, causes a fully reversible elongation, $\varepsilon = \Delta L/L_0$, of a tensile bar. The limit is an idealised value within the present theory, which may be identified with the lower yield point, R_{eL}, or a proof stress, R_p, of real materials and will be addressed as "yield strength" in the following. Deformations follows Hooke's law,

$$\sigma \leq R_0 : \quad \sigma = E\varepsilon, \tag{3.2}$$

with E being Young's modulus. As soon as the applied stress exceeds R_0, the stress strain curve becomes nonlinear, see Fig. 3.1, and permanent (plastic) strains remain after unloading,

$$\varepsilon = \varepsilon_e + \varepsilon_p = \frac{\sigma}{E} + \varepsilon_p. \tag{3.3}$$

The constitutive behaviour for $\sigma > R_0$ is characterised by a yield condition, a flow curve, Hooke's law of isotropic elasticity and a loading/unloading criterion.

- **Yield condition**

Stresses always have to remain below the limiting curve, $R_F(\varepsilon_p)$, which depends on the present plastic deformation,

$$\sigma \leq R_F(\varepsilon_p) , \quad R_F(0) = R_0. \tag{3.4}$$

$R_F(\varepsilon_p)$ is called (uniaxial) flow curve of the material. Starting from $\sigma < R_F(\varepsilon_p)$ results in elastic changes of strains, only; stresses $\sigma > R_F(\varepsilon_p)$ are not admissible. A material without hardening $R_F(\varepsilon_p) = R_0$ is called perfectly plastic.

- **Hooke's law**

Holding for elastic (total) strains or elastic fraction, ε_e, of total strains,

$$\sigma = E\varepsilon_e = E\big(\varepsilon - \varepsilon_p\big). \tag{3.5}$$

- **Loading/unloading criterion**

Loading, $\dot{\sigma} > 0$, occurs along the flow curve, $R_F(\varepsilon_p)$, and is associated with additional plastic deformations; unloading, $\dot{\sigma} < 0$, follows Hooke's linear slope, see arrows in Fig. 3.1

$$\begin{array}{lll} \dot{\sigma} > 0: & \dot{\varepsilon}_p > 0 & \text{loading} \\ \dot{\sigma} < 0: & \dot{\varepsilon}_p = 0 & \text{unloading} \end{array}. \tag{3.6}$$

3.2 Generalisation to Triaxial Stress States

- **Additive decomposition of strain rates**

Different from the uniaxial situation, no additive decomposition of total strains as in Eq. (3.3) is possible because the principal axes of ε_{ij} may rotate. Instead, a decomposition of elastic and plastic strain rates is postulated,

$$\dot{\varepsilon}_{ij} = \dot{\varepsilon}^e_{ij} + \dot{\varepsilon}^p_{ij}. \tag{3.7}$$

This is an approximation for small elastic strains of the multiplicative decomposition of the elastic and plastic deformation gradient. Total plastic strains follow by integration over the deformation history

$$\varepsilon^p_{ij} = \int_{\tau=0}^{t} \dot{\varepsilon}^p_{ij}\, d\tau. \tag{3.8}$$

Plastic deformations are due to motions of dislocations which do not result in any volume change. Hence, the incompressibility condition,

$$\dot{\varepsilon}^p_{kk} = 0, \tag{3.9}$$

holds, and thus $\dot{\varepsilon}^p_{ij} = \dot{\varepsilon}^p_{kk}\delta_{ij} + \dot{\varepsilon}'^p_{ij} = \dot{\varepsilon}'^p_{ij}$ is deviatoric. The trace (first invariant) of the strain tensor, ε_{kk}, is the volume dilatation, and the deviatoric strains, $\varepsilon'_{ij} = \varepsilon_{ij} - \varepsilon_{kk}\delta_{ij}$, describe distortion. Materials containing micro-voids are

plastically compressible. A special plasticity theory of porous media has been developed for these materials, see Sect. 8.3.

- **Yield condition**

A yield function $\Phi\left(\sigma_{ij}, \varepsilon_{ij}^{\mathrm{p}}\right) \leq 0$ characterises all physically admissible stress states. Starting from stress states $\Phi < 0$ results in elastic changes of deformation, only, and $\Phi = 0$ defines the limiting yield surface in the stress space. It is commonly postulated as being convex [2, 3], because a straight loading path between two elastic stress states, $\Phi < 0$, should not be associated with permanent deformations. Convexity follows also from Drucker's postulates of stability [10–12], Sect. 6.1.1. Assuming an "associated flow rule", the yield function equals the flow potential, see Eq. (3.12) below. For plastically incompressible materials, Eq. (3.9), yielding does not depend on the hydrostatic stresses, $\sigma_{\mathrm{h}} = \frac{1}{3}\sigma_{kk}$, and the yield function takes the form,

$$\Phi\left(\sigma'_{ij}, \varepsilon_{ij}^{\mathrm{p}}\right) \leq 0\,, \quad \sigma'_{ij} = \sigma_{ij} - \sigma_{\mathrm{h}}\delta_{ij}, \tag{3.10}$$

which is represented by a (convex) cylinder in the principal stress space whose axis is along the diagonal, see Fig. 3.2 [5].

- **Hooke's law of isotropic elasticity**

Hooke's law, Eq. (2.1), is expressed in terms of stress rates and elastic strain rates, $\dot{\varepsilon}_{ij}^{\mathrm{e}}$. The latter can be total strain rates for $\Phi < 0$ or unloading as well as the elastic part of total strain rates as in Eq. (3.7) for $\Phi = 0$.

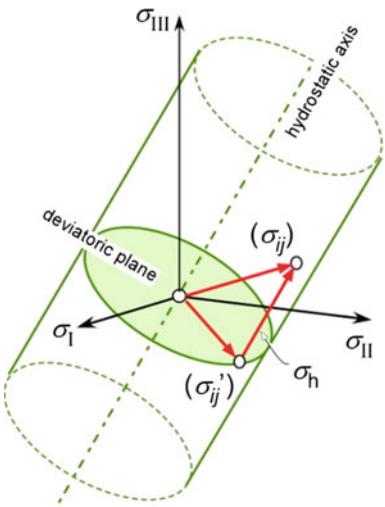

Fig. 3.2 Flow cylinder in the space of principal stresses, σ_{I}, σ_{II}, σ_{III}

Table 3.1 Material constants of isotropic elasticity: Lamé's coefficients, λ, μ, Young's modulus, E, Poisson's ratio, ν, shear modulus, G, bulk modulus, K

	$\lambda =$	$\mu =$	$E =$	$\nu =$	$K =$	$G =$
λ, μ	λ	μ	$\frac{\mu(3\lambda+2\mu)}{\lambda+\mu}$	$\frac{\lambda}{2(\lambda+\mu)}$	$\lambda+\frac{2}{3}\mu$	μ
G, K	$K-\frac{2}{3}G$	G	$\frac{9KG}{3K+G}$	$\frac{3K-2G}{6K+2G}$	K	G
E, ν	$\frac{E\nu}{(1+\nu)(1-2\nu)}$	$\frac{E}{2(1+\nu)}$	E	ν	$\frac{E}{3(1-2\nu)}$	$\frac{E}{2(1+\nu)}$

If the elastic strain rate tensor is split into a volumetric and a distortional part respective relations to the hydrostatic and the deviatoric stress rate tensors via the bulk modulus, K, and the shear modulus, G, are obtained,

$$\dot{\varepsilon}_{ij}^{\mathrm{e}} = \dot{\varepsilon}_{ij}^{\prime\mathrm{e}} + \frac{1}{3}\dot{\varepsilon}_{kk}^{\mathrm{e}}\delta_{ij} = \frac{1}{E}\left[(1+\nu)\dot{\sigma}_{ij} - \nu\dot{\sigma}_{kk}\delta_{ij}\right] = \frac{\dot{\sigma}_{ij}^{\prime}}{2G} + \frac{\dot{\sigma}_{\mathrm{h}}\delta_{ij}}{3K}. \tag{3.11}$$

The material constants of isotropic elasticity are compiled in Table 3.1. Two at a time are independent, (E, ν), (λ, μ), (G, K).

- **Flow rule**

As for the elastic strain rates, a constitutive law for the plastic strain rates is required. Commonly, an associated flow rule,

$$\dot{\varepsilon}_{ij}^{\mathrm{p}} = \dot{\lambda}_{\mathrm{p}}\frac{\partial \Phi}{\partial \sigma_{ij}}, \tag{3.12}$$

is assumed, for which the plastic potential equals the yield function. The plastic strain rates are aligned orthogonal to the yield surface, and hence, Eq. (3.12) is also addressed as "normality rule", which, like the convexity condition, can be derived from the postulates of stability [10–12]. The magnitude of plastic strain rates is governed by the plastic multiplier, $\dot{\lambda}_{\mathrm{p}}$, which can be determined from the uniaxial flow curve, $R_{\mathrm{F}}(\varepsilon_{\mathrm{p}})$, considering the principle of equivalence of dissipation rate densities linking up triaxial and uniaxial stress states.

- **Equivalence of dissipation rate densities**

Triaxial and uniaxial stress states have to meet the postulate of equivalence of dissipation rate densities,

$$\dot{w}^{\mathrm{p}} = \sigma_{ij}\dot{\varepsilon}_{ij}^{\mathrm{p}} = \dot{\lambda}_{\mathrm{p}}\frac{\partial \Phi}{\partial \sigma_{ij}}\sigma_{ij} = \bar{\sigma}\,\dot{\bar{\varepsilon}}^{\mathrm{p}}, \tag{3.13}$$

with appropriately defined equivalent uniaxial stresses, $\bar{\sigma}$, and equivalent plastic strain rates, $\dot{\bar{\varepsilon}}^{\mathrm{p}}$, which are work-conjugate.

- **Loading/unloading criterion**

Discerning loading and unloading is a bit more difficult than in the tensile test. The respective condition is based on the angle between the directions of stress rates, $\dot{\sigma}_{ij}$, and the normal to the yield surface, $\partial\Phi/\partial\sigma_{ij}$,

$$\frac{\partial\Phi}{\partial\sigma_{ij}}\dot{\sigma}_{ij}\begin{cases}\geq 0 & \text{loading} \quad \dot{\varepsilon}^{\mathrm{p}}_{ij}\neq 0\\ <0 & \text{unloading} \quad \dot{\varepsilon}^{\mathrm{p}}_{ij}=0\end{cases}. \tag{3.14}$$

Different from the uniaxial case, also a neutral rearrangement of stresses is possible, $\left(\partial\Phi/\partial\sigma_{ij}\right)\dot{\sigma}_{ij}=0$, which is associated with plastic deformations $\dot{\varepsilon}^{\mathrm{p}}_{ij}\neq 0$.

- **Hardening law**

The flow curve changes with increasing plastic deformation, Fig. 2.1, and likewise, the change of the yield function, Eq. (3.10), has to be described mathematically in dependence on the loading history. This is realised by introducing scalar and tensorial inner variables, $\bar{\kappa}_n$ and $\xi^{(n)}_{ij}$,

$$\Phi\left(\sigma'_{ij},\varepsilon^{\mathrm{p}}_{ij}\right)=\tilde{\Phi}\left(\sigma'_{ij},\xi^{(n)}_{ij},\bar{\kappa}_n\right)=0, \tag{3.15}$$

which follow specific evolution laws

$$\begin{aligned}\dot{\bar{\kappa}}_n &= f_n\left(\sigma_{ij},\xi^{(n)}_{ij},\bar{\kappa}_n,\varepsilon^{\mathrm{p}}_{ij},\dot{\varepsilon}^{\mathrm{p}}_{ij},\bar{\varepsilon}^{\mathrm{p}},\dot{\bar{\varepsilon}}^{\mathrm{p}}\right)\\ \dot{\xi}^{(n)}_{ij} &= g^{(n)}_{kl}\left(\sigma_{kl},\xi^{(n)}_{kl},\bar{\kappa}_n,\varepsilon^{\mathrm{p}}_{kl},\dot{\varepsilon}^{\mathrm{p}}_{kl},\bar{\varepsilon}^{\mathrm{p}},\dot{\bar{\varepsilon}}^{\mathrm{p}}\right)\end{aligned}. \tag{3.16}$$

The number of inner variables is mostly restricted to two, namely a stress measure, $\bar{\kappa}$, which is work-conjugate to the accumulated plastic strain, $\bar{\varepsilon}^{\mathrm{p}}=\int_{\tau=0}^{t}\dot{\bar{\varepsilon}}^{\mathrm{p}}\,d\tau$, and the deviatoric "back stress" tensor, $\xi_{ij}=\xi'_{ij}$. If the yield function is assumed to take the special form (which is not possible for Tresca's yield condition, however, see Sect. 3.3.1),

$$\tilde{\Phi}\left(\sigma'_{ij},\xi_{ij},\bar{\kappa}\right)=\bar{\Phi}\left(s'_{ij}\right)-\bar{\kappa}^2(\bar{\varepsilon}^{\mathrm{p}})=0, \tag{3.17}$$

defining an "effective" stress tensor, $s_{ij}=\sigma_{ij}-\xi_{ij}$, and an equivalent uniaxial effective stress $\bar{s}=\sqrt{\frac{3}{2}\bar{\Phi}\left(s'_{ij}\right)}$, scalar and tensorial internal variables can be interpreted as follows:

- $\bar{\kappa}$ describes the increase of some "radius" of the flow cylinder, Fig. 2.2, characterising the "isotropic hardening" in dependence on $\bar{\varepsilon}^{\mathrm{p}}$, and
- ξ_{ij} is the shift of its axis, the "kinematic hardening", which is essential for cyclic loading [13].

Whereas $\bar{\kappa}(\bar{\varepsilon}^{\mathrm{p}})$ can be directly measured in a uniaxial tensile test, ξ_{ij} require an evolution law according to Eq. (3.16) with cyclic and, where necessary, multiaxial tests for identifying the respective parameters. Two classical approaches, $\dot{\xi}_{ij} = c(\bar{\varepsilon}^{\mathrm{p}})\dot{\varepsilon}^{\mathrm{p}}_{ij}$ and $\dot{\xi}_{ij} = c(\bar{\varepsilon}^{\mathrm{p}})\big(\sigma_{ij} - \xi_{ij}\big)$, date back to Prager [19] and Ziegler [27], respectively. More advanced evolution laws have been introduced by Chaboche and Rousselier [8] and Chaboche [7] to describe complex hardening phenomena and loading histories, see Brocks and Olschewski [4].

3.3 Isotropic Yielding

Further simplifying assumptions and special cases of the above equations will be considered in the following,

- **Isotropic yield surface**

The representation of the yield surface must not depend on the choice of the coordinate system. Thus, it may only depend on the 2nd and 3rd invariants, $\mathbb{J}_2(s'_{ij})$, $\mathbb{J}_3(s'_{ij})$, of the effective deviatoric stress tensor [1, 3, 11, 18]. The 1st invariant vanishes due to the incompressibility condition, Eq. (3.9). Kinematic hardening is still possible, however.

- **Purely isotropic hardening**

If kinematic hardening is excluded, $\xi_{ij} = 0$, the equivalent stress becomes,

$$\bar{s} = \bar{\sigma} = \sqrt{\frac{3}{2}\bar{\Phi}\Big(\mathbb{J}_2(\sigma'_{ij}), \mathbb{J}_3(\sigma'_{ij})\Big)}, \tag{3.18}$$

with the invariants

$$\begin{aligned}
\mathbb{J}_2(\sigma'_{ij}) &= \frac{1}{2}\big(\sigma'_{ik}\sigma'_{ki}\big) \\
&= \frac{1}{6}\Big[\big(\sigma_{xx} - \sigma_{yy}\big)^2 + \big(\sigma_{yy} - \sigma_{zz}\big)^2 + \big(\sigma_{zz} - \sigma_{xx}\big)^2\Big] + \sigma^2_{xy} + \sigma^2_{yz} + \sigma^2_{xz} \\
\mathbb{J}_3(\sigma'_{ij}) &= \det(\sigma'_{ij}) = \frac{1}{3}\sigma_{ij}\,\sigma_{jk}\,\sigma_{ki}.
\end{aligned} \tag{3.19}$$

The first invariant of the deviatoric stresses vanishes by definition.

- **Effect of the 3rd invariant**

The yield surface $\tilde{\Phi} = \mathbb{J}_2(\sigma'_{ij}) - \bar{\kappa}^2 = 0$, which represents the yield condition by von Mises [25, 26] described below in Sect. 3.3.2, is rotationally symmetric and illustrated by a circular cylinder in the stress space, see Fig. 3.2, or a sphere in the space of deviatoric stresses. The 3rd invariant, $\mathbb{J}_3(\sigma'_{ij})$, allows for describing

deviations from rotational symmetry. A number of yield conditions exist which include the 3rd invariant, Betten [1, 3], Ismar and Mahrenholtz [15, 16], Mahrenholtz and Ismar [17], the most well known of them is Tresca's yield condition, see Sect. 3.3.1 and Eq. (3.23) below. Yield functions having the form $\bar{\Phi}\left(\mathbb{J}_2^3 + c\mathbb{J}_3^2\right)$ describe symmetric yielding in tension and compression, Drucker [9, 11], whereas $\bar{\Phi}\left(\mathbb{J}_2^{3/2} + c\mathbb{J}_3\right)$ represent an asymmetric yielding in tension and compression [2, 3, 6] as $\mathbb{J}_3$ is an uneven cubic function of stresses. In both cases, the convexity condition confines the range of admissible values of the constant, c [11, 18].

3.3.1 The Yield Condition of Tresca

Tresca's yield condition [24] is also known as hypothesis of maximum shear stresses. It is commonly expressed as piecewise linear relations in terms of principal stresses, $\sigma_\alpha\,(\alpha = \mathrm{I, II, III})$, known as the Tresca hexagon, Fig. 3.3.

$$\left\{\begin{array}{ll} \sigma_\mathrm{I} \geq \sigma_\mathrm{II} \geq \sigma_\mathrm{III}: & \tilde{\Phi}_1 = \sigma_\mathrm{I} - \sigma_\mathrm{III} - 2\tau_\mathrm{F} = 0 \\ \sigma_\mathrm{II} \geq \sigma_\mathrm{I} \geq \sigma_\mathrm{III}: & \tilde{\Phi}_2 = \sigma_\mathrm{II} - \sigma_\mathrm{III} - 2\tau_\mathrm{F} = 0 \\ \sigma_\mathrm{II} \geq \sigma_\mathrm{III} \geq \sigma_\mathrm{I}: & \tilde{\Phi}_3 = \sigma_\mathrm{II} - \sigma_\mathrm{I} - 2\tau_\mathrm{F} = 0 \\ \sigma_\mathrm{III} \geq \sigma_\mathrm{II} \geq \sigma_\mathrm{I}: & \tilde{\Phi}_4 = \sigma_\mathrm{III} - \sigma_\mathrm{I} - 2\tau_\mathrm{F} = 0 \\ \sigma_\mathrm{III} \geq \sigma_\mathrm{I} \geq \sigma_\mathrm{II}: & \tilde{\Phi}_5 = \sigma_\mathrm{III} - \sigma_\mathrm{II} - 2\tau_\mathrm{F} = 0 \\ \sigma_\mathrm{I} \geq \sigma_\mathrm{III} \geq \sigma_\mathrm{II}: & \tilde{\Phi}_6 = \sigma_\mathrm{I} - \sigma_\mathrm{II} - 2\tau_\mathrm{F} = 0 \end{array}\right\}. \tag{3.20}$$

The yield limit in shear, τ_F, is related to the uniaxial yield strength, R_F, by

$$\tau_\mathrm{F}(\varepsilon_\mathrm{p}) = \frac{1}{2} R_\mathrm{F}(\varepsilon_\mathrm{p}), \tag{3.21}$$

and the associated equivalent stress is

$$\bar{\sigma}_\mathrm{T} = \max_{\alpha \neq \beta} \left|\sigma_\alpha - \sigma_\beta\right| = \max_{\alpha \neq \beta} \sqrt{\left(\sigma_\alpha - \sigma_\beta\right)^2}, \quad (\alpha, \beta = \mathrm{I,II,III}). \tag{3.22}$$

If the principal stresses are arranged by their magnitudes, $\sigma_\mathrm{I} \geq \sigma_\mathrm{II} \geq \sigma_\mathrm{III}$, only $\tilde{\Phi}_1$ is relevant as yield condition. However, calculations of the plastic strain rates in one of the corners, $\sigma_\mathrm{I} = \sigma_\mathrm{II} > \sigma_\mathrm{III}$ or $\sigma_\mathrm{I} > \sigma_\mathrm{II} = \sigma_\mathrm{III}$, have to consider $\tilde{\Phi}_2$ or $\tilde{\Phi}_6$ as well, see Eq. (3.25) below.

Considering that the product of all piecewise yield functions, $\tilde{\Phi}_i$ (i = 1, …, 6), vanishes, Tresca's yield condition may be written in closed form of the 2nd and 3rd invariants, $\mathbb{J}_2(\sigma'_{ij})$, $\mathbb{J}_3(\sigma'_{ij})$, Eq. (3.19),

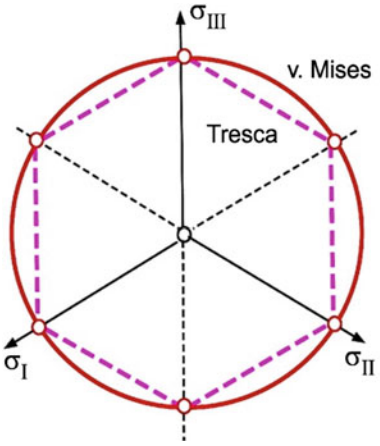

Fig. 3.3 Yield conditions of Tresca and von Mises displayed in the deviatoric plane

$$\tilde{\Phi}_{\mathrm{T}}(\mathbb{J}_2,\mathbb{J}_3)=\prod_{i=1}^{6}\tilde{\Phi}_i=4\mathbb{J}_2^3-27\mathbb{J}_3^2-9R_{\mathrm{F}}^2\mathbb{J}_2^2+6R_{\mathrm{F}}^4\mathbb{J}_2-R_{\mathrm{F}}^6=0. \tag{3.23}$$

As the yield function is piecewise defined, the same holds for the associated flow rule, Eq. (3.12), for example $\sigma_{\mathrm{I}}>\sigma_{\mathrm{II}}>\sigma_{\mathrm{III}}$,

$$\dot{\boldsymbol{\varepsilon}}^{\mathrm{p}}=\dot{\varepsilon}_\alpha^{\mathrm{p}}\mathbf{n}_\alpha=\dot{\lambda}_{\mathrm{p}}\frac{\partial\tilde{\Phi}_1}{\partial\sigma_\alpha}\mathbf{n}_\alpha=\dot{\lambda}_{\mathrm{p}}(\mathbf{n}_{\mathrm{I}}-\mathbf{n}_{\mathrm{III}}), \tag{3.24}$$

where $\mathbf{n}_{\mathrm{I}}$, $\mathbf{n}_{\mathrm{II}}$, $\mathbf{n}_{\mathrm{III}}$, are the unit vectors along the principal axes. In the corner, $\sigma_{\mathrm{I}}=\sigma_{\mathrm{II}}>\sigma_{\mathrm{III}}$,

$$\dot{\boldsymbol{\varepsilon}}^{\mathrm{p}}=\dot{\lambda}_1^{\mathrm{p}}\frac{\partial\tilde{\Phi}_1}{\partial\sigma_\alpha}\mathbf{n}_\alpha+\dot{\lambda}_2^{\mathrm{p}}\frac{\partial\tilde{\Phi}_2}{\partial\sigma_\alpha}\mathbf{n}_\alpha=\dot{\lambda}_{\mathrm{p}}(\mathbf{n}_{\mathrm{I}}+\mathbf{n}_{\mathrm{II}}-2\mathbf{n}_{\mathrm{III}}), \tag{3.25}$$

holds, assuming $\dot{\lambda}_1^{\mathrm{p}}=\dot{\lambda}_2^{\mathrm{p}}=\dot{\lambda}_{\mathrm{p}}$ for isotropic materials. The condition of incompressibility, Eq. (3.9), $\sum_{\alpha=\mathrm{I}}^{\mathrm{III}}\dot{\varepsilon}_\alpha^{\mathrm{p}}=0$, is met. The plastic multiplier, $\dot{\lambda}_{\mathrm{p}}$, follows from comparison with plastic deformations, $\dot{\boldsymbol{\varepsilon}}^{\mathrm{p}}=\dot{\varepsilon}_\alpha^{\mathrm{p}}\mathbf{n}_\alpha=\dot{\lambda}_{\mathrm{p}}(2\mathbf{n}_{\mathrm{I}}-\mathbf{n}_{\mathrm{II}}-\mathbf{n}_{\mathrm{III}})$, in a uniaxial tensile test, $\boldsymbol{\sigma}=\sigma_{\mathrm{I}}\,\mathbf{n}_{\mathrm{I}}$ $(\sigma_{\mathrm{I}}>\sigma_{\mathrm{II}}=\sigma_{\mathrm{III}}=0)$, by accounting for the equivalence of dissipations rate densities, Eq. (3.13),

$$\dot{w}^{\mathrm{p}}=\sigma_\alpha\dot{\varepsilon}_\alpha^{\mathrm{p}}=2\dot{\lambda}_{\mathrm{p}}\sigma_{\mathrm{I}}=\bar{\sigma}_{\mathrm{T}}\,\dot{\bar{\varepsilon}}^{\mathrm{p}}=R_{\mathrm{F}}\dot{\varepsilon}_{\mathrm{p}}. \tag{3.26}$$

as $\dot{\lambda}_{\mathrm{p}}=\frac{1}{2}\dot{\varepsilon}_{\mathrm{p}}$, i.e.

$$\dot{\boldsymbol{\varepsilon}}^{\mathrm{p}}=\dot{\varepsilon}_{\mathrm{p}}\left(\mathbf{n}_{\mathrm{I}}-\frac{1}{2}\mathbf{n}_{\mathrm{II}}-\frac{1}{2}\mathbf{n}_{\mathrm{III}}\right). \tag{3.27}$$

Aside from the mathematical drawback that Tresca's yield condition is not continuously differentiable in the corners, the inevitable transformation to principal coordinates and the elaborate formulation of the flow rule are major reasons for preferring the yield condition of von Mises [25, 26] particularly for numerical applications. Frequently, the Tresca condition is even combined with a flow rule associated to the Mises condition, which violates the equivalence of dissipations rate densities.

3.3.2 The Theory of Von Mises, Prandtl and Reuß

The most commonly applied incremental theory of plasticity consists of the yield condition of von Mises [25, 26] and the equations for plastic deformations by Prandtl [20] and Reuß [23]. The yield condition is based on the 2nd invariant,

$$\tilde{\Phi}_{\mathrm{vM}} = 3\mathbb{J}_2 - \frac{3}{2}\bar{\kappa}^2(\varepsilon_{\mathrm{p}}) = \bar{\sigma}^2_{\mathrm{vM}} - R^2_{\mathrm{F}}(\varepsilon_{\mathrm{p}}) = 0, \tag{3.28}$$

which results in the definition of the equivalent stress,

$$\bar{\sigma}_{\mathrm{vM}} = \sqrt{3\mathbb{J}_2} = \sqrt{\frac{3}{2}\sigma'_{ij}\sigma'_{ij}}. \tag{3.29}$$

Hence, the theory of von Mises is often addressed as $\mathbb{J}_2$-theory. It is represented by a circle in the deviatoric plane, Fig. 3.3. The yield conditions of Tresca and von Mises coincide for principal stress states. Different from Eq. (3.21), the relation between the uniaxial yield strength, R_{F}, and the yield limit in shear, τ_{F}, is

$$R_{\mathrm{F}}(\varepsilon_{\mathrm{p}}) = \sqrt{3}\,\tau_{\mathrm{F}}(\varepsilon_{\mathrm{p}}). \tag{3.30}$$

Thus, the two yield conditions differ by $2/\sqrt{3} = 1.15$, at most.

The associated flow rule follows from Eq. (3.12),

$$\dot{\varepsilon}^{\mathrm{p}}_{ij} = \dot{\lambda}_{\mathrm{p}}\sigma'_{ij}, \tag{3.31}$$

and the equivalence of dissipations rate densities, Eq. (3.13), provides a work-conjugate equivalent plastic strain rate

$$\dot{\bar{\varepsilon}}^{\mathrm{p}}_{\mathrm{vM}} = \sqrt{\frac{2}{3}\dot{\varepsilon}^{\mathrm{p}}_{ij}\dot{\varepsilon}^{\mathrm{p}}_{ij}}. \tag{3.32}$$

Note, that this definition is only valid in combination with the von Mises yield condition! The plastic multiplier can again be calculated from the yield curve, $R_{\mathrm{F}}(\varepsilon_{\mathrm{p}})$, of the uniaxial tensile test,

$$\dot{\varepsilon}_{ij}^{\mathrm{p}} = \frac{3}{2}\frac{\dot{\bar{\varepsilon}}_{\mathrm{vM}}^{\mathrm{p}}}{R_{\mathrm{F}}}\sigma'_{ij} = \frac{3}{2}\frac{\dot{\bar{\sigma}}_{\mathrm{vM}}}{T_{\mathrm{p}}R_{\mathrm{F}}}\sigma'_{ij}, \tag{3.33}$$

where $T_{\mathrm{p}}(\varepsilon_{\mathrm{p}}) = dR_{\mathrm{F}}/d\varepsilon_{\mathrm{p}}$ is the plastic tangent modulus.

Finally, the criterion for loading or unloading writes as

$$\sigma'_{ij}\dot{\sigma}_{ij}\begin{cases} >0 & \text{loading} \quad \dot{\varepsilon}_{ij}^{\mathrm{p}} \neq 0 \\ <0 & \text{unloading} \quad \dot{\varepsilon}_{ij}^{\mathrm{p}} = 0 \end{cases}. \tag{3.34}$$

Adding up elastic, Eq. (3.11), and plastic, Eq. (3.33), strain rates according to Eq. (3.7) results in the equations of Prandtl [20] and Reuß [23] for the total strain rates,

$$\dot{\varepsilon}_{ij} = \dot{\varepsilon}_{ij}^{\mathrm{e}} + \dot{\varepsilon}_{ij}^{\mathrm{p}} = \dot{\varepsilon}_{ij}^{\prime e} + \frac{1}{3}\dot{\varepsilon}_{kk}^{\mathrm{e}}\delta_{ij} + \dot{\varepsilon}_{ij}^{\prime \mathrm{p}} = \frac{1}{2G}\dot{\sigma}'_{ij} + \frac{1}{3K}\dot{\sigma}_{\mathrm{h}}\delta_{ij} + \frac{3}{2T_{\mathrm{p}}}\frac{\dot{\bar{\sigma}}_{\mathrm{vM}}}{R_{\mathrm{F}}}\sigma'_{ij}. \tag{3.35}$$

Volume dilatation is purely elastic, $\dot{\varepsilon}_{kk} = \dot{\varepsilon}_{kk}^{\mathrm{e}}$, distortion consists of an elastic and a plastic part, $\dot{\varepsilon}'_{ij} = \dot{\varepsilon}_{ij}^{\prime e} + \dot{\varepsilon}_{ij}^{\prime \mathrm{p}}$.

The constitutive Eqs. (3.28)–(3.35) do not allow for analytical closed form solutions, generally, and, different from elasticity, load versus displacement curves as well as stress and strain fields are dependent on the loading history, so that only a step-wise integration for a certain loading path is possible. Just a limited number of analytical solutions for uniaxial stress states as in tension and pure bending or for axisymmetric or rotationally symmetric stress states exist.

3.3.3 *Example: Pressure Vessel*

The cylinder of Fig. 2.5 is considered without a crack and cylindrical coordinates (r, φ, z) are introduced, again. The elastic boundary value problem yields Lamé's equations for the distribution of stresses in the cylinder wall, Eq. (2.33). The elastic limit is reached, if von Mises equivalent stress,

$$\bar{\sigma}_{\mathrm{vM}} = \sqrt{\frac{1}{2}\left[\left(\sigma_{rr} - \sigma_{\varphi\varphi}\right)^2 + \left(\sigma_{rr} - \sigma_{zz}\right)^2 + \left(\sigma_{\varphi\varphi} - \sigma_{zz}\right)^2\right]} = \frac{\sqrt{3}}{2}\left(\sigma_{\varphi\varphi} - \sigma_{rr}\right), \tag{3.36}$$

considering Eq. (2.32), equals the yield strength, R_0, at $r = r_{\mathrm{i}}$. The corresponding elastic limit pressure is

$$p_{\mathrm{el}} = \frac{R_0}{\sqrt{3}}\left(1 - \frac{r_\mathrm{i}^2}{r_\mathrm{o}^2}\right) \tag{3.37}$$

The total rest of the cylinder, $r_\mathrm{i} < r \leq r_\mathrm{o}$, is still elastic so that the pressure may further increase until the whole wall is plastified. The respective pressure is called plastic limit pressure, p_pl, assuming a perfectly plastic material, $R_\mathrm{F}(\varepsilon_\mathrm{p}) = R_0$. The stress distribution can be easily calculated by introducing the yield condition into the balance Eq. (2.30),

$$\frac{d\sigma_{rr}}{dr} - \frac{2}{\sqrt{3}}\frac{R_0}{r} = 0. \tag{3.38}$$

The solution of this first order differential equation, with the boundary conditions $\sigma_{rr}(r_\mathrm{o}) = 0$, $\sigma_{rr}(r_\mathrm{i}) = -p$, and the yield condition finally result in,

$$\begin{aligned} \sigma_{rr} &= \tfrac{2R_0}{\sqrt{3}} \ln \tfrac{r}{r_\mathrm{o}} \\ \sigma_{\varphi\varphi} &= \tfrac{2R_0}{\sqrt{3}} \left(1 + \ln \tfrac{r}{r_\mathrm{o}}\right), \\ \sigma_{zz} &= \tfrac{2R_0}{\sqrt{3}} \left(\tfrac{1}{2} + \ln \tfrac{r}{r_\mathrm{o}}\right) \end{aligned} \tag{3.39}$$

which are graphically displayed in Fig. 3.4. The stress distributions for the intermediate range, $p_\mathrm{el} < p < p_\mathrm{pl}$, can be found in Reckling [22] or Burth and Brocks [5].

The plastic limit pressure results from the boundary condition, $\sigma_{rr}(r_\mathrm{i}) = -p$,

$$p_\mathrm{pl} = \frac{2R_0}{\sqrt{3}} \ln \frac{r_\mathrm{o}}{r_\mathrm{i}}. \tag{3.40}$$

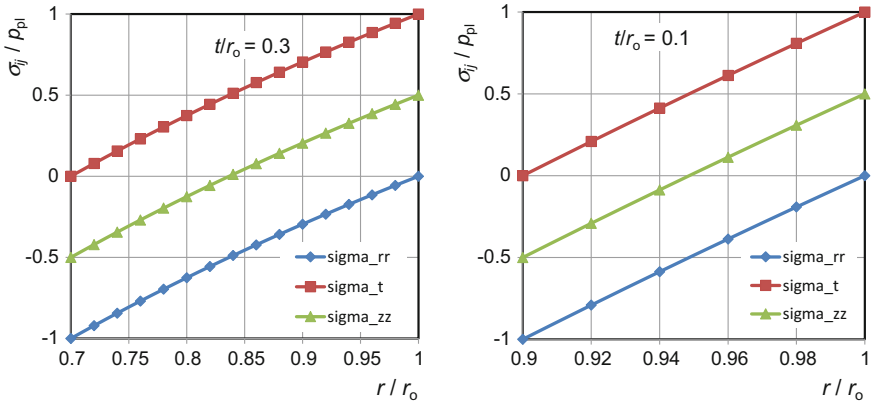

Fig. 3.4 Radial, circumferential (tangential) and axial stresses, σ_{rr}, $\sigma_\mathrm{t} \equiv \sigma_{\varphi\varphi}$, σ_{zz}, in a thick-walled cylinder at plastic limit pressure, p_pl

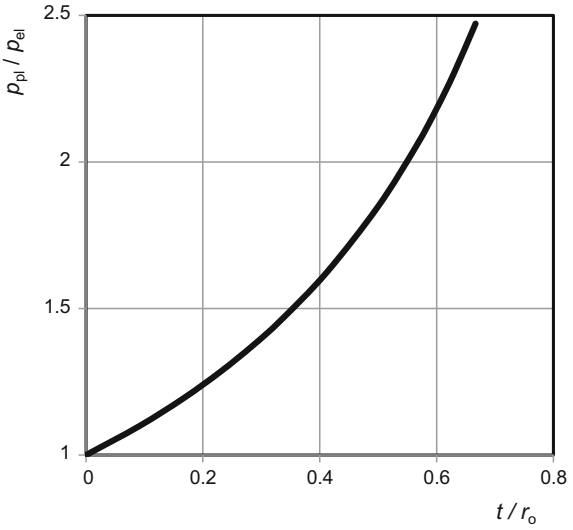

Fig. 3.5 Limit load factor, p_{pl}/p_{el}, for a thick-walled cylinder under internal pressure in dependence on wall-thickness, t

Elastic and plastic limit pressure may both be taken as design criteria if brittle fracture can be excluded according to Eq. (2.44). The plastic limit state is unique and not dependent on the loading history. It can hence be determined without considering intermediate steps. The ratio of plastic and elastic limit pressure is called limit load factor and characterises the capacity for excessive loading beyond the elastic limit until failure due to plastic collapse (see Sect. 6.1.2), Fig. 3.5,

$$\frac{p_{pl}}{p_{el}} = \frac{\ln(r_o/r_i)}{1-(r_i/r_o)^2}. \tag{3.41}$$

3.4 Deformation Theory of Plasticity

In contrast to the incremental equation of Prandtl [20] and Reuß [23], Eq. (3.35), Hencky [14] suggested a finite deformation law for non-linear constitutive behaviour, which is particularly used in fracture mechanics in combination with the hardening law of Ramberg and Osgood [21]. Actually, it does not describe plastic but non-linear elastic (hyperelastic) behaviour. It is advantageous with respect to its mathematically simpler handling which allows for closed-form solutions of boundary value problems like the HRR equations for stress and strain fields at a crack tip along the lines of LEFM, Eq. (2.14). Under the severely restrictive assumption of proportional loading, $\sigma_{ij}(t) = \sigma_{ij}^0 \zeta(t)$, $\zeta(0) = 1$, in each point of the continuum, which excludes any kind of local rearrangement of stresses or unloading, the finite Hencky equations can be derived from Prandtl-Reuß equations.

The conditions of isotropy and incompressibility, Eq. (3.9), and von Mises hypothesis, Eq. (3.29), still apply. But instead of the additive decomposition of strain rates, Eq. (3.7), an additive decomposition of total strains is assumed,

$$\varepsilon_{ij} = \varepsilon_{ij}^{\mathrm{e}} + \varepsilon_{ij}^{\mathrm{p}}, \tag{3.42}$$

and instead of the incremental flow rule, Eq. (3.31), a finite deformation law,

$$\varepsilon_{ij}^{\mathrm{p}} = \lambda_{\mathrm{p}} \sigma'_{ij}. \tag{3.43}$$

is assumed, and the finite plastic multiplier is determined via the uniaxial flow curve as above,

$$\lambda_{\mathrm{p}} = \frac{3}{2}\frac{\varepsilon_{\mathrm{p}}}{R_{\mathrm{F}}} = \frac{3}{2S_{\mathrm{p}}}, \tag{3.44}$$

with $S_{\mathrm{p}}(\varepsilon_{\mathrm{p}}) = R_{\mathrm{F}}/\varepsilon_{\mathrm{p}}$ as plastic secant modulus. As only loading is admissible $\bar{\sigma}_{\mathrm{vM}} = R_{\mathrm{F}}(\varepsilon_{\mathrm{p}})$ is always met. Total strains result from

$$\varepsilon_{ij} = \left(\frac{1}{2G} + \frac{3}{2S_{\mathrm{p}}}\right)\sigma'_{ij} + \frac{1}{3K}\sigma_{\mathrm{h}}\delta_{ij}. \tag{3.45}$$

The analogy to Hooke's law with a Poisson's ratio of $\nu = 0.5$ is obvious. Defining

$$S_{\mathrm{p}}(\varepsilon_{\mathrm{p}}) = \frac{\sigma_0}{\alpha\varepsilon_0}\left(\frac{\bar{\sigma}_{\mathrm{vM}}}{\sigma_0}\right)^{1-n} \tag{3.46}$$

according to Ramberg and Osgood [21] with the material parameters $\alpha > 0$ and $n \geq 1$ and normalising quantities, σ_0, ε_0, the plastic part of Hencky's law, Eq. (3.45), becomes

$$\frac{\varepsilon_{ij}^{\mathrm{p}}}{\varepsilon_0} = \frac{3}{2}\alpha\left(\frac{\bar{\sigma}_{\mathrm{vM}}}{\sigma_0}\right)^{n-1}\frac{\sigma'_{ij}}{\sigma_0}. \tag{3.47}$$

This equation is known as three-dimensional generalisation of the Ramberg-Osgood power law,

$$\frac{\varepsilon}{\varepsilon_0} = \frac{\sigma}{\sigma_0} + \alpha\left(\frac{\sigma}{\sigma_0}\right)^{n}, \tag{3.48}$$

which is displayed in Fig. 3.6. Commonly, $\sigma_0 = R_0$ and $\varepsilon_0 = \sigma_0/E$ are assumed. This law is non-linear from the beginning and there is no distinct transition from elastic to plastic behavior and hence no yield conditions.

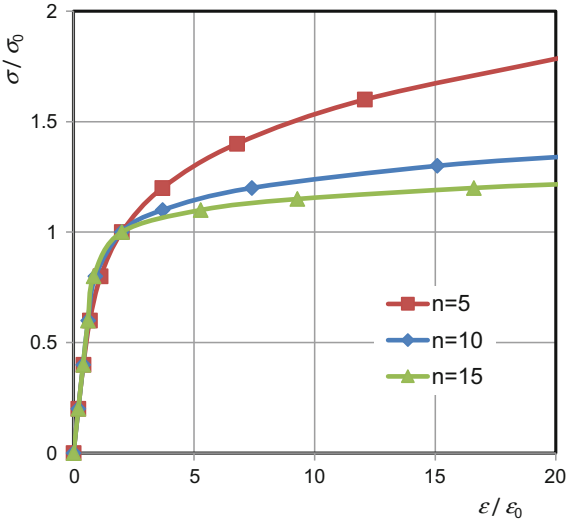

Fig. 3.6 Power law hardening according to Ramberg and Osgood [21]

Though the term "deformation theory" solely characterises the finite theory (or "flow theory") of plasticity it is frequently identified by the combination of Hencky's equations with the Ramberg-Osgood power law in elasto-plastic facture mechanics (EPFM).

References

1. Betten J (1976) Ein Beitrag zur Invariantentheorie in der Plastomechanik inkompressibler iso-troper Werkstoffe. Stahlbau 5
2. Betten J (1979) Über die Konvexität von Fließkörpern isotroper und anisotroper Stoffe. Acta Mech 32:233–247
3. Betten J (1985) Elastizitäts- und Plastizitätslehre. Vieweg, Braunschweig
4. Brocks W, Olschewski J (1989) Application of internal time and internal variable theories of plasticity to complex load histories. Arch Mech 41:133–155
5. Burth K, Brocks W (1992) Plastizität - Grundlagen und Anwendungen für Ingenieure. Vieweg, Braunschweig
6. Cazacu O, Barlat F (2004) A criterion for description of anisotropy and yield differential effects in pressure insensitive metals. Int J Plast 20:2027–2045
7. Chaboche JL (1989) Constitutive equations for cyclic plasticity and cyclic viscoplasticity. Int J Plast 5:247–302
8. Chaboche JL, Rousselier G (1983) On the plastic and viscoplastic constitutive equations—Part I: Rules developed with internal variables. J Pressure Vessel Technol 105:153–158
9. Drucker DC (1949) Relation of experiments to mathematical theories of plasticity. J Appl Mech 16:349–357
10. Drucker DC (1950) Some implications of work hardening and ideal plasticity. Q Appl Math 7:411–418

11. Drucker DC (1959) A definition of stable inelastic material. Trans ASME, J Appl Mech, pp 101–106
12. Drucker DC (1964) On the postulate of stability of materials in the mechanics of continua. J Mécanique 3:235–249
13. Halama R, Sedlák J, Šofer M (2012) Phenomenological modelling of cyclic plasticity. In: Miidla P (ed) Numerical modelling. InTech, ISBN 978-953-51-0219-9
14. Hencky H (1924) Zur Theorie plastischer Deformationen und der hierdurch im Material hervorgerufenen Nachspannungen. Z Angew Math Mech 4:323–334
15. Ismar I, Mahrenholtz O (1979) Technische Plastomechanik. Vieweg, Braunschweig
16. Ismar I, Mahrenholtz O (1982) Über Beanspruchungshypothesen für metallische Werkstoffe. Konstruktion 34:305–310
17. Mahrenholtz H, Ismar (1981) Zum elastisch-plastischen Übergangsverhalten metallischer Werkstoffe. Arch Appl Mech 50:217–224
18. Prager W (1945) Strain hardening under combined stresses. J Appl Phys 16:837–840
19. Prager W (1955) The theory of plasticity: a survey of recent achievements. Proc Int Mech Eng 169:41–57
20. Prandtl L (1928) Ein Gedankenmodell zur kinetischen Theorie der festen Körper. Z Angew Math Mech 8:85–106
21. Ramberg W, Osgood WR (1945) Description of stress strain curves by three parameters. NACA Technical Note No 902
22. Reckling KA (1967) Plastizität und ihre Anwendung auf Festigkeitsprobleme. Springer, Berlin
23. Reuß A (1930) Berücksichtigung der elastischen Formänderung in der Plastizitätstheorie. Z Angew Math Mech 10:266–274
24. Tresca H (1864) Mémoire sur l'écoulement des corps solides soumis à de forts pression. Comptes Rendus Acad Sci Paris 20:75–135
25. von Mises R (1913) Die Mechanik der festen Körper im plastisch deformablen Zustand. Nachr Königl Ges Wiss Göttingen: 582–592
26. von Mises R (1928) Mechanik der plastischen Formänderung von Metallen. Z Angew Math Mech 8:161–185
27. Ziegler H (1959) A modification of Prager's hardening rule. Q Appl Math 17:55–65

Chapter 4
Extension of LEFM for Small-Scale Yielding

Abstract Linear elastic fracture mechanics as introduced in Chap. 2 is extended to account for plastic deformations at the crack tip. The concept of an equivalent elastic crack and an effective stress intensity factor for small-scale yielding is explicated. Size and shape of the plastic zone ahead of the crack tip are calculated and the effect of biaxial external loading is discussed. The crack tip opening displacement (CTOD) is introduced as an alternative intensity parameter.

The stresses calculated at a notch root can exceed the yield strength so that local plastification occurs. In any case, the yield strength is exceeded at a crack tip in LEFM, as the stress field has a singularity. The size of the resulting plastic zone, which is assumed to be small compared to the ligament, $W - a$, and the actual stress distribution depend on the stress triaxiality.

4.1 The Equivalent Elastic Crack (Mode I)

Irwin [12] presented the idea to calculate the size of the plastic zone approximately from the stress field in the elastic continuum and to introduce a fictitious crack extension with a modified effective SIF. This idea is explicated in the following for the two limiting conditions of plane stress, $\sigma_{zz} = 0$, and plane strain, $\varepsilon_{zz} = 0$. Shear stresses in the ligament vanish for mode I, normal stresses are principal stresses, and the yield conditions of von Mises and Tresca accord.

- **Plane stress** ($\sigma_{zz} = 0$)

According to Eq. (2.14) and Table 2.2, the in-plane normal stresses in the ligament, $\theta = 0$, are

$$\sigma_{xx}(x) = \sigma_{yy}(x) = \frac{K_\mathrm{I}}{\sqrt{2\pi x}} \tag{4.1}$$

W. Brocks, *Plasticity and Fracture*, Solid Mechanics and Its Applications 244,
DOI 10.1007/978-3-319-62752-6_4

The yield condition for a perfectly plastic material requires $\sigma_{yy}(r) = R_0$ in a range $0 \leq x \leq x_p$. In particular, it characterises the point, $x = x_p$, where the stresses of LEFM reach the yield strength,

$$x_p = \frac{1}{2\pi}\left(\frac{K_I}{R_0}\right)^2 \tag{4.2}$$

- **Plane strain** ($\varepsilon_{zz} = 0$)

Equation (4.1) holds and the third principal stress follows from Eq. (2.1) as $\sigma_{zz} = \nu\,(\sigma_{xx} + \sigma_{yy})$, which result in the yield condition $(1 - 2\nu)\,\sigma_{yy}(x) = R_0$ and

$$x_p = \frac{(1-2\nu)^2}{2\pi}\left(\frac{K_I}{R_0}\right)^2 = \frac{1}{2\pi}\left(\frac{K_I}{R_0'}\right)^2, \tag{4.3}$$

with $R_0' = R_0/(1-2\nu)$ for plane strain. The difference between plane stress and plane strain, i.e. the different triaxiality of the respective stress states, affects the size of the plastic zone. The following considerations are independent of the stress state, however.

The truncated stresses in the range $[0, x_p]$ where the yield limit is reached,

$$\int_0^{x_p} \sigma_{yy}(x)\,dx - R_0' x_p = \int_0^{x_p} \frac{K_I}{\sqrt{2\pi x}}dx - R_0' x_p = \sqrt{\frac{2x_p}{\pi}} - R_0' x_p = R_0' x_p, \tag{4.4}$$

see Fig. 4.1, have to be compensated. This is realised by introducing a fictitious crack of "effective" length,

$$a_{eff} = a + x_p, \tag{4.5}$$

where the conditions of LEFM hold. The respective "effective" SIF for small plastic zones, $x_p \ll a$, is approximately

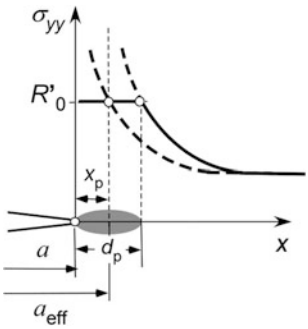

Fig. 4.1 Irwin's concept of an effective crack tip

$$K_{\mathrm{I}}^{\mathrm{eff}} = \sqrt{\frac{a_{\mathrm{eff}}}{a}} \frac{Y(a_{\mathrm{eff}})}{Y(a)} K_{\mathrm{I}}. \tag{4.6}$$

Stresses ahead of the notional crack tip are described by Eq. (4.1) with $K_{\mathrm{I}} \Rightarrow K_{\mathrm{Ieff}}$. They reach the yield limit, R_0', in a distance of x_{p}, and the total extension of the plastic zone in the ligament is

$$d_{\mathrm{p}}^{\mathrm{Irwin}} = 2x_{\mathrm{p}} = \frac{1}{\pi} \left(\frac{K_{\mathrm{I}}}{R_0'} \right)^2, \tag{4.7}$$

with

$$R_0' = \begin{cases} \frac{R_0}{1-2\nu} & \text{for plane strain, } \varepsilon_{zz} = 0 \\ R_0 & \text{for plane stress, } \sigma_{zz} = 0 \end{cases}. \tag{4.8}$$

Analogously, an "effective" energy release rate for small scale yielding (SSY) can be calculated according to Eq. (2.16),

$$\mathcal{G}_{\mathrm{eff}} = \frac{\left(K_{\mathrm{I}}^{\mathrm{eff}}\right)^2}{E'}. \tag{4.9}$$

The concept of an effective crack length is picked up in ASTM E 561 [2] for determination of K-based resistance curves, $K_{\mathrm{R}}(a_{\mathrm{eff}})$, for metal sheets (see Sect. 7.2.4 on crack extension in thin structures). Crack extension under plane stress conditions and SSY is assumed and a_{eff} is either calculated from Eq. (4.2) or (experimentally) determined from the compliance.

A SSY correction for semi-elliptical surface cracks (see Sect. 2.3.2) is applied by modifying the elliptical integral, $E(k)$, Eq. (2.37), and defining a shape factor according to ASME BPVC [1],

$$Q(k) = E^2(k) - 0.212 \frac{\sigma_{\mathrm{m}} + \sigma_{\mathrm{b}}}{R_0}, \tag{4.10}$$

instead, Fig. 2.8, which results in

$$K_{\mathrm{I}}^{\mathrm{max}} = (M_{\mathrm{m}}\sigma_{\mathrm{m}} + M_{\mathrm{b}}\sigma_{\mathrm{b}}) \sqrt{\frac{\pi a}{Q}}. \tag{4.11}$$

4.2 Crack Tip Opening Displacement (CTOD)

An important fracture parameter for plastic materials can be defined based on Irwin's concept, namely the crack tip opening displacement (CTOD), δ_t. according to Eq. (2.15) with $\theta = \pi$. The elastic crack opening in mode I is

$$u_y(r,\pi) = 4\frac{K_I}{E}\sqrt{\frac{r}{2\pi}}\begin{cases} 1 & \text{for plane stress} \\ 1-\nu^2 & \text{for plane strain} \end{cases}. \tag{4.12}$$

Following a conception of Wells [22], the CTOD is defined by the elastic opening of the "effective" crack at the locus of the real crack, see Fig. 4.2,

$$\delta_t = 2u_y(x_p). \tag{4.13}$$

Introducing Irwin's Eqs. (4.2) and (4.3) results in

$$\delta_t^{\text{Irwin}} = \frac{4}{\pi}\frac{K_I^2}{ER_0}\begin{cases} 1 & \text{for plane stress} \\ (1-\nu^2)(1-2\nu) & \text{for plane strain} \end{cases}. \tag{4.14}$$

CTOD has become a fracture parameter besides the *J*–integral in EPFM (see Sect. 5.3.3 on CTOD and CTOA). Aside from Eq. (4.13), other definitions exist [19]; ASTM E 2472 [3]; BS 7448 [7]. The CTOD concept is based on the physical perception that a critical plastic deformation, $\delta_t = \delta_c$, is responsible for the initiation of crack extension. It has particularly become relevant for thin-walled structures like panels and shells in aircraft construction [17, 20] where the application of *J* exceeds its validity.

4.3 Shape of the Plastic Zone

In Sect. 4.1, the extension of the plastic zone in the ligament has been calculated. Since the complete distribution of stresses according to the asymptotic approximation, Eq. (2.14), is known, the two-dimensional shape of the plastic zone in SSY

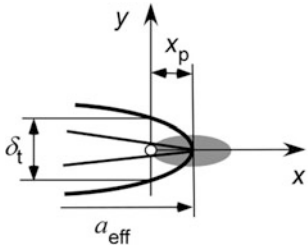

Fig. 4.2 Wells' definition of CTOD based on Irwin's concept of an effective crack tip

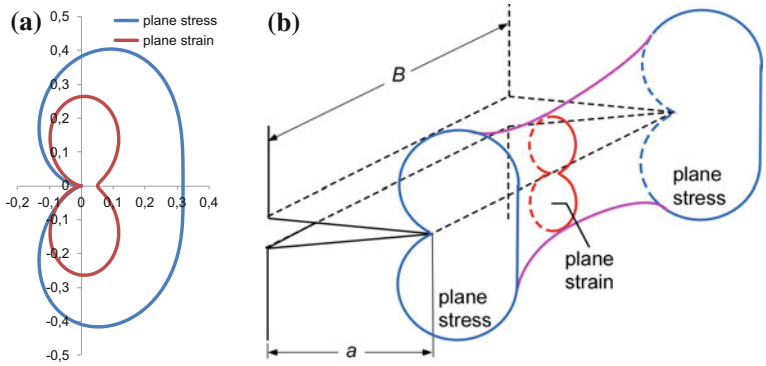

Fig. 4.3 **a** Shape of the plastic zones in plane stress and plane strain: abscissa and ordinate normalised by $(K_I/R_0)^2$; **b** "dog-bone" model

can be determined from the yield condition, $\bar{\sigma}_{vM}|_{r_p} = R_0$. The boundary of the plastic zone is [10, 13]

$$d_p(\theta) = \frac{1}{2\pi}\left(\frac{K_I}{R_0}\right)^2 \begin{cases} 1 + \frac{3}{2}\sin^2\theta + \cos\theta & \text{for plane stress} \\ \frac{3}{2}\sin^2\theta + (1-2\nu)^2(1+\cos\theta) & \text{for plane strain} \end{cases}, \quad (4.15)$$

see Fig. 4.3a. For $\theta = 0$, Eq. (4.7) is obtained, but this is obviously not the maximum extent of the plastic zone.

The shape of the plastic zone changes along the crack front in three-dimensional structures. Assuming stress states of plane strain in the centre and plane stress at the surface, Hahn and Rosenfield [11] suggested the "dog-bone" model for the three-dimensional plastic zone in SSY, Fig. 4.3b.

Figure 4.3a reveals that the maximum extent of the plastic zone is not at $\theta = 0$, of course, which is obvious from the angular stress distributions in Fig. 2.4. It is rather at 87.0° for plane strain and 70.5° for plane stress, see Fig. 4.4.

Size and shape of the plastic zone are of vital importance for the definition of valid fracture toughness values, K_{Ic} (see Sect. 7.2.2 on linear-elastic plane-strain fracture toughness). Fierce discussions on the "geometry dependence" of fracture toughness in the 1990s stimulated a revival of earlier considerations on the "biaxiality" of stress states and "two-parameter concepts" of fracture mechanics. Since the singularity of stresses appeared so dominant, the constant term, Eq. (2.21), in the series expansion of Williams [23], Eq. (2.20), had been neglected since Irwin [12] and then forgotten for a long time. Larsson and Carlsson [14] investigated the "*influence of non-singular stress terms and specimen geometry on small scale yielding at crack-tips*" by FEM analyses and found that both the size and the shape of the plastic zone were significantly affected by the biaxiality of loading and the specimen geometry. Rice [18] studied the "*limitations to the small scale yielding approximation for crack tip plasticity*" and introduced the *T*-stress, Eq. (2.22), which is the ancestor of all

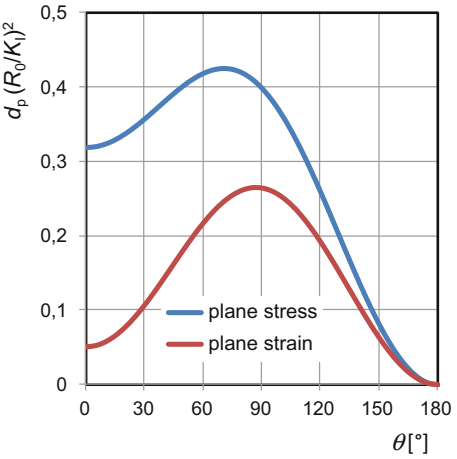

Fig. 4.4 Normalised extent of the plastic zone at the crack tip in SSY according to Irwin's model

"second parameters" in fracture mechanics. He also presented an analytical estimate of the T-stress effect on the extent of the plastic zone, $d_p(\theta)$,

$$d_p(\theta) = \frac{3\pi}{32}\left(\frac{K_I}{R_0}\right)^2 \frac{\sin^2\theta(1+\cos\theta)}{[1+(T/\tau_0)\sin\theta\cos\theta]^2}, \tag{4.16}$$

displayed in Fig. 4.5 in comparison with Irwin's model, Eq. (4.15). Figure 4.5a shows the various shapes of the plastic zone, Fig. 4.5b the maximum of d_p and Fig. 4.5c the respective angle at which it occurs. The orientation of the plastic zone is significantly affected by the T-stress. A major effect on the size occurs for

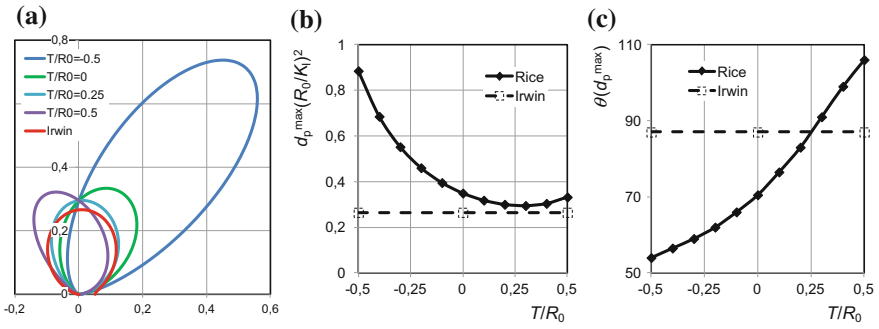

Fig. 4.5 Plastic zone at the crack tip according to Rice's model in dependence on T-stress compared to Irwin's plane strain model: **a** shape, abscissa and ordinate normalised by $(K_I/R_0)^2$, **b** maximum extent, d_p^{max}, normalised by $(K_I/R_0)^2$, **c** angle, $\theta\left(d_p^{max}\right)$, at which the maximum occurs

Table 4.1 *T*-stress values for standard fracture specimens [18]

Specimen	T/R_0
Centre cracked panel, M(T)	−0.33
Double edge cracked panel, DE(T)	−0.07
Single edge crack bar in bending, SE(B)	0.02
Compact specimen, C(T)	0.16

negative *T*-stress whereas the effect of positive *T*-stress is negligible, meaning that no additional plastic constraint beyond plane strain and $T = 0$ can be applied.

Finally, Leevers and Radon [15] further investigated the "*inherent stress biaxiality in various fracture specimen geometries*". It became clear, in the end, that specimen geometry and stress biaxiality have a major effect on both, size and orientation of the plastic zone in SSY and hence require a "second parameter".

Table 4.1 summarises *T*-stress values for some standard fracture specimens [18].

4.4 The Models of Barenblatt and Dugdale

Sharp cracks induce singularities of stresses and strains in the theory of elasticity. Griffith's theory of brittle fracture obviates this problem by the energetic approach. Barenblatt [4] offered the physically motivated idea to introduce a cohesive zone at the end of the crack in order to avoid the singularity, Fig. 4.6a, and he suggests that brittle fracture will occur if the stresses in a "process zone" exceed the cohesive forces of atomic or molecular attraction.

The difficulty with applying this model is that the distribution of cohesive stresses, $\sigma(x)$, ahead of the crack tip is not known and cannot be measured. Modern adaptions of Barenblatt's model use cohesive models in which the cohesive stresses depend on a separation, δ, characterising the creation of new surfaces in the process zone. This dependence is established by a cohesive law, $\sigma(\delta)$, see e.g. Brocks et al. [6], Brocks [5] and Chap. 9.

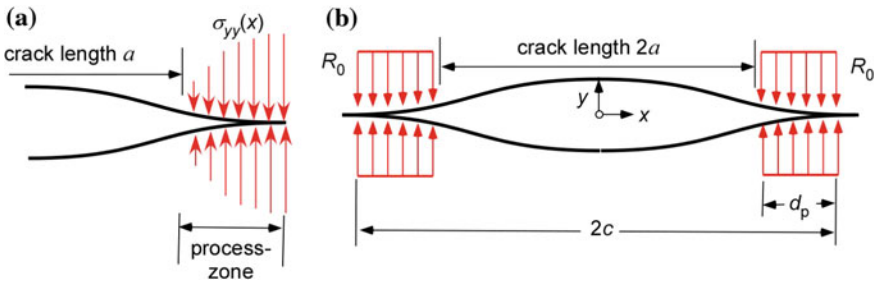

Fig. 4.6 **a** Barenblatt model; **b** Dugdale model

Closely related to Barenblatt's model is the "strip yield" model of Dugdale [8], who found that a narrow band of plastic deformations developed ahead of the crack tip in thin steel sheets. His basic idea is that for a perfectly plastic material in plane stress,

$$\sigma_{yy}(x,0) = R_0\,, \quad a \le |x| \le a + d_\mathrm{p} \tag{4.17}$$

is reached, Fig. 4.6b. The effect of yielding is studied by assuming a fictitious crack of length, $2c = 2a + 2d_\mathrm{p}$, which is closed by stresses R_0 in the plastic zones, $a \le |x| \le c$. Stresses σ_{yy} are limited to R_0 and have no singularity, which determinates the size, d_p, of the plastic zone. Two solutions for cracks of length, $2c$,

(1) with stress-free crack faces under remote stresses, σ_∞, and
(2) with crack faces partly loaded by compressive stresses, $\sigma_{yy} = -R_0$, at the ends, $a \le |x| \le c$, without remote loading.

are superimposed. The respective SIFs are,

$$K_\mathrm{I}^{(1)} = \sigma_\infty \sqrt{\pi c}, \quad K_\mathrm{I}^{(2)} = -\frac{2}{\pi} R_0 \sqrt{\pi c}\, \arccos\frac{a}{c}, \tag{4.18}$$

see Muschelishwili [16] or Hahn [10] for the solution of the second problem. The crack length, c, follows from the condition that the singularities neutralise each other, $K_\mathrm{I}^{(1)} + K_\mathrm{I}^{(2)} = 0$,

$$\frac{a}{c} = \cos\left(\frac{\pi}{2}\frac{\sigma_\infty}{R_0}\right) \tag{4.19}$$

and the size of the plastic zone follows from $d_\mathrm{p} = c - a$ as

$$d_\mathrm{p}^{\mathrm{Dugdale}} = c\left[1 - \cos\left(\frac{\pi}{2}\frac{\sigma_\infty}{R_0}\right)\right] = a\left[\sec\left(\frac{\pi}{2}\frac{\sigma_\infty}{R_0}\right) - 1\right] \tag{4.20}$$

Though the condition $a/W \ll 1$ for the Griffith crack has to hold, no assumption on the size of the plastic zone has yet been made. A series expansion of the cosine for SSY, $\sigma_\infty/R_0 \ll 1$, results in

$$d_\mathrm{p}^{\mathrm{Dugdale}} \approx \frac{\pi^2}{8} c \left(\frac{\sigma_\infty}{R_0}\right)^2 \approx 1.23\, a \left(\frac{\sigma_\infty}{R_0}\right)^2. \tag{4.21}$$

The CTOD in Dugdales model results from the definition in Eq. (4.13), again,

$$\delta_\mathrm{t}^{\mathrm{Dugdale}} = 2u_y(x=a) = \frac{8}{\pi}\frac{R_0}{E} a\, \ln \sec\left(\frac{\pi}{2}\frac{\sigma_\infty}{R_0}\right) \tag{4.22}$$

For comparison, Irwin's model for the Griffith crack in plane stress yields

$$d_{\mathrm{p}}^{\mathrm{Irwin}} = \frac{1}{\pi}\left(\frac{K_{\mathrm{I}}}{R_0}\right)^2 = a\left(\frac{\sigma_\infty}{R_0}\right)^2 \tag{4.23}$$

for the extension of the plastic zone in the ligament and

$$\delta_{\mathrm{t}}^{\mathrm{Irwin}} = 4a\frac{R_0}{E}\left(\frac{\sigma_\infty}{R_0}\right)^2 \tag{4.24}$$

for the CTOD.

As an example, a centre cracked panel of thickness B, width $2\,W$ and crack length $2a$ is considered as in Fig. 2.2. It is loaded by nominal stresses, $\sigma_\infty = F/(2BW)$. This configuration is designated as "middle cracked", M(T), specimen in the fracture standards (see Sect. 7.2.1 on nomenclature). Numerous approximate equations for the geometry function, Eq. (2.25), exist (Tada et al. [21]), mostly based on Isida's Laurent series expansion of a complex stress potential. Here, the equation of Feddersen [9],

$$Y(a/W) = \sqrt{\sec(\pi a/2W)} = \frac{1}{\sqrt{\cos(\pi a/2W)}} \tag{4.25}$$

with an accuracy of 0.3% for $a/W \leq 0.7$ is applied.

Figure 4.7 shows the extension of the plastic zone in the ligament, the CTOD and the effective SIF according to the above equations by Irwin (plane strain and plane stress) and Dugdale (plane stress) for $a/W = 0.5$ in dependence on $\sigma_\infty/R_0 \leq 0.5$.

The diagrams are clipped at $d_{\mathrm{p}}/W \leq 0.1$, i.e. $d_{\mathrm{p}}/(W-a) \leq 0.2$, $K_{\mathrm{eff}}/K \leq 1.1$ and $(\delta_{\mathrm{t}}/W)(E/R_0) \leq 0.4$ as higher values may in no case be considered as "small scale" yielding, which implies $\sigma_\infty/R_0 \leq 0.4$ for plane stress. The considerable large differences between plane strain and plane stress conditions are obvious. Irwin's plane stress and Dugdale's model show no significantly different results with respect to d_{p} and K_{eff}.

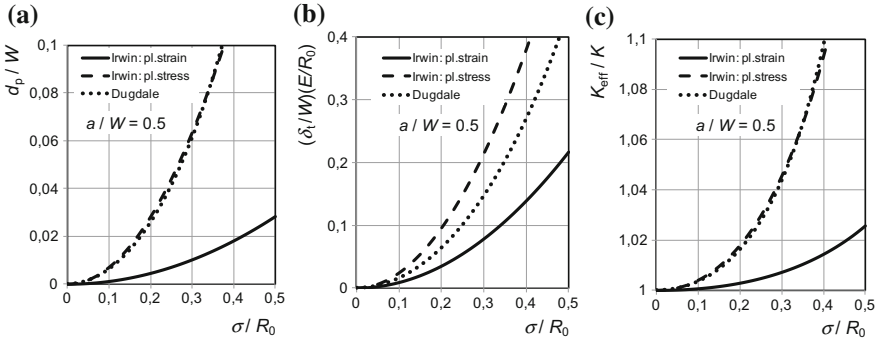

Fig. 4.7 SSY approximations for an M(T) specimen: **a** normalised extension of the plastic zone in the ligament; **b** normalised crack tip opening displacement; **c** normalised effective SIF in dependence on σ_∞/R_0

References

1. ASME BPVC (2015) Boiler and Pressure Vessel Code. The American Society of Mechanical Engineers
2. ASTM E 561 (2008) Standard test method for K–R curve determination. Annual book of ASTM standards, vol 03.01, American Society for Testing and Materials, Philadelphia
3. ASTM E 2472 (2006) Standard test method for determination of resistance to stable crack extension under low-constraint conditions, Annual Book of ASTM Standards, vol 03.01, American Society for Testing and Materials, Philadelphia
4. Barenblatt G (1959) The formation of equilibrium cracks during brittle fracture: general ideas and hypothesis, axially symmetric cracks. Appl Math Mech 23:623–636
5. Brocks W (2005) Cohesive strength and separation energy as characteristic parameters of fracture toughness and their relation to micromechanics. Struct Int Durab 1:233–243
6. Brocks W, Cornec A, Scheider I (2003) Computational aspects of nonlinear fracture mechanics. In: Milne I, Ritchie RO, Karihaloo B (eds) Comprehensive structural integrity—numerical and computational methods, Elsevier, vol 3, pp 127–209
7. BS 7448 (1997), Part 2: Fracture mechanics toughness tests. Method for determination of KIc, critical CTOD and critical J values of welds in metallic materials. British Standard Institution, London
8. Dugdale DS (1960) Yielding of steel sheets containing slits. J Mech Phys Solids 8:100–104
9. Feddersen RE (1966) Discussion to: Plane strain crack toughness testing. In: Brown WF, Srawley JE (eds) Plane Strain Crack Toughness Testing of High Strength Metallic Materials, ASTM STP, 410, pp 77–79
10. Hahn HG (1976) Bruchmechanik. Teubner, Stuttgart
11. Hahn GT, Rosenfield AR (1965) Local yielding and extension of a crack under plane stress. Acta Metall 13:293–306
12. Irwin GR (1964) Structural aspects of brittle fracture. Appl Mater Res 3:65–81
13. Kuna M (2010) Numerische Beanspruchungsanalyse von Rissen, 2nd edn. Vieweg + Teubner, Wiesbaden
14. Larsson SG, Carlsson AJ (1973) Influence of non-singular stress terms and specimen geometry on small scale yielding at crack-tips in elastic plastic materials. J Mech Phys Solids 21:263–278
15. Leevers PS, Radon JC (1982) Inherent stress biaxiality in various fracture specimen geometries. Int J Fracture 19:311–325
16. Muschelishwili NI (1971) Einige Grundaufgaben zur mathematischen Elastizitätstheorie. Hanser, München
17. Newman JC, James MA, Zerbst U (2003) A review of the CTOA/CTOD fracture criterion. Eng Fract Mech 70:85–371
18. Rice J (1974) Limitations to the small scale yielding approximation for crack tip plasticity. J Mech Phys Solids 22:17–26
19. Schwalbe KH (1995) Introduction of δ5 as an operational definition of the CTOD and its practical use. In Reuter WG, Underwood JH, Newman JC (eds) Fracture mechanics: 26th vol, ASTM STP 1256, American Society for Testing and Materials, 763–778
20. Schwalbe KH, Newman JC, Shannon J (2005) Fracture mechanics testing on specimens with low constraint—standardisation activities within ISO and ASTM. Eng Fract Mech 72:557–576
21. Tada H, Paris PC, Irwin GR (2000) The stress analysis of cracks handbook, 3rd edn. ASME. doi:10.1115/1.801535
22. Wells AA (1961) Brittle fracture strength of welded and notched three inch thick steel plates. Brit Weld J 8
23. Williams ML (1957) On the stress distribution at the base of a stationary crack. J Appl Mech 24:109–114

Chapter 5
Elastic-Plastic Fracture Mechanics

Abstract Deformation theory of plasticity is applied to generalise fracture mechanics concepts to nonlinear material behaviour. Special emphasis is put on the J-integral as energy release rate and crack-tip intensity parameter in perfect analogy to linear-elastic fracture mechanics. Its definition as path independent integral and calculation from experimental records is addressed. Requirements, extensions, applications, validity and limitations of J as "crack driving force" are discussed, in particular its application to ductile crack extension. The asymptotic J-dominated stress and strain fields at the crack tip are derived. Alternative fracture parameters like dissipation rate, crack-tip opening displacement (CTOD) and angle (CTOA) are introduced and procedures for structural integrity assessment based on these parameters are briefly introduced.

The advantage of LEFM is that due to the linearity of the constitutive equations and backed by the assumption of small strains, closed form solutions for stress and strain fields at a crack tip can be obtained. This is generally impossible in incremental plasticity, as the constitutive equations are not only non-linear but the current stress-strain state depends on the loading history. With the approach of deformation theory of plasticity (see Sect. 3.4) and the introduction of a "path-independent integral" by Cherepanov [24] and Rice [68], a perfect analogy to LEFM could be established in elastic-plastic fracture mechanics (EPFM). This so-called J-integral gained significance as an intensity parameter of the crack-tip fields as well as a plastic energy release rate.

5.1 The *J*-Integral

5.1.1 Definition and Path Independence

The *J*-integral of EPFM is a special case of path independent integrals, in general, which represent primarily a purely mathematical concept. Assume that $\psi(x_i)$ is a scalar, vectorial or tensorial field function which is steadily differentiable in a domain $\mathcal{B}$ and

W. Brocks, *Plasticity and Fracture*, Solid Mechanics and Its Applications 244,
DOI 10.1007/978-3-319-62752-6_5

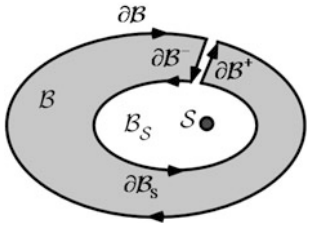

Fig. 5.1 Domain $\mathcal{B}$ with singularity $\mathcal{S}$

$$\psi_{,i} \doteq \frac{\partial \psi}{\partial x_i} = 0 \quad \text{in} \quad \mathcal{B}. \tag{5.1}$$

The divergence theorem states that

$$\int_{\mathcal{B}} \psi_{,i}\, dv = \int_{\partial \mathcal{B}} \psi n_i\, da = 0, \tag{5.2}$$

with n_i being the outward normal to the boundary $\partial\mathcal{B}$ of $\mathcal{B}$. If a singularity, $\mathcal{S}$, exists in $\mathcal{B}$, then $\psi(x_i)$ is not differentiable in this point. The divergence theorem is only applicable in a domain, $\mathcal{B}_0 = \mathcal{B} - \mathcal{B}_s$, excluding the singularity with the closed boundary $\partial\mathcal{B}_0 = \partial\mathcal{B} \cup \partial\mathcal{B}_\mathcal{S} \cup \partial\mathcal{B}^+ \cup \partial\mathcal{B}^-$, Fig. 5.1,

$$\int_{\partial \mathcal{B}_0} \psi n_i\, da = \oint_{\partial \mathcal{B}} \psi n_i\, da + \oint_{\partial \mathcal{B}^-} \psi n_i\, da + \oint_{\partial \mathcal{B}_\mathrm{S}} \psi n_i\, da + \oint_{\partial \mathcal{B}^+} \psi n_i\, da = 0\,. \tag{5.3}$$

From

$$\oint_{\partial \mathcal{B}^+} (..) = -\oint_{\partial \mathcal{B}^-} (..) \quad \text{and} \quad \oint_{\partial \mathcal{B}} (..) = -\oint_{\partial \mathcal{B}} (..)\,, \tag{5.4}$$

the path independence of all contour integrals surrounding the singularity in the same sense results,

$$\oint_{\partial \mathcal{B}} \psi n_i\, da = \oint_{\partial \mathcal{B}_\mathrm{S}} \psi n_i\, da\,. \tag{5.5}$$

Eshelby [33] derived a conservation principle for the energy momentum tensor,

$$P_{ij} = \bar{w}\delta_{ij} - \frac{\partial \bar{w}}{\partial u_{k,j}} u_{k,i} \quad \text{with} \quad P_{ij,j} = 0. \tag{5.6}$$

where $\bar{w}$ is an energy density, e.g. the strain energy density of a hyperelastic material, and $u_i(x_j)$ is the displacement field. The Eshelby tensor allows for calculating material forces acting on a singularity (defect) like dislocations or inclusions in a continuum [48, 51],

$$F_i = \oint_{\partial\mathcal{B}} P_{ij} n_j \, da \,. \tag{5.7}$$

The J-integral of Cherepanov [24] and Rice [68] is such a material force for the singular crack tip. Consider the boundary value problem for quasistatic loading of a body $\mathcal{B}$ which is described by the following equations:

- Balance equations, neglecting body forces like weight,

$$\sigma_{ij,j} = 0 \quad \text{in } \mathcal{B}, \tag{5.8}$$

- Boundary conditions for surface forces and displacements,

$$\begin{aligned} \sigma_{ij} n_i &= \widehat{t}_j \quad \text{on } \partial\mathcal{B}_\sigma \\ u_i &= \widehat{u}_i \quad \text{on } \partial\mathcal{B}_u \end{aligned}, \tag{5.9}$$

- Small (linear) strains,

$$\varepsilon_{ij} = \frac{1}{2}\left(u_{i,j} + u_{j,i}\right) \quad \text{in } \mathcal{B}, \tag{5.10}$$

- Hyper-elastic material,

$$\sigma_{ij} = \frac{\partial \bar{w}}{\partial \varepsilon_{ij}} \quad \text{in } \mathcal{B}. \tag{5.11}$$

Particularly, the assumption of Eq. (5.11) is crucial. It postulates the existence of a strain energy density, $\bar{w} = \int \sigma_{ij} \dot{\varepsilon}_{ij} dt$, as potential from which the stresses can be derived. This postulate is met by the "deformation theory" (Sect. 3.4) but violated by incremental theory of plasticity.

The components of the material force,

$$F_i = \oint_{\partial\mathcal{B}} \left[\bar{w}(\varepsilon_{ij}) n_i - \sigma_{jk} n_k u_{j,i} \right] da \,, \tag{5.12}$$

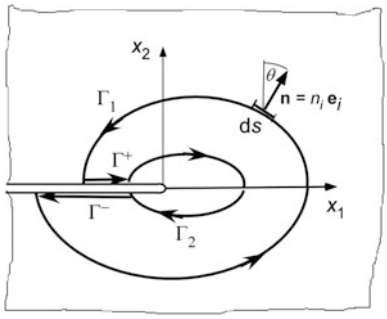

Fig. 5.2 Definition of *J*-integral

are non-zero if $\mathcal{B}$ contains a singularity. The integral is now applied to a panel of constant thickness, B, having a straight crack along the x_1 axis, Fig. 5.2. The area within the closed contour,

$$\Gamma_0 = \Gamma_1 \cup \Gamma^+ \cup \Gamma_2 \cup \Gamma^-, \tag{5.13}$$

does not include any singularity, hence

$$\frac{F_i}{B} = \oint_{\Gamma_0} \left[\bar{w} n_i - \sigma_{jk} n_k u_{j,i} \right] ds = \oint_{\Gamma_1} [..]\, ds + \oint_{\Gamma^+} [..]\, ds + \oint_{\Gamma_2} [..]\, ds + \oint_{\Gamma^-} [..]\, ds = 0\,. \tag{5.14}$$

The integral

$$J_i = \oint_{\Gamma_1} \left[\bar{w} n_i - \sigma_{jk} n_k u_{j,i} \right] ds\,, \quad (i = 1,2,3) \tag{5.15}$$

is called "*J*-vector" and is a force per thickness.

Assume that the crack faces, $\theta = \pm\pi$, are straight and stress free,

$$\left.\begin{array}{c} n_1\, ds = \sin\theta ds = \mp dx_2 = 0 \\ \sigma_{jk} n_k = \bar{t}_j = 0 \end{array}\right\} \quad \text{on} \quad \Gamma^+, \Gamma^-, \tag{5.16}$$

then the first component of the *J*-vector vanishes along the contours Γ^+, Γ^-,

$$\oint_{\Gamma^+} \left[\bar{w}\, n_i - \sigma_{jk} n_k u_{j,i} \right] ds \;=\; \oint_{\Gamma^-} \left[\bar{w} n_i - \sigma_{jk} n_k u_{j,i} \right] ds = 0, \tag{5.17}$$

(note that Γ^+, Γ^-, may have different lengths) and with

$$\oint_{\Gamma_2} [..]\, ds = -\oint_{\Gamma_2} [..]\, ds\,. \tag{5.18}$$

as in Eq. (5.4), the path independence of J_1 is obtained

$$J_1 = \oint_{\Gamma_1} \left[\bar{w} n_1 - \sigma_{jk} n_k u_{j,1} \right] ds = \oint_{\Gamma_2} \left[\bar{w} n_1 - \sigma_{jk} n_k u_{j,1} \right] ds \,, \tag{5.19}$$

for arbitrary contours, Γ_1, Γ_2. This holds for the other two components, J_2, J_3, if and only if the contours around the crack tip and the loading are symmetric to the x_1-axis. Equation (5.19) defines the J-integral as it has been introduced into fracture mechanics by Cherepanov [24] and Rice [68],

$$J = \oint_{\Gamma} \left[\bar{w} \, dx_2 - \sigma_{jk} n_k u_{j,1} ds \right] \geq 0 \ . \tag{5.20}$$

The integration on an arbitrary contour, Γ, is done anti-clock-wise, i.e. mathematically positively. Because of its path independence, J can be calculated in the remote field and determines the near-field state at the crack tip likewise, which constitutes its suitability as fracture parameter and "crack driving force". A criterion for fracture instability or the onset of crack extension,

$$J(a) = J_{\mathrm{c}}, \tag{5.21}$$

(see Sect. 7.2.3) can hence be established. Different from brittle materials, this crack extension does not necessarily implicate catastrophic structural failure, since plasticity is another source of dissipation, see Sect. 5.3.1 on dissipation rate.

For a circular contour of radius, r, around the crack tip, J becomes,

$$J = r \int_{-\pi}^{+\pi} \left[\bar{w}(r, \theta) \, \cos\theta - \sigma_{ij}(r, \theta) n_j u_{i,x} \right] d\theta, \tag{5.22}$$

It retains a finite, non-zero value for $r \to 0$ if and only if the strain energy density, $\bar{w}$, has a singularity of the order $\mathcal{O}(1/r)$. This is ensured in LEFM, where stresses and strains have a singularity of $\mathcal{O}(1/\sqrt{r})$, see Sect. 2.2. For singularities in EPFM see Sect. 5.2.2 and in particular Eq. (5.64).

It is important to well remember the assumptions introduced above, namely

- time-independent processes,
- neglect of body forces,
- small deformations (linear strains),
- homogeneous hyper-elastic material,
- plane stress and strain fields, i.e. no dependence on the x_3 coordinate,
- straight and stress free crack surfaces parallel to x_1.

Any violation of one of these prerequisites will compromise the path-independence (see Sect. 7.1.4). Extensions and corrections with respect to three-dimensional configurations, dynamic processes, body forces and multiphase materials will be presented in Sects. 5.1.3 and 5.1.4. The requirement of a hyper-elastic material,

Eq. (5.11), is equivalent with the assumption of deformation theory of plasticity. Misleadingly, it is frequently argued that a restriction to monotonic loading is sufficient to guarantee path independence in incremental plasticity. This is definitely unfounded, as only under the severely restrictive assumption of proportional loading, $\sigma_{ij}(t) = \zeta(t)\,\sigma_{ij}^0$, in each point of the continuum, which forbids all local rearrangements of stresses due to plasticity, the finite Hencky equations can be derived from the incremental Prandtl-Reuß equations.

5.1.2 *J as Energy Release Rate*

Rice [68] and Rice et al. [71] have also shown that the *J*-integral is identical to Griffith's energy release rate for plane crack extension, $B\Delta a$, in an elastic material, Eq. (2.10), as well as in a hyper-elastic material meeting Eq. (5.11). In LEFM, *J* is therefore related to the SIFs by Eq. (2.18).

The property of being an energy release rate is exploited for the experimental determination of *J* from the load versus load-point displacement curve of fracture mechanics specimens, see Fig. 5.3. The procedure is of course also based on hyper-elastic behaviour which differs from the behaviour of real materials. To begin with, a constant crack length $a = a_0$ is assumed. Physical crack extension, Δa, will be considered in Sect. 5.1.5 on resistance curves to ductile crack extension.

The potential energy is split into an elastic and a plastic part,

$$U = \int F\,dv_\mathrm{L} = U^\mathrm{e} + U^\mathrm{p} = \frac{1}{2}Fv_\mathrm{L}^\mathrm{e} + \int F\,dv_\mathrm{L}^\mathrm{p}, \tag{5.23}$$

with $v_\mathrm{L}^\mathrm{e} = v_\mathrm{L} - v_\mathrm{L}^\mathrm{p}$ according to the assumption of "finite" plasticity. A small increase of the crack area, ΔA_c, under "fixed grips", v_L = const, releases mechanical work, and the negative ratio $\Delta U/\Delta A_\mathrm{c}$ for $\Delta A_\mathrm{c} \to 0$ is the *J*-integral,

$$J = \mathcal{G} = -\lim_{\Delta A_\mathrm{c}\to 0}\left(\frac{\Delta U}{\Delta A_\mathrm{c}}\right)_{v_\mathrm{L}}. \tag{5.24}$$

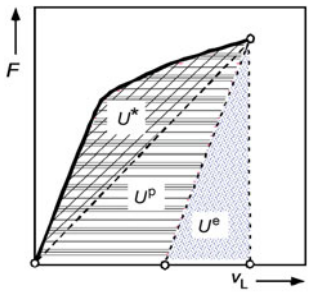

Fig. 5.3 Load versus load-point displacement curve of a fracture mechanics specimen

For panels of constant thickness, B, where $\Delta A_c = B\Delta a$, this becomes,

$$J = -\frac{1}{B}\lim_{\Delta a\to 0}\left(\frac{\Delta U}{\Delta a}\right)_{v_L} = -\frac{1}{B}\left(\frac{\partial U}{\partial a}\right)_{v_L} = \frac{1}{B}\left(\frac{\partial U}{\partial b}\right)_{v_L}, \tag{5.25}$$

with $b = W\text{-}a$ being the ligament width. A crack extension of $2\Delta a$ as in Eq. (2.10) applies to specimens with a crack length of $2a$ and two crack tips like centre cracked and double edge cracked panels. Because of Eq. (5.23), J can also be split into an elastic and a plastic part, where the elastic one follows from the mode I SIF, Eq. (2.16),

$$J = J^e + J^p = \frac{K_I^2}{E'} - \frac{1}{B}\left(\frac{\partial U^p}{\partial a}\right)_{v_L}. \tag{5.26}$$

Alternatively to Eq. (5.25),

$$J = \frac{1}{B}\int\left(\frac{\partial v_L}{\partial a}\right)_F dF = -\frac{1}{B}\int\left(\frac{\partial v_L}{\partial b}\right)_F dF \tag{5.27}$$

and

$$J^p = \frac{1}{B}\int\left(\frac{\partial v_L^p}{\partial a}\right)_F dF = -\frac{1}{B}\int\left(\frac{\partial v_L^p}{\partial b}\right)_F dF. \tag{5.28}$$

hold for fixed load according to Begley and Landes [9] and Rice et al. [71].

As the derivative, $\partial U^p/\partial a$, is required in Eq. (5.25) which cannot be realised experimentally, relations with U^p have been deduced analytically [9], resulting in

$$J^p = \eta_J \frac{U^p}{B(W-a)}, \tag{5.29}$$

for bend-type specimens, like a C(T), Fig. 5.4a or a single-edge bend specimen, SE(B). The respective η-factors can be found in ASTM E1820 [6].

For a centre cracked panel, Fig. 5.4b, Rice et al. [71] derived the relation

$$J^p = \frac{U^*}{bB} = \frac{U^*}{B(W-a)}, \tag{5.30}$$

with the area U^*, in the load-displacement diagram, Fig. 5.3,

$$U^* = \int F dv_L - \tfrac{1}{2}Fv_L. \tag{5.31}$$

Provided that no plastic deformations occur between the points of force transmission and the measuring points, M, for crack (mouth) opening displacement

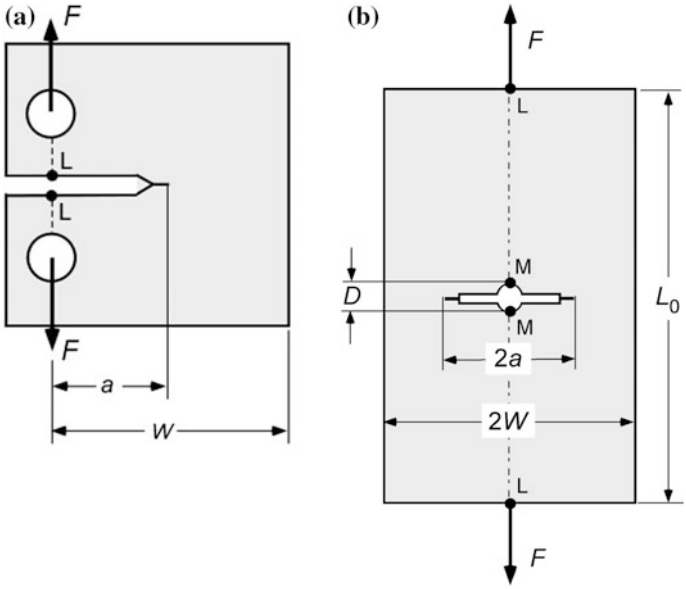

Fig. 5.4 Geometries of fracture specimens: **a** compact specimen, C(T); **b** centre cracked panel, M(T)

(CMOD) in the symmetry line, the plastic load point displacements and the plastic crack opening are equal,

$$v_{\mathrm{L}}^{\mathrm{p}} = v_{\mathrm{L}} - v_{\mathrm{L}}^{\mathrm{e}} = v_{\mathrm{M}}^{\mathrm{p}} = v_{\mathrm{M}} - v_{\mathrm{M}}^{\mathrm{e}}, \tag{5.32}$$

which requires a minimum measuring length, $L_0 \geq 3(W\text{-}a_0)$, of the specimen. Note that this equality holds for the plastic part, only, but not for the elastic part and hence not for the total displacements, $v_{\mathrm{L}} \neq v_{\mathrm{M}}$.

The Eqs. (5.29) and (5.30) are used for determining J from experimental records, but they can also be exploited for the evaluation of numerical results to check J-integral values calculated by the contour integral, Eq. (5.20). The property of J as an energy release rate, Eq. (5.24), also constitutes an alternative technique of calculating it by a domain integral. Numerical evaluations of the contour integral are quite unfavourable in FEM as coordinates and displacements refer to nodal points and stresses and strains to Gaussian integration points. Stress fields are generally discontinuous over element boundaries and extrapolation of stresses to nodes requires additional assumptions. Hence, a domain integral method is commonly used in FEM codes to evaluate contour integrals [1]. The J-integral is defined in terms of an energy release rate associated with a fictitious small local crack extension, Δa. For further details see Sect. 7.1.2. Because of this interpretation, the domain integral method is also known as "virtual crack extension" (VCE) method. "Path dependence" of J, if it occurs, becomes a "domain dependence". The domain

integral method accounts for three-dimensional configurations [26]. If the whole crack front is shifted by the same amount, Δa, an average value, $\bar{J} = (1/\ell_c)\int_0^{\ell_c} J(s_c)\, ds_c$, for the total structure is obtained as in the experimental procedures, ASTM E1820 [6].

5.1.3 The Three-Dimensional J

Holding to the assumption of a plane crack surface in the (x_1, x_3)-plane, the J-integral can also be applied to three-dimensional problems with straight or curved crack fronts. It is defined locally, $J(s_c)$, in dependence on the crack front coordinate, s_c, ([2, 8, 46]. A local coordinate system, ξ_1, $\xi_2 = x_2$, ξ_3) is introduced in any point P tangential to the crack front as in Fig. 5.5, so that the (ξ_1, ξ_2)-plane is perpendicular to the crack, Fig. 5.5a.

The domain $\mathcal{B}_0 = \mathcal{B} - \mathcal{B}_s$, is again a material sheet of constant thickness, Δs_c, with $\Delta s_c \to 0$, but as this is a three-dimensional problem, its border now also contains the upper and lower faces, S^+ and S^- in the (ξ_1, ξ_2)-plane, Fig. 5.5b,

$$\partial\mathcal{B}_0 = \Gamma_0 \cup S^+ \cup S^-, \tag{5.33}$$

Equation (5.14) becomes

$$\frac{F_i}{\Delta s_c} = \oint_{\Gamma_0} \left[\bar{w} n_i - \sigma_{jk} n_k u_{j,i}\right] ds + \iint_{S^+} [..]\, ds + \iint_{S^-} [..]\, ds = 0. \tag{5.34}$$

and for an infinitesimal thickness Δs_c, the Taylor expansion,

$$\iint_{S^+} [..]\, dS = -\iint_{S^-} [..]\, dS - \Delta s_c \iint_{S^-} \frac{\partial [..]}{\partial \xi_3}\, dS, \tag{5.35}$$

holds. With the same assumptions and the same arguments as above, the first component of the three-dimensional J-integral is obtained,

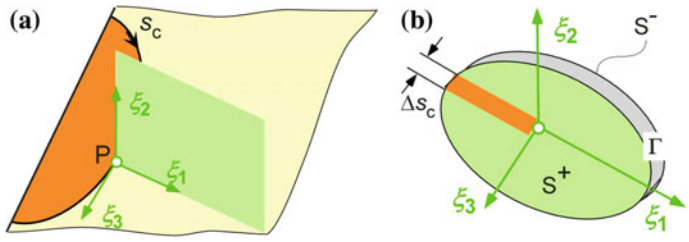

Fig. 5.5 Three-dimensional J: **a** local coordinates; **b** integration contours

$$J(s_c) = \oint_{\Gamma} \left[\bar{w}\, dx_2 - \sigma_{jk} n_k u_{j,1} ds \right] - \iint_{S^-} \frac{\partial}{\partial \xi_3} \left[\bar{w} - \sigma_{jk} n_k u_{j,1} \right] ds \tag{5.36}$$

It is a local value and varies along the crack front. The second term vanishes if J is constant with respect to the crack front coordinate but may contribute significantly if strong gradients occur, e.g. at the specimen surface. The domain integral (or VCE) method, Eq. (7.1) in Sect. 7.1.2, already includes three-dimensional terms [26].

As an example, a cylinder under internal pressure, Fig. 2.5, made of a high strength - high toughness steel with a semi-elliptical outer surface crack, Fig. 2.7, $a/c = 0.77$, $a/t = 0.39$, is considered [3, 4]. LEFM predicts that crack initiation starts at the deepest point, i.e. the centre of the crack where $K_I(\phi)$ is maximum, Eq. (2.38). It is always followed by catastrophic failure of the whole structure. For ductile materials, crack extension may take place in a stable or at least controlled manner (see Sect. 5.1.5 on resistance curves), however, but it will not necessarily initiate at the deepest point and the crack may grow in axial direction. This effect has been addressed as "canoe" shape of the crack. It is crucial with respect to safety as a crack penetrating through the vessel wall is preferable to one extending in axial direction and finally resulting in rupture of the vessel. The former can be detected and will release the internal pressure before global failure occurs. The respective concept of "leak-before-break" (LBB) failure has hence been a big issue in pressure-vessel technology and research in the 1980s, see e.g. Brocks and Noack [19]; Brocks et al. [15].

Figure 5.6a illustrates that the maximum J occurs around $\phi = \pm 30°$ and respective tests by Arafah et al. [4] indicate that this is indeed the location of maximum crack extension along the crack front, Fig. 5.7.

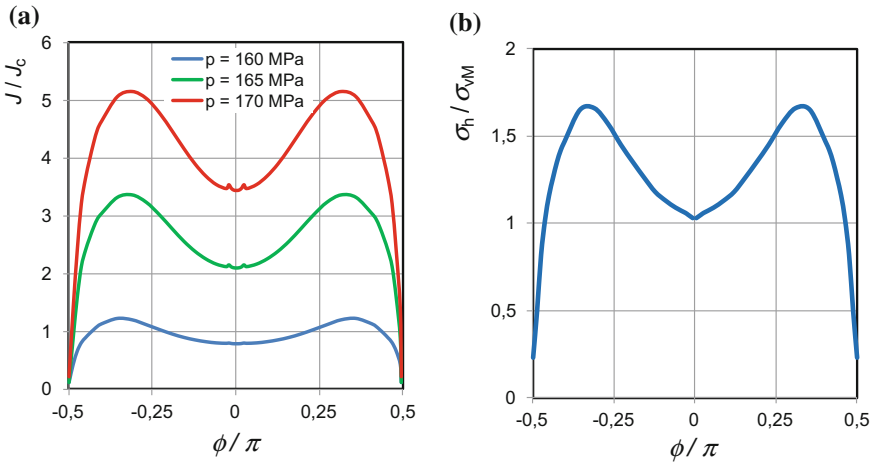

Fig. 5.6 Pressure vessel with semi-elliptical surface flaw [3]: **a** normalised J along the crack front; **b** triaxiality, $\eta = \sigma_h / \bar{\sigma}_{vM}$, at $r = 2\ J/R_0$ for $J = J_c$ along the crack front

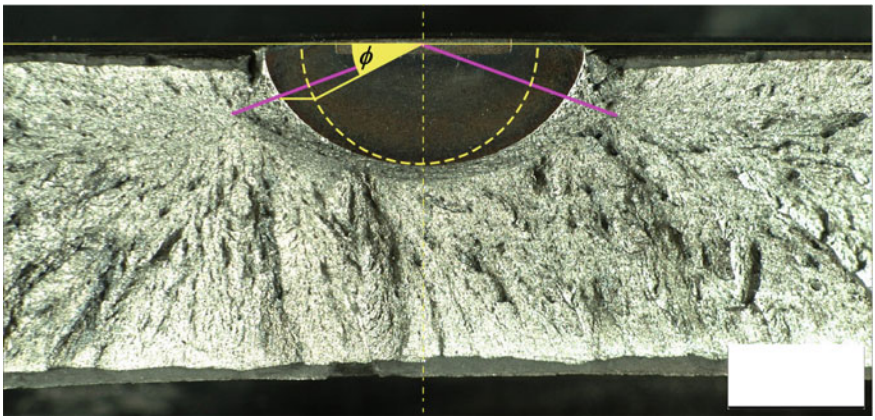

Fig. 5.7 Pressure vessel with semi-elliptical surface flaw: Canoe-shape of ductile crack extension [3]

Earlier experimental and numerical investigations of large-scale pressure vessels gave evidence, that this "canoeing" may also occur if the maximum J is somewhere else. This motivated research on a second parameter (like T stress in LEFM) affecting ductile tearing resistance [10, 18, 61, 62] and, indeed, it could be shown that the experimentally observed canoe shape could be explained with the variation of stress triaxiality,

$$\eta = \sigma_{\mathrm{h}}/\bar{\sigma}_{\mathrm{vM}}, \tag{5.37}$$

along the crack front [15–17]. Figure 5.6b shows that the locations of maximum J and maximum triaxiality coincide in the present case. The issue of a "second parameter" in EPFM (O'Dowd and Shih [61]) will be addressed in Sects. 5.1.6 and 5.2.5 on the validity of R-curves and the HRR solution, again. The stress triaxiality, in particular, governs the evolution of ductile damage due to void growth (Sect. 8.2.2).

5.1.4 *Extensions for Multi-phase Materials, Body Forces, Surface Tractions and Thermal Loading*

Some of the restrictions listed in Sect. 5.1.1 can be overcome by special correction terms which re-establish the path (or domain) independence of J. One of them is the assumption of a homogeneous material. The assessment of defects in composite or gradient materials or in welded structures requires an extension to multi-phase materials. A correction term is introduced which eliminates the effect of an additional singularity occurring at the material interface. In addition, the boundary conditions become asymmetric resulting in a mixed mode problem, so that the

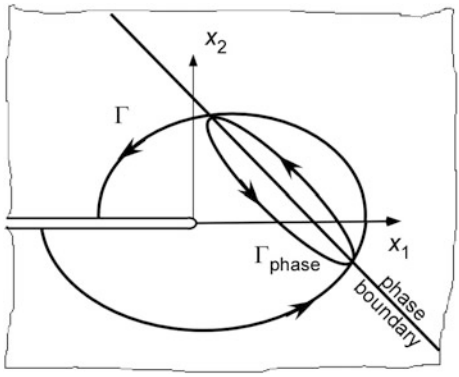

Fig. 5.8 *J*-integral near a phase boundary

complete *J*-vector, Eq. (5.15), is required to characterise the crack tip field, in particular J_1 and J_2 in 2D problems.

If the contour Γ passes a phase boundary between two materials near the crack tip, Fig. 5.8, it includes an additional singularity of stresses and strains [85]. This contribution has to be eliminated by a closed contour integral along the phase boundary, Γ_{phase}, [45],

$$J_i = \oint_{\Gamma} \left[\bar{w} n_i - \sigma_{jk} n_k u_{j,i} \right] ds - \oint_{\Gamma_{\text{phase}}} \left[\bar{w} n_i - \sigma_{jk} n_k u_{j,i} \right] ds \,. \tag{5.38}$$

The equilibrium conditions, Eq. (5.8), postulate that the stress tensor is divergence free. They are restricted to static and stationary processes without body forces or heat sources acting in $\mathcal{B}$. Constant body forces like gravitational forces, which have a potential not explicitly depending on the coordinates, x_i, can easily be included in the $\bar{w}$-term and do not affect path independence. In all other cases, *J* becomes path dependent unless an extra term is added [25, 90],

$$J = \frac{1}{\Delta A_c} \iiint_V \left[\left(\sigma_{ij} u_{j,k} - \bar{w}\, \delta_{ik} \right) \Delta x_{k,i} - f_i u_{i,j} \Delta x_j \right] dV. \tag{5.39}$$

The forces f_i can be body forces like gravitational forces, $f = \rho g$, or inertial forces, $f_i = \rho \ddot{x}_i$ in the case of dynamic loading.

The boundary conditions, Eq. (5.9), state that the crack faces, Γ^+, Γ^- are traction free. A respective surface correction term,

$$J = \frac{1}{\Delta A_c} \left\{ \iiint_V [\ldots] dV - \iint_{S_c} t_i\, u_{i,j} \Delta x_j \, dS \right\}, \tag{5.40}$$

accounts for surface tractions (or pressure), t_i, acting on the crack faces, S_c, [25, 90].

The correction term for thermal fields is

$$J = \frac{1}{\Delta A_c}\left\{ \iiint_V [\ldots] dV + \iiint_V \sigma_{ij}\left[\frac{\partial \alpha}{\partial \Theta}(\Theta - \Theta_0) + \alpha_{th}\right]\frac{\partial \Theta}{\partial x_k}\delta_{ij}\Delta x_k dV \right\}, \quad (5.41)$$

where $\Theta(x_i)$ is the temperature field, Θ_0 the reference temperature and αth the coefficient of thermal expansion [58, 89, 90].

The above correction terms are available in commercial FE codes like Abaqus [1]. Actually, Eqs. (5.39) to (5.41) do not use the contour integral definition of J but employ the VCE method (Sect. 7.1.2) based on the property of J as an energy release rate.

5.1.5 *Resistance Curves Against Ductile Crack Extension*

Ductile crack extension may occur in a stable manner, i.e. under increasing force, or at least deformation controlled, because plasticity provides a source of energy dissipation. A so-called "resistance curve" describes the dependence of a quantity like J or CTOD on crack extension, Δa. For thick-walled components, R-curves are commonly based on J [6], whereas crack growth in metal sheets is described by CTOD R-curves [7, 60, 74, 78], see Sect. 5.3.1. ASTM E561 [5] describes the determination of K_R-curves for metal sheets based on the SIF.

The formulas derived for C(T), Eq. (5.29), and for M(T), Eq. (5.30), respectively, have to be extended to increasing crack length, $a + \Delta a$. Starting from a plastic J-value at the initial crack length, a_0, $J^p_{(i)} = J^p\left(a_{(i)}\right)$ is successively calculated for increments, $\Delta a_{(i)} = a_{(i)} - a_{(i-1)}$ according to recursion formulas.

According to ASTM E1820 [6]

$$J^p_{(i)} = \left(J^p_{(i-1)} + \frac{\eta_J^{(i-1)}}{b_{(i-1)}}\frac{\Delta U^p_{(i)}}{B}\right)\left(1 - \gamma_J^{(i-1)}\frac{\Delta a_{(i)}}{b_{(i-1)}}\right), \quad (5.42)$$

with

$$\eta_J^{(i)} = 2.0 + 0.522\left(b_{(i)}/W\right), \quad \gamma_J^{(i)} = 1.0 + 0.76\left(b_{(i)}/W\right), \quad (5.43)$$

holds for a C(T) specimen. The changes of the work of plastic strains are calculated from the area under the load-displacement curve, Fig. 5.3, by the trapezoidal rule,

$$\Delta U^p_{(i)} = U^p_{(i)} - U^p_{(i-1)} = \int_{v^p_{LL(i-1)}}^{v^p_{LL(i)}} F\, dv^p_{LL(i)} \approx \frac{1}{2}\left(F_{(i)} + F_{(i-1)}\right)\Delta v^p_{LL(i)}. \quad (5.44)$$

The plastic load-line displacement,

$$v^{\mathrm{p}}_{\mathrm{LL}(i)} = v_{\mathrm{LL}(i)} - v^{\mathrm{e}}_{\mathrm{LL}(i)} = v_{\mathrm{LL}(i)} - F_{(i)} C_{\mathrm{LL}(i)}, \tag{5.45}$$

is determined from the total displacement by means of the elastic compliance, C_{LL}, of the specimen, see ASTM E1820 [6].

Respective considerations [12] for M(T) specimens generalising Eq. (5.30) of Rice et al. [71] result in

$$J^{\mathrm{p}}_{(i)} = J^{\mathrm{p}}_{(i-1)} \frac{b_{(i)}}{b_{(i-1)}} + \frac{F_{(i-1)} v^{\mathrm{p}}_{\mathrm{L}(i)} - F_{(i)} v^{\mathrm{p}}_{\mathrm{L}(i-1)}}{2B b_{(i-1)}}. \tag{5.46}$$

Local plastic deformations at the point of applied load, which are not relevant for J, are disregarded. As long as no plastic deformations occur in the symmetry line between the load points and the measuring points of crack opening (CMOD) Eq. (5.32) holds. The elastic parts, $v^{\mathrm{e}}_{\mathrm{L}}$ and $v^{\mathrm{e}}_{\mathrm{M}}$, of the total displacements can be calculated from the respective compliances, C_{L} and C_{M} [5, 32, 93]. No standards exists for J_{R}-curves of M(T) specimens except ASTM E561 [5] for thin metal sheets. The respective literature is hence considerable and the number of different equations confusing. A critical review and a validation of various formulas are given by Brocks et al. [13].

Though the application of J_{R}-curves for characterisation of ductile tearing resistance is subject to certain criteria with respect to the specimen dimensions, B and W, (see Sect. 7.2.3 on measurement of fracture toughness in EPFM), so-called validity conditions, no respective conditions exist with respect to the evaluation formulas, which can be applied to metal sheets, as well. Unfortunately, the term "validity" is often used ambiguously, denoting both the physical significance of a J_{R}-curve and the accuracy of evaluation formulas. The following statements refer to the latter, only.

As there is no possibility of deciding on the correctness of evaluation formulas for J based on experimental data, a validation can only be performed based on numerical simulations. Brocks et al. [13] have analysed numerical results of crack extension simulations with the cohesive model (Chap. 9) for C(T) and M(T) specimens, $W = 150$ mm, $B = 3$ mm, made of an aluminium alloy [73]. The parameters of the cohesive model have been determined from C(T) specimens. The evaluation presented in Fig. 5.9 is based on consistent (numerical) data, namely domain-integral [1] and $F(v_{\mathrm{L}}, \Delta a)$ results, for quite large crack extensions up to $0.67 b_0$ for the C(T) and $0.54 b_0$ for the M(T).

Little differences between contour integral and release rate results exist up to crack extensions $\Delta a \leq 0.13 b_0$ for the C(T) and $\Delta a \leq 0.08 b_0$ for the M(T), respectively, but significant deviations occur for large crack extensions. ASTM E561 (r_{p}) based on the SSY correction, Eqs. (4.2), (4.5) and (4.6), fails beyond $\Delta a = 0.13 b_0$ even yielding a physically meaningless decreasing J_{R}-curve for the C(T), and it does not provide any useful results at all for the M(T), which is even more notable as this standard is particularly used for centre-cracked panels in the

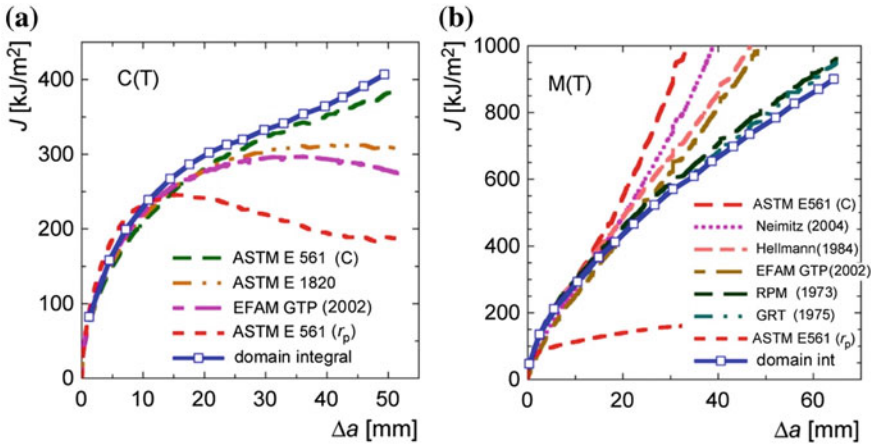

Fig. 5.9 Validation of evaluation formulas for J_R-curves [13]: **a** C(T), $a_0/W = 0.5$; **b** M(T), $a_0/W = 0.2$

aircraft industry. ASTM E561 (C), however, calculating a_{eff} from the compliance, Eq. (7.15), gives the best approximation over the whole range up to Δa_{max} for the C(T) and a reasonable one for $\Delta a \leq 0.10 b_0$ for the M(T). ASTM E1820 is specific for the C(T) but becomes improper beyond $\Delta a > 0.27 b_0$. The formula by Garwood et al. [35], curve GRT, and Eq. (5.46) generalising the formula of Rice et al. [71], curve RPM, provide quite perfect approximations for the M(T) up to Δa_{max}. Notably, "new" formulas have been presented by Hellmann and Schwalbe [38], Neimitz et al. [59] and in the test procedure EFAM GTP [31] long after a better one by Garwood et al. [35] existed.

Considering the above spectrum of different approximations, results of experimental J_R-curves and all the more respective conclusions drawn in the literature must be treated with caution, as long as it remains unclear how they have been determined.

5.1.6 Application and Validity of Resistance Curves

The analogy to LEFM which had been established based on J in EPFM and which worked reasonably well for stationary cracks, $a = a_0$, was somewhat later extended for crack extension, and J_R-curves were suggested to provide a sound tool for safety analyses in EPFM [71, 86]. According to this approach, a cracked structure is "safe", as long as the "applied" J-value ("driving force") for some crack extension, Δa, balances the material resistance curve,

$$J(F, a_0 + \Delta a) = J_R(\Delta a). \tag{5.47}$$

Based on this consideration, Paris et al. [64] and Hutchinson and Paris [42] established the stability condition

$$\left(\frac{\partial J}{\partial a}\right)_v \leq \frac{\partial J_R}{\partial a}. \tag{5.48}$$

and introduced the "tearing modulus", $\left(E/R_0^2\right)(\partial J/\partial a)$, as a dimensionless quantity for stability analyses.

Application of Eqs. (5.47) or (5.48) requires that J is "valid" and something like a "material" resistance curve exists. More and more evidence arose however, that J_R-curves may depend on the specimen geometry, for instance Garwood [34], Hellmann and Schwalbe [38] and Turner [95]. The J_R-curves in Fig. 5.9 clearly demonstrate that they are considerably different for C(T) and M(T) specimens, which is supported by Fig. 5.10, displaying the correspondent experimental results presented by Scheider et al. [73]. The test data for the C(T) have been evaluated according to ASTM E1820 [6] and of the M(T) by Eq. (5.46). In addition, numerical analyses by Brocks and Yuan [22] and Yuan and Brocks [99] indicated that J becomes increasingly path dependent and even vanishes close to the crack tip.

The geometry dependence of R-curves and the path dependence of J have been a highly controversial subjects in the fracture mechanics community in the 1980s and 1990s, and respective evidence was brushed aside as "anomalous" Two ASTM conferences were dedicated to "*constraint effects in fracture*" before these effects were finally accepted as real. Requirements for the applicability of J_R-curves, so-called "validity conditions" were established [87], disregarding the difficulty that these conditions can be enforced for specimens but are ineffective for real structures. Two-parameter approaches came up in which the global quantity, J, was combined with local field parameters like the crack-tip triaxiality, η, Fig. 5.6b. They were purely phenomenological after all and could not overcome the physical factum

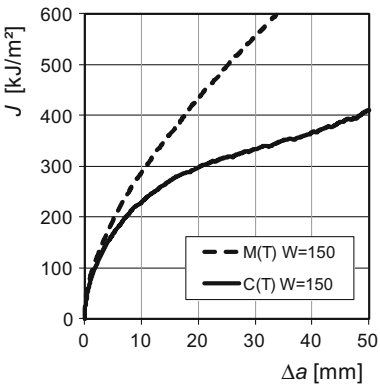

Fig. 5.10 Geometry dependence of J_R-curves: test results of an aluminium alloy by Scheider et al. [73]

that the incremental nature of plasticity is not captured by a cumulative quantity like J, which ceases to be an energy-release rate as soon as the crack starts extending [95], see Sect. 5.3.1 on the dissipation rate.

5.2 Asymptotic Solution of Stress and Strain Fields in Mode I

The constitutive behaviour is described by the deformation theory of plasticity (Sect. 3.4) and the Ramberg-Osgood [67] power law, Eq. (3.48), confining to the nonlinear ("plastic") part.

5.2.1 The Boundary Value Problem

As in LEFM, the near field at the crack tip is described in a polar coordinate system, $\{r,\theta\}$, Fig. 2.3, and the limiting cases of plane stress, $\sigma_{zz} = \sigma_{rz} = \sigma_{\theta z} = 0$, and plane strain, $\varepsilon_{zz} = \varepsilon_{rz} = \varepsilon_{\theta z} = 0$, are considered. The von Mises equivalent stress, Eq. (3.29), becomes

$$\bar{\sigma}^2_{\mathrm{vM}} = \begin{cases} \sigma_{rr}^2 - \sigma_{rr}\sigma_{\theta\theta} + \sigma_{rr}^2 + 3\sigma_{r\theta}^2 & \text{in plane stress} \\ \frac{3}{4}(\sigma_{rr} - \sigma_{\theta\theta})^2 + 3\sigma_{r\theta}^2 & \text{in plane strain} \end{cases}. \tag{5.49}$$

The balance equations for plane problems, $\partial()/\partial z = 0$, in polar coordinates are identically fulfilled by introducing Airy's stress function, $\Psi(r,\theta)$, with

$$\begin{aligned} \sigma_{rr} &= \frac{1}{r}\frac{\partial \Psi}{\partial r} + \frac{1}{r^2}\frac{\partial^2 \Psi}{\partial \theta^2} \doteq \frac{1}{r}\Psi' + \frac{1}{r^2}\ddot{\Psi} \\ \sigma_{r\theta} &= -\frac{\partial}{\partial r}\left(\frac{1}{r}\frac{\partial \Psi}{\partial \theta}\right) \doteq -\left(\frac{1}{r}\dot{\Psi}\right)' \\ \sigma_{\theta\theta} &= \frac{\partial^2 \Psi}{\partial r^2} \doteq \Psi'' \end{aligned}, \tag{5.50}$$

defining $\partial\Psi/\partial r = \Psi'$ and $\partial\Psi/\partial\theta = \dot{\Psi}$ as simplified notations. Two partial nonlinear homogeneous 4th order differential equations for $\Psi(r,\theta)$ can be deduced in plane stress and plane strain, respectively, by eliminating the strains in the compatibility condition,

$$\frac{1}{r}(r\varepsilon_{\theta\theta})'' + \frac{1}{r^2}\ddot{\varepsilon}_{rr} - \frac{1}{r}\varepsilon'_{rr} - \frac{2}{r^2}(r\dot{\varepsilon}_{r\theta})' = 0, \tag{5.51}$$

via the constitutive Eq. (3.47), see details in Brocks et al. [14]. The stress-free crack faces, $\sigma_{\theta\theta}(r, \theta = \pm\pi) = \sigma_{r\theta}(r, \theta = \pm\pi) = 0$, are realised by the boundary conditions for Ψ,

$$\begin{aligned} \Psi(r, \theta = \pm\pi) &= 0 \\ \dot{\Psi}(r, \theta = \pm\pi) &= 0. \end{aligned} \tag{5.52}$$

5.2.2 Singular Crack Tip Fields

A separation ansatz is made for the asymptotic solution,

$$\Psi(r, \theta) = K_\sigma r^s \widehat{\psi}(\theta). \tag{5.53}$$

The exponent, s, represents the dominating singular term of a more general power series in r. Introducing this ansatz in Eq. (5.50) yields

$$\begin{aligned} \sigma_{rr} &= K_\sigma r^{s-2}\left(s\widehat{\psi} + \dot{\widehat{\psi}}\right) = K_\sigma r^{s-2}\widehat{\sigma}_{rr}(\theta) \\ \sigma_{r\theta} &= K_\sigma r^{s-2}(1-s)\dot{\widehat{\psi}} = K_\sigma r^{s-2}\widehat{\sigma}_{r\theta}(\theta) \\ \sigma_{\theta\theta} &= K_\sigma r^{s-2}s(s-1)\widehat{\psi} = K_\sigma r^{s-2}\widehat{\sigma}_{\theta\theta}(\theta) \end{aligned} \tag{5.54}$$

The equivalent stress, Eq. (5.49) has the same form, $\bar{\sigma}_{\mathrm{vM}} = K_\sigma r^{s-2}\widehat{\sigma}(\theta)$, so that generally,

$$\sigma_{ij} = K_\sigma r^{s-2}\widehat{\sigma}_{ij}(\theta), \tag{5.55}$$

can be written. The correspondent strain field follows from Eq. (3.47) as

$$\varepsilon_{ij} = \frac{3}{2}\alpha\varepsilon_0\left(\frac{K_\sigma}{\sigma_0}\right)^n r^{n(s-2)}\widehat{\sigma}(\theta)\widehat{\sigma}'_{ij}(\theta) = \alpha\varepsilon_0\left(\frac{K_\sigma}{\sigma_0}\right)^n r^{n(s-2)}\widehat{\varepsilon}_{ij}(\theta). \tag{5.56}$$

In order to describe a singular field, $s < 2$ has to hold. On the other hand, the strain energy stored in a circular disk of thickness, B, and radius, r_0, around the crack tip,

$$w = B\int_{r=0}^{r_0}\int_{\theta=-\pi}^{\pi}\bar{w}(r, \theta)\, r\, dr\, d\theta, \tag{5.57}$$

has to remain finite, which requires that the strain energy density,

$$\bar{w} = \int \sigma_{ij}\dot{\varepsilon}_{ij}dt = \alpha\varepsilon_0\sigma_0\frac{n}{n+1}\left(\frac{K_\sigma}{\sigma_0}\right)^{n+1} r^{(s-2)(n+1)}\,\tilde{\sigma}^{n+1}, \tag{5.58}$$

has a singularity not exceeding $\mathcal{O}(r^{-2})$, hence $s \geq 2n/(n+1)$, Hutchinson [40].

The separation ansatz, Eq. (5.55), allows for reducing the partial differential equation in $\Psi(r,\theta)$ to an ordinary nonlinear differential equation in $\tilde{\psi}(\theta)$, which is linear in its highest derivative,

$$\overset{\cdots\cdot}{\tilde{\psi}} = f\left(\overset{\cdots}{\tilde{\psi}}, \ddot{\tilde{\psi}}, \dot{\tilde{\psi}}, \tilde{\psi}\right), \tag{5.59}$$

and the boundary conditions become

$$\begin{matrix}\tilde{\psi}(\theta = \pm\pi) = 0 \\ \dot{\tilde{\psi}}(\theta = \pm\pi) = 0\end{matrix}, \tag{5.60}$$

which can alternatively be written as,

$$\begin{matrix}\dot{\tilde{\psi}}(\theta = \pi) = 0, & \ddot{\tilde{\psi}}(\theta = \pi) = 0 \\ \overset{\cdots}{\tilde{\psi}}(\theta = 0) = 0, & \overset{\cdots}{\tilde{\psi}}(\theta = 0) = 0\end{matrix}, \tag{5.61}$$

accounting for the symmetry conditions, $\sigma_{rr}(r,-\theta) = \sigma_{rr}(r,+\theta)$, $\sigma_{\theta\theta}(r,-\theta) = \sigma_{\theta\theta}(r,+\theta)$, $\sigma_{r\theta}(r,\theta) = 0$, in mode I.

The homogeneous differential Eq. (5.59) and the homogeneous boundary conditions, Eq. (5.61), constitute an eigenvalue problem with the exponent s as eigenvalue. Hutchinson [40] derived

$$s = \frac{2n+1}{n+1} \tag{5.62}$$

from numerical analyses, and Rice and Rosengren [72] received the same result from the conclusion that the strain energy density of Eq. (5.58) must have a r^{-1} singularity,

$$\bar{w} = \alpha\varepsilon_0\sigma_0\frac{n}{n+1}\left(\frac{K_\sigma}{\sigma_0}\right)^{n+1} r^{-1}\,\tilde{\sigma}^{n+1}, \tag{5.63}$$

in order to ensure a finite, non-zero value of the J-integral for $r \to 0$, see Eq. (5.22).

Finally, the singular stress and strain fields are

$$\begin{aligned}\sigma_{ij} &= K_\sigma r^{-1/(n+1)} \widetilde{\sigma}_{ij}(\theta) \\ \varepsilon_{ij} &= \alpha\varepsilon_0 \left(\frac{K_\sigma}{\sigma_0}\right)^n r^{-n/(n+1)} \widetilde{\varepsilon}_{ij}(\theta)\end{aligned}, \tag{5.64}$$

which take the well-known $1/\sqrt{r}$ singularity of LEFM for $n = 1$. They are called HRR field, in summary, with the initials of the authors Hutchinson [40, 41], Rice and Rosengren [72]. The dimensionless angular functions, $\widetilde{\sigma}_{ij}(\theta)$ and $\widetilde{\varepsilon}_{ij}(\theta)$, can be obtained from numerical solutions of Eq. (5.59) and have been tabulated for Cartesian and polar coordinates by Shih [83] and Brocks et al. [14]. Figure 5.11 shows examples in Cartesian coordinates for plane strain and plane stress for three different hardening exponents, n. The correspondent stress-strain curves are shown in Fig. 3.6. Different from the stress fields in LEFM, Fig. 2.4, the HRR fields are different in plane strain and plane stress, because the stresses σ_{zz} affect the yield condition.

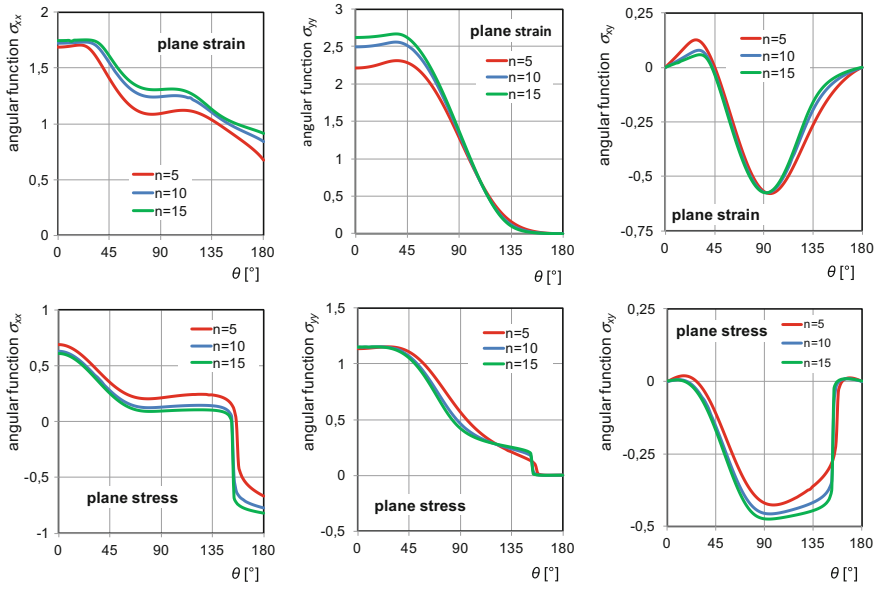

Fig. 5.11 Angular functions, $\widetilde{\sigma}_{xx}(\theta)$, $\widetilde{\sigma}_{yy}(\theta)$, $\widetilde{\sigma}_{xy}(\theta)$, of the HRR field in plane strain (*above*) and plane stress (*below*) for $n = 5$, 10, 15

5.2.3 J-Integral as Crack-Tip Intensity

In every eigenvalue problem, the intensity parameter K_σ is undetermined. It depends on the external loading. As in LEFM, Eq. (2.16), the stress intensity is related to the energy release rate or J-integral which has been generalised to nonlinear material behaviour, Eq. (5.24). Writing J for a circular contour around the crack tip as in Eq. (5.22), taking the strain energy density, $\bar{w}(r,\theta)$, Eq. (5.63), and

$$\sigma_{ij} n_j u_{i,x} = \cos\theta\left(\sigma_{rr} u_{r,r} + \sigma_{r\theta} u_{\theta,r}\right) + \sin\theta\left[\frac{\sigma_{rr}}{r}\left(u_\theta - u_{r,\theta}\right) - \frac{\sigma_{r\theta}}{r}\left(u_r - u_{\theta,\theta}\right)\right], \tag{5.65}$$

finally yields the relation,

$$K_\sigma = \sigma_0 \left(\frac{J}{\alpha \sigma_0 \varepsilon_0 I_n}\right)^{1/(n+1)}, \tag{5.66}$$

after integration of the strain displacement relations and some lengthy calculations, see details in Brocks et al. [14]. For $n = 1$, the intensity factor becomes, $K_\sigma \sim \sqrt{J} \sim K_\mathrm{I}$, as the SIF in LEFM. The parameter I_n is an integral along θ of angular stress and displacement functions, $\widehat{\sigma}_{ij}(\theta)$, $\widehat{u}_i(\theta)$, depending on n and the stress state, which can only be numerically evaluated, see Fig. 5.12.

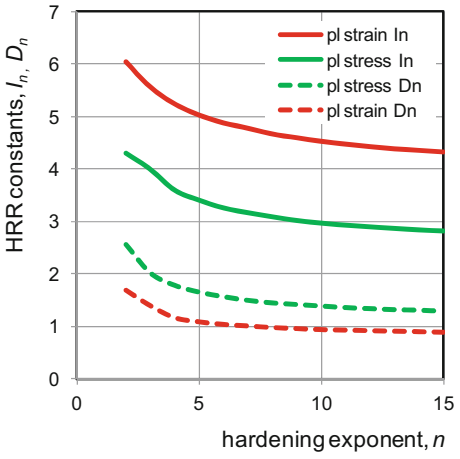

Fig. 5.12 HRR parameters I_n (*solid lines*) and D_n (*dashed lines*)

5.2.4 Crack Tip Opening Displacement

The HRR displacement field

$$u_i = \alpha\varepsilon_0 \left(\frac{J}{\alpha\sigma_0\varepsilon_0 I_n} \right)^{n/(n+1)} r^{1/(n+1)}\, \widehat{u}_i(\theta) \tag{5.67}$$

provides a simple definition of the crack tip opening displacement (CTOD), δ_t, by the intersection of two 45° secants with the opening profile of the crack [82],

$$\delta_t = 2u_y(r_t, \pi) \quad \text{with} \quad r_t - u_x(r_t, \pi) = u_y(r_t, \pi) \tag{5.68}$$

see Fig. 5.13, which results in a linear relationship between J and δ_t,

$$\delta_t = d_n \frac{J}{\sigma_0}. \tag{5.69}$$

The proportionality factor is

$$d_n = (\alpha\varepsilon_0)^{1/n} D_n = \frac{2(\alpha\varepsilon_0)^{1/n}}{I_n} \left(\widehat{u}_x(\pi) + \widehat{u}_y(\pi) \right)^{1/n} \widehat{u}_y(\pi), \tag{5.70}$$

and the constant D_n is plotted in Fig. 5.12 (dashed lines) in dependence on n for plane strain and plane stress.

5.2.5 Validity of the HRR Solution

The size of the HRR dominated zone has been investigated for 2D FE models under plane strain and fully plastic conditions by McMeeking [53], McMeeking and Parks [55], Shih [84], Shih and German [87], applying incremental plasticity but small deformations. It was found to be

$$r_{HRR} = \begin{cases} 0.07(W-a) & \text{in bending} \\ 0.01(W-a) & \text{in tension} \end{cases}. \tag{5.71}$$

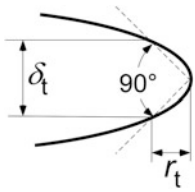

Fig. 5.13 Definition of CTOD by Shih [82]

A small portion of bending increases the size of the J dominated zone quite quickly to the pure bending case [84].

FE calculations by McMeeking [53] and Brocks and Olschewski [20], the latter for large deformations, confirmed the linear relation between J and δ_t. according to Eq. (5.69). Both quantities are hence equivalent as fracture mechanics parameters characterising the crack tip field.

The CTOD controls the regime where large displacements affect the stress field and the HRR solution deviates from the "real" stresses calculated with incremental plasticity. No stress singularities occur at the blunting crack tip, and the boundary condition requires that $\sigma_{xx} \to 0$ for $r \to 0$. A stress maximum like that at a notch appears, instead. Figure 5.14 shows FE results for the stresses in the ligament at a crack tip obtained with incremental plasticity for two different J values. The abscissa is normalised by $J/\sigma_0 \sim \delta_t$, indicating that the stresses are indeed J-controlled, even in the regime of large displacements. Note that the stresses follow the plane-strain condition, $\sigma_{zz} = (\sigma_{xx} + \sigma_{yy})/2$, in this zone. FE calculations by Rice and Johnson [70], McMeeking [54] and Brocks and Olschewski [20] proved that the zone of large deformations is about two to three times δ_t. In order to have a J-dominated zone, $r_{HRR} > 3\delta_t$ has to hold. Size conditions can now be derived from Eq. (5.71) with $d_n = 2$ as,

$$W - a \geq \begin{cases} 20J/R_0 & \text{for bend specimens} \\ 150J/R_0 & \text{for tensile specimens} \end{cases}, \tag{5.72}$$

which differ from the size conditions for bend specimens in ASTM E1820 [6], see Sect. 7.2.3 on measurement of fracture toughness in EPFM.

Parks and Wang [65] and Brocks and Noack [19] analysed problems of real three-dimensional structures with curved crack fronts. Again, the J-dominance of stress fields depends on the type of loading and the geometry. Due to the variety of geometries and the complexity of 3D elastic-plastic analyses, no general conclusions can be made.

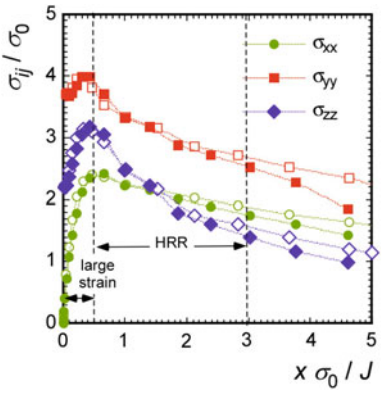

Fig. 5.14 Normalised stresses in the ligament over normalised abscissa, $x/(J/\sigma_0) \sim x/\delta_t$ at the crack tip of a C(T) specimen for two J-values, plane strain FE analysis with incremental plasticity

Discussions on J-dominance finally resulted in the introduction of a "second parameter" like the T-stress in LEFM. Sharma and Aravas [81] investigated higher order terms in the series expansion of the stress fields. O'Dowd and Shih [61, 62] introduced the Q-stress,

$$\sigma_{ij}(r,\theta) = \sigma_{ij}^{\mathrm{HRR}}(r,\theta) + Q\sigma_0\delta_{ij} \quad \text{for} \quad |\theta| < \pi/2, \tag{5.73}$$

mimicking Eq. (2.22). It is not based on an analytical solution, however, but a phenomenological approximation of several non-singular terms based on FE analyses. The Q-stress has been suggested as a second term to calibrate R-curves and thus capture phenomena of geometry dependence. It competed with approaches based on T-stress [97], stress triaxiality, η, Eq. (5.37), Brocks and Schmitt [21], and several other "second parameters". Obviously, Q is directly related to σ_h and η [100]. All approaches are purely phenomenological and cannot remedy the physical deficiency of J in incremental plasticity.

5.3 Extended and Alternative Concepts

The stringent theoretical foundation of J notably by the contributions of Rice and co-authors and the successful transfer of Griffith' concept of the energy release rate as crack driving force from LEFM to EPFM promoted not only its application in fracture mechanics based concepts of safety assessments particularly in the USA but also motivated attempts to extend its applicability to non-monotonic loading. Other concepts and approaches based on CTOD have been particularly developed in the UK and became part of respective design procedures. Discussions on the geometry dependence of J_R-curves fostered an alternative view considering incremental plasticity. The following sections can only give a condensed overview over the respective concepts, approaches and procedures.

5.3.1 Dissipation Rate

Various inconsistencies in the characterisation of ductile tearing resistance in terms of J_R-curves, in particular their geometry dependence and the increase of J with Δa, are due to the fact that J is actually not the true driving force any more if the crack is extending. Turner [95] proposed a straight transfer of Griffith's energy release rate criterion, Eq. (2.8), to plastic processes, instead, and defined the energy dissipation rate as a physically more meaningful quantity which is consistent with the incremental nature of plastic deformations,

$$R_{\mathrm{dis}} = \left(\frac{\partial U_{\mathrm{dis}}}{\partial A_{\mathrm{c}}}\right)_{v_{\mathrm{L}}} = \left(\frac{\partial W_{\mathrm{ext}}}{\partial A_{\mathrm{c}}}\right)_{v_{\mathrm{L}}} - \left(\frac{\partial U^{\mathrm{e}}}{\partial A_{\mathrm{c}}}\right)_{v_{\mathrm{L}}} = \left(\frac{\partial U^{\mathrm{p}}}{\partial A_{\mathrm{c}}}\right)_{v_{\mathrm{L}}} + \frac{dU_{\mathrm{sep}}}{dA_{\mathrm{c}}}, \qquad (5.74)$$

where W_{ext} is the external work, and U^{e} and U^{p} are the recoverable elastic strain energy and the work of plastic deformation, respectively. The dissipation rate consists of two contributions, namely the work rate of remote plastic deformation, $\partial U^{\mathrm{p}}/\partial A_{\mathrm{c}}$, and the local work rate of separation, $dU_{\mathrm{sep}}/dA_{\mathrm{c}} = \Gamma_{\mathrm{c}}$.

The dilemma of R-curves becomes obvious from a simple energy balance as in Fig. 5.15: what people measure as "fracture resistance" does to a great deal not result from local material separation, $\Gamma_c \ll \partial U^{\mathrm{p}}/\partial A_{\mathrm{c}}$, but from remote plasticity [47], which is different for bend and tensile specimens. The geometry dependence is hence inherent and cannot be remedied. Attempts to establish "*an alternative view of R-curve testing*" based on the dissipation rate [56, 92, 96] did not become accepted, however, because no possibility based on continuum mechanics was found to split the two contributions in Eq. (5.74). Only an understanding of the energy dissipation mechanisms in the process zone at the crack tip can help to identify "fracture toughness" as a material property [91].

Turner's approach is helpful, however, to understand the shape of J_{R}-curves. ASTM E1820 [6] simply suggests a power-law regression,

$$J(\Delta a) = C_1 \left(\frac{\Delta a}{k}\right)^{C_2}, \qquad (5.75)$$

with C_1, C_2 as adjustable parameters, but this is a pure curve fit without any physical background. Analysing R-curves for various materials and various specimen geometries, Brocks and Anuschewski [11] found that the dissipation rate, $R_{\mathrm{dis}}(\Delta a)$, like CTOA (Sect. 5.3.3), reaches a constant steady state value, R_∞, after a transition region and can hence be fitted by a function,

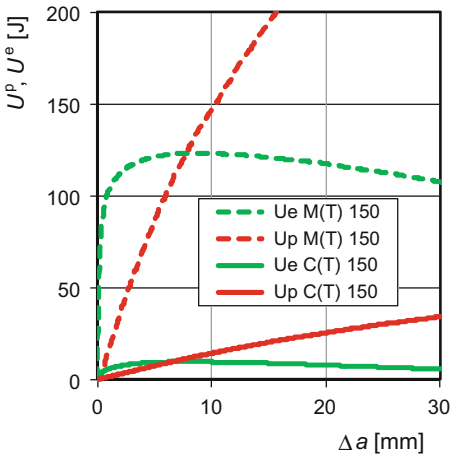

Fig. 5.15 Energy balance for crack extension in C(T) and M(T), results by Scheider et al. [73]

$$R_{\mathrm{dis}}(\Delta a) = R_{\infty}\left[1 + C_1 \exp\left(-C_2 \frac{\Delta a}{W - a_0}\right)\right], \tag{5.76}$$

with three adjustable parameters, R_{∞}, C_1, C_2. Since according to their respective definitions, $R_{\mathrm{dis}}(\Delta a)$ and $J(\Delta a)$ are related by

$$R_{\mathrm{dis}}(\Delta a) = \begin{cases} \left(\frac{W-a}{\eta_J}\right)\frac{\mathrm{d}J^{\mathrm{p}}}{\mathrm{d}a} + J^{\mathrm{p}}\frac{\gamma}{\eta_J} & \text{for SE(B) and C(T)} \\ (W-a)\frac{\mathrm{d}J^{\mathrm{p}}}{\mathrm{d}a} & \text{for DE(T) and M(T)} \end{cases}, \tag{5.77}$$

the typical shapes of $J(\Delta a)$-curves can be obtained by integration of Eq. (5.76), Fig. 5.16. The correspondent solutions are geometry specific, namely logarithmic functions for M(T), straight lines for SE(B) and some lengthy expressions of exponential functions for C(T) specimens [11], which underlines the general geometry dependence of J_{R}-curves and its physical background.

5.3.2 *J-Integral for Cyclic Plasticity*

In analogy to the cyclic SIF, ΔK, of Paris and Erdogan [63], Eq. (2.19), Dowling and Begley [28] and Dowling [27] suggested a "cyclic J-integral", ΔJ, for application to low-cycle fatigue (LCF). The justification was and is still mostly based on cursory arguments "*by analogy to the original J-integral*" [52]. Though being aware that "*for elastic-plastic materials, J loses its interpretation in terms of the potential energy available for crack extension*", Dowling [27] argues that it "*retains physical significance as a measure of the characteristic crack-tip strain field*",

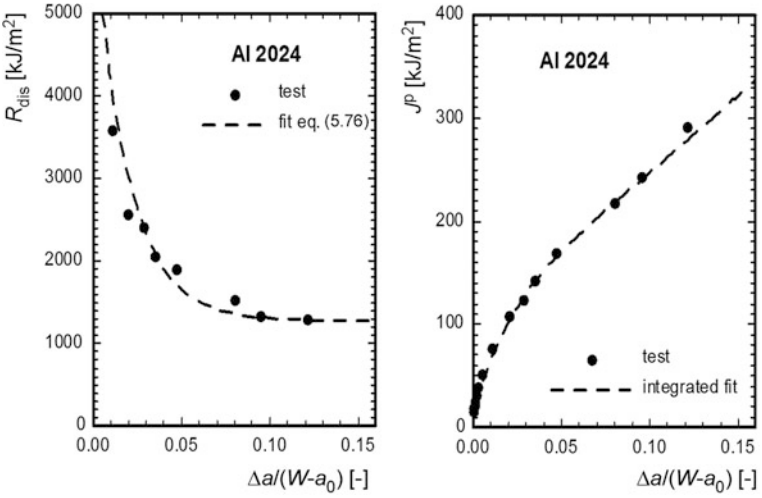

Fig. 5.16 Dissipation rate, R_{dis}, and cumulative plastic J for an M(T) specimen

leaving the obvious question unanswered what a *characteristic crack-tip strain field* in a cyclic process is supposed to be.

Tanaka [94] specifies that ΔJ "*may be interpreted as a measure of the intensity of the field of cyclic strains around the crack tip*". This has apparently become consensus among the followers of a cyclic J though no evidence has ever been presented. It is necessary, "*to assume that the material behaves according to kinematic hardening*" [29] and shows Masing behaviour [57] resulting in a stabilised "cyclic" stress-strain curve, $\Delta\sigma(\Delta\varepsilon_p)$, which relates the strain range to the stress range and is, of course, different from the monotonic curve, $\sigma(\varepsilon_p)$, Fig. 3.1.

Contradicting Dowling's argument of 1976, McClung et al. [52] postulate that the cyclic J "*is related to the rate of change of potential energy with change in crack size*", since this is vital for its experimental determination. Note, however, that the release rate definition of J in Eq. (5.24) is based on a mathematical variation of the crack length, a. No physical crack extension, Δa, occurs for constant J in EPFM, whereas in cyclic plasticity a constant ΔJ is supposed to induce a crack extension rate, da/dN. Thus, not even the physical meaning of a "release rate" is clear with respect to ΔJ.

Whereas $\Delta\sigma = \sigma_{max} - \sigma_{min}$ and $\Delta\varepsilon = \varepsilon_{max} - \varepsilon_{min}$, the "cyclic J" is no difference between two states, $\Delta J \neq J_{max}–J_{min}$, because unlike Eq. (2.14) in LEFM the relation between J and stresses and strains is nonlinear. Instead, stresses, strains and displacements in the contour integral definition of J, Eq. (5.20), are replaced by ranges of the respective quantities [29],

$$\Delta J = \oint_{\Gamma} \left[\Delta w_{\varepsilon}\, dy - \Delta t_i \frac{\partial(\Delta u_i)}{\partial x} ds \right] , \tag{5.78}$$

with

$$\Delta w_{\varepsilon} = \int \Delta\sigma_{ij} d(\Delta\varepsilon_{ij}). \tag{5.79}$$

McClung et al. [52] admit that "*in this sense, 'Delta J' is something of a misnomer*." The authors fail to explain how to evaluate the contour integral of Eq. (5.78). The experimental determination of the J-integral in EPFM is not based on the contour integral, Eq. (5.20), but on its property as energy release rate [71], Eq. (5.24). Likewise, the evaluation of the cyclic J would require a science-based release rate interpretation, which is still missing. Dowling and Begley [28] determined "*values of cyclic J ... from areas under load versus deflection lines during rising load*" but gave no explicit formula.

Though numerous experimental investigations on ΔJ are published, its theoretical background and foundation have remained nebulous. There is no reason that basic and substantial features should hold for a quantity which fails to meet the requirements of J, in particular Eq. (5.11). Substantiations are just based on "analogy" arguments. After all, it may be some measure of dissipation energy per loading cycle which correlates with crack growth.

5.3.3 CTOD and CTOA

Historically, the first elastic-plastic fracture mechanics concept was developed in the UK, where Wells [98] suggested that the crack tip deformation at the instant of initiation of crack extension should be taken as a material property and

$$\delta_t = \delta_c, \tag{5.80}$$

as fracture criterion. The CTOD test method developed at The Welding Institute (TWI) became the British Standard BS 5762 [23] and was later included in ISO 12135 [43]. Harrison et al. [37] suggested the Design Curve as a simple assessment method for short cracks where the CTOD is proportional to the local strain.

Analytical foundations of CTOD are given in LEFM by Eq. (4.14) where δ_t is related to the SIF, or in EPFM by Eq. (5.69) where it is related to J. Thus, the CTOD concept can be viewed as equivalent to the K- or J-concept, and any preference for δ_t may be motivated by its feature that it is an observable quantity which can be (more or less) directly measured without encountering uncertainties of evaluation formulas as for the J-integral.

However, the above definitions work for stationary cracks, only, since a growing crack does not exhibit any blunting at the tip. Schwalbe [74] introduced a technique where the CTOD is measured on the specimen surface over a gauge length of 5 mm at the location of the initial crack tip, Fig. 5.17a. It is particularly suited for growing cracks in thin specimens and became part of the standards ISO 22889 [44] and ASTM E2472 [7] for specimens under low constraint conditions [78].

Figure 5.17b shows that the validity range is significantly larger than for the J_R-curves of the same specimens, compare Fig. 5.10. Hellmann and Schwalbe [38]

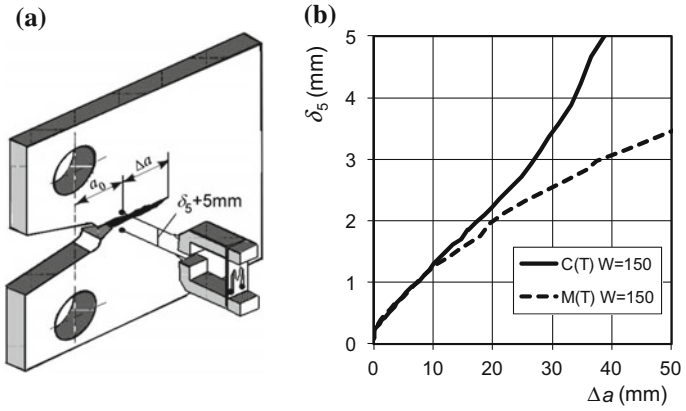

Fig. 5.17 CTOD δ_5 according to Schwalbe [74]: **a** Clip gauge and specimen arrangement; **b** δ_{5R}-curves for C(T) and M(T), same material as in Fig. 5.10, Scheider et al. [73]

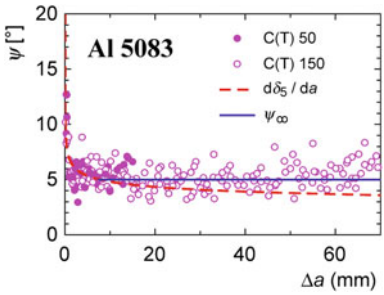

Fig. 5.18 Crack-tip opening angle (CTOA) from direct measurements [39] and from the δ_{5R}-curve

investigated geometry and size effects on J_R- and δ_{5R}-curves under plane stress conditions for various materials and Heerens and Schödel [39] established criteria for the validity of δ_{5R}-curves. The latter are independent of the specimen width, W, if

- $\Delta a \leq 0.25(W\text{-}a_0)$ for C(T) specimens,
- $\Delta a \leq W\text{-}a_0\text{-}4B$, $W\text{-}a_0 > 4B$ for M(T) specimens.

Another parameter applied to simulations of large ductile crack extension particularly in metal sheets is the crack tip opening angle, CTOA, Scheider et al. [73]. It has been observed that the $\psi_R(\Delta a)$ curve reaches a constant saturation value, ψ_∞, after some transition region, Fig. 5.18. Direct measurements suffer from large scatter, but the transition region can be easily determined from the slope of the δ_{5R}-curve, Heerens and Schödel [39],

$$\psi(\Delta a) \approx \frac{d\delta_5}{da}. \tag{5.81}$$

and ψ_∞ can be identified from simulations of tests. The CTOA test method is also included in the standards ASTM E2472 [7] and ISO 22889 [44].

The theoretical background of CTOA can be found in the analysis of the near-tip field at a growing crack by Rice et al. [69]. Newman et al. [60] give a review of the CTOA and CTOD fracture criteria.

5.3.4 Assessment Procedures

Numerous engineering assessment procedures have been developed by different institutions from various countries and for different sectors of industry. Standardisation is required in order to make assessments independent of individual persons using them. Just a short overview can be given here and the reader is referred to the literature. Basically, they all have to satisfy the condition that a "crack driving force" like K, J, δ_t has to be less than the correspondent material resistance [101], see Eqs. (2.12), (2.17), (5.21), (5.47) and (5.80). The analytical or

numerical calculation of the crack driving forces has been elaborated above, and the determination of material resistance will be addressed in Sect. 7.2 on test methods and standards. The information to be gained from such an assessment are the maximum load which a component is able to carry, a critical crack size or residual life time. Inspection intervals can be quantified in order to find cracks before they become critical.

Along with the "Design Curve" by Harrison et al. [37], the "Failure Assessment Diagram" (FAD) was developed in the UK. It is based on the two-criteria approach by Dowling and Townly [30], which covers the range from brittle to ductile failure and divides an area of safety from one of unsafe conditions, Fig. 5.19. Its ordinate represents the applied SIF normalised by the respective critical value, $K_r = K/K_c$, and is a measure of proximity to LEFM failure. The abscissa is the applied load normalised by a plastic limit load, $L_r = F/F_{pl}$, and is a measure of proximity to plastic collapse, see Sect. 6.1.2. F_{pl} is the applied force at net section yielding, see Madia et al. [50] for surface cracks, for instance. The borderline between the areas of safe and unsafe conditions is [36]

$$K_r = L_r \left[\left(\frac{8}{\pi^2} \right) \ln \sec \left(\frac{\pi L_r}{2} \right) \right]^{-1/2}. \tag{5.82}$$

Several enhancements have been executed in the meantime to adjust the FAD to the development in fracture mechanics, see e.g. Zerbst et al. [102]. It has become essential part of the British R6 procedure [66].

A handbook for J as a driving force parameter has been developed by the Electric Power Research Institute (EPRI) in the US in the 1970s and 80s [49, 88]. It is based on partitioning the J integral into an elastic and a plastic component, Eq. (5.26), with

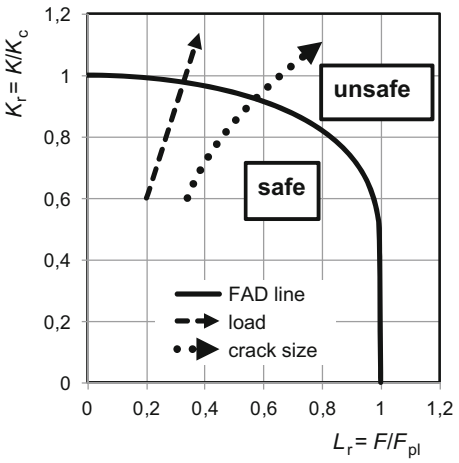

Fig. 5.19 Two criteria approach: failure assessment diagram

$$J^{\mathrm{p}} = \alpha g(a/W, n)\left(\frac{F}{F_{\mathrm{pl}}}\right)^{(1+n)/n} \tag{5.83}$$

where α and n are the parameters of the Ramberg-Osgood strain hardening law. The function $g(a/W, n)$ represents the effects of the geometry and strain hardening. It has been determined and tabulated for a number of configurations from finite element analyses. A parameter explosion due to the combination of geometry and material parameters finally terminated the project. However the approach to develop J-formulas has influenced other authors.

Schwalbe [75] developed the "Engineering Treatment Model" (ETM) as a method for the determination of the driving force parameter δ_5 in analytical form [79, 80]. For fully plastic conditions ($F \geq F_{\mathrm{pl}}$), the respective formula is

$$\frac{\delta_5}{\delta_{5\mathrm{pl}}} = \left(\frac{F}{F_{\mathrm{pl}}}\right)^{\frac{1}{N}} = \left(\frac{J}{J_{\mathrm{pl}}}\right)^{\frac{1}{1+N}}. \tag{5.84}$$

with $0 < N < 1$ being the hardening exponent of the stress strain curve,

$$\frac{\sigma}{R_0} = \left(\frac{\varepsilon}{\varepsilon_0}\right)^{N}. \tag{5.85}$$

Note that the Ramberg-Osgood exponent, n, is approximately the inverse of N in Eq. (5.85) for $\alpha = 1$.

The procedure has been extended to the analysis of yield-strength mismatched welded joints [77], which is characterised by a bi-material model consisting of the base metal and a strip of weld metal. The respective document includes plastic limit load solutions for some standard cases.

The ETM is part of the "Engineering Flaw Assessment Method" [76] which is a comprehensive assessment scheme also incorporating the experimental determination of the material properties including corrosive environments, strength mis-matched welded joints and high temperature behaviour.

The "Structural Integrity Assessment Procedure for European Industry" (SINTAP) was developed in a European Brite-Euram project of seventeen institutions from nine European countries. It offers the FAD routine of R6 as well as crack driving force routines like ETM which have been harmonised in order to deliver identical results. The user has the option to alternatively use the J-integral or the CTOD. Several levels of analysis are provided [102].

A second European project, the "Fitness-for Service Network" (FITNET) comprised about 50 organisations. The document incorporates a fracture module based on the SINTAP options and modules for fatigue crack extension, fatigue life, corrosion and creep.

References

1. Abaqus (2014) User's Manual, Version 6.12. Dassault Systèmes Simulia Corp, Providence, RI, USA
2. Amestoy M, Bui HD, Labbens R (1981) On the definition of local path independent integrals in 3D crack problems. Mechanics Research Communications
3. Arafah D (2014) Fracture assessment of cracked components under biaxial loading. PhD Thesis, Department of Mechanical Engineering, Politecnico di Milano
4. Arafah D, Madia M, Zerbst U, Beretta S, Cristea ME (2015) Instability analysis of pressurized pipes with longitudinal surface cracks. Int J Press Vess Piping 126–127:48–57
5. ASTM E561 (2015) Standard test method for K–R curve determination. Annual book of ASTM standards, Vol 03.01, American Society for Testing and Materials, West Conshohocken (PA), USA
6. ASTM E1820 (2015) Standard test method for measurement of fracture toughness, Annual Book of ASTM Standards, Vol 03.01, American Society for Testing and Materials, West Conshohocken (PA), USA
7. ASTM E2472 (2012) Standard test method for determination of resistance to stable crack extension under low-constraint conditions, Annual Book of ASTM Standards, Vol 03.01, American Society for Testing and Materials, West Conshohocken (PA), USA
8. Bakker A (1984) The three-dimensional J-Integral. PhD Thesis, Delft University of Technology (The Netherlands), Report WTHD 167
9. Begley JA, Landes JD (1972) The J-integral as a fracture criterion. Fracture Toughness, ASTM STP 514:1–23
10. Betegón C, Hancock JW (1991) Two-parameter characterization of elastic-plastic crack tip fields. J Appl Mech 58:104–110
11. Brocks W, Anuschewski P (2004) Parametrising ductile tearing resistance by four parameters. Eng Fract Mech 71:127–146
12. Brocks W, Anuschewski P (2008) Risswiderstandskurven von Blechen. Technical Note GKSS/WMS/08/06, Institute of Materials Research, GKSS Research Centre, Geesthacht
13. Brocks W, Anuschewski P, Scheider I (2010) Ductile tearing resistance of metal sheets. Eng Failure Anal 17:607–616
14. Brocks W, Klingbeil D, Olschewski J (1990) Lösung der HRR-Feld-Gleichungen der elastisch-plastischen Bruchmechanik, Research Report 175. Bundesanstalt für Materialforschung und -prüfung, Berlin
15. Brocks W, Krafka H, Künecke G, Wobst K (1990) Ductile crack growth of semi-elliptical surface flaws in pressure vessels. In: Coleman CE (ed) Leak-before-break in water reactor piping and vessels. Elsevier Applied Science, London, pp 301–316
16. Brocks W, Krafka H, Künecke G, Wobst K (1990) Ductile crack growth of semi-elliptical surface flaws in pressure vessels. Int J Pres Vess Piping 43:301–316
17. Brocks W, Künecke G, Wobst K (1989) Stable crack growth of axial surface flaws in pressure vessels. Int J Pres Ves Piping 40:77–90
18. Brocks W, Künecke G, Noack HD, Veith H (1989) On the transferability of fracture mechanics parameters to structures using FEM. Nucl Eng Des 112:1–14
19. Brocks W, Noack HD (1988) J-integral and stresses at an inner surface flaw in a pressure vessel. Int J Pres Ves Piping 31:187–203
20. Brocks W, Olschewski J (1986) On J-dominance of crack-tip fields in largely yielded 3D structures. Int J Solids Structures 22:693–708
21. Brocks W, Schmitt W (1995) The second parameter in J-R curves: constraint or triaxiality? In: Kirk M, Bakker A (eds) 2nd Symp Constraint Effects, ASTM STP 1224, Philadelphia, pp 209–231
22. Brocks W, Yuan H (1989) Numerical investigations on the significance of J for large stable crack growth. Eng Fract Mech 32:459–468

23. BS 5762 (1979) Methods for crack opening displacement (COD) testing. British Standards Institution
24. Cherepanov CP (1967) Crack propagation in continuous media. Appl Math Mech 31:476–488
25. DeLorenzi HG (1982) Energy release rate calculations by the finite element method. General Electric Technical Information Series, Report No. 82CRD205
26. DeLorenzi HG (1982) On the energy release rate and the J-integral for 3D crack configurations. J Fracture 19:183–193
27. Dowling NE (1977) Crack growth during low-cycle fatigue of smooth axial specimens. ASTM STP 637:97–121
28. Dowling NE, Begley JA (1976) Fatigue crack growth during gross plasticity and the J-integral. ASTM STP 590:82–103
29. Dowling NE, Iyyer NS (1987) Fatigue crack growth and closure at high cyclic strains. Mater Science Eng 96:99–107
30. Dowling AR, Townly CHA (1975) The effect of defects on structural failure: a two criteria approach. Int J Press Ves Piping 3:77–107
31. Efam GTP (2002) The GKSS procedure for determining the fracture behaviour of materials. GKSS-Forschungszentrum Geesthacht, Germany
32. Eftis J, Liebowitz H (1972) On the modified Westergaard equation for certain plane crack problems. Int J Fract Mech 8(1972):383–392
33. Eshelby JD (1965) The continuum theory of lattice defects. Prog Solid States Phys 3:79–114
34. Garwood SJ (1979) Effect of specimen geometry on crack growth resistance. In: Smith CW (ed) ASTM STP 677. American Society for Testing and Materials, pp. 511–532
35. Garwood SJ, Robinson JN, Turner CE (1975) The measurement of crack growth resistance curves (R-curves) using the J integral. Int J Fracture 11:528–530
36. Goodier JN, Field FA (1963) Plastic energy dissipation in crack propagation. In: Drucker DC, Gilman JJ (eds) Fracture of solids. Wiley, New York, pp 103–118
37. Harrison JD, Dawes MG, Archer GL, Kamath KD (1978) The COD approach and its application to welded structures. Research Report 55/1978/E, The Welding Institute, Cambridge
38. Hellmann D, Schwalbe KH (1984) Geometry and size effects on J-R and δ-R curves under plane stress conditions. In: Sanford RJ (ed) Fracture Mechanics, 15th Symposium. ASTM STP 833, pp 577–605
39. Heerens J, Schödel M (2009) Characterization of stable crack extension in aluminium sheet material using the crack tip opening angle determined optically and by the δ5 clip gauge technique. Eng Fract Mech 76:101–113
40. Hutchinson JW (1968) Singular behaviour at the end of a tensile crack in a hardening material. J Mech Phys Solids 16:13–31
41. Hutchinson JW (1968) Plastic stress and strain fields at a crack tip. J Mech Phys Solids 16:337–347
42. Hutchinson, JW, Paris, PC (1979) Stability analysis of J-controlled crack growth. In: Landes JH, Begley, JA, Clarke GA (eds) Elastic-Plastic Fracture, ASTM STP 668:37–64
43. ISO 12135 (2002) Metallic materials—Unified method of test for the determination of quasistatic fracture toughness. International Standards Organisation, Geneva, Switzerland
44. ISO 22889 (2007) Metallic materials—method of test for the determination of resistance to stable crack extension using specimens of low constraint. International Standards Organisation, Geneva, Switzerland
45. Kikuchi M, Miyamoto H (1982) Evaluation of JK integrals for a crack in multiphase materials. Recent research on mechanical behavior of materials. Bull Fracture Mechanics Lab, vol 1, Science University of Tokyo
46. Kikuchi M, Miyamoto H, Sakaguchi, Y (1979) Evaluation of three-dimensional J integral of semi-elliptical surface crack in pressure vessel. In: Trans 5th SMiRT, paper G7/2, Berlin
47. Kolednik O (1993) A simple model to explain the geometry dependence of J-Δa-curves. Int J Fract 63:263–274

48. Kolednik O, Predan J, Fischer FD (2010) Cracks in inhomogeneous materials: comprehensive assessment using the configurational forces concept. Eng Fract Mech 77:2698–2711
49. Kumar V, German MD, Shih CF (1981) An Engineering Approach for elastic-plastic fracture analysis. EPRI-Report NP-1931, EPRI, Palo Alto, CA
50. Madia M, Arafah D, Zerbst U (2014) Reference load solutions for plates with semi-elliptical surface cracks subjected to biaxial tensile loading. Int J Press Vess Piping 119:19–28
51. Maugin GA (1995) Material forces: concepts and applications. Appl Mech Rev 48:213–245
52. McClung RC, Chell GG, Lee YD, Russel DA, Orient DE (1999) Development of a practical methodology for elastic-plastic and fully plastic fatigue crack growth. NASA/CR-1999-209428, Marshall Space Flight Center • MSFC, Alabama 35812
53. McMeeking RM (1977) Path dependence of the J-Integral and the role of J as a parameter characterizing the near-tip field. In Barsom JM (ed) Flaw growth and fracture, ASTM STP 631, pp 28–41
54. McMeeking RM (1977) Finite deformation analyses of crack-tip opening in elastic-plastic materials and implications for fracture. J Mech Phys Solids 25:357–381
55. McMeeking RM, Parks DM (1979) On criteria for J-dominance of crack-tip fields in large scale yielding. In: Landes JH, Begley, JA, Clarke GA (eds) Elastic-Plastic Fracture, ASTM STP 668, pp 175–194
56. Memhard D, Brocks W, Fricke S (1993) Characterization of ductile tearing resistance by energy dissipation rate. Fatigue Fract Eng Mater Struct 16:1109–1124
57. Mughrabi H, Bayerlein M, Christ HJ (1987) Microstructural foundation of cyclic stress-strain response and Masing behaviour. In: Anderson et al (eds) Constitutive relations and their physical basis, 8th Risø Int Symp Metallurgy and Material Science, Roskilde, Denmark
58. Muscati A, Lee DJ (1984) Elastic-plastic finite element analysis of thermally loaded cracked structures. Int J Fracture 25:246–2276
59. Neimitz A, Dzioba I, Galkiewicz G, Molasy R (2004) A study of stable crack growth using experimental methods, finite elements and fractography. Eng Fract Mech 71:1325–1355
60. Newman JC, James MA, Zerbst U (2003) A review of the CTOA/CTOD fracture criterion. Eng Fract Mech 70:85–371
61. O'Dowd NP, Shih CF (1991) Family of crack-tip fields characterized by a triaxiality parameter: I Structure of fields. J Mech Phys Solids 39:989–1015
62. O'Dowd NP, Shih CF (1992) Family of crack-tip fields characterized by a triaxiality parameter: II Fracture applications. J Mech Phys Solids 40:939–963
63. Paris PC, Erdogan F (1963) A critical analysis of crack propagation laws. J Basic Eng Trans Am Soc Mech Eng D85:528–534
64. Paris PC, Tada H, Zahoor A, Ernst H (1979) The theory of instability of the tearing mode of elastic-plastic crack growth. In: Landes JH, Begley JA, Clarke GA (eds) Elastic-Plastic Fracture, ASTM STP 668, pp 5–36
65. Parks DM, Wang YY (1988) Elastic-plastic analysis of part-through surface cracks. In: Rosakis AJ, Ravi-Chandar K, Rajapakse Y (eds) Analytical, numerical and experimental aspects of three dimensional fracture processes, New York, ASME AMD-vol 91, pp 19–32
66. R6 (2009) Assessment of the integrity of structures containing defects. Revision 4, British Energy Generation Ltd.
67. Ramberg W, Osgood WR (1945) Description of stress strain curves by three parameters. NACA Technical Note No 902
68. Rice JR (1968) A path independent integral and the approximate analysis of strain concentrations by notches and cracks. J Appl Mech 35:379–386
69. Rice JR, Drugan WJ, Sham TL (1979) Elastic Plastic analysis of growing cracks. Technical Report No. 65 of US DOE, Brown University, Providence, RI
70. Rice JR, Johnson MA (1970) The role of large crack tip geometry changes in plane strain fracture. In: Kanninen MF, Adler W, Rosenfield A, Jaffe R (eds) Elastic behaviour of solids. McGraw Hill, New York

71. Rice JR, Paris PC, Merkle JG (1973) Some further results of J-integral analysis and estimates. In: Kaufman J, Swedlow J, Corten H, Srawley J, Heyer R, Wessel E, Irwin G (eds) Progress in flaw growth and fracture toughness testing, ASTM STP 536, pp 231–245
72. Rice JR, Rosengren GF (1968) Plane strain deformation near a crack-tip in a power-law hardening material. J Mech Phys Solids 16:1–12
73. Scheider I, Schödel M, Brocks W, Schönfeld W (2006) Crack propagation analyses with CTOA and cohesive model: Comparison and experimental validation. Eng Fract Mech 73:252–263
74. Schwalbe KH (1995) Introduction of δ5 as an operational definition of the CTOD and its practical use. In Reuter WG, Underwood JH, Newman JC (eds) Fracture mechanics: vol 26, ASTM STP 1256, American Society for Testing and Materials, pp 763–778
75. Schwalbe KH (1998) EFAM ETM 97—the ETM method for assessing the significance of crack-like defects in engineering structures, comprising the versions ETM 97/1 and ETM 97/2. GKSS Research Centre, Geesthacht, Germany
76. Schwalbe KH (1998) The Engineering Flaw Assessment Method (EFAM). Fatigue Fract Eng Mater Struct 21:1203–1213
77. Schwalbe KH, Kim YJ, Hao S, Cornec A, Kocak M (1997) EFAM ETM-MM 96—the ETM method for assessing the significance of crack-like defects in joints with mechanical heterogeneity (strength mismatch). GKSS Report 97/E/9, GKSS Research Centre, Geesthacht, Germany
78. Schwalbe KH, Newman JC, Shannon J (2005) Fracture mechanics testing on specimens with low constraint—standardisation activities within ISO and ASTM. Eng Fract Mech 72:557–576
79. Schwalbe KH, Zerbst U, Brocks W, Cornec A, Heerens J, Amstutz H (1998) The ETM method for assessing the significance of crack-like defects in engineering structures. Fatigue Fract Eng Mater Struct 21:1215–1231
80. Schwalbe KH, Zerbst U (2000) The engineering treatment model. Int J Press Vess Piping 77:905–918
81. Sharma SM, Aravas N (1991) Determination of higher order terms in asymptotic elastoplastic crack tip solutions. J Mech Phys Solids 39:1043–1072
82. Shih CF (1981) Relationships between the J-integral and the crack opening displacement for stationary and extending cracks. J Mech Phys Solids 29:305–326
83. Shih CF (1983) Tables of the Hutchinson-Rice-Rosengren singular field quantities. Report MRL E-147, Brown University, Providence (RI)
84. Shih CF (1985) J-dominance under plane strain fully plastic conditions: the edge crack panel subject to combined tension and bending. Int J Fracture 29:73–84
85. Shih CF, Asaro RJ (1988) Elastic-plastic analysis of cracks on bimaterial interfaces: part I—small scale yielding. J Appl Mech 55:299–316
86. Shih CF, DeLorenzi HG, Andrews WR (1979) Studies on crack initiation and stable crack growth. In: Landes JH, Begley, JA, Clarke GA (eds) Elastic-Plastic Fracture, ASTM STP 668
87. Shih CF, German MD (1985) Requirements for a one parameter characterization of crack tip fields by the HRR-singularity. Int J Fracture 29:73–84
88. Shih CF, Hutchinson JW (1976) Fully plastic solutions and large-scale yielding estimates for plane stress crack problems. J Eng Mat Tech 98:289–295
89. Shih CF, Moran B, Nakamura T (1986) Energy release rate along a three-dimensional crack front in a thermally stressed body. Int J Fracture 30:79–102
90. Siegele D (1989) 3D crack propagation using ADINA. Comp Struct 32:639–645
91. Siegmund T, Brocks W (2000) A numerical study on the correlation between the work of separation and the dissipation rate in ductile fracture. Eng Fract Mech 6:139–154
92. Sumpter JDG (1999) An alternative view of R-curve testing. Eng Fract Mech 64:161–176
93. Tada H, Paris PC, Irwin GR (2000). The stress analysis of cracks handbook, 3rd edn. ASME, doi:10.1115/1.801535

94. Tanaka K (1983) The cyclic J-integral as a criterion for fatigue crack growth. Int J Fract 22:91–104
95. Turner CE (1990) A re-assessment of ductile tearing resistance, Part I: The geometry dependence of J-R curves in fully plastic bending, Part II: Energy dissipation rate and associated R-curves on normalized axes. In: Firrao D (ed) Fracture behaviour and design of materials and structures, vol II, 8th European conference on fracture, Engineering Mechanics Advisory Services, Warley, pp 933–949, 951–968
96. Turner CE, Kolednik O (1994) Application of energy dissipation rate arguments to stable crack growth. Fatigue Fract Eng Mater Struct 20:1109–1127
97. Tvergaard V, Hutchinson JW (1994) Effect of T stress on mode I crack growth resistance in a ductile solid. Int J Solids Struct 31:823–833
98. Wells AA (1961) Unstable crack propagation in metals: cleavage and fast fracture. In: Proceedings of the crack propagation symposium, Cranfield, UK, vol 2, pp 210–230
99. Yuan H, Brocks W (1991) On the J-integral concept for elastic-plastic crack extension. Nucl Eng Design 131:157–173
100. Yuan Y, Brocks W (1998) Quantification of constraint effects in elastic-plastic crack front fields. J Mech Phys Solids 46:219–241
101. Zerbst U, Ainsworth RA, Schwalbe KH (2000) Basic principles of analytical flaw assessment methods. Int J Press Vess Piping 77:855–867
102. Zerbst U, Schödel M, Webster S, Ainsworth R (2007) Fitness-for-service fracture assessment of structures containing cracks. Elsevier, Oxford, UK

Chapter 6
Solutions for Fully Plastic Conditions

Abstract The concept of limit-load analysis is presented which allows for an analytical assessment of the critical load for fully plastic conditions, the "collapse" load, in incremental plasticity. It is suited as approximation of the ultimate load of a structure if instability or fracture can be excluded or as reference load in some fracture assessment procedures. Theorems and extremum principles based on Drucker's postulates of stability have been established which provide upper and lower bounds of the collapse load. Analytical solutions for plane strain plastic flow can be obtained by the method of characteristics. This approach is known as slip line theory and is generally suited for calculating plastic limit loads of fracture mechanics specimens.

The ambiguous nature of the constitutive equations in incremental plasticity does generally not allow for unique solutions of boundary value problems as in elasticity or hyper-elasticity. It is rather necessary to calculate the state of stresses and deformations step by step for a particular loading history. Under the assumption of a perfectly plastic material, however, the final state of fully plastic conditions in a structure does not depend on this history. The corresponding "plastic limit load" (see example in Sect. 3.3.3) is characterised by the feature that plastic deformations increase unboundedly under constant loads. Theorems have been established for determining or at least estimating the respective load without calculating all intermediate steps by extremum principles which provide upper and lower bounds.

Whereas analytical solutions for arbitrary three-dimensional configurations and elastic-plastic materials are basically impossible, the problem of plane strain flow can be described by a system of two first order partial differential equations whose solution is obtained by the method of characteristics. This approach is known as slip line theory and has been successfully applied in metal forming. It is generally suited for calculating plastic limit loads and hence plays also an important role in elastic-plastic fracture mechanics.

W. Brocks, *Plasticity and Fracture*, Solid Mechanics and Its Applications 244,
DOI 10.1007/978-3-319-62752-6_6

6.1 Plastic Collapse and Limit Load Theorems

If the plastic limit load in a perfectly-plastic body is reached, plastic flow is unbounded. For geometrically linear systems, this ultimate state can be regarded as failure state. It is called "plastic collapse" and allows for a simple assessment of the "ultimate load" of an elastic-plastic structure. The latter is defined as the highest load in a sequence of stable equilibrium states which a structure can bear. Geometric instabilities like buckling and unstable crack extension are out of scope, however, and have to be considered in a separate analysis, see e.g. the "two-criteria approach" in Sect. 5.3.4.

The limit load theorems are established by means of Drucker's stability postulates for materials. They are well-known and used for structural assessment in civil engineering [9] but much less among mechanical engineers.

6.1.1 Drucker's Postulates of Stability

The idea of material stability has been introduced into plasticity by Drucker [4, 5] in 1950 and further elaborated in later years [6, 7]. In combination with the conception of yield surfaces, it enabled to generalise phenomena observed in uniaxial tensile tests to multiaxial stress states (Sect. 3.2). This concept is particularly important for inelastic material behaviour: Starting from a stress state on the yield surface, inelastic (permanent) deformations can occur under rising, constant or decreasing stresses. The respective behaviour is called hardening, perfectly plastic or softening. The meaning of the term "stability" is obvious.

Drucker applied the energy criterion of stability to deformable bodies made of inelastic but time-independent material. Starting from an equilibrium state at some time, t_0, of the actual loading path, an arbitrary additional external load ("perturbation") is applied quasi-statically and removed again. The structure is called stable if the work done by the perturbation forces or stresses on the correspondent displacements or strains is positive. This so-called "limited criterion" refers to a fixed initial state. In order to capture instabilities going along with changes of the load, he extended the classical criterion: A perturbation is applied at t_0, which changes the loading path. The structure is called stable if the work of the additional stresses done on the strain differences between the original and the disturbed state are non-negative. This "extended postulate" is a condition for uniqueness rather than a stability criterion. Different from classical criteria, where the perturbations are commonly infinitesimally small, Drucker's postulates also allow for large perturbations.

From these criteria, Drucker [6] derived the definition of stability of materials by excluding all geometrical effects which can significantly affect the structural stability. One may imagine a material cube subject to a homogeneous stress and strain state. The concept serves as indicator for classifying material behaviour according to the known categories of the theory of stability and allows for fundamental

conclusions on the shape of the yield curve and the flow rule [19, 23, 24]. It can be consistently applied to materials as well as to structural elements, components and structures including geometrical effects [2], [21], [22].

Consider an actual and a disturbed path in the stress space, $\sigma_{ij}^{(1)}(t)$ and $\sigma_{ij}^{(2)}(t)$, respectively, for the most general case. The perturbation is finite and applied at time, t_0. Then Drucker's *extended large scale postulate* requires,

$$\int_{t_0}^{t_0+\Delta t} \left(\sigma_{ij}^{(2)} - \sigma_{ij}^{(1)}\right)\left(\dot{\varepsilon}_{ij}^{(2)} - \dot{\varepsilon}_{ij}^{(1)}\right) dt > 0. \tag{6.1}$$

The *small scale postulate* follows from a Taylor expansion for an infinitesimally neighbouring state,

$$\left(\dot{\sigma}_{ij}^{(2)} - \dot{\sigma}_{ij}^{(1)}\right)\left(\dot{\varepsilon}_{ij}^{(2)} - \dot{\varepsilon}_{ij}^{(1)}\right) > 0. \tag{6.2}$$

If the state (1) is time independent, $\sigma_{ij}^{(1)}(t) = \sigma_{ij}^{(1)}(t_0) = \sigma_{ij}^0$ and $\dot{\varepsilon}_{ij}^{(1)} = 0$, one obtains the *limited postulates*. Omitting superscript (2), $\sigma_{ij}^{(2)} = \sigma_{ij}$, the *large scale postulate*,

$$\int_{t_0}^{t_0+\Delta t} \left(\sigma_{ij} - \sigma_{ij}^0\right) \dot{\varepsilon}_{ij}\, dt > 0, \tag{6.3}$$

and the *small-scale postulate*,

$$\dot{\sigma}_{ij}\, \dot{\varepsilon}_{ij} = \dot{\sigma}_{ij}\left(\dot{\varepsilon}_{ij}^{\mathrm{e}} + \dot{\varepsilon}_{ij}^{\mathrm{p}}\right) > 0, \tag{6.4}$$

can be derived from Eqs. (6.1) and (6.2), respectively.

These postulates apply to monotonic loading. Additionally, Drucker considered loading cycles during which perturbations, $\sigma_{ij}(t)$, of a fixed initial state, σ_{ij}^0, meeting the yield condition, $\Phi\left(\sigma_{ij}^0\right) \leq 0$, are applied and removed, again. The work done during this cycle has to be non-negative for a stable material, that is

$$\left(\sigma_{ij} - \sigma_{ij}^0\right) \dot{\varepsilon}_{ij}^{\mathrm{p}} \geq 0, \quad \Phi\left(\sigma_{ij}^0\right) \leq 0 \tag{6.5}$$

for a *large-scale cycle* and

$$\dot{\sigma}_{ij}\, \dot{\varepsilon}_{ij}^{\mathrm{p}} \geq 0. \tag{6.6}$$

for a *small-scale cycle*. These postulates are only relevant for inelastic material behaviour, because the elastic deformations are reversible and hence, the respective work done during a cycle vanishes. If the initial state is a "safe", i.e. elastic state, $\sigma_{ij}^{0} = \sigma_{ij}^{(s)}$ with $\Phi\left(\sigma_{ij}^{(s)}\right) < 0$, then Eq. (6.5) for a large-scale cycle yields

$$\left(\sigma_{ij} - \sigma_{ij}^{(s)}\right) \dot{\varepsilon}_{ij}^{p} > 0, \quad \Phi\left(\sigma_{ij}^{(s)}\right) < 0. \tag{6.7}$$

A small-scale loading cycle in a perfectly plastic material results in

$$\dot{\sigma}_{ij}\, \dot{\varepsilon}_{ij}^{p} = 0. \tag{6.8}$$

The postulate of Eq. (6.5) is also known as Prager's minimum principle [25] and represents the fundamental relation for the proof of the limit theorems of plasticity [8]. Materials complying this postulate have convex yield surfaces and the plastic strain rates are normal to the yield surface, Eq. (3.12), see Phillips and Sierakowski [24], Justusson and Phillips [19]. The latter is also known as normality rule or associated flow rule.

Drucker's postulates differ in rigorousness. The most severe restriction follows from Eq. (6.1) for finite perturbations. All others can be derived from it by reducing some restrictions, but they are not necessarily equivalent and do not follow any hierarchy. A material exhibiting an upper yield point is locally softening beyond it and hence violates the postulate Eq. (6.6) for a small cycle, but it may meet Eq. (6.5) for a large cycle [23]. The postulates of Eqs. (6.2) and (6.4) impose the least restrictions, where Eq. (6.4) is the classical stability criterion and eq. (6.2) a condition for bifurcation of equilibrium [2].

6.1.2 *Plastic Limit State (Collapse): Definitions and Theorems*

Whereas the ultimate load is generally also affected by geometrically non-linear behaviour, the definition of the plastic limit load disregards geometrical effects and the balance equations are established with respect to the undeformed configuration.

Definition (I) The plastic limit state of a structure of perfectly-plastic material, denoted by a subscript or superscript "pl", is the state in which for the first time in the loading history the displacements, u_i, can increase under constant external forces, if geometrical changes are disregarded,

$$\dot{u}_i^{(\mathrm{pc})} \neq 0 \quad \text{for} \quad \begin{cases} \dot{f}_j = 0 & \text{in } V \\ \dot{t}_j = 0 & \text{on } \partial V \end{cases}, \tag{6.9}$$

where $\dot{u}_i^{(\mathrm{pc})}$ is the velocity field of the collapse mechanism, f_j are the volume forces (like weight) and t_j the surface forces (like pressure) acting on the body.

Since the plastic limit state is a state of equilibrium, the principle of virtual work,

$$\int_{\partial V} t_j^{\mathrm{pl}} \delta u_j \, dS + \int_V f_j^{\mathrm{pl}} \delta u_j \, dV = \int_V \sigma_{ij}^{\mathrm{pl}} \delta \varepsilon_{ij} \, dV, \tag{6.10}$$

holds. The virtual displacement and strain fields, δu_i and $\delta \varepsilon_{ij}$, have to be kinematically admissible, i.e. fulfil the geometrical boundary conditions and the compatibility conditions. These conditions are of course met by the actual velocity field of the limit state, that is by the collapse mechanism,

$$\delta u_j = \dot{u}_j^{(\mathrm{pc})} \Delta t, \quad \delta \varepsilon_{ij} = \dot{\varepsilon}_{ij}^{(\mathrm{pc})} \Delta t = \frac{1}{2}\left(\dot{u}_{i,j}^{(\mathrm{pc})} + \dot{u}_{j,i}^{(\mathrm{pc})}\right) \Delta t, \tag{6.11}$$

and Eq. (6.10) can be written as

$$\int_{\partial V} t_j^{\mathrm{pl}} \dot{u}_j^{(\mathrm{pc})} \, dS + \int_V f_j^{\mathrm{pl}} \dot{u}_j^{(\mathrm{pc})} \, dV = \int_V \sigma_{ij}^{\mathrm{pl}} \dot{\varepsilon}_{ij}^{(\mathrm{pc})} \, dV. \tag{6.12}$$

According to definition (I) and the decomposition of strain rates, Eq. (3.7),

$$0 = \int_{\partial V} \dot{t}_j \dot{u}_j^{(\mathrm{pc})} \, dS + \int_V \dot{f}_j \dot{u}_j^{(\mathrm{pc})} \, dV = \int_V \dot{\sigma}_{ij} \dot{\varepsilon}_{ij}^{(\mathrm{pc})} \, dV = \int_V \dot{\sigma}_{ij} \dot{\varepsilon}_{ij}^{(\mathrm{pc})\mathrm{e}} \, dV + \int_V \dot{\sigma}_{ij} \dot{\varepsilon}_{ij}^{(\mathrm{pc})\mathrm{p}} \, dV. \tag{6.13}$$

holds for an infinitesimal change of state. The postulate of Eq. (6.4) requires that $\dot{\sigma}_{ij} = 0$ and Hooke's law yields $\dot{\varepsilon}_{ij}^{(\mathrm{pc})\mathrm{e}} = 0$ for the elastic part of the strains. Different from frequent statements in the literature, the limit load theorems do not require the assumption of a rigid-plastic material behaviour. Elastic deformation rates vanish as a natural outcome of definition (I).

Theorem (I) If the plastic limit load (collapse load) is reached, stresses remain constant, $\dot{\sigma}_{ij} = 0$, and the elastic strain rates vanish, $\dot{\varepsilon}_{ij}^{(\mathrm{pc})\mathrm{e}} = 0$. Only plastic strain rates and deformation rates appear, $\dot{\varepsilon}_{ij}^{(\mathrm{pc})} = \dot{\varepsilon}_{ij}^{(\mathrm{pc})\mathrm{p}}$, $\dot{u}_i^{(\mathrm{pc})} = \dot{u}_i^{(\mathrm{pc})\mathrm{p}}$.

Any solution of a mechanical boundary value problem has to satisfy equilibrium equations (or principle of virtual work), physical and kinematic boundary conditions, compatibility conditions and constitutive equations. States complying with a less number of these conditions are easier to determine, but some show significant characteristics, nevertheless.

Definition (II) A stress state is called *statically admissible*, $\sigma_{ij}^{(\mathrm{sa})}$, if it satisfies the equilibrium conditions, $\sigma_{ij,i}^{(\mathrm{sa})} + f_j = 0$, within the volume V, the physical boundary conditions, $n_i \sigma_{ij,i}^{(\mathrm{sa})} = t_j$, on its boundary ∂V and the yield condition, $\Phi\left(\sigma_{ij}^{(\mathrm{sa})}\right) \leq 0$ in V. It is called statically admissible and safe, $\sigma_{ij}^{(\mathrm{s})}$, if $\Phi\left(\sigma_{ij}^{(\mathrm{s})}\right) < 0$.

The existence of a safe stress state for a particular load level guarantees that the structure does not fail by plastic collapse, independent of whether or not the respective stress distribution is "real". It will in general not meet the flow rule, Eq. (3.12).

Theorem (II) Static theorem As long as a statically admissible and safe stress distribution, $\sigma_{ij}^{(\mathrm{s})}$, can be found at every load level, no collapse occurs under the respective load.

As long as no collapse occurs, a statically admissible and safe stress distribution, $\sigma_{ij}^{(\mathrm{s})}$, can be found at every load level.

The existence of a collapse mechanism $\dot{u}_i^{(\mathrm{c})}$, even though a statically admissible and safe stress distribution $\sigma_{ij}^{(\mathrm{s})}$ can be found, would contradict Drucker's postulate, Eq. (6.6).

Definition (II) A velocity field is called kinematically possible (collapse mechanism), $\dot{u}_i^{(\mathrm{k})}$, if it satisfies the geometrical boundary conditions on ∂V and the incompressibility condition, $\dot{\varepsilon}_{ii}^{(\mathrm{k})} = \dot{u}_{i,i}^{(\mathrm{k})} = 0$, i.e. $\dot{\varepsilon}_{ij}^{(\mathrm{k})\mathrm{p}} = \dot{\varepsilon}_{ij}^{(\mathrm{k})} = \frac{1}{2}\left(\dot{u}_{i,j}^{(\mathrm{k})} + \dot{u}_{j,i}^{(\mathrm{k})}\right)$ in V and if the stresses resulting from the flow rule, $\dot{\varepsilon}_{ij}^{(\mathrm{k})} = \dot{\lambda}_{\mathrm{p}} \partial \Phi / \partial \sigma_{ij}$, meet the yield condition, $\Phi\left(\sigma_{ij}^{(\mathrm{k})}\right) \leq 0$.

This collapse mechanism indicates that a load level at or beyond the plastic limit load is reached.

Theorem (II) Kinematic theorem If a kinematically possible (collapse) mechanism, $\dot{u}_i^{(\mathrm{k})}$, can be found at some load level for which the equilibrium condition is violated,

$$\int_{\partial V} t_j \dot{u}_j^{(\mathrm{k})}\, dS + \int_V f_j \dot{u}_i^{(\mathrm{k})}\, dV > \int_V \sigma_{ij}^{(\mathrm{k})} \dot{\varepsilon}_{ij}^{(\mathrm{k})}\, dV,$$

the structure cannot bear this load any more.

If a kinematically possible (collapse) mechanism, $\dot{u}_i^{(\mathrm{k})}$, can be found at some load level for which the equilibrium condition is satisfied,

$$\int_{\partial V} t_j \dot{u}_j^{(\mathrm{k})}\, dS + \int_V f_j \dot{u}_i^{(\mathrm{k})}\, dV = \int_V \sigma_{ij}^{(\mathrm{k})} \dot{\varepsilon}_{ij}^{(\mathrm{k})}\, dV,$$

collapse of the structure will occur under this load.

The first part of this theorem follows again from proving a contradiction to Drucker's postulate, Eq. (6.6), if a safe stress state, $\sigma_{ij}^{(\mathrm{s})}$, is assumed. Assuming a statically admissible stress field, $\sigma_{ij}^{(\mathrm{sa})}$, does not implicate any contradiction.

The theorems (II) and (III) immediately result in

Theorem IV If a statically admissible stress state, $\sigma_{ij}^{(\mathrm{sa})}$, and a kinematic possible collapse mechanism, $\dot{u}_i^{(\mathrm{k})}$, can be found for some load, then this load is the plastic limit load of the structure, $\sigma_{ij}^{(\mathrm{sa})} = \sigma_{ij}^{(\mathrm{k})} = \sigma_{ij}^{\mathrm{pl}}$, and $\dot{u}_i^{(\mathrm{k})} = \dot{u}_i^{(\mathrm{pc})}$

Some immediately evident conclusions of these theorems are

- Adding (weightless) material cannot degrade the plastic limit load;
- Removing (weightless) material cannot increase the plastic limit load;
- Increasing the yield stress in some part cannot increase the plastic limit load;
- Residual stresses, $\tilde{\sigma}_{ij}$, do not affect the plastic limit load as they are self balanced, $\int_V \tilde{\sigma}_{ij} \dot{\varepsilon}_{ij}\, dV = 0$.

So far, continuous stress and displacement fields have been implicitly assumed. A generalisation to discontinuous fields is based on the argument that any discontinuities in a continuum are merely large gradients of the respective field in a thin layer. An example of a "discontinuous" stress field for generating a statically admissible stress state is given below. Discontinuous displacement fields

constituting kinematically possible mechanisms can be devised with the slip-line theory (see Sect. 6.2).

The application of the theorems is simplified if they are specialised to proportional loading. Volume forces are neglected, $f_j = 0$, as they cannot be applied proportionally. Surface forces are assumed to increase proportionally, $t_j = \zeta t_j^0$, $\zeta \geq 0$, with t_j^0 as a fixed reference distribution sufficiently below plastic collapse . According to definition (II), $\zeta_{sa} > 1$ denotes a statically admissible load factor, $t_j^{(sa)} = \zeta_{sa} t_j^0$, and $\zeta_s > 1$ a (statically admissible and) safe load factor, $t_j^{(s)} = \zeta_s t_j^0$. As in definition (III), $\zeta_k > 1$ is a load factor, $t_j^{(k)} = \zeta_k t_j^0$, which goes along with a kinematically possible collapse mechanism, and $\zeta_{pl} > 1$ is the plastic limit load factor, $t_j^{pl} = \zeta_{pl} t_j^0$.

With these definitions, the limit load theorems take the form

Theorem (IIa) Static theorem, lower bound The plastic limit load factor is the largest statically admissible load factor, $\zeta_s < \zeta_{sa} \leq \zeta_{pl}$

and

Theorem (IIIa) Kinematic theorem, upper bound The plastic limit load factor is the smallest load factor belonging to a kinematically possible mechanism, $\zeta_k \geq \zeta_{pl}$

In summary, the plastic limit load factor is confined as follows,

$$\zeta_s < \zeta_{sa} \leq \zeta_{pl} \leq \zeta_k. \tag{6.14}$$

The problem of determining the plastic limit load is reduced to finding sufficiently close upper and lower bounds according to the definitions given above.

6.2 Example of a Statically Admissible Stress Field

Definition (II) and the static theorem (IIa) of Sect. 6.1.2 are applied to find a lower bound of the plastic limit load for the flat notched tensile bar shown in Fig. 6.1a. The simplest assumption is that the net section stress, σ_{net}, that is the nominal tensile stress in the narrowest section, $W - a$, reaches the yield strength, R_0, and hence $\sigma_\infty^{(sa)} = R_0(W - a)/W \leq \sigma_\infty^{pl}$. This corresponds to a homogeneous uniaxial stress state and is equivalent to the assumption of a plane stress state together with Tresca's yield condition as will be shown below.

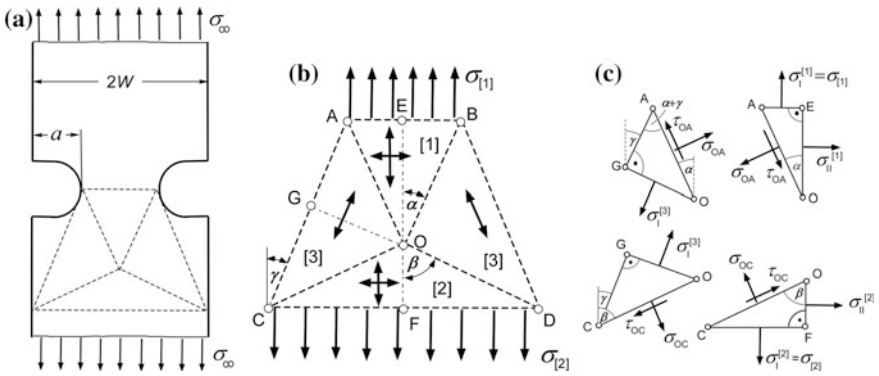

Fig. 6.1 Flat notched tensile bar **a** and trapezoidal stress discontinuity field **b** with homogeneous segments **c**

However, the stress state in the smallest section is bi-axial (in plane stress) or triaxial (in plane strain), which allows for normal stresses higher than the yield strength and increases the limit load. This effect is called plastic constraint, and the ratio

$$L_{\mathrm{pl}} = \frac{\sigma_{\mathrm{net}}^{\mathrm{pl}}}{R_0} = \frac{\sigma_{\infty}^{\mathrm{pl}}}{R_0}\frac{W}{W-a} \geq 1, \tag{6.15}$$

is called plastic constraint factor.

A statically admissible stress state accounting for the biaxiality of the stress state can be realised by means of a simple trapezoidal discontinuity field displayed in Fig. 6.1b, which consist of homogeneous segments, see Burth and Brocks [3]. The stress field is discontinuous along the lines OA, OB, OC, OD, and only normal and shear stresses, σ and τ, are continuous. The stress states in the segments [1, 2, 3] are:

[1] Triangle AOB is subject to principle stresses $\sigma_{\mathrm{I}}^{[1]} = \sigma_{[1]}$ and $\sigma_{\mathrm{II}}^{[1]} < \sigma_{\mathrm{I}}^{[1]}$;

[2] Triangle COD is subject to principle stresses $\sigma_{\mathrm{I}}^{[2]} = \sigma_{[2]} = \sigma_{\infty}$ and $\sigma_{\mathrm{II}}^{[2]} < \sigma_{\mathrm{I}}^{[2]}$;

[3] Triangles AOC and BOD are under uniaxial tension $\sigma_{\mathrm{I}}^{[3]}$ parallel to the edges AC and BD, respectively.

They fulfil the physical boundary conditions. Overall equilibrium and theorem (IIa) state that

$$\sigma_{\infty}^{(\mathrm{sa})} = \sigma_{[2]}^{(\mathrm{sa})} = \frac{W-a}{W}\sigma_{[1]}^{(\mathrm{sa})} \leq \sigma_{\infty}^{\mathrm{pl}}. \tag{6.16}$$

The trapezium is defined by the base and top edges, $\overline{\mathrm{CD}} = 2W$ and $\overline{\mathrm{AB}} \approx 2(W-a)$, the latter holding for small notch radii, and three angles, α, β, γ, with

$$\frac{W-a}{\tan\alpha}+\frac{W}{\tan\beta}=\frac{a}{\tan\gamma}. \tag{6.17}$$

The angles have to be identified such that the highest statically admissible load, $\left[\sigma_{[2]}^{(sa)}\right]_{max}$, is achieved, which provides the best approach to the plastic limit. The stress state must satisfy the equilibrium conditions along OA and OC, Fig. 6.1c,

$$\begin{aligned}
\sigma_{OA} &= \sigma_I^{[1]}\sin^2\alpha+\sigma_{II}^{[1]}\cos^2\alpha=\sigma_I^{[3]}\sin^2(\alpha+\gamma)\\
\tau_{OA} &= \left(\sigma_I^{[1]}-\sigma_{II}^{[1]}\right)\sin\alpha\,\cos\alpha=\sigma_I^{[3]}\sin(\alpha+\gamma)\cos(\alpha+\gamma)\\
\sigma_{OC} &= \sigma_I^{[2]}\sin^2\beta+\sigma_{II}^{[2]}\cos^2\beta=\sigma_I^{[3]}\sin^2(\beta-\gamma)\\
\tau_{OC} &= \left(\sigma_I^{[2]}-\sigma_{II}^{[2]}\right)\sin\beta\,\cos\beta=\sigma_I^{[3]}\sin(\beta-\gamma)\cos(\beta-\gamma)
\end{aligned}, \tag{6.18}$$

resulting in

$$\begin{aligned}
\sigma_I^{[1]} &= \sigma_I^{[3]}\frac{\sin(\alpha+\gamma)\cos\gamma}{\sin\alpha}\\
\sigma_{II}^{[1]} &= \sigma_I^{[3]}\frac{\sin(\alpha+\gamma)\sin\gamma}{\cos\alpha}\\
\sigma_I^{[2]} &= \sigma_I^{[3]}\frac{\sin(\beta-\gamma)\cos\gamma}{\sin\beta}\\
\sigma_{II}^{[2]} &= \sigma_I^{[3]}\frac{\sin(\beta-\gamma)\sin\gamma}{\cos\beta}
\end{aligned}. \tag{6.19}$$

The yield conditions of Tresca, Eq. (3.20), and von Mises, Eq. (3.28), depend on the stress state, i.e. plane stress or plane strain, Fig. 6.2.

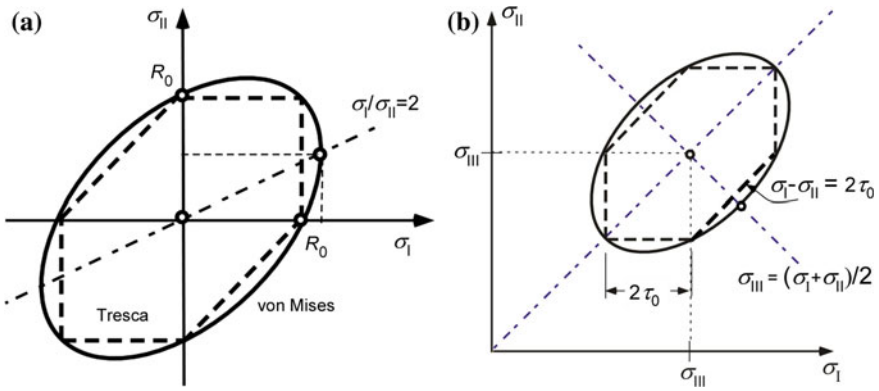

Fig. 6.2 Yield surfaces of von Mises and Tresca in the (σ_I,σ_{II})-plane for **a** plane stress and **b** conditions

- Plane stress and Tresca's criterion:

$$\begin{array}{ll} [1]\ \text{AOB}: & \sigma_{\mathrm{I}}^{[1]} \le 2\tau_0^{\mathrm{T}} = R_0 \\ [2]\ \text{COD}: & \sigma_{\mathrm{I}}^{[2]} \le 2\tau_0^{\mathrm{T}} = R_0\,; \\ [3]\ \text{AOC, BOD}: & \sigma_{\mathrm{I}}^{[3]} \le 2\tau_0^{\mathrm{T}} = R_0 \end{array} \tag{6.20}$$

Since $\sigma_{\mathrm{I}}^{[2]} < \sigma_{\mathrm{I}}^{[1]}$, Eq. (6.16), the yield condition for segment [1] is more stringent than that for segment [2]. The condition $\sigma_{\mathrm{I}}^{[3]} \le \sigma_{\mathrm{I}}^{[1]}$ and Eq. $(6.18)_1$ require that $\alpha \le \pi/2 - \gamma$. The premise of a plane stress state in combination with Tresca's yield condition is equivalent to the assumption that the normal stresses in the narrowest section, like in a smooth tensile bar, cannot exceed the yield strength, R_0.

- Plane stress and von Mises' criterion:

$$\begin{array}{ll} [1]\ \text{AOB}: & \left(\sigma_{\mathrm{I}}^{[1]}\right)^2 - \sigma_{\mathrm{I}}^{[1]}\sigma_{\mathrm{II}}^{[1]} + \left(\sigma_{\mathrm{II}}^{[1]}\right)^2 \le R_0^2 \\ [2]\ \text{COD}: & \left(\sigma_{\mathrm{I}}^{[2]}\right)^2 - \sigma_{\mathrm{I}}^{[2]}\sigma_{\mathrm{II}}^{[2]} + \left(\sigma_{\mathrm{II}}^{[2]}\right)^2 \le R_0^2 \\ [3]\ \text{AOC, BOD}: & \sigma_{\mathrm{I}}^{[3]} \le R_0 \end{array} \tag{6.21}$$

Segment [1] is determinant, again. The highest value which σ_{I} can take in the von Mises ellipse, Fig. 6.2a, is,

$$\left[\sigma_{[\mathrm{I}]}^{(\mathrm{sa})}\right]_{\max}^{\mathrm{vM,pl.stress}} = \left[\sigma_{\mathrm{I}}^{[1]}\right]_{\max} = \left(2\Big/\sqrt{3}\right)R_0 > \left[\sigma_{[\mathrm{I}]}^{(\mathrm{sa})}\right]_{\max}^{\mathrm{T,pl.stress}}. \tag{6.22}$$

The correspondent value of the second principal stress fulfilling the yield condition is $\sigma_{\mathrm{II}}^{[1]} = \left(1/\sqrt{3}\right)R_0$. The yield criterion for segment [3], Eq. $(6.21)_3$ and Eq. (6.19) provide the side condition

$$\cos^2\gamma \le 2\left(1 - 1\Big/\sqrt{3}\right), \tag{6.23}$$

that is $\gamma \ge 23°$.

A plane stress state is a lower limit for thin specimens. The upper limit for specimens of finite thickness is a plane strain state.

- Plane strain and von Mises or Tresca criterion, respectively, Fig. 6.2b.

$$\begin{array}{ll} [1]\ \text{AOB}: & \sigma_{\mathrm{I}}^{[1]} - \sigma_{\mathrm{II}}^{[1]} \le 2\tau_0 \\ [2]\ \text{COD}: & \sigma_{\mathrm{I}}^{[2]} - \sigma_{\mathrm{II}}^{[21} \le 2\tau_0\,, \\ [3]\ \text{AOC, BOD}: & \sigma_{\mathrm{I}}^{[3]} \le 2\tau_0 \end{array} \tag{6.24}$$

with the shear strength,

$$\tau_0 = \begin{cases} \tau_0^{\mathrm{T}} = R_0/2 & \text{Tresca} \\ \tau_0^{\mathrm{vM}} = R_0/\sqrt{3} & \text{von Mises} \end{cases}, \tag{6.25}$$

according to Eqs. (3.21) and (3.30), respectively. The principal stresses in the segments [I] and [II] are proportional to $\sigma_{\mathrm{I}}^{[3]}$, Eq. (6.19), whose greatest value is $2\tau_0$. This results in the conditions,

$$\begin{array}{ll} [1]\ \text{AOB:} & \tan 2\alpha \geq \cot\gamma \\ [2]\ \text{COD:} & \sin 2\gamma/\sin 2\beta \geq 0 \end{array}. \tag{6.26}$$

The condition of Eq. (6.26) for segment [2] is met for all $0 \leq \gamma < \beta \leq \pi/2$, and the condition for segment [1] requires $\alpha \geq \pi/4 - \gamma/2$. In order to get the greatest value of $\sigma_{\mathrm{I}}^{[1]}$ in Eq. $(6.19)_1$, the smallest value $\alpha = \pi/4 - \gamma/2$ has to be taken, and finally

$$1.39 \leq \frac{\left[\sigma_{[\mathrm{I}]}^{(\mathrm{sa})}\right]_{\max}^{\text{pl.strain}}}{2\tau_0} = \cos^2\gamma\left[1 + \frac{\tan\gamma}{\tan(\pi/4 - \gamma/2)}\right] < 1.71 \tag{6.27}$$

is obtained, where $23° \leq \gamma < 45°$ depends on a/W and is determined from an extremum condition. As the right-hand side of Eq. (6.27) is monotonously increasing with γ, the greatest value of $\gamma < \pi/4$ which for a given a/W still yields a value $\beta < \pi/2$ in Eq. (6.15) provides the closest approximation to the plastic limit load. Figure 6.3 shows the angle α and corresponding values of β for increasing a/W in dependence on γ. Solutions exist only for deeply notched bars, $a/W \geq 0.4$.

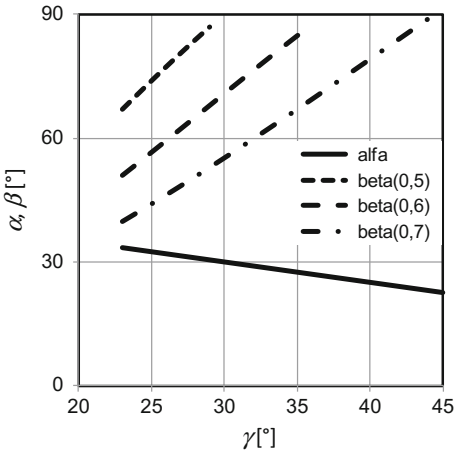

Fig. 6.3 Geometry of the statically admissible trapezoidal stress discontinuity field shown in Fig. 6.1b for plane strain states: angles α and $\beta(a/W)$

6.3 Slip Line Theory

The boundary value problem of plane plastic flow can be described by a system of coupled partial differential equations of hyperbolic type whose characteristics, the "slip lines", are lines of maximum shear stresses and shear strain rates and represent kinematically possible velocity fields according to definition (II) in Sect. 6.1.2. The construction of respective fields for specific boundary conditions provides solutions for upper bounds of the stress states under fully plastic conditions.

6.3.1 Basic Equations for Plane-Strain Conditions

In a perfectly plastic body under plane strain conditions, $\dot{\varepsilon}_{zz} = \dot{\varepsilon}_{xz} = \dot{\varepsilon}_{yz} = 0$, a two-dimensional velocity field of yielding, $\dot{u}_x(x, y)$, $\dot{u}_y(x, y)$, $\dot{u}_z = 0$, with purely plastic strain rates,

$$\dot{\varepsilon}_{ij} = \dot{\varepsilon}_{ij}^{\mathrm{p}} = \frac{1}{2}\left(\dot{u}_{i,j} + \dot{u}_{j,i}\right), \tag{6.28}$$

$(i, j) \hat{=} (x, y)$, $\dot{u}_{i,j} \doteq \partial u_i / \partial x_j$, arises at sufficiently high loading. No shear stresses σ_{xz} and σ_{yz} exist and the stress state can be entirely described by the superposition of the hydrostatic mean normal stress,

$$\hat{\sigma} = \sigma_{zz} = \frac{1}{2}\left(\sigma_{xx} + \sigma_{yy}\right) = \frac{1}{2}(\sigma_{\mathrm{I}} + \sigma_{\mathrm{II}}), \tag{6.29}$$

and the maximum shear stress,

$$\tau_{\mathrm{m}} = \frac{1}{2}\sqrt{\left(\sigma_{xx} - \sigma_{yy}\right)^2 + 4\sigma_{xy}^2} = \tau_0, \tag{6.30}$$

where the latter has to meet the yield condition with τ_0 according to Eq. (6.25). Whereas only maximum and minimum principal stresses, σ_{I}, σ_{II}, affect Tresca's condition, Eq. (3.20), the condition of von Mises, Eq. (3.28), includes also the mean principal stress, σ_{III}, see Fig. 6.2b. The principal stresses become

$$\begin{aligned} \sigma_{\mathrm{I}} &= \hat{\sigma} + \tau_{\mathrm{m}} = \hat{\sigma} + \tau_0 \\ \sigma_{\mathrm{II}} &= \hat{\sigma} - \tau_{\mathrm{m}} = \hat{\sigma} - \tau_0 \\ \sigma_{\mathrm{III}} &= \hat{\sigma} \end{aligned} . \tag{6.31}$$

see Mohr's circle in Fig. 6.4.

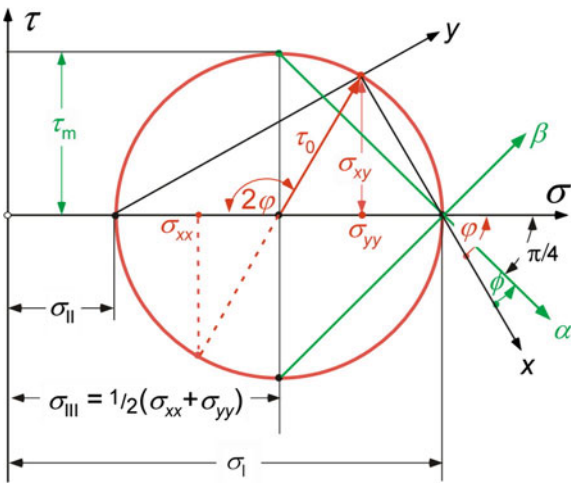

Fig. 6.4 Mohr's circle for a plane-strain state

The equilibrium conditions,

$$\begin{aligned} \sigma_{xx,x} + \sigma_{xy,y} &= 0 \\ \sigma_{xy,x} + \sigma_{yy,y} &= 0 \end{aligned}, \tag{6.32}$$

and the yield condition, Eq. (6.30), provide three equations for three stress components. Elimination of the stress σ_{yy} by means of Eq. (6.30) yields a system of two coupled quasilinear first order partial differential equations,

$$\begin{aligned} &\sigma_{xx,x} + \sigma_{xy,y} = 0 \\ &\sigma_{xx,y} + \sigma_{xy,x} \pm \frac{2\sigma_{xy}}{\sqrt{\tau_0^2 - \sigma_{xy}^2}} \sigma_{xy,y} = 0 \end{aligned}, \tag{6.33}$$

which can be converted to one second order differential equation

$$\sigma_{xy,xx} - \sigma_{xy,yy} \pm \frac{2\sigma_{xy}}{\sqrt{\tau_0^2 - \sigma_{xy}^2}} \sigma_{xy,yx} = 0. \tag{6.34}$$

The solution depends on its type. If it can be integrated for specified stress boundary conditions, the yield state is statically determined, and the velocity field can be calculated by means of the flow rule.

6.3.2 *Cauchy's Initial Value Problem*

The general form of a quasi-linear second order partial differential equation of a function $v(x,y)$ is

$$\begin{aligned} c_0(x,y,v,v_x,v_y)v_{xx} + 2c_1(x,y,v,v_x,v_y)v_{xy} + c_2(x,y,v,v_x,v_y)v_{yy} \\ = r(x,y,v,v_x,v_y) \end{aligned} . \tag{6.35}$$

The behaviour of its solution, hyperbolic, parabolic or elliptic, depends on the sign of the discriminant,

$$D = c_1^2 - c_0 c_2 \begin{cases} > 0 & \text{hyperbolic} \\ = 0 & \text{parabolic} \\ < 0 & \text{elliptic} \end{cases} . \tag{6.36}$$

Cauchy's initial value problem intends to find a surface, $v(x, y)$, passing through an arbitrary curve, $\mathcal{C}_0$, in the three-dimensional space, $\{x, y, v\}$, which is defined by initial values,

$$v(x(s), y(s)) = \hat{v}(s) \quad \text{along} \quad \mathcal{C}_0 : [x(s), y(s)]. \tag{6.37}$$

The function $\hat{v}(s)$ is assumed as being continuously differentiable. Its derivatives tangential and normal to $\mathcal{C}_0$ are,

$$\begin{aligned} \hat{v}_t(s) &\doteq \frac{d\hat{v}}{ds} = \frac{d\hat{v}}{dx}\frac{dx}{ds} + \frac{d\hat{v}}{dy}\frac{dy}{ds} = \hat{v}_x x_s + \hat{v}_y y_s \\ \hat{v}_n(s) &\doteq \frac{d\hat{v}}{dn} = \frac{d\hat{v}}{dx}\frac{dx}{dn} + \frac{d\hat{v}}{dy}\frac{dy}{dn} = -\hat{v}_x y_s + \hat{v}_y x_s \end{aligned} , \tag{6.38}$$

where $d()/ds = ()_s$.

This is a linear system of equations for the two partial derivatives, $\hat{v}_x(s)$, $\hat{v}_y(s)$, which has a unique solution for $x_s^2 + y_s^2 > 0$, and Eqs. (6.37) and (6.38) thus determine an infinitesimal band of $v(x, y)$. A continuation of this band to a full solution may be tried by a Taylor expansion. Three linear equations,

$$\begin{aligned} x_s \hat{v}_{xx} + y_s \hat{v}_{yx} &= \hat{v}_{t,x}(s) \\ x_s \hat{v}_{xy} + y_s \hat{v}_{yy} &= \hat{v}_{t,y}(s) \\ c_0 \hat{v}_{xx} + 2c_1 \hat{v}_{xy} + c_2 \hat{v}_{yy} &= r(s) \end{aligned} . \tag{6.39}$$

are available for the second partial derivatives. A unique solution requires that the determinant,

$$\Delta = \begin{vmatrix} x_s & y_s & 0 \\ 0 & x_s & y_s \\ c_0 & 2c_1 & c_2 \end{vmatrix} = c_0 y_s^2 - 2c_1 x_s y_s + c_2 x_s^2, \tag{6.40}$$

does not vanish. If $\Delta \neq 0$ holds for all points of $\mathcal{C}_0$, the Cauchy problem has a unique solution.

For $\Delta = 0$, either no solution at all or more than one solution for the second derivatives exist, depending on the right hand side of Eq. (6.38). Curves $\mathcal{C}_0$ along which $\Delta = 0$, that is,

$$c_0 y'^2 - 2c_1 y' + c_2 = 0, \tag{6.41}$$

$y' = y_s/x_s$, are of particular interest. This ordinary differential equation is called "characteristic differential equation" and its solutions are "characteristics". The quadratic Eq. (6.41) has the solutions,

$$y'_{1,2}(x) = \frac{c_1 \pm \sqrt{c_1^2 - c_0 c_2}}{c_0} \tag{6.42}$$

which are governed by the discriminant, Eq. (6.36), in particular

- two real families of characteristics exist for hyperbolic differential equations, $D > 0$,
- one real family of characteristics exists for parabolic differential equations, $D = 0$,
- two complex families of characteristics exist for elliptic differential equations, $D < 0$.

6.3.3 The Characteristics of Plane Strain Flow

If initial conditions

$$\begin{aligned} \sigma_{xx}(x(s), y(s)) &= \widehat{\sigma}_{xx}(s) \\ \sigma_{xy}(x(s), y(s)) &= \widehat{\sigma}_{xy}(s) \end{aligned} \tag{6.43}$$

with continuous derivatives

$$\begin{aligned} \widehat{\sigma}_{xx,s} &= \sigma_{xx,x} x_s + \sigma_{xx,y} y_s \\ \widehat{\sigma}_{xy,s} &= \sigma_{xy,x} x_s + \sigma_{xy,y} y_s \end{aligned}, \tag{6.44}$$

are given along some curve $\mathcal{C}_0$, the partial derivatives $\widehat{\sigma}_{xx,x}$, $\widehat{\sigma}_{xx,y}$, $\widehat{\sigma}_{xy,x}$, $\widehat{\sigma}_{xy,y}$ on $\mathcal{C}_0$ can be calculated provided that the determinant

$$\Delta = \begin{vmatrix} x_s & y_s & 0 & 0 \\ 0 & 0 & x_s & y_s \\ 1 & 0 & 0 & 0 \\ 0 & 1 & 1 & \pm\frac{2\sigma_{xy}}{\sqrt{\tau_0^2-\sigma_{xy}^2}} \end{vmatrix} \tag{6.45}$$

is non-zero. The correspondent characteristic equation,

$$y'^2 \mp \frac{2\sigma_{xy}}{\sqrt{\tau_0^2 - \sigma_{xy}^2}} y' - 1 = 0, \tag{6.46}$$

is hyperbolic, and its solutions,

$$\begin{aligned} y_1' &= \frac{\pm\sigma_{xy} + \tau_0}{\sqrt{\tau_0^2 - \sigma_{xy}^2}} = \tan\phi \\ y_2' &= \frac{\pm\sigma_{xy} - \tau_0}{\sqrt{\tau_0^2 - \sigma_{xy}^2}} = \tan(\phi + \frac{\pi}{2}) \end{aligned} . \tag{6.47}$$

provide the direction fields of two families of orthogonal characteristics, which physically represent lines of maximum shear stresses or maximum shear rates, called slip lines. The angle ϕ signifies the direction of maximum shear stresses,

$$\phi = \varphi \pm \frac{\pi}{4}. \tag{6.48}$$

and φ the direction of maximum normal stresses (see Fig. 6.4). Along the slip lines,

$$\sigma_{nt} = \pm\tau_{\mathrm{m}} = \pm\tau_0, \tag{6.49}$$

holds, with n, t being the normal and the tangent to the slip line. The components in the (x,y) coordinate system are

$$\begin{aligned} \sigma_{xx} &= \hat{\sigma} - \tau_0 \sin 2\phi \\ \sigma_{yy} &= \hat{\sigma} + \tau_0 \sin 2\phi \\ \sigma_{xy} &= \tau_0 \cos 2\phi \end{aligned} . \tag{6.50}$$

Thereby, the stress state is completely determined in every point by the mean principal stress, $\hat{\sigma} = \sigma_{\mathrm{III}}$, and the angle, ϕ, of the lines of maximum shear stress against the x-axis. Equation (6.48) represents an orthogonal mesh of curves. Those which are rotated anti-clockwise by ϕ against the x-axis, i.e. in a mathematically

positive sense, are called α-lines, and the curves orthogonal to the α-lines are β-lines. The first principal axis divides the right angle between them. Stresses $\sigma_{\mathrm{I,II}} = \hat{\sigma} \pm \tau_0$, $\sigma_{\mathrm{III}} = \hat{\sigma}$ act on a material element which is oriented along the principal axes. The equilibrium conditions, Eq. (6.32), become

$$\begin{aligned} \hat{\sigma}_x - 2\tau_0 \cos(2\phi)\phi_x - 2\tau_0 \sin(2\phi)\phi_y = 0 \\ -2\tau_0 \sin(2\phi)\phi_x + \hat{\sigma}_y + 2\tau_0 \cos(2\phi)\phi_y = 0 \end{aligned} . \tag{6.51}$$

Its resolvability condition yields Henky's equation (Hencky [16]),

$$\frac{\mathrm{d}\hat{\sigma}}{\mathrm{d}\phi} \mp 2\tau_0 = 0 \quad \text{for} \quad \begin{cases} \alpha - \text{lines} \\ \beta - \text{lines} \end{cases}, \tag{6.52}$$

stating that the derivative of $\hat{\sigma} \mp 2\tau_0 \phi$ vanishes along the α- and β-lines and thus $\hat{\sigma} \mp 2\tau_0\phi$ is constant,

$$\begin{aligned} \hat{\sigma} - 2\tau_0 \phi = C_\alpha \quad \text{along } \alpha - \text{line} \\ \hat{\sigma} + 2\tau_0 \phi = C_\beta \quad \text{along } \beta - \text{line} \end{aligned} . \tag{6.53}$$

The constants C_α and C_β vary from one α- or β-line to the next.

As stress and strain rate tensor are collinear for isotropic materials, the characteristics of the stress and the deformation rate equations are the same, and Geiringer's equations [13],

$$\begin{aligned} \frac{\mathrm{d}\dot{u}_\alpha}{\mathrm{d}\phi} - \dot{u}_\beta = 0 \quad \text{along } \alpha - \text{line} \\ \frac{\mathrm{d}\dot{u}_\beta}{\mathrm{d}\phi} + \dot{u}_\alpha = 0 \quad \text{along } \beta - \text{line} \end{aligned} , \tag{6.54}$$

are obtained as the equivalent to Hencky's Eq. (6.52).

6.3.4 Generation of Slip-Line Fields—Boundary Conditions

A Cauchy problem is on hand, if the stresses, σ_{xx}, σ_{yy}, σ_{xy}, are prescribed along a non-characteristic $\widehat{\mathrm{AB}}$, Fig. 6.5a. Then a unique solution exists in the triangle ABP, and according to Eq. (6.53),

$$\begin{aligned} \hat{\sigma}_\mathrm{C} - 2\tau_0\phi_\mathrm{C} = \hat{\sigma}_\mathrm{E} - 2\tau_0\phi_\mathrm{E} \\ \hat{\sigma}_\mathrm{D} + 2\tau_0\phi_\mathrm{D} = \hat{\sigma}_\mathrm{E} + 2\tau_0\phi_\mathrm{E} \end{aligned} , \tag{6.55}$$

holds in the intersection point, E, of the α- and β-lines passing C and D, respectively, that is

$$\begin{aligned} \phi_E &= \frac{1}{4\tau_0}(\hat{\sigma}_D - \hat{\sigma}_C) + \frac{1}{2}(\phi_D + \phi_C) \\ \hat{\sigma}_E &= \frac{1}{2}(\hat{\sigma}_D + \hat{\sigma}_C) + 2\tau_0(\phi_D - \phi_C) \end{aligned} \quad . \tag{6.56}$$

If the arc $\widehat{AB}$ is stress free, its normal is a principal direction and the slip lines intersect with the surface contour by $\pm 45°$. The slip-line field ABP is determined by the shape of the boundary. At a straight boundary, Fig. 6.5b, the stress state is homogeneous,

$$\begin{aligned} \sigma_{xx} &= \pm 2\tau_0 \\ \sigma_{zz} &= \pm \tau_0 \\ \sigma_{yy} &= \sigma_{xy} = 0 \end{aligned} \quad . \tag{6.57}$$

At a circular stress-free boundary of radius a, Fig. 6.5c, radial and circumferential directions are principal directions which are cut by the characteristics at an angle of $\pm 45°$. The slip lines become logarithmic spirals described by

$$\varphi \mp \ln \frac{r}{a} = C_{\alpha,\beta} \tag{6.58}$$

in a polar coordinate system, (r, φ). Along $\widehat{BP}$ (α-line) and $\widehat{AP}$ (β-line), respectively,

$$\begin{aligned} \varphi_B &= -\gamma = \varphi - \ln \frac{r}{a} = -\ln \frac{r_P}{a} \\ \varphi_A &= \gamma = \varphi + \ln \frac{r}{a} = \ln \frac{r_P}{a} \end{aligned} \quad . \tag{6.59}$$

hold with $r_P = \overrightarrow{OP}$.

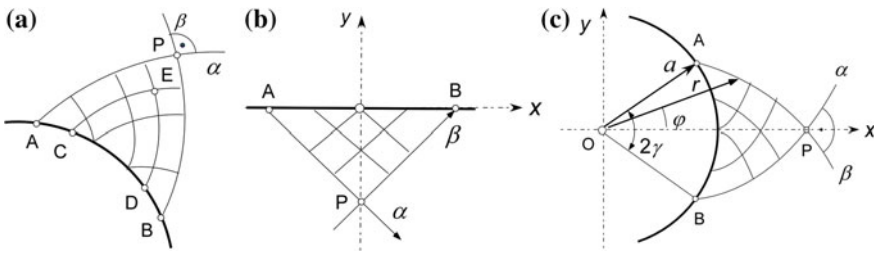

Fig. 6.5 Generation of slip-line fields: **a** arbitrary non-characteristic $\widehat{AB}$, **b** straight stress-free boundary, **c** circular stress-free boundary

The stress state in an arbitrary point along the x-axis ($\varphi = 0$) in a distance of $x \geq a$ follows from Eqs. (6.50), and (6.53) as [17].

$$\begin{aligned}\sigma_{xx} &= \sigma_{rr}(\varphi = 0) = 2\tau_0 \ln\left(\frac{x}{a}\right)\\ \sigma_{yy} &= \sigma_{\varphi\varphi}(\varphi = 0) = 2\tau_0\left[1 + \ln\left(\frac{x}{a}\right)\right]\\ \sigma_{xy} &= \sigma_{r\varphi}(\varphi = 0) = 0\end{aligned} \cdot \tag{6.60}$$

The logarithmic slip-line field of Eq. (6.58) provides also a solution for the fully plastic state of a cylinder under internal pressure (Sect. 3.3.3), Fig. 6.6, which does not only represent a kinematically possible velocity field but at the same time a statically admissible stress state. Thus the corresponding internal pressure is the plastic limit pressure, p_{pl}, according to the theorems of Sect. 6.1.2.

Though the inner surface, $r = r_{\mathrm{i}}$, is not stress free, but $\sigma_{rr} = -p$, radial and circumferential directions are principal directions due to axial symmetry and $\sigma_{r\varphi} = 0$, and hence Eq. (6.58) holds for the slip-lines. The direction of the greatest principal stress bisects the right angle between α- and β-lines. The stress state in point C is $\sigma_{rr} = 0$, $\sigma_{\varphi\varphi} = \sigma_{\mathrm{I}} = 2\tau_0$, and hence $\widehat{\mathrm{ABC}}$ is an α-line with

$$\varphi_{\mathrm{A}} - \ln\frac{r_{\mathrm{i}}}{r_{\mathrm{i}}} = 0 = \varphi_0 - \ln\frac{r_{\mathrm{o}}}{r_{\mathrm{i}}}. \tag{6.61}$$

The plastic limit pressure follows from the boundary condition and Eq. (6.31),

$$\sigma_{rr}(r_{\mathrm{i}}) = \sigma_{rr}^{\mathrm{A}} = \hat{\sigma}_{\mathrm{A}} - \tau_0 = -p_{\mathrm{pl}}, \tag{6.62}$$

where $\hat{\sigma}_{\mathrm{A}}$ can be calculated from Hencky's Eq. (6.53) regarding Eqs. (6.48) and (6.29)

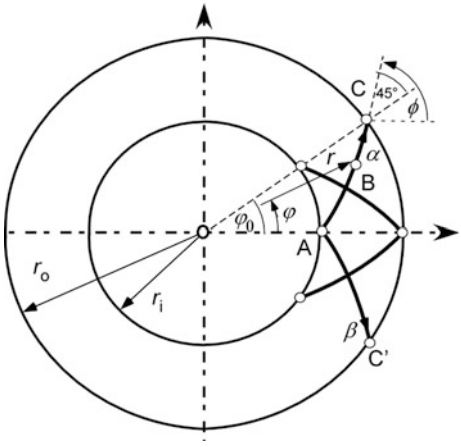

Fig. 6.6 Slip-lines for a pressure vessel

$$\hat{\sigma}_A = \hat{\sigma}_C - 2\tau_0\,(\phi_C - \phi_A) = \hat{\sigma}_C - 2\tau_0\,(\varphi_C - \varphi_A) = \tau_0 - 2\tau_0\,\varphi_0 \tag{6.63}$$

which finally results in

$$p_{pl} = 2\tau_0 \ln\left(\frac{r_o}{r_i}\right), \tag{6.64}$$

taking φ_0 from Eq. (6.61). This is Eq. (3.40), again, with τ_0 according to Eq. (6.25).

6.3.5 *Examples of Notched Structures*

Besides applications in metal forming [18], slip-line fields have gained importance in fracture mechanics for calculating approximations of the plastic limit load for notched and cracked specimens. Hill [17] gave a solution for a notched tensile bar as in Fig. 6.1a, which works only for a specific ratio of the notch radius, r_0, to the half ligament width, $b = W - a$, however.

The notch surface is stress free, $\sigma_{rr}(r_0, \varphi) = \sigma_{r\varphi}(r_0, \varphi) = 0$, and the circumferential stress is the greatest principal stress, $\sigma_{\varphi\varphi}(r_0, \varphi) = \sigma_I(r_0, \varphi) = 2\tau_0$. The slip lines are logarithmic spirals, Eq. (6.58), again, cutting the surface at $\pm 45°$. $\widehat{AOB}$ is an α-line and $\widehat{DOC}$ a β-line, Fig. 6.7a. With $\varphi_A = -\varphi_0$, $r_A = r_0$, $\varphi_O = 0$, $r_O = r_0 + b$, we have $-\varphi_0 = -\ln[(r_0 + b)/r_0]$ along $\widehat{AO}$ and hence

$$\varphi_0 = \ln\left(1 + \frac{b}{r_0}\right). \tag{6.65}$$

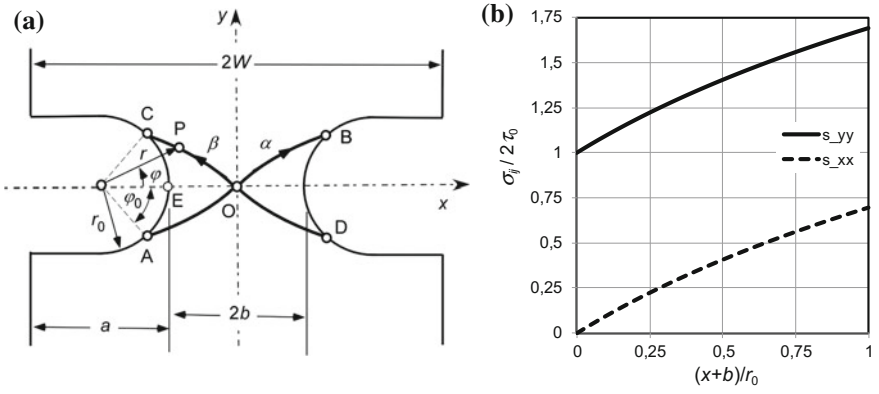

Fig. 6.7 Hill's slip-line solution for a notched tensile bar, $b/r_0 < 3.81$: **a** geometry, **b** stress distribution

Because of $\varphi_0 \leq \pi/2$, a ratio of

$$\frac{b}{r_0} \leq e^{\pi/2} - 1 = 3.81 \tag{6.66}$$

has to be observed in order to realise the slip-line field. The hydrostatic stress in the specimen centre, point O, follows from Hencky's Eq. (6.53), $\hat{\sigma}_O = \hat{\sigma}_A + 2\tau_0(\phi_O - \phi_A) = \hat{\sigma}_A + 2\tau_0\varphi_0$, with boundary and yield conditions as

$$\hat{\sigma}_O = \tau_0(1 + 2\varphi_0), \tag{6.67}$$

and for an arbitrary point, P, on $\widehat{COD}$ with $\varphi_P = \varphi$, $r_P = r$, we finally obtain

$$\hat{\sigma}_P = \hat{\sigma}(r, \varphi) = \tau_0[1 + 2(\varphi_0 - \varphi)] = \tau_0\left[1 + 2\ln\left(\frac{r}{r_0}\right)\right]. \tag{6.68}$$

Principal stresses and stresses in the ligament, $\varphi = 0$, result from Eq. (6.31),

$$\begin{aligned} \sigma_{xx}(x) &= 2\tau_0 \ln\left(1 + \frac{b+x}{r_0}\right) \\ \sigma_{yy}(x) &= 2\tau_0\left[1 + \ln\left(1 + \frac{b+x}{r_0}\right)\right] \end{aligned}, \tag{6.69}$$

which are plotted in Fig. 6.7b. They represent the stress state for a kinematically possible mechanism according to definition (II) in Sect. 6.1.2. The corresponding force is obtained by integration,

$$F_k = B\int_{-b}^{+b} \sigma_{yy}^{(k)}(x)\,dx = 4Bb\,\tau_0\left(1 + \frac{r_0}{b}\right)\ln\left(1 + \frac{b}{r_0}\right) \geq F_{pl}, \tag{6.70}$$

which is an upper bound to F_{pl}. The plastic constraint factor according to Eq. (6.15) becomes $L_{pl} \leq 1.98$ for $(b/r_0)_{max} = 3.81$. The plastic limit load of a notched specimen can hence become nearly double as high as that of a smooth tensile bar of same net width, $2b$, which more than once has caught experimentalists by surprise when testing notched bars.

If the limit condition of Eq. (6.66) is exceeded, the slip line field has to be complemented by triangular constant stress fields according to Fig. 6.5b along the straight flanks of the notch, GHC, and in the specimen centre, RSO, see Fig. 6.8a.

Stresses in the triangle RSO are constant,

$$\begin{aligned} \sigma_{xx} &= \tau_0\,\pi \\ \sigma_{yy} &= 2\tau_0\left(1 + \frac{\pi}{2}\right) \end{aligned}, \tag{6.71}$$

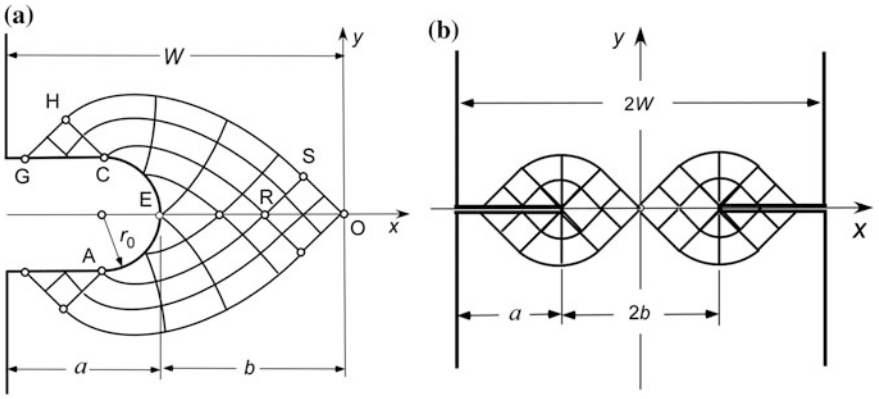

Fig. 6.8 **a** Slip-line fields for (**a**) double edge notched tensile bar with $b/r_0 > 3.81 b/r_0 < 3.81$; **b** double edge-cracked specimen, DE(T)

and the stress distribution between E and R follows from Eq. (6.69). The plastic limit load factor becomes

$$L_{\mathrm{pl}} \leq \left(1 + \frac{\pi}{2}\right)\left(1 + \frac{r_0}{b}\right) - \frac{r_0}{b}\mathrm{e}^{\pi/2}. \tag{6.72}$$

In the limit of a crack, that is $r_0 \to 0$, the slip-line field of Fig. 6.8b is obtained. The stresses in the ligament are the same as in the triangle RSO of the notched bar, Eq. (6.71), and the plastic constraint factor is obtained from Eq. (6.72) for $r_0 \to 0$, $L_{\mathrm{pl}} \leq 1 + \pi/2 = 2.57$.

Slip-line fields for V-notched tensile bars can be found in Ewing and Hill [12] and Ewing [10], and a substantial number of publications exists also for bending of notched bars: Green [14], Green and Hundy [15], Lianis and Ford [20], Alexander and Komoly [1], Wilshaw and Pratt [26], Ewing [11] etc.

References

1. Alexander JM, Komoly TJ (1962) On the yielding of a rigid/plastic bar with an Izod notch. J Mech Phys Solids 10:265–275
2. Brocks W, Burth K (1977) Über den Zusammenhang von Elementstabilität und Systemstabilität von Tragwerken aus elastischem und elastisch–plastischem Werkstoff". Forsch Ingenieurwes 43:190–198
3. Burth K, Brocks W (1992) Plastizität - Grundlagen und Anwendungen für Ingenieure. Vieweg, Braunschweig
4. Drucker DC (1950) Some implications of work hardening and ideal plasticity. Q Appl Math 7:411–418
5. Drucker DC (1951): A more fundamental approach to plastic stress-strain relations. In: Proceedings of 1st US Nat Congr Appl Mech, ASME, pp 487–491

6. Drucker DC (1959) A definition of stable inelastic material. Trans ASME, J Appl Mech, pp 101–106
7. Drucker (1964) On the postulate of stability of materials in the mechanics of continua. J Mécanique 3:235–249
8. Drucker DC, Prager W, Greenberg HJ (1952) Extended limit design theorems for continuous media. Q Appl Mech 9:382–389
9. EN1993 (2004) Eurocode 3: design of steel structures. European Committee for Standardization
10. Ewing DJF (1968) Plastic yielding of V-notched tension bars with circular roots. J Mech Phys Solids 16
11. Ewing DJF (1968) Calculations of the bending of rigid/plastic notched bars. J Mech Phys Solids 16
12. Ewing DJF, Hill R (1967) The plastic constraint of V-notched tension bars. J Mech Phys Solids 15
13. Freudenthal AM, Geiringer H (1958) The mathematical theories of the slip-line field in plane plastic flow, Handbook of Physics VI. Springer, Berlin
14. Green AP (1956) The plastic yielding of shallow notched bats due to bending. J Mech Phys Solids 4
15. Green AP, Hundy BB (1956) Initial plastic yielding in notch bend tests. J Mech Phys Solids 4
16. Hencky H (1923) Über einige statisch bestimmte Fälle des Gleichgewichts in plastischen Körpern. Z angew Math Mech 3:211–251
17. Hill R (1949) The plastic yielding of notched bars under tension. Quart J Appl Math 2:40–52
18. Johnson W, Sowerby R, Venter RD (1982) Plane strain slip line fields for metal deformation. a source book and bibliography. Pergamon, Oxford
19. Justusson JW, Phillips A (1966) Stability and convexity in plasticity. Acta Mech 2:251–267
20. Lianis G, Ford H (1958) Plastic yielding of single notched bars due to bending. J Mech Phys Solids 7
21. Maier G, Drucker DC (1966) Elastic-plastic continua containing unstable elements obeying normality and convexity relations. Schweiz Bauztg 84:447–450
22. Maier G, Drucker DC (1973) Effects of geometry change on essential features of inelastic behavior. Proc ASCE 99:819–834
23. Palmer AC, Maier G, Drucker DC (1967) Normality relations and convexity of yield surfaces for unstable materials or structural elements. J Appl Mech 34:464–470
24. Phillips A, Sierakowski RL (1965) On the concept of the yield surface. Acta Mech 1:29–35
25. Prager W, Hodge PG (1954) Theorie ideal plastischer Körper. Springer, Wien
26. Wilshaw TR, Pratt RP (1966) On the plastic deformation of Charpy specimens prior to general yield. J Mech Phys Solids 14

Chapter 7
Determination of Fracture Parameters

Abstract Numerical methods for determining fracture mechanics parameters or "crack-driving forces" like J-integral or energy release rate and stress intensity factors by finite element analyses are presented and explained. Special emphasis is placed on the capabilities of the finite element code ABAQUS. Path dependence of the J-integral in incremental plasticity is addressed and rules for calculating physically meaningful J values are given. Likewise, experimental procedures for determining the fracture toughness in terms of J or K as codified in the ASTM standards are described, starting with a discussion on fracture mechanics terminology.

Fracture criteria as in Eqs. (2.12), (2.17), (5.21), (5.47), (5.80) compare applied "crack driving forces" like $\mathcal{G}, K, J, \delta$ with the respective crack resistance of the material, $\mathcal{G}_c, K_{Ic}, J_{Ic}, \delta_c$, as single values or R-curves, J_R or δ_R, respectively. A fracture mechanics assessment requires the determination of both driving force and resistance. The previous chapters were primarily concerned with the definition of the respective quantities and simple analytical formulas for their evaluation. Calculations for real structures and particularly for non-linear material behaviour require numerical methods, where most frequently the finite element method (FEM) is applied [22]. The present chapter focuses on numerical analyses of cracked structures and the determination of driving forces like $\mathcal{G}, J, K$ by commercial FE-codes in its first part and on the standards for experimental determination of material parameters in its second.

7.1 Numerical Methods: Crack Driving Forces

Cracks and crack-like defects cause high stress and strain gradients which call for a fine discretisation of the FE mesh. This results in large numbers of elements and degrees of freedom. Nonlinear simulations of components with stress concentrators can therefore be quite expensive with respect to computation time and memory.

W. Brocks, *Plasticity and Fracture*, Solid Mechanics and Its Applications 244,
DOI 10.1007/978-3-319-62752-6_7

Some leads for an appropriate and effective layout of FE meshes are given in the following, and common methods for determining energy release rate, J-integral and stress intensity factors are presented. Particular emphasis is focussed on the elasto-plastic J and its path dependence.

7.1.1 FE Meshes for Structures with Cracks

Modelling means simplification and reduction of complexity. Models should only be as complex as inevitable to include significant effects. For plane specimen geometries two-dimensional models should be employed, at least for pre-analyses of a new problem. Thin specimens and sheet metal components are commonly adequately represented by plane-stress, and thick or side-grooved specimens by plane strain models. Three-dimensional analyses are necessary, of course, if the geometry is not plane or if 3D effects through the thickness and along the crack front shall be studied. All additional possibilities for reducing the number of degrees of freedom should be exploited like (i) coarsening the mesh remote from the defect, (ii) introducing symmetry conditions. For more details and examples see Brocks et al. [10] and Brocks [9], for example.

Figure 7.1 shows examples of two-dimensional FE meshes near the crack tip of a fracture mechanics specimen for mode I. As loading and geometry are symmetric, just the upper half is modelled and vertical displacements are suppressed in the ligament, $u_y = 0$. Collapsed elements are used for the analysis of a stationary crack, Fig. 7.1a, and a regular element arrangement for the analysis of an extending crack, Fig. 7.1b. Both meshes demonstrate common strategies used for coarsening the mesh away from the crack.

Singular elements were suggested by Barsoum [8] to increase the accuracy of stress calculations and K-factors at a time when computer capacities were limited. Triangular or prismatic isoparametric elements which are obtained by collapsing one side reveal a $1/\sqrt{r}$-singularity of strains in linear elasticity as well as a $1/r$-singularity for perfectly plastic materials. A pure $1/\sqrt{r}$-singularity is obtained if

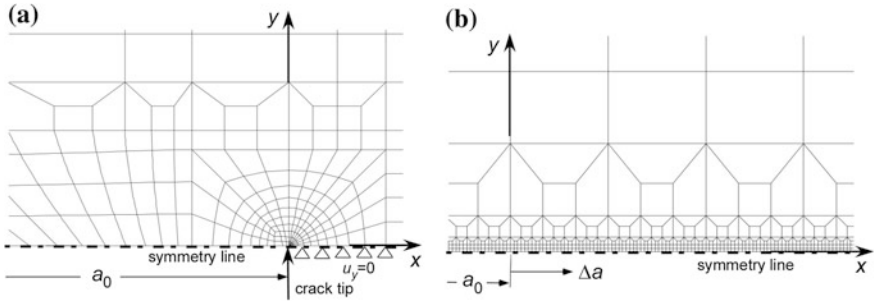

Fig. 7.1 Details of FE meshes at the crack tip for **a** stationary crack. **b** extending crack

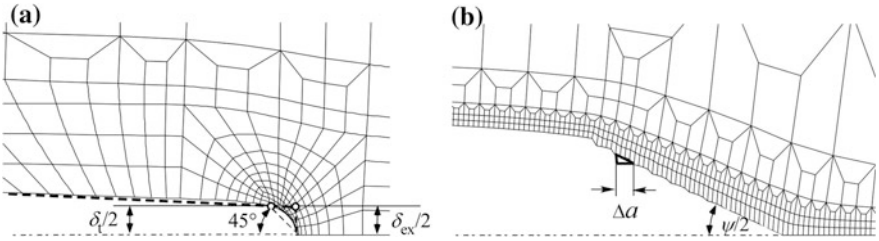

Fig. 7.2 **a** CTOD, δ, at a blunting crack tip **b** CTOA, ψ, for an extending crack

additionally the respective mid-side nodes of the crack-tip elements are shifted to quarter positions. The strain energy remains finite for $r \to 0$ in linear elasticity as well as for HRR-like fields, because the strain energy density, $\bar{w}$, has a singularity of $\mathcal{O}(r^{-1})$. Numerical studies by McMeeking and Rice [25] and Brocks et al. [12] have shown that triangular or prismatic collapsed elements are well suited for calculations in EPFM. Crack tip blunting can be simulated applying a large-strain analysis, Fig. 7.2a, and principal stresses exhibit a maximum ahead of the crack tip as in Fig. 5.14. CTOD can be evaluated either according to the definition of Fig. 5.13, δ_t, or by extrapolation of the crack opening profile to the crack tip, δ_{ex}.

Singular elements for stationary cracks lost importance in recent years because SIFs are no longer calculated from stress fields but from the energy release rate (Sect. 5.1.2), and because J calculations by the virtual crack extension method (Sect. 7.1.2) yield accurate results even for rather coarse meshes. Singular elements cannot be applied at all for crack growth simulations, which require a regular arrangement of elements in the ligament as shown in Fig. 7.1b. These meshes, however, do not provide sufficiently accurate results of CTOD or stresses at the crack tip for stationary cracks.

If a critical value of some fracture parameter, J_c or δ_c, is exceeded, a crack starts to grow. For ductile materials, this may occur in a stable manner, i.e. under still growing external forces, or at least deformation controlled even beyond maximum load. Crack growth can be simulated by

- node release controlled by an R-curve for J, CTOD or CTOA (Sects. 5.1.5 and 5.3.3), e.g. Siegele and Schmitt [39]; Brocks and Yuan [15]; Brocks et al. [11]; Gullerud et al. [21];
- cohesive elements (Chap. 9);
- constitutive equations based on damage mechanics concepts (Chap. 8).

Figure 7.2b illustrates crack growth by node release [34] which is controlled by a criterion assuming constant crack tip opening angle (Fig. 5.16), $\psi_R(\Delta a)$.

7.1.2 Energy Release Rate and J-Integral

Griffith [20] defined the (elastic) energy release rate as the negative change of strain energy, ΔU, with some crack advance, Δa, Eq. (2.10). Rice et al. [32] showed that the J-integral is identical to Griffith's energy release rate not only in an elastic material but also in a hyper-elastic material, Eq. (5.24). The mathematical background of this equivalence is the divergence theorem, Eq. (5.2), which converts the contour integral, Eq. (5.20), into an area integral in two dimensions or a volume integral in three dimensions over a finite domain surrounding the crack front. The relation between $\mathcal{G}$ and J constitutes a unique methodology for their respective analytical, numerical and experimental determination, which has been addressed in Sect. 5.1.2, already.

The determination of J in FE codes is based on the domain integral method (see Sect. 11.4.2 on contour integral evaluation in Abaqus [1], e.g.), which was first suggested by Parks [27, 28], further worked out by DeLorenzi [17, 18] and has became an established technique [38]. The method is quite robust, and accurate values are obtained even for quite coarse meshes [23]. As the domain integral is based on energy quantities and is taken over a finite region of elements, discontinuities of stresses or any other numerical imprecisions of local field quantities have less effect. The J-integral is defined in terms of the energy release rate, associated with a fictitious small crack advance. Because of this interpretation, the domain integral method is also known as "virtual crack extension" (VCE) method.

The change of energy in a domain, $\mathcal{B}_0$, for some (fictitious) small crack extension, Δa, see Fig. 7.3, is calculated as

$$\mathcal{G}_\theta = \frac{1}{B\Delta a} \iint_{\mathcal{B}_0} \left[\sigma_{ij} u_{j,k} - \bar{w}\delta_{ik}\right] \Delta x_{k,i} \, \mathrm{d}V, \tag{7.1}$$

where $\bar{w} = \int \sigma_{ij} \dot{\varepsilon}_{ij} dt$ is the strain energy density and Δx_k the shift of the crack front coordinates. Equation (7.1) allows for an arbitrary shift of the crack tip coordinates, Δx_k, yielding the energy release rate, $\mathcal{G}_\theta$, in the respective direction, $\theta = \arctan(\Delta x_2/$

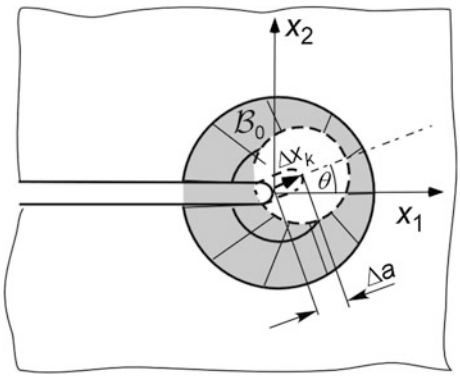

Fig. 7.3 Virtual crack extension for calculating the energy release rate

Δx_1), which can be applied for investigations of mixed mode fracture problems. The respective results for $\theta = 0$ and $\theta = \pi/2$ equal the first two components of the J-integral vector, Eq. (5.15),

$$J_1 = \mathcal{G}_1 = \mathcal{G}_{\theta=0}, \quad J_2 = \mathcal{G}_2 = \mathcal{G}_{\theta=\pi/2}. \tag{7.2}$$

The volume integral of Eq. (7.1) already includes three-dimensional effects as in the contour definition of J in Eq. (5.36), DeLorenzi [18]. Local values, $J(s_c)$, along the crack front are calculated if rings around single crack tip nodes are shifted. Thus $J(\phi)$ in Fig. 5.6a for the semi-elliptical surface flaw in the pressure vessel has been calculated. If the whole crack front is moved by the same amount, Δa, an average value, $\overline{J} = (1/B) \int_0^B J(z)\, dz$, is obtained for a fracture specimen of finite thickness, B, which equals the global J-integral calculated from the $F(v_L)$ data. The extensions of J for body forces, surface tractions and thermal loading presented in section by Eqs. (5.39)–(5.41) are also based on the domain integral method.

7.1.3 Stress Intensity Factors

Stress intensity factors (SIF) can be calculated from Eqs. (2.23) or (2.24) if the asymptotic stress fields, $\sigma_{ij}(r, 0)$, or the crack edge displacements, $u_i(r, \pi)$ are known from numerical calculations. This does not yield sufficiently accurate results, however, particularly if they are based on stresses. More advanced methods exploit the relation to the energy release rate, which is commonly evaluated by a domain integral. The components of J or $\mathcal{G}$, Eq. (7.2), are related to the SIFs of mode I and II by

$$\mathcal{G}_1 = \mathcal{G}_{\theta=0} = \frac{K_I^2 + K_{II}^2}{E'}, \quad \mathcal{G}_2 = \mathcal{G}_{\theta=\pi/2} = -2\frac{K_I K_{II}}{E'}. \tag{7.3}$$

Bear in mind not to mistake the components, $\mathcal{G}_1, \mathcal{G}_2$, in Eq. (7.3) for the energy release rates in mode I and II, $\mathcal{G}_I, \mathcal{G}_{II}$, in Eq. (2.18), respectively.

Two equations for two unknowns exist, but as Eq. (7.3) is symmetric in K_I, K_{II} the resulting quadratic equation for K^2 does not offer a unique solution which is K_I and which is K_{II},

$$K_{I/II}^2 = \frac{1}{2} E' \mathcal{G}_1 \pm \frac{1}{2} \sqrt{E'^2 \left(\mathcal{G}_1^2 - \mathcal{G}_2^2\right)}, \tag{7.4}$$

and side conditions based on Eqs. (2.23) or (2.24) are required to decide.

Shih and Asaro [37] developed the interaction integral method to extract the individual SIFs for a crack under mixed-mode loading (Sect. 2.16.2 in Abaqus [1]). It is s applicable to cracks in isotropic and anisotropic linear materials and, of course, for 3D configurations [19].

The relation (2.18) can be written more generally as

$$\mathcal{G} = \{\mathrm{K}\}^{\mathrm{T}}\{\mathrm{B}\}^{-1}\{\mathrm{K}\}, \tag{7.5}$$

where $\{\mathrm{K}\}$ is the column matrix of the three SIFs, $\{\mathrm{K}\}^{\mathrm{T}} = \{K_{\mathrm{I}}, K_{\mathrm{II}}, K_{\mathrm{III}}\}$ and $\{\mathrm{B}\}$ a matrix of elastic constants, which becomes

$$\{\mathrm{B}\} = \begin{Bmatrix} E' & 0 & 0 \\ 0 & E' & 0 \\ 0 & 0 & 2G \end{Bmatrix}, \tag{7.6}$$

for isotropic materials. If a mode I "auxiliary" crack tip field with SIF, $K_{\mathrm{I}}^{\mathrm{aux}}$, and release rate, $\mathcal{G}_{\mathrm{I}}^{\mathrm{aux}} = K_{\mathrm{I}}^{\mathrm{aux}} B_{11}^{-1} K_{\mathrm{I}}^{\mathrm{aux}}$, is defined and superimposed onto the actual field, the total energy release rate for mode I becomes

$$\begin{aligned} \mathcal{G}_{\mathrm{I}}^{\mathrm{tot}} = {} & \left(K_{\mathrm{I}} + K_{\mathrm{I}}^{\mathrm{aux}}\right) B_{11}^{-1} \left(K_{\mathrm{I}} + K_{\mathrm{I}}^{\mathrm{aux}}\right) + 2\left(K_{\mathrm{I}} + K_{\mathrm{I}}^{\mathrm{aux}}\right) B_{12}^{-1} K_{\mathrm{II}} \\ & + 2\left(K_{\mathrm{I}} + K_{\mathrm{I}}^{\mathrm{aux}}\right) B_{13}^{-1} K_{\mathrm{III}} + (\ldots). \end{aligned} \tag{7.7}$$

Since the terms (…) not involving K_{I} or $K_{\mathrm{I}}^{\mathrm{aux}}$ in $\mathcal{G}_{\mathrm{I}}^{\mathrm{tot}}$ and $\mathcal{G}$ are equal, an "interaction integral" can be defined as,

$$\mathcal{G}_{\mathrm{I}}^{\mathrm{int}} = \mathcal{G}_{\mathrm{I}}^{tot} - \mathcal{G} - \mathcal{G}_{\mathrm{I}}^{aux} = 2K_{\mathrm{I}}^{\mathrm{aux}}\left(B_{11}^{-1} K_{\mathrm{I}} + B_{12}^{-1} K_{\mathrm{II}} + B_{13}^{-1} K_{\mathrm{III}}\right). \tag{7.8}$$

Repeating this for mode II and III finally results in a linear system of equations,

$$\mathcal{G}_{(\alpha)}^{\mathrm{int}} = 2K_{(\alpha)}^{\mathrm{aux}} B_{(\alpha)\beta}^{-1} K_{\beta}, \quad \alpha, \beta = \mathrm{I}, \mathrm{II}, \mathrm{III}, \tag{7.9}$$

(no summation on α). If the $K_{\alpha}^{\mathrm{aux}}$ are assigned unit values, Eq. (7.9) yields the solution

$$\{\mathrm{K}\} = \frac{1}{2}\{\mathrm{B}\}^{-1}\{\mathcal{G}^{\mathrm{int}}\} \quad \text{with} \quad \{\mathcal{G}^{\mathrm{int}}\} = \begin{Bmatrix} \mathcal{G}_{\mathrm{I}}^{\mathrm{int}} \\ \mathcal{G}_{\mathrm{II}}^{\mathrm{int}} \\ \mathcal{G}_{\mathrm{III}}^{\mathrm{int}} \end{Bmatrix}. \tag{7.10}$$

The interaction integrals, $\mathcal{G}_{\alpha}^{\mathrm{int}}$, are calculated with the domain integral method, Eq. (7.1). Numerical errors due to discretisation may lead to a domain dependence, see the following example of a surface crack in a railway axle.

The fatigue life of a railway axle under service loads, Fig. 7.4, can be assessed with help of the Paris Eq. (2.19), Zerbst et al. [41]. It requires the determination of mode I, II and III SIFs for some postulated surface flaw. Here, the surface crack is

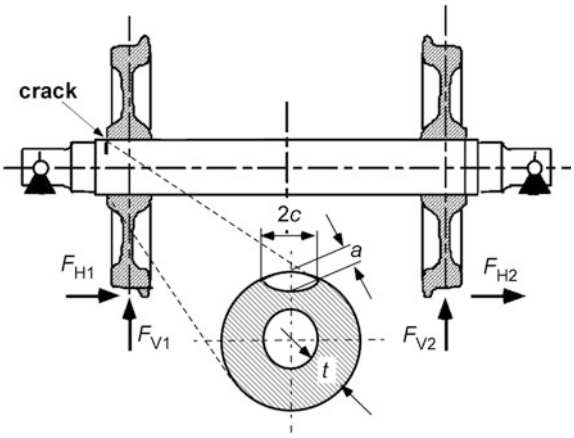

Fig. 7.4 Railway axle with assumed semi-elliptical surface flaw under service loads

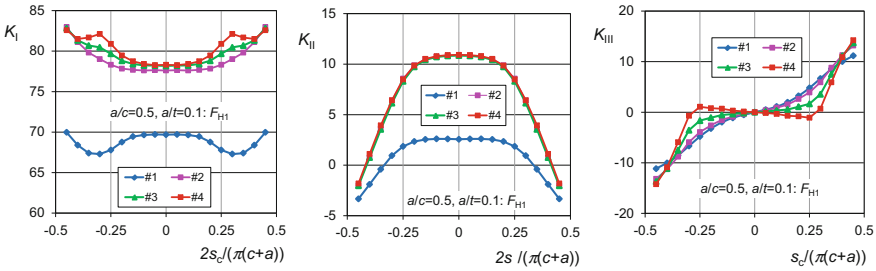

Fig. 7.5 SIFs (in MPa$\sqrt{\text{m}}$) for modes I, II, III at a semi-elliptical surface crack in a railway axle with assumed semi-elliptical surface flaw under horizontal force, F_{H1} = 100 kN, acting at a wheel

assumed as semi-elliptical of aspect ratio a/c = 0.5 and penetrating 10% of the wall thickness. The structure is subject to normal stresses, bending and shear by vertical and horizontal forces acting at the contact points of wheels and rail. As the position of the crack changes due to the rotation of the axle, the K-factors vary with time between maximum and minimum values. Due to the linearity of the problem, the analyses can be performed successively for unit reference values of the four forces, F_{V1}, F_{V2}, F_{H1}, F_{H2}, and the resulting K-factors for the actual time dependent values superimposed according to Eq. (2.26).

The local SIFs, K_I, K_{II}, K_{III}, in MPa$\sqrt{\text{m}}$ along the crack front for a horizontal force, F_{H1} = 100 kN, are displayed in Fig. 7.5. The crack front coordinate is the normalised arc length, $-0.5 \leq 2s_c/(\pi(c+a)) \leq 0.5$. The K-values at the end points where the crack front penetrates the free surface are defective and not

displayed since no $1/\sqrt{r}$ singularity is present in these points. The curve numbers, #1–4, indicate increasing sizes of the integration domain around the crack tip. Whereas the first (blue) curve which represents the closest contour around the crack tip is definitely inappropriate for K_{I} and K_{II} the domain dependence decreases with increasing domain size for K_{I} and has completely vanished for K_{II}. The courses of K_{I} and K_{II} are symmetric to the centre, K_{I} having a minimum in the centre and K_{II} a maximum, and it is antisymmetric for K_{III}. The domain dependence of K_{III} is less distinct; obviously $K_{\mathrm{III}} \approx 0$ for $-0.25 \leq 2s_c/(\pi(c+a)) \leq 0.25$.

The same analyses have to be performed for the other forces, F_{H2}, F_{V1}, F_{V2}. Assuming a mixed-mode criterion for fatigue, for instance based on an equivalent cyclic SIF [33], a life estimate based on Eq. (2.19) for monitored service loads can be conducted [41].

7.1.4 Path (Domain) Dependence of J in Incremental Plasticity

Whereas the domain dependence in the previous example of a linear-elastic material results from numerical errors due to discretisation, path (or domain) dependence of the elasto-plastic J may have a second reason originating in violations of the assumptions of small strains and deformation theory of plasticity (Sect. 5.1.1). Particularly, violation of the requirement of hyper-elastic material behaviour, Eq. (5.11), is the most frequent trouble in numerical calculations of J, and it appears to be one of the most "mysterious" problems in the literature: "*J-integral estimates from different rings may vary because of the approximate nature of the finite element solution*" (Sect. 11.4.2 in [1]). This is indeed true for the determination of SIFs but path dependence of J in incremental plasticity is a physical phenomenon and a consequence of energy dissipation [40]. Any pseudo restriction that "*the J-integral calculated is suitable only for monotonic loading of elastic-plastic materials*" is a necessary but not at all sufficient condition since local rearrangements of stresses owing to plastic yielding may nevertheless occur. Likewise, recommendation to refine the FE mesh in order to increase the "accuracy" of J-calculations is counterproductive and rather escalates the problem.

For small scale and contained yielding, a path independent integral can be computed outside the plastic zone. This means that the contour, Γ, has to be large enough to surround the plastic zone and pass through the elastic region only, which is also recommended in the Abaqus manual. In gross plasticity, this is not possible, however, and some more or less pronounced path-dependence will always occur.

The following example is supposed to illustrate this phenomenon and how to deal with it. The mechanical behaviour of an M(T) specimen with a constant (initial) crack length, Fig. 5.4b, under monotonic loading made of an aluminium alloy has been simulated as a 2D model using Abaqus [1] by Brocks and Rabbolini

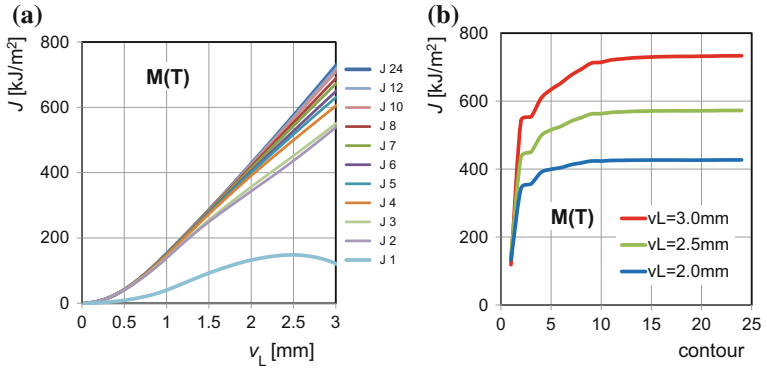

Fig. 7.6 Path (domain) dependence of the numerical *J*-Integral in incremental plasticity calculated for an M(T) specimen, $W = 50$ mm, $B = 20$ mm, $a_0 = 33$ mm

[13]. The results of the *J*-analysis applying the domain integral option are displayed in Fig. 7.6.

Various contours or domains have been defined, starting with "J1" which is the first ring of elements around the crack tip. The correspondent *J* values are definitely useless. The size of the domains increases with their number, and "J24" was the largest possible one not touching the specimen boundary. For contours larger than "J10", the *J* values start saturating. Path dependence increases with load-point displacement, v_L.

Because of its relation to the global energy release rate, Eq. (5.24), *J* has to be understood as a "saturated" value reached in the "far-field" remote from the crack tip. This is the only meaningful definition which is compatible with the experimental evaluation of *J*. Figure 7.7 demonstrates that indeed the domain integral values obtained in the far-field coincide with the results of Eqs. (5.26) and (5.30) based on the numerical F-v_L curve and also match the test results. The minor

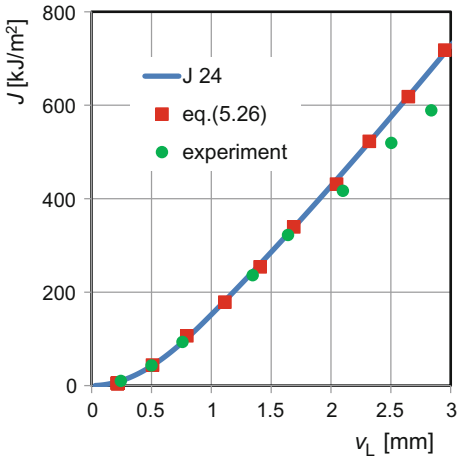

Fig. 7.7 Far-field *J*-integral and global energy release rate

deviation between experimental and numerical results arising beyond $v_L \geq 2$ mm can be traced back to some crack extension occurring in the test which is not considered in the present FE analysis.

The J-integral is a monotonously increasing function of the distance, r, to the crack tip [40],

$$J_{tip} \leq J(r) \leq J_{farfield}, \tag{7.11}$$

Any other behaviour would mean an energy production instead of energy dissipation and therefore violate the second law of thermodynamics. Hence the highest calculated J-value with increasing domain size is always closest to the "real" far-field J. This characteristic also substantiates that any "near-field" integrals [7, 16] are physically meaningless. Considerable stress re-arrangements occur at a blunting crack tip violating the assumption of small strains, Eq. (5.10), as well as the assumption of a hyperelastic material, Eq. (5.11), and the correspondent path dependence increases strongly. This explains why recommendations to refine the FE mesh at the crack tip or to apply a geometrically non-linear, large strain analysis are absurd. A finite value of J in the limit of a vanshingly small contour is only ensured if the strain energy density, $\bar{w}$, has a singularity of $\mathcal{O}(r^{-1})$. As there is no stress singularity at the blunting crack tip in incremental plasticity at all, see Fig. 5.14, J will even vanish at the crack tip,

$$J_{tip} = \lim_{r \to 0} \int_{-\pi/2}^{-\pi/2} \bar{w}\, r \cos\theta \, d\theta \Rightarrow 0. \tag{7.12}$$

The same occurs at growing cracks [15, 40], where stresses and strains are still singular but their singularity is not strong enough to provide a non-zero local energy release rate. Rice et al. [31] showed that the singularity of the strain energy density at a moving crack is $\ln(r^{-1})$ in incremental plasticity. Rice [29, 30] emphasised this as the "*paradox of elastic-plastic fracture mechanics*" that no "*energy surplus*" exists for crack propagation

Conclusions and recommendations how to calculate reliable J-values were given by Brocks and Scheider [14]. If analytical formulas for calculating J from the global energy release rate are available, FE data of contour or domain integrals should always be compared with the results of the respective formulas.

7.2 Test Methods and Standards: Material Resistance

Fracture toughness, "*a generic term for measures of resistance to extension of a crack*" (ASTM E1823 [5]), is an empirical material property that is determined by conducting a test following standard test procedures. These test standards have traditionally been written by national and international organisations: in the USA by the American Society for Testing and Materials (ASTM), in the UK by the British Standards Institution (BSI), in Japan by the Japanese Standards Association (JSA), in Europe through the European Structural Integrity Society (ESIS) and worldwide through the International Standards Organization (ISO), see Schwalbe et al. [35] for an overview.

The following sections are confined to fracture mechanics standards of ASTM because of having a major international impact, and in particular to the general terminology and facture toughness testing. Standards for fatigue testing will not be addressed.

7.2.1 Standard Terminology

ASTM E1823 [5] regulates the terminology relating to fatigue and fracture testing. It contains definitions, symbols, and abbreviations approved for use in standards on fatigue and fracture testing. The definitions are preceded by two alphabetical lists, namely of symbols used and of relevant abbreviations. Definitions range from accuracy ("*the quantitative difference between a test measurement and a reference value*") to zero crossings ("*in fatigue loading, the number of times that the force-time history crosses zero force level*"). Technical definitions in standards are primarily operational and may thus differ from colloquial language. Collins Compact Dictionary defines "accuracy" as "*faithful representation of the truth*", for instance, which is obviously no useful definition for measurements.

With some exceptions, the present book keeps to the ASTM definitions, symbols, and abbreviations used in fracture mechanics. The major exceptions are:

- The yield strength (σ_{YS}) is denoted by the generic symbol, R_0, in Eqs. (3.2) and (3.4) in Chap. 3 on the theory of time- and rate-independent plasticity, which represents an idealised upper limit of elastic behaviour and may be identified with the lower yield point, R_{eL}, or a proof stress, R_p, of real materials, respectively.
- The tensile strength (σ_{TS}) is denoted by R_m, and not considered as a material property but just related to the maximum load, F_m, in a tensile test at the onset of necking. Correspondingly, the "effective" yield strength (σ_Y) is $R_{eff} = 0.5\ (R_0 + R_m)$.
- Forces are denoted by the symbol F for "force", not by P (for "power") as in the ASTM standards.

- The crack length, a, is always considered as "physical" and hence the subscript "p" is omitted.
- The ASTM definition of "crack-tip plane stress" as "*a stress-strain field (near the crack tip) that is not in plane strain*" is definitely nonsensical as it disagrees with the evident meaning that no stresses exist in the out-of-plane direction, $\sigma_{zz} = 0$.
- The "*crack-extension force, G*", defined as "*the elastic energy per unit of new separation area that is made available at the front of an ideal crack in an elastic solid during a virtual increment of forward crack extension*" is actually Griffith's energy release rate, $\mathcal{G}$, which seems to be a more evident and coherent denomination than "force". Since J is an energy release rate as well, it is inconsistent to call it "J-integral" but the energy release rate, $\mathcal{G}$, "force". Both may be considered as "material forces" [24], however, and the generic term "crack driving force" is common for all parameters, $K, \mathcal{G}, J, \delta$, characterising the crack tip fields. The symbol $\mathcal{G}$ avoids that it is confused with the shear modulus G.
- The definition of "stable crack extension" as "*a displacement-controlled crack extension*" is inconsistent with the mechanical definition of stability (Sect. 6.1.1). Unfortunately, this confusion occurs frequently in the fracture mechanics literature.

The terminology for designating fracture mechanics specimens displayed in Fig. 7.8 is used throughout the present book. The symbol code of abbreviations for specimen configuration has one or two capital letters and the applied loading code, bending or tension, consists of a one-letter abbreviation that is enclosed in

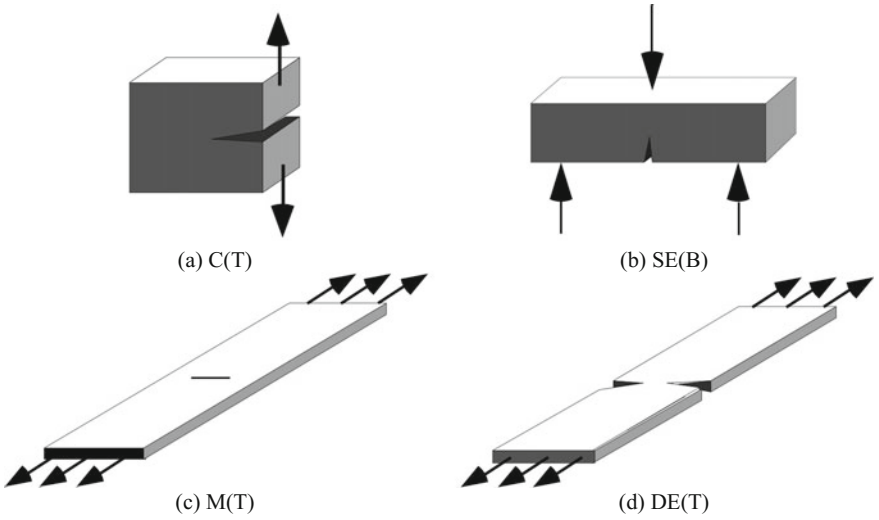

Fig. 7.8 Designation of most common fracture specimens **a** compact (tension). **b** single edge crack in bending. **c** middle crack in tension. **d** double edge crack in tension

parentheses. Note however that the ligament of the C(T) specimen is predominantly in bending. Further specimen configurations like modified compact (MC), disk-shaped compact (DC), arc (A), double beam (DB), round double beam (RDB) or round bar (R-BAR), which are adapted to special material blanks, are not considered here. For the part-through surface (PS) specimen see Fig. 2.7.

7.2.2 Linear-Elastic Plane-Strain Fracture Toughness

ASTM E399 [2] is the standard test method for linear-elastic plane-strain fracture toughness, K_{Ic}. The significance and use of this characteristic parameter is described as

- "*Characterizes the resistance of a material to fracture in a neutral environment in the presence of a sharp crack under essentially linear-elastic stress and severe tensile constraint, such that (1) the state of stress near the crack front approaches tritensile plane strain, and (2) the crack-tip plastic zone is small compared to the crack size, specimen thickness, and ligament ahead of the crack*;
- *Is believed to represent a lower limiting value of fracture toughness*;
- *May be used to estimate the relation between failure stress and crack size for a material in service wherein the conditions of high constraint described above would be expected;*
- *Only if the dimensions of the product are sufficient to provide specimens of the size required for valid K_{Ic} determination*."

Note the cautious statements "*is believed to*" and "*may be used*" which mirror the doubts arising with the discussions on "constraint effects" in the 1990s.

Specimen configurations are restricted to bend type considering that bending is dominant in the C(T). Thickness is specified by $B = 0.5\ W$. The SE(B) is loaded in three-point bending, Fig. 7.8b, with a support span, $S = 4\ W$. Specimens are fatigue precracked from a starter notch, and the total crack size (crack starter plus fatigue crack) has to be in the range of $0.45 \leq a/W \leq 0.55$. Thus, a nearly square shaped ligament is realised, which guarantees the highest constraint. The requirement that "*the crack-tip plastic zone is small compared to the ... ligament ahead of the crack*" is specified by the size condition,

$$W - a \geq 2.5 \left(\frac{K_{Ic}}{R_0}\right)^2, \tag{7.13}$$

where $R_0 = \sigma_{YS} = R_{p0.2}$ is the 0.2% offset yield strength. It results from Eq. (4.3) with the assumption that $d_p = 2x_p \leq 0.02(W - a)$. The condition of Eq. (7.13) cannot be assured in advance but has to be checked after testing. Thus, specimen dimensions shall be conservatively selected for the first test in a series.

After static testing, a force F_Q is determined by a 5% offset secant in the force-displacement record. If $F_{max}/F_Q \leq 1.1$ a value K_Q is calculated as

$$K_Q = \frac{F_Q}{BW} Y\left(\frac{a}{W}\right), \tag{7.14}$$

depending on the specimen configuration. If the size condition of Eq. (7.13) is met, then $K_{IC} = K_Q$. Ductile materials may require unreasonably large specimens at room temperature, which exceed the disposable raw material and thus set limitations to K_{Ic} testing.

7.2.3 Measurement of Fracture Toughness in EPFM

ASTM E1820 [4] is the standard test method for measurement of fracture toughness for mode I loading using the parameters K, J, and δ. Toughness can be measured as R-curve or as single value. The recommended specimens are single-edge bend, SE (B), compact, C(T), and disk-shaped compact. All specimens contain notches that are sharpened with fatigue cracks. No size conditions as in ASTM E399 are required. Hence, this test method is particularly useful when the material response cannot be anticipated before the test.

Characteristic parameters defined by this standard are

J_c fracture toughness at fracture instability prior to the onset of significant stable tearing crack extension,
J_u fracture instability after the onset of significant stable tearing crack extension,
δ_{Ic} near the onset of slow stable crack extension, defined as occurring at $\Delta a = 0.2\ \text{mm} + 0.7\delta_{Ic}$
δ_c at the onset of unstable crack extension when $\Delta a < 0.2\ \text{mm} + 0.7\delta_c$,
δ_u at the onset of unstable crack extension, when the event is preceded by $\Delta a > 0.2\ \text{mm} + 0.7\delta_u$,
δ_c^* fracture toughness at fracture instability prior to the onset of significant stable tearing crack extension.

The definitions given for characteristic values of J and δ are not completely consistent. A J_{Ic} value as in former standards is not explicitly defined here, any more. It may be understood as converted from K_{Ic} according to Eq. (2.16), addressed as J_{KIC} in annex A9.10. In contrast to the definitions given in section 3 of ASTM E1823 [5] on terminology, J_{Ic} is addressed as "*a size independent value of fracture toughness*" in the annex A9.9, "*if*

- *thickness* $B > 10\ J_Q/\sigma_Y$,
- *initial ligament,* $b_0 > 10\ J_Q/\sigma_Y$", compare Eq. (5.72),
- "*the slope of the power law regression line, dJ/da, evaluated at* Δa_Q *is less than* σ_Y", see Eq. (5.75),

where $\sigma_Y = R_{eff} = 0.5(R_0 + R_m)$, and J_Q is a preliminary value for the load F_Q as K_Q in ASTM E390.

Beside the single values defined above, the standard is particularly relevant for the determination of R-curves, see Sect. 5.1.5 where the respective formulas for evaluating J from the experimental $F(v_L)$ data can be found. Due to severe criticism and uncertainties with respect to J_R-curves in the 1990s (Sect. 5.1.6), the significance and use of the toughness values identified by this test method are qualified to

- "*Serve as a basis for material comparison, selection and quality assurance; rank materials within a similar yield strength range;*
- *Serve as a basis for structural flaw tolerance assessment*."

But: "*Awareness of differences that may exist between laboratory test and field conditions is required to make proper flaw tolerance assessment*". This is all the more important as some statements are not completely consistent as indicated above. Cautionary statements are added

- "*Particular care must be exercised in applying to structural flaw tolerance assessment the fracture toughness value associated with fracture after some stable tearing has occurred. ... This response is especially sensitive to material inhomogeneity and to constraint variations that may be induced by planar geometry, thickness differences, mode of loading, and structural details*."
- "*The J-R curve from bend-type specimens ... has been observed to be conservative with respect to results from tensile loading configurations*"—see Fig. 5.10.
- "*The values of* δ_c, δ_u, J_c, *and* J_u *may be affected by specimen dimensions*", since they are not subject to size conditions.

7.2.4 Crack Extension in Thin Structures

Thick-walled structures like pressure vessels in nuclear power plants have been the primary industrial application area of classical EPFM from the 1960s to 1980s. Respective standards like ASTM E399 and ASTM E1820 and its precursors are hence focused on "high constraint" conditions. Starting with the accident of a de Havilland Comet in 1954 fatigue failure cracks of aircrafts came into focus, and with the Aloha Airlines accident in 1988 ductile rupture of light-weight structures has become an increasingly important issue. Classical EPFM and its testing procedures were not applicable to metal sheets and "low constraint" conditions. In addition, the respective structures are subject to tension rather than bending.

ASTM E561 [3] has been established as the standard test method for determination of the resistance to fracture under quasi-static mode I loading using M(T) or C(T) specimens by a K-R curve, which is defined as continuous record of toughness development in terms of K_R plotted against "effective" crack extension. The standard allows for tension type specimens, and "*materials are not limited by strength,*

thickness or toughness, so long as specimens are of sufficient size to remain predominantly elastic". Any specification what is understood as "sufficient" and "predominant" is missing, however. The term K_R is indistinct as well, since K characterises stress fields in LEFM, and fracture occurs in an unstable manner if K_{Ic} is exceeded. Nothing like a curve $K(\Delta a)$ can hence exist in a strict sense, but before people became acquainted with J they used to formally convert J to K by the relation $K = \sqrt{JE}$. The standard is obviously aimed at small-scale yielding under plane stress conditions in large thin panels and shells, and is therefore particularly applied in aircraft industry.

Different options for the determination of the effective crack length, a_{eff}, exist, either by adding the plastic zone size according to Irwin's Eq. (4.2) to the measured "physical" crack length, Eq. (4.5), or by determining it from the loading compliance,

$$v_L = C_L(a)F + v_L^p = C_L(a_{eff})F \tag{7.15}$$

The physical crack size can be measured by direct observation or by the elastic unloading compliance.

Results of numerical investigations of J_R-curves for thin specimens displayed in Fig. 5.9 show that ASTM E561 based on the SSY correction, Eqs. (4.2) and (4.5), yielded a partly physically meaningless decreasing J_R-curve for the C(T), and did not provide any useful results at all for the M(T) specimen. However calculating a_{eff} from the compliance, Eq. (7.15), gave the best approximation over the whole range up to Δa_{max} for the C(T) and a reasonable one for $\Delta a \leq 0.10(W - a_0)$ for the M(T). On the whole, ASTM E561 is obsolete and its practical use questionable.

ASTM E2472 [6] has been established much later as a standard test method for determination of resistance to stable crack extension in terms of critical crack-tip opening angle (CTOA), ψ_c, and/or crack tip opening displacement (CTOD) as δ_5 resistance curve. Materials are not limited by strength, thickness or toughness, as long as $a/B \geq 4$ and $b/B \geq 4$, ensuring low constraint conditions in M(T) and C (T) specimens. It thus covers the same area of application as ASTM E561, namely ductile rupture of thin structures, but is much more advanced and scientifically up-to date. The background has been addressed in Sect. 5.3.4 and is further described in Newman et al. [26] and Schwalbe et al. [36].

References

1. Abaqus (2014) User's manual, version 6.12. Dassault Systèmes Simulia Corp, Providence, RI, USA
2. ASTM E399 (2012) Standard test method for linear-elastic plane-strain fracture toughness K_{Ic} of metallic materials. Annual book of ASTM standards, vol 03.01. American Society for Testing and Materials, West Conshohocken (PA), USA

3. ASTM E561 (2015) Standard test method for K–R curve determination. Annual book of ASTM standards, vol 03.01. American Society for Testing and Materials, West Conshohocken (PA), USA
4. ASTM E1820 (2015) Standard test method for measurement of fracture toughness. Annual book of ASTM standards, vol 03.01. American Society for Testing and Materials, West Conshohocken (PA), USA
5. ASTM E1823 (2013) Standard terminology relating to fatigue and fracture testing. Annual book of ASTM standards, vol 03.01. American Society for Testing and Materials, West Conshohocken (PA), USA
6. ASTM E2472 (2012) Standard test method for determination of resistance to stable crack extension under low-constraint conditions, Annual book of ASTM Standards, vol 03.01. American Society for Testing and Materials, West Conshohocken (PA), USA
7. Atluri SN, Nishioka T, Nakagaki M (1984) Incremental path-independent integrals in inelastic and dynamic fracture mechanics. Eng Fract Mech 20:209–244
8. Barsoum RS (1977) Triangular quarterpoint elements as elastic and perfectly-plastic crack tip elements. Int J Num Meth Eng 11:85–98
9. Brocks W (2010) Computational fracture mechanics. In: Blockley R, Shyy W (eds) Encyclopedia of aerospace engineering, vol 3. John Wiley & Sons
10. Brocks W, Cornec A, Scheider I (2003) Computational aspects of nonlinear fracture mechanics. In: Milne I, Ritchie RO, Karihaloo B (eds) Comprehensive structural integrity—Numerical and computational methods, vol. 3. Elsevier, pp 127–209
11. Brocks W, Eberle A, Fricke W, Veith H (1994) Large stable crack growth in fracture mechanics specimens. Nucl Eng Design 151:387–400
12. Brocks W, Müller W, Olschewski J (1985) Experiences in applying ADINA to the analysis of crack tip fields in elastic-plastic fracture mechanics. Comput Struct 21:137–158
13. Brocks W, Rabbolini S (2015) Computational fracture mechanics. Report students project, Dipartimento di Meccanica, Politecnico di Milano
14. Brocks W, Scheider I (2003) Reliable J-values—Numerical aspects of the path-dependence of the J-integral in incremental plasticity. Materialpruefung 45:264–275
15. Brocks W, Yuan H (1989) Numerical investigations on the significance of J for large stable crack growth. Eng Fract Mech 32:459–468
16. Brust FW, Nishioka T, Atluri SN (1985) Further studies on elastic-plastic stable fracture utilizing the T*-integral. Eng Fract Mech 22:1079–1103
17. DeLorenzi HG (1982) Energy release rate calculations by the finite element method. General Electric Technical Information Series, Report No. 82CRD205
18. DeLorenzi HG (1982) On the energy release rate and the J-integral for 3D crack configurations. J Fracture 19:183–193
19. Gosz M, Dolbow J, Moran G (1998) Domain integral formulation for stress intensity factor computation along curved three-dimensional interface cracks. Int J Solids Stuctures 35: 1763–1783
20. Griffith AA (1920) The phenomena of rupture and flow in solids. Phil Trans Roy Soc London A211:163–198
21. Gullerud AS, Dodds RH, Hampton RW, Dawicke DS (1999) Three-dimensional modeling of ductile crack growth in thin sheet metals, computational aspects and validation. Eng Fract Mech 63:347–374
22. Kuna M (2013) Finite elements in fracture mechanics. Springer, Dordrecht
23. Li FZ, Shih CF, Needleman A (1985) A comparison of methods for calculating energy release rates. Eng Fract Mech 21:405–421
24. Maugin GA (1995) Material forces: concepts and applications. Appl Mech Rev 48:213–245
25. McMeeking RM, Rice JR (1975) Finite-element formulations for problems of large elastic-plastic formulations. Int J Solids Struct 11:601–616

26. Newman JC, James MA, Zerbst U (2003) A review of the CTOA/CTOD fracture criterion. Eng Fract Mech 70:371–385
27. Parks DM (1974) A stiffness derivative finite element technique for determination of crack tip stress intensity factors. Int J Fract 10:487–502
28. Parks DM (1977) The virtual crack extension method for nonlinear material behaviour. Comp Meth Appl Mech Eng 12:353–364
29. Rice JR (1965) An examination of the fracture mechanics energy balance from the point of view of continuum mechanics. In: Yokobori T, Kawasaki T, Swedlow JK (eds) Proceedings of 1st international of conference fracture, Sendai, Japan, pp 309–340
30. Rice JR (1979) The mechanics of quasi-static crack growth. In: Kelly RE (ed) Proceedings of 8th international congress for applied mechanics, pp 191–216
31. Rice JR, Drugan WJ, Sham TL (1980) Elastic-plastic analysis of growing cracks. In: Paris PC (ed) Fracture Mechanics, ASTM STP 700. American Society for Testing and Materials
32. Rice JR, Paris PC, Merkle JG (1973) Some further results of J-integral analysis and estimates. In: Kaufman J, Swedlow J, Corten H, Srawley J, Heyer R, Wessel E, Irwin G (eds) Progress in Sih GE (1974) Strain energy density factor applied to mixed mode crack problems. Int J Fracture 10:305–321
33. Richard HA, Fulland M, Sander M (2005) Theoretical crack path predictions. Fatigue Fract Eng Mater Struct 28:3–12
34. Scheider I, Schödel M, Brocks W, Schönfeld W (2006) Crack propagation analyses with CTOA and cohesive model: Comparison and experimental validation. Eng Fract Mech 73:252–263
35. Schwalbe KH, Landes JD, Heerens J (2007) Classical fracture mechanics methods. In: Milne I, Ritchie RO, Karihaloo B (eds) Comprehensive structural integrity–Fracture of materials from nano to macro, vol 11. Elsevier, pp 9–42
36. Schwalbe KH, Newman JC, Shannon J (2005) Fracture mechanics testing on specimens with low constraint—standardisation activities within ISO and ASTM. Eng Fract Mech 72: 557–576
37. Shih CF, Asaro RJ (1988) Elastic-plastic analysis of cracks on bimaterial interfaces: part I – small scale yielding. J Appl Mech 55:299–316
38. Shih CF, Moran B, Nakamura T (1986) Energy release rate along a three-dimensional crack front in a thermally stressed body. Int J Fracture 30:79–102
39. Siegele D, Schmitt W (1983) Determination and simulation of stable crack growth in ADINA. Comput Struct 17:697–703
40. Yuan H, Brocks W (1991) On the J-integral concept for elastic-plastic crack extension. Nucl Eng Design 131:157–173
41. Zerbst U, Schödel M, Beier HT (2011) Parameters affecting the damage tolerance behaviour of railway axles. Eng Fract Mech 78:793–809

Chapter 8
Damage and Fracture

Abstract Micromechanical aspects, mechanisms and models of fracture are addressed, which have become increasingly topical since the 1990s though the basic ideas and perceptions date back to the early years of fracture mechanics. The characteristics of brittle and ductile damage on the micro-scale and the respective fractographic appearance are outlined and the implications on local criteria of fracture are specified. Two approaches for establishing constitutive equations of damage are distinguished, namely micro-mechanical models which aim at describing the physical processes of damage on the micro-scale following the concept of representative volume elements and phenomenological constitutive equations for stresses and strains describing macroscopically observable effects of degradation based on thermodynamical principles. Two particular models of major significance, the Gurson and the Rousselier yield function are described. A brief introduction to parameter identification ends the chapter.

The following chapter turns from the macroscopic to a microscopic view, i.e. to the mechanisms of damage and fracture at the scale of the micro-structure of polycrystals and their mathematical modelling. Since the respective literature fills books, just a rather raw overview on characteristic phenomena can be given intending to convey some physical understanding of the micromechanical background of macroscopic fracture. Though local approaches like the statistical theory of brittle fracture by Weibull [67, 68] or the RKR criterion of Ritchie et al. [44] were proposed prior or in parallel to the progress of macroscopic fracture mechanics, the latter became much more successful for engineering applications, in the beginning. It encountered limits, however: Controversial discussions in the 1980s and 1990s on unrecognised phenomena like geometry dependence of fracture parameters and R-curves could only be cleared after reconsidering the micro-mechanisms of fracture [16] and establishing respective damage models. Damage mechanics complements fracture mechanics but cannot substitute it, however, as dislocation dynamics helps in understanding phenomena of plastic deformation but cannot replace phenomenological plasticity.

W. Brocks, *Plasticity and Fracture*, Solid Mechanics and Its Applications 244,
DOI 10.1007/978-3-319-62752-6_8

The literature on damage models is vast and fills books [30, 31]. Any claim for completeness would be hubristic. The present chapter hence focuses to some aspects of brittle and predominantly to models of ductile fracture of metals to complete the present view on ductile fracture.

8.1 Phenomena and Models

During deformation, the cohesion of matter is conserved. Elastic deformations of metals occur on the atomic level by reversible changes of the interspaces. This alters the volume of a body. Plastic deformations happen on crystallographic planes by motion of dislocations resulting in permanent shifts of atoms of one plane against the atoms of the neighbouring plane. The volume is not changed by this process. Pile-up of dislocations at grain boundaries, particles or intersecting planes induces macroscopic hardening. The phenomenological behaviour on the macro-scale is stable in Drucker's sense (Sect. 6.1.1) for both elastic and plastic deformations.

In contrast to this, damage is characterised by the development of laminar or volumetric discontinuities at the micro-scale like micro-cracks or -voids. The discontinuities are induced by local concentration of deformation like pile-up of dislocations in metals, changes of molecular bonds in organic substances, micro-decohesions at crystallographic imperfections in minerals. Damage evolution is an irreversible process whose global manifestation can hardly be discerned from inelastic deformations. The effects of damage are significantly different, however. Damage causes reduction of performance (degradation) of structures and softening, i.e. unstable material behaviour. Macroscopic effects comprise decreasing of elastic modulus, yield strength, hardness, density, sound-propagation velocity, increasing of creep strain rate, electrical resistance etc. Damage can result in macroscopic cracks and finally global failure of a structure. Examples for damage processes are micro-cracking or ductile damage of metals, creep damage, fiber cracking or fiber-matrix delamination in reinforced composites, corrosion, fatigue etc.

Failure under macroscopically elastic deformation is called "brittle" fracture though it is preceded by micro-plasticity in metals. It is characterised by intergranular separation or transgranular cleavage at the microscale. Fractographic images display typical shining facets, Fig. 8.1a. Ductile fracture or rupture occurs at significant global plastic deformation and is the outcome of growth of micro-voids. The fracture surface is matted and shows a honeycombed structure with dimples at larger magnification, Fig. 8.1b. Fatigue fracture is the initiation and growth of macro-cracks by micro-plasticity under alternating loads. Creep fracture is due to the growth of cavities mainly at grain boundaries by diffusion processes at high temperatures. Both fatigue and creep fracture finally lead to fast fracture and global failure after a critical crack length is reached. Stress corrosion cracking is the unexpected sudden failure of normally ductile metals subjected to tensile stresses in a corrosive environment.

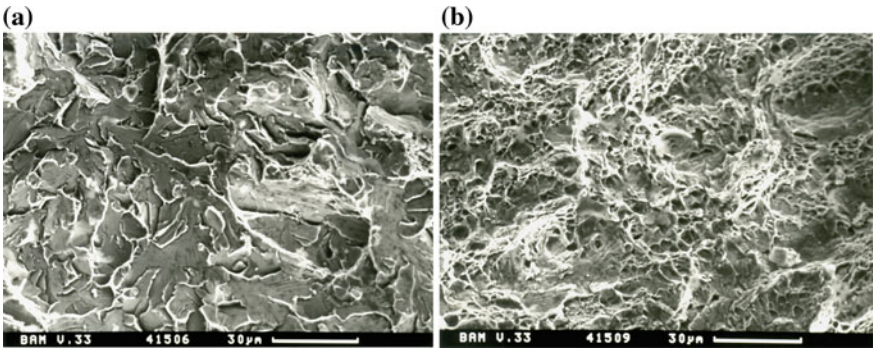

Fig. 8.1 Fracture surfaces of the steel 15NiCuMoNb5 **a** cleavage and **b** ductile rupture, Aurich et al. [1]

The point-shaped crack tip of classical fracture mechanics is a mathematical idealisation. In reality, a finite region, the process zone, exists where material is damaged and finally separated so that new surfaces are created. In this region, micromechanical mechanisms of damage are dominant. Three levels of abstraction exist for modelling this process:

- The process zone has shrunk to a point in classical fracture mechanics. Material behaviour is characterised by conventional constitutive equations like elasticity, plasticity or viscoplasticity, and a macroscopic criterion for crack growth based on "driving forces" like K, J, CTOD, CTOA is required. Crack growth is realised by node release in FEM [49].
- The process zone is assumed as a surface, the cohesive zone, and separation is determined by phenomenological decohesion laws (see Chap. 9 on the cohesive model) by which new crack faces are created. The material outside of this zone is described by conventional constitutive equations.
- The process zone is an actual volume in which the degradation of the material occurs. The softening is captured by additional internal variables characterising the local damage which evolves with loading. Critical values of these variables represent the fracture criterion. Two approaches can be distinguished, namely
  - Micro-mechanical models which aim at describing the physical processes of damage on the micro-scale, which are nucelation, growth and coalescence of micro-voids, initiation of micro-cracks etc., following the concept of representative volume elements (Sect. 8.2.3), and
  - Phenomenological constitutive equations for stresses and strains describing macroscopically observable effects of degradation based on thermodynamical principles (Sect. 8.4).

8.2 Local and Micromechanical Approaches

8.2.1 Brittle Fracture and Cleavage

Genuine brittle materials are ceramics, glass, rocks etc., which do not show any inelastic deformation. Initiation sites of micro-cracks are "built-in" defects and imperfections like micro-cavities in sintered materials or interfaces in rocks. The term "brittle" for polycrystals is macroscopically motivated, because failure occurs abruptly out of the elastic regime though it is associated with some local plasticity at the grain-scale. The initiation of micro-cracks in metals is due to dislocation pile-up at obstacles like grain boundaries, inclusions or particles, or at intersecting dislocations, Fig. 8.2. Different from ceramics, initiation sites in polycrystals evolve with loading. Obstacles which stop the free motion of dislocations are beneficial for strength and hardening of metals. Refinement of grains or precipitation hardening is therefore often executed to produce high-strength alloys. But at the same time, this procedure increases the predisposition to micro-crack initiation and thus the risk of "catastrophic" failure. Numerous examples of unexpected failure can be found because engineers chose a "high strength" material to reduce the weight of a structure or to improve the fatigue resistance but did not consider the increased susceptibility of the material to crack initiation.

As material separation occurs along lattice planes, crack growth is discontinuous and has to follow the lattice orientations of the grains. This leads to the typical facets of the fracture surface as displayed in Fig. 8.1a. The microstructurally justified term for this type of fracture is transgranular fracture or cleavage.

Initiation and coalescence of micro-cracks is stress controlled. Since a number of geometrical and physical parameters like grain size, orientation of lattice planes to global loading, inhomogeneous local toughness properties etc. affect this process, it is highly stochastic, and as no dissipative terms like macroscopic plasticity are involved, global brittle failure reveals scatter as well. Particularly in body centred cubic (bcc) materials, a transition region in dependence on the temperature from low-toughness cleavage to high-toughness ductile tearing exists where significant scatter occurs [29, 66]. Existing micromechanical models of cleavage [12, 19] are based on both deterministic and stochastic approaches.

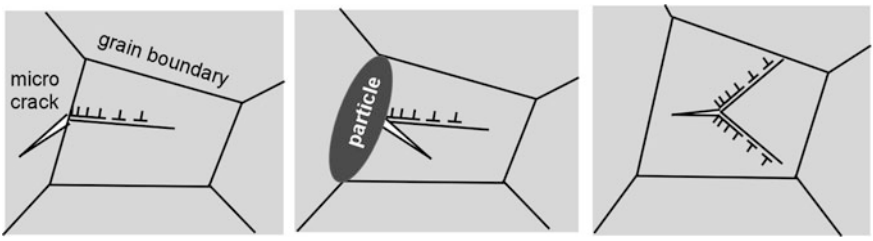

Fig. 8.2 Initiation of micro-cracks due to dislocation pile-up at grain boundary, inclusion (particle) or intersecting dislocations

The Swedish engineer and mathematician Weibull [67, 68] was the first who studied the stochastic nature of brittle failure. His basic idea is the so-called "weakest link" assumption that the probability of having cleavage fracture of a structure at any given load equals the probability that its weakest element (link) fails at this load. The macroscopic failure criterion of Griffith, Eq. (2.13), is established on a "mesoscopic" level for every material element, (i), which is subject to a principal stress, $\sigma_{\mathrm{I}}^{(i)}$. The corresponding critical length, $\ell_{\mathrm{c}}^{(i)} = 2a_{\mathrm{c}}^{(i)}$, of an assumed microcrack derives from Griffith's criterion as

$$\ell_{\mathrm{c}}^{(i)} = \frac{4E'\gamma}{\pi\left(\sigma_{\mathrm{I}}^{(i)}\right)^2}. \tag{8.1}$$

Now assume that the probability of having a crack in the element (i) is inversely proportional to its length, $P(\ell_i) = \alpha_1/\ell_i^{\alpha_2}$, where α_1 and α_2 are parameters depending on the material's microstructure and mechanism of microcrack formation. Then its failure probability becomes

$$P_{\mathrm{f}}^{(i)}\left(\sigma_{\mathrm{I}}^{(i)}\right) = \int_{\ell_{\mathrm{c}}^{(i)}}^{\infty} P(\ell_i)d\ell_i = \left(\frac{\sigma_{\mathrm{I}}^{(i)}}{\sigma_{\mathrm{u}}}\right)^m \tag{8.2}$$

with the Weibull parameters,

$$m = 2(\alpha_2 - 1), \tag{8.3}$$

and

$$\sigma_{\mathrm{u}} = \left(\frac{\alpha_2 - 1}{\alpha_1}\right)^{1/m}\sqrt{\frac{4E'\gamma}{\pi}}. \tag{8.4}$$

According to the weakest link assumption, the survival probability of a structure of n elements is

$$1 - P_{\mathrm{f}} = \prod_{i=1}^{n}\left[1 - P_{\mathrm{f}}^{(i)}\left(\sigma_{\mathrm{I}}^{(i)}\right)\right]. \tag{8.5}$$

For $P_{\mathrm{f}}^{(i)} \ll 1$, this equation can be transformed as $\ln(1 - P_{\mathrm{f}}) \approx \sum_{i=1}^{n} P_{\mathrm{f}}^{(i)}\left(\sigma_{\mathrm{I}}^{(i)}\right)$ so that the failure probability [69] of the entire structure becomes

$$P_{\mathrm{f}}(\sigma_{\mathrm{W}}) = 1 - \exp\left[-\left(\frac{\sigma_{\mathrm{W}}}{\sigma_{\mathrm{u}}}\right)^m\right], \tag{8.6}$$

where the Weibull stress, σ_W, is obtained by a summation of the maximum principal stresses, which can be done by an integration,

$$\sigma_W = \left[\frac{1}{V} \int_V \left(\sigma_1^{(i)} \right)^m dV \right]^{1/m}, \tag{8.7}$$

if the stress distribution is known analytically or by a summation over the finite elements

$$\sigma_W = \left[\sum_{i=1}^{n} \left(\sigma_1^{(i)} \right)^m \frac{V_i}{V_0} \right]^{1/m}, \tag{8.8}$$

with some reference volume, V_0, if the stress distribution results from a numerically analysis.

The French team of authors, Beremin [4], which stands for Dominique François, François Mudry, André Pineau, presented this model as a "local approach" for calculating the failure probability of ferritic steels [28]. Since plastic deformations are a prerequisite for the initiation of micro-cracks in a metal, the integration or summation is performed over the plastically deformed part of the volume, only. Using a summation over "elements" instead of an integration over the volume does not only refer to its application in FEM but also accounts for the necessity of averaging stresses over some characteristic volume, particularly in regions of steep stress gradients as at a crack tip. The choice of V_0 is controversial. There is some minimum volume for a given microstructure for which statistical independence (see Sect. 8.2.3 on representative volume elements) can be assumed. Average stress values over much smaller volumes are not reasonable. That is why the reference volume is often taken as the minimum mesh size [35]. For low stress gradients the mesh size is not significant and V_0 may be chosen arbitrarily [4], but as it affects the reference stress, σ_u, by $\sigma_u^m V_0 = \text{constant}$, a transfer of Weibull distributions from specimens to components is only admissible for a fixed reference volume. No physical meaning should be assigned to σ_u in the case of an arbitrarily chosen V_0, anyway.

Though the Weibull parameters, m and σ_u, are related to physical quantities, Eqs. (8.3) and (8.4), they are phenomenological and determined by tests of notched tensile bars complemented by a FE analysis [17]. A sample of N specimens is tested and the specimens are ordered in ascending sequence with respect to a monotonically increasing loading parameter, commonly the external displacement, which uniquely characterises the event of cleavage failure. A relative failure probability, $P_j = (j-0.5)/N$, is correlated with the respective Weibull stress, σ_W, Eq. (8.8), which is determined in dependence on the loading parameter by an elastoplastic FE analysis. As m is unknown in the beginning, the evaluation starts with an assumed value which is updated in an iterative procedure. The data are plotted as ln [ln (1/(1 $-P_f$))] versus ln (σ_W/MPa) to assure that they follow a Weibull distribution with

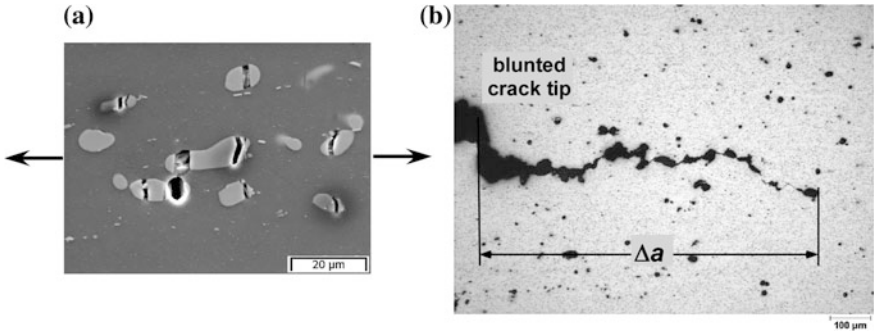

Fig. 8.3 Ductile crack extension: **a** nucleation of voids by particle fracture or matrix decohesion at particles; **b** coalescence of voids ahead of a crack tip

sufficient accuracy. The parameters, m and σ_u, are assessed by the maximum likelihood method.

Whereas the determination of Weibull parameters as material properties is common practice for ceramics, their application to cleavage fracture of metals encountered numerous problems. The definition of V_0 has been addressed above, already. A second problem is the magnitude of the Weibull exponent m for common steels, which is about 20. Thus, when calculating $\sqrt[20]{\sigma_I^{20}}$ in Eq. (8.8) one must not only take care of numerical inaccuracy but the result equals more or less the maximum of σ_I occurring in the structure, i.e. the stresses in the crack tip element which are of dubious significance. A third one appeared with experimental efforts to predict the temperature dependence of fracture toughness, where it was assumed that Weibull parameters do not depend on the temperature. Respective investigations of various specimens at different temperatures and loading rates raised doubts, however. The reason is quite obvious: Different from ceramics where the defect distribution is material specific and determined by the manufacturing process, defects in a ductile metal form with plastic deformation and the defect distribution will therefore depend on the loading history. In addition, nucleated defects may just enlarge in a ductile manner (Sect. 8.2.2) and not become the origin of cleavage. Several phenomenological modifications introducing the plastic strain among others, have been proposed for this reason (Mudry [35], Bernauer et al. [6]). After all, the expectance liaised with this local approach was not fulfilled.

Ritchie et al. [44] suggested a deterministic model based on a material specific cleavage fracture stress, σ_c, known as RKR model according to the names of the authors. As stresses become infinite at the crack tip in LEFM, they introduced an additional parameter, x_c, the critical distance from the crack tip, which was assumed to be a material parameter depending on the grain size [14, 15]. Cleavage occurs if

$$\sigma_{yy}(x_c) \geq \sigma_c. \tag{8.9}$$

Discussions on the significance of the cleavage strength and its temperature dependence have been topical in the 1980s for predicting the transition behaviour of ferritic steels but statistical models gained more interest and importance after all [29].

8.2.2 *Ductile Damage und Fracture*

Ductile damage and fracture of metals is governed by the nucleation of voids at inclusions or particles and their growth up to final coalescence [2, 3, 53, 59–61]. Figure 8.3 shows the nucleation of voids by breaking particles or matrix decohesion for an aluminium alloy and the growth of a crack by coalescence of voids ahead of the crack tip. Coalescence may occur by the formation of shear bands between larger voids or along a second population of smaller particles like carbides. It is preceded by localisation of deformation [62]. Whereas models of stress or strain controlled void nucleation have been established [13] and void growth has been intensively studied both analytically and numerically [34, 43, 59], the process of void coalescence is more complex [27, 60] and often just captured empirically by fitting numerical simulations to test data [63].

Void growth is strain controlled but depends on the hydrostatic stress as was shown by McClintock [34] for a 2D plane strain model, Fig. 8.4a, and Rice and Tracey [43] for a spherically symmetric void, Fig. 8.4b. This dependence explains the experimental result of Bridgmen [7] that the failure strain of tensile bars depends on hydrostatic pressure (and is hence no physically meaningful material parameter).

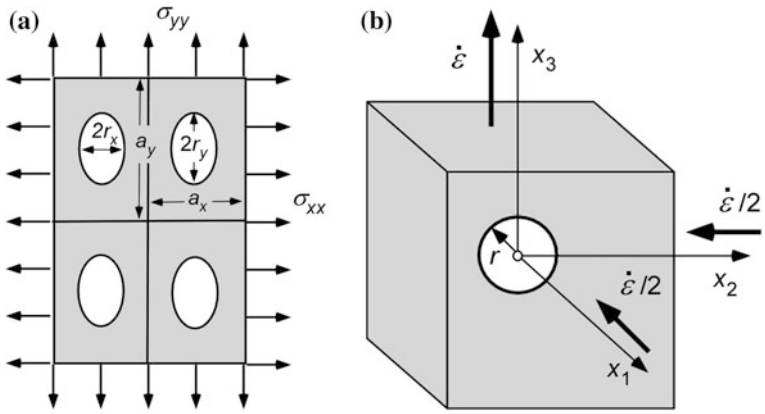

Fig. 8.4 Void growth models of **a** McClintock [34], **b** Rice and Tracey [43]

McClintock [34] considered a regular arrangement of unit cells (Sect. 8.2.3) in plane strain having the dimensions a_x, a_y including elliptical voids with principal axes, $2r_x$, $2r_y$, Fig. 8.4a, and introduced the logarithmic damage measure

$$D_{zx} = \int dD_{zx} = \int \frac{d[\ln(r_x/a_x)]}{\ln\left(a_x^0/r_x^0\right)} \leq 1. \tag{8.10}$$

which becomes 1 in the case of void coalescence, $2r_x = a_x$. For a power-law hardening material, $\bar{\sigma} = c\bar{\varepsilon}_{\mathrm{p}}^N \approx c\bar{\varepsilon}^N$, the damage evolution can be calculated,

$$\frac{dD_{zx}}{d\bar{\varepsilon}} = \frac{1}{\ln\left(a_x^0/r_x^0\right)} \left[\frac{\sqrt{3}}{2(1-N)} \sinh\left(\frac{\sqrt{3}(1-N)}{2} \frac{\left(\sigma_{xx}+\sigma_{yy}\right)}{\bar{\sigma}} \right) + \frac{3}{4} \frac{\sigma_{xx}-\sigma_{yy}}{\bar{\sigma}} \right], \tag{8.11}$$

and the coalescence criterion yields the fracture strain,

$$\varepsilon_{\mathrm{f}} = \frac{(1-N)\ln\left(a_x^0/r_x^0\right)}{\sinh\left(\left[(1-N)\left(\sigma_{xx}+\sigma_{yy}\right)/\left(2\bar{\sigma}/\sqrt{3}\right)\right]\right)}, \tag{8.12}$$

which depends exponentially on the stress triaxiality, Eq. (5.37),

$$\eta = \frac{\sigma_{\mathrm{h}}}{\bar{\sigma}} = \frac{\sigma_{xx}+\sigma_{yy}}{2\bar{\sigma}}. \tag{8.13}$$

Rice and Tracey [43] consider a spherical cavity of radius, r, in a strain field meeting the incompressibility condition of Eq. (3.9), $\dot{\varepsilon}_{33} = \dot{\varepsilon}$, $\dot{\varepsilon}_{11} = \dot{\varepsilon}_{22} = -\frac{1}{2}\dot{\varepsilon}$, of an infinite perfectly plastic continuum, Fig. 8.4b. The assumption of a "rigid"-plastic material, which is often spread in the literature, is unnecessary as is shown by Theorem (I) in Sect. 6.1.2 on plastic collapse. Rice and Tracey provide an approximate solution,

$$D = \frac{\dot{r}}{\dot{\varepsilon} r} \approx 0.283 \exp\left(\frac{2}{3}\eta\right). \tag{8.14}$$

Huang [25] presented a modification of the proportionality factor in Eq. (8.14) for high triaxialities but also confirmed the exponential dependence of void growth on η, Eq. (5.37). Thus, the attempt to use η as a second parameter for scaling J_{R}-curves has some micromechanical justification, at least. The drawback is that η is a local quantity depending on the distance to the crack tip whereas J is a global fracture parameter.

Based on the void-growth model of Rice and Tracey, Eq. (8.14), Beremin [3, 4] suggested a local approach to ductile fracture. Crack initiation occurs for $D = D_{\mathrm{c}}$, which is determined from a test of a notched tensile bar [17]. It is an uncoupled model, which, like the model of cleavage fracture, allows for an a posteriori

calculation of damage from the conventionally evaluated stress and strain field, only. Thus, only the crack initiation and no crack extension can be predicted. A coupling of damage as an inner variable in the constitutive equations has been realised in the models of Gurson [24] and Rousselier [45], see Sect. 8.3 on porous metal plasticity.

8.2.3 The Concept of Representative Volume Elements

A material element is an infinitesimal neighbourhood, $\Delta V = \Delta x \Delta y \Delta z \rightarrow 0$, of a material point in classical (local) continuum mechanics. Material properties, stresses and strains of these idealised materials are assumed as homogeneous in ΔV. In real materials, however, the material neighbourhood is not homogeneous but exhibits a complex and evolving micro-structure.

Micromechanics now tackles the problem of expressing the constitutive equations in terms of quantities which characterise the micro-structure and its properties [39]. For this, the concept of representative volume elements (RVE) is used. An RVE is a material volume which is considered as statistically representative for the microstructure of the material and constitutes the neighbourhood of an arbitrary material point. It will, in general, contain a number of cavities, cracks, particles or inclusions. If the microstructure is idealised as periodic arrangement of volume elements with just one cavity or particle as in Fig. 8.5, these elements are sometimes called unit cells or "computational cells" [2, 18, 20, 47, 70, 71].

The constitutive behaviour is described on a meso-scale by mesoscopic stress and strain fields defined by homogenisation (averaging) over the RVE

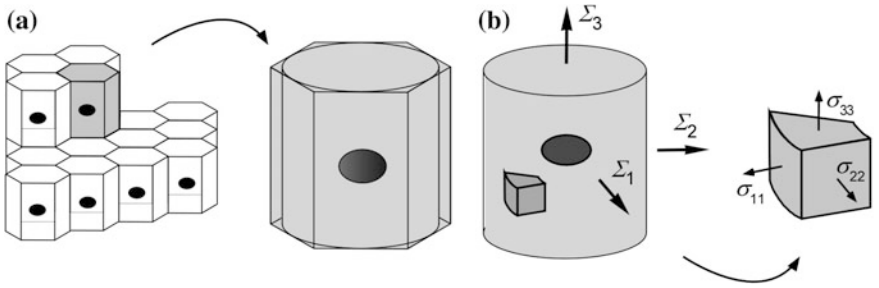

Fig. 8.5 Schematic of micromechanical approach: **a** macro-scale (structure), **b** meso-scale (unit cell)

$$\Sigma_{ij} = \frac{1}{V_0}\int\limits_{V_0} \sigma_{ij}(x_k)dV = \frac{1}{\partial V_0}\int\limits_{\partial V_0} x_i t_j \, dS$$
$$E_{ij} = \frac{1}{V_0}\int\limits_{V_0} \frac{1}{2}\left(u_{i,j} + u_{j,i}\right)dV = \frac{1}{\partial V_0}\int\limits_{\partial V_0} \frac{1}{2}\left(n_i u_j + n_j u_i\right) dS. \tag{8.15}$$

Typical unit cells for describing ductile damage are cylinders with spherical or ellipsoidal cavities, Koplik and Needleman [28]. Figure 8.6 displays the mesoscopic response in terms of mesoscopic stresses, Σ_{33}, versus logarithmic strains, E_{33}, of a cylindrical unit cell of initial diameter, d_0, and height, $h_0 = d_0$, with a spherical void of volume fraction $f_v^0 = 0.005$, Brocks et al. [10]. It confirms the effect of (mesoscopic) triaxiality, $\eta = \Sigma_h/\bar{\Sigma} = \Sigma_{kk}/3\bar{\Sigma}$, on maximum stress and ductility: increasing triaxiality raises ultimate stress but lowers failure strain. Actually, the area under the $\Sigma_{33}(E_{33})$ curve represents the work of separation in Eq. (5.75) for a crack extension of $\Delta A_c = \pi d^{\,2}/4$,

$$h\int \Sigma_{33} dE_{33} = \frac{\Delta U_{sep}}{\Delta A_c} = \Gamma_c. \tag{8.16}$$

The steep decrease of Σ_{33} in the final stage is due to local internal necking. In an arrangement of unit cells like in Fig. 8.5a, the void would start interacting with neighbouring voids.

The mesoscopic behaviour depends also on the void shape, of course. Gologanu et al. [21, 22] studied unit cells with elliptical voids. Constitutive equations for porous materials are just one possible application of micromechanics, of course.

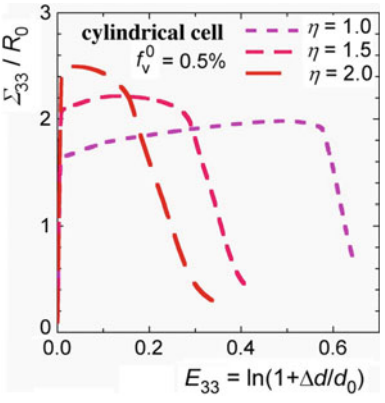

Fig. 8.6 Mesoscopic response of a cylindrical unit cell, diameter d_0, with spherical void, $f_v^0 = 0.005$, in dependence on triaxiality, Brocks et al. [10]

8.3 Porous Metal Plasticity

Porous metal plasticity accounts for the fact that real materials are not ideally dense but contain cavities at the microscale which grow with hydrostatic tension (Sect. 8.2.2). The basic features that no plastic volume dilatation occurs, Eq. (3.9), and that the yield condition does not depend on the hydrostatic stress are lost. If the softening effect of void growth exceeds plastic hardening, the material does not meet Drucker's stability condition, Eq. (6.6), any more. The yield surface is still supposed to be convex, and an associated flow rule, Eq. (3.12), is adopted. The effect of voids on elasticity, i.e. Young's modulus is disregarded.

8.3.1 Gurson Model

Gurson [24] calculated the mesoscopic yield surface of a perfectly plastic material by homogenisation of two- and three-dimensional unit cells containing cylindrical or spherical cavities, respectively,

$$\frac{\bar{\Sigma}^2}{R_0^2} + 2f_\mathrm{v}\cosh\left(\frac{3\Sigma_\mathrm{h}}{2R_0}\right) - 1 - f_\mathrm{v}^2 = 0, \tag{8.17}$$

which depends on the local void-volume fraction,

$$f_\mathrm{v} = \frac{\Delta V_\mathrm{void}}{\Delta V_\mathrm{RVE}}, \tag{8.18}$$

representing volumetric damage. Actually, ΔV_void is the total volume of all voids within ΔV_RVE and not just a single void as in the unit cell, and f_v is the average porosity. For $f_\mathrm{v} = 0$, Eq. (8.17) turns into the von Mises yield condition, $\bar{\Sigma}^2 - R_0^2 = 0$, with $\bar{\Sigma} = \sqrt{\frac{3}{2}\bar{\Sigma}'_{ij}\bar{\Sigma}'_{ij}}$ as mesoscopic equivalent stress.

The yield surface of Gurson is no cylinder as in Fig. 3.2 anymore but capped at the ends, Fig. 8.7a. It is symmetric in hydrostatic tension and compression.

Damage evolution results from void growth,

$$\dot{f}_\mathrm{v}^\mathrm{growth} = (1 - f_\mathrm{v})\dot{E}_{kk}^\mathrm{p}, \tag{8.19}$$

which is derived from conservation of mass and incompressibility of the plastic matrix material. Note that due to void growth the "mesoscopic" plastic volume dilatation of porous materials, $\dot{E}_{kk}^\mathrm{p}$, is not zero, of course.

Equation (8.17) is limited to a perfectly plastic matrix material and does not account for the interaction of neighbouring voids. Tvergaard and Needleman [63] and Needleman and Tvergaard [37, 38] introduced several phenomenological

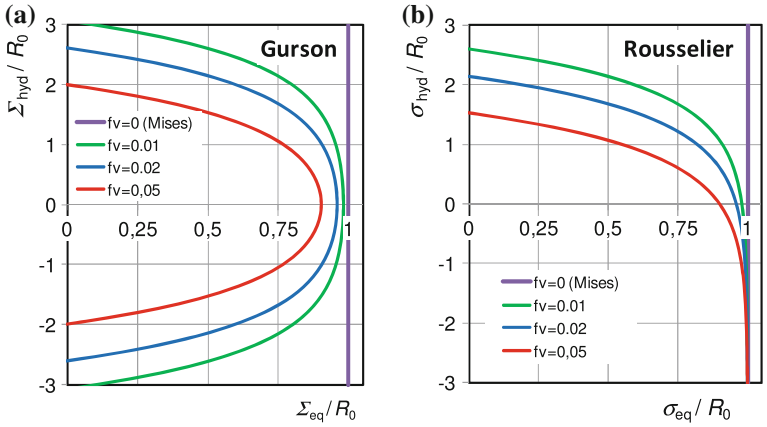

Fig. 8.7 Effect of void volume fraction, f_v, on yield surfaces of **a** Gurson [24], $\Sigma_{eq} \equiv \bar{\Sigma}$, **b** Rousselier [45], $\sigma_{eq} \equiv \bar{\sigma}$, perfectly plastic matrix material

modifications for the application of the Gurson model to ductile crack extension and fracture of metals. They replaced the yield strength, R_0, by the flow curve, $R_F(\varepsilon_p)$, inserted three adjustable parameters, q_1, q_2, q_3, and incorporated the effect of void coalescence by modifying the damage variable, $f_v \rightarrow f_v^*(f_v)$,

$$\frac{\bar{\Sigma}^2}{R_F^2(\varepsilon_p)} + 2q_1 f_v^* \cosh\left(q_2 \frac{3\Sigma_h}{2R_F^2(\varepsilon_p)}\right) - 1 - q_3 f_v^{*2} = 0. \tag{8.20}$$

The modified damage variable equals the void volume fraction up to a critical value, f_v^c, which characterises the onset of void coalescence, and increases more rapidly by a factor κ_f beyond,

$$f_v^*(f_v) = \begin{cases} f_v & \text{for} \quad f_v \le f_v^c \\ f_v^c + \kappa_f\left(f_v - f_v^c\right) & \text{for} \quad f_v > f_v^c \end{cases}. \tag{8.21}$$

The factor κ_f is defined as

$$\kappa_f = \frac{f_u^* - f_v^c}{f_v^f - f_v^c}, \tag{8.22}$$

with f_v^f as the void volume fraction at failure, i.e. loss of stress carrying capacity, and

$$f_u^* = \frac{q_1 - \sqrt{q_1^2 - q_3}}{q_3} \tag{8.23}$$

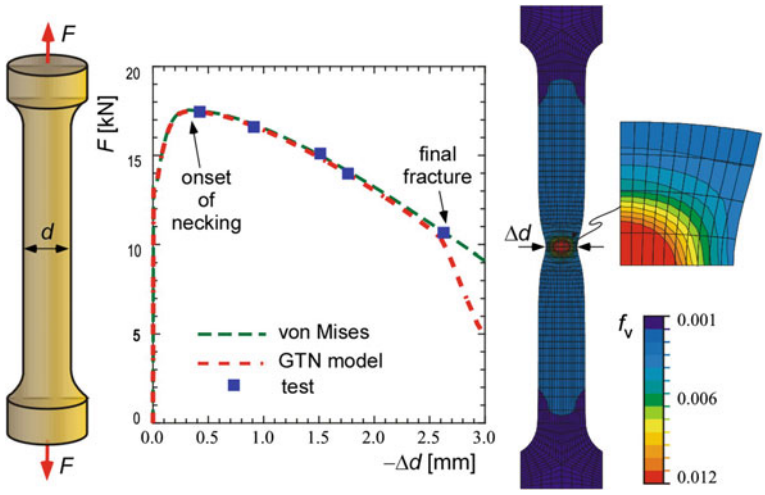

Fig. 8.8 Tensile test of a round bar, test data and simulations with Mises-Prandtl-Reuß equations and GTN model: force, F, versus reduction of diameter, $-\Delta d$

as the respective ultimate damage value. In practice, κ_f is not determined from Eq. (8.22) but empirically fixed as some large number in order to match the steep decrease of the force in a tensile test after the onset of fracture, Fig. 8.8. The parameters q_1, q_2, q_3 are commonly assumed as $q_1 = 1.5$, $q_2 = 1$, $q_3 = q_1^2 = 2.25$ [65], and hence $f_u^* = 1/q_1 = 2/3$.

The yield function (plastic potential) of Eq. (8.20) is known as GTN model owing to the initials of the authors. It has found frequent applications for simulations of ductile crack extension in metals, e.g. Sun et al. [58], Brocks et al. [8], Bernauer and Brocks [7], Steglich [52]. The parameters are partly identified from tensile tests. Figure 8.8 displays respective results in terms of force versus reduction of diameter. Localised necking of the bar starts at maximum force and results in a decreasing curve due to (macroscopic) geometric instability, while the true stress-strain curve is still increasing due to plastic hardening. A large-strain analysis with the Mises-Prandtl-Reuß equations (Sect. 3.3.2) matches this macroscopic behaviour. Any effects of damage are negligible in this state. The von Mises theory will not predict fracture, however, but an unlimited reduction of diameter. A rather sudden evolution of damage in the necking zone as described by the GTN model results in a much steeper decrease of the load which indicates fracture. The respective point is triggered by the parameter f_v^c characterising the onset of void coalescence, which is hence commonly identified by fitting numerical simulations to test data. As it interacts with the value of the initial void-volume fractions, f_v^0, this procedure is not unique. Zhang et al. [73] implemented a coalescence criterion based on a model of Thomason [59]. They call their approach the "complete" Gurson model and use the tensile test data for identifying f_v^0.

For further information on parameter identification see Sect. 8.5 and Brocks and Steglich [9]. The GTN model predicts that damage starts in the centre of a smooth tensile bar and at the notch root for sharply notched bars. It is also capable of predicting the geometry effect on J_R-curves, Fig. 8.9, which additionally contains simulation results obtained with the cohesive model (Chap. 9), Siegmund et al. [50]. As shown in Fig. 8.6, local void growth and coalescence and hence dU_{sep}/dA_c are dependent on triaxiality, but this effect is minor compared to the effect of global plastic dissipation, dU^p/dA_c, on the total dissipation rate, Eq. (5.74).

Equation (8.19) describes void growth starting from an initial void volume fraction, f_v^0. Chu and Needleman [13] introduced additional evolution equations for stress and strain induced void nucleation,

$$\dot{f}_v = \dot{f}_v^{nucl} + \dot{f}_v^{growth}. \tag{8.24}$$

The GTN model has also been applied to dynamic processes by Sun et al. [57] who considered both the effect of strain rate on plastic hardening and the coupled effect of thermal softening by incorporating a strain rate, $\dot{\varepsilon}_p$, and temperature, Θ, dependent flow curve, $R_F(\varepsilon_p, \dot{\varepsilon}_p, \Theta)$, in Eq. (8.20).

Extensions of the GTN model to ellipsoidal voids [23, 41] account for anisotropic ductile damage [55].

Due to the large number of adjustable and material parameters applications of the GTN model in industrial practice are rare. Parameter identification (Sect. 8.5) requires some expert knowledge, simulation results may be user dependent [5] and no accepted standards exist. Expectations that the parameters can be completely identified by tensile tests did not realise. The intrinsic triaxiality dependence requires test data of fracture specimens representing stress states of high constraint. In addition, the fine mesh which is required in the ligament due to the mesh dependence of results (see Sect. 8.3.3) interferes with FE modelling of large structures.

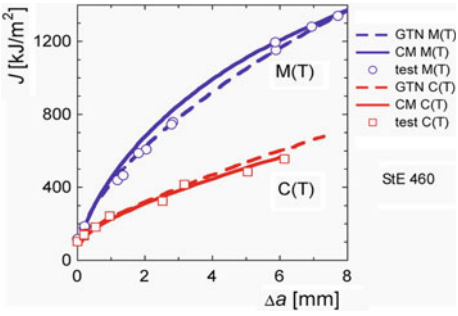

Fig. 8.9 Simulations of J_R-curves of a C(T) and a M(T) specimen by GTN model and cohesive model (CM), Siegmund et al. [50]

8.3.2 Rousselier Model

Rousselier [45] derived a similar yield function based on arguments of continuum damage mechanics (Sect. 8.4), namely the concept of "effective" stresses, $\tilde{\sigma}_{ij} = \sigma_{ij}/(1 - D)$, where D is a scalar damage parameter. Without particular insight into the micromechanical mechanisms of void growth and identification of damage with void volume fraction, $D \equiv f_v$, Eq. (8.18), it would not be suited as a constitutive description of ductile damage in real materials,

$$\frac{\tilde{\sigma}}{\tilde{R}_F(\varepsilon_p)} + cf_v \frac{2R_f}{3} \exp\left(\frac{3\tilde{\sigma}_h}{2\tilde{R}_f}\right) - 1 = 0, \tag{8.25}$$

with

$$\tilde{\sigma} = \frac{\bar{\sigma}_{vM}}{1 - f_v}, \quad \tilde{\sigma}_h = \frac{\sigma_h}{1 - f_v}, \quad \tilde{R}_F = \frac{R_F}{1 - f_v^0}, \quad \tilde{R}_f = \frac{R_f}{1 - f_v^0}. \tag{8.26}$$

c is some constant which "*can be considered as material independent*", $c = 2$, and R_f an adjustable parameter which as "*a first try is the mean of*" $R_F(\varepsilon_p)$ "*over the range of deformation*", $0 \leq \varepsilon_p \leq \varepsilon_f$, "*experienced by smooth tensile specimens*" [46], which becomes

$$R_f = \frac{c\varepsilon_f^N}{N+1} = \frac{R_F(\varepsilon_f)}{N+1} \tag{8.27}$$

for power law hardening matrix materials, $R_F(\varepsilon_p) = c\varepsilon_p^N$. In order to keep to a consistent nomenclature in the present book, Rousselier's notation has been partly modified.

Figure 8.7b shows Rousselier's yield surface for a perfectly plastic material, $R_F = R_0$, $N = 0$, and varying $f_v = f_v^0$. It is capped for tensile hydrostatic stress but unlimited for compressive hydrostatic stress. Considering that Gurson's model contains adjustable parameters, too, both models will not yield fundamentally different results for cases of tensile hydrostatic stresses. Significant differences will occur however for applications to cyclic plasticity [42, 54], but neither model is qualified for application to cyclic loading, anyway, because the damage evolution, Eq. (8.19), should be different in tension and compression in general. Note also that models of void growth due to hydrostatic stress are not suited for shear failure. A respective generalisation of the Gurson model has been presented by Nahshon and Hutchinson [36], for instance. Likewise, applications of the GTN or the Rousselier model to thin structures close to plane stress conditions will fail due to the low stress triaxiality.

8.3.3 Length Scales and Local Instability

Different from local constitutive equations in classical continuum theory, modelling at the meso-scale considering the micro-structure is not invariant against changes of the length scale. This has severe consequences for damage mechanics. Since damage is assumed as homogeneous within the RVE and described by an average defect density like f_v, no difference can be made between many small or few large micro-voids or micro-cracks. For a real material, this difference is essential, however.

Softening materials behave unstable which results in localisation of deformation (slip bands) and damage. This localisation is limited by the microstructure (grain size) in a real material and by the discretisation, i.e. the element size, in a finite element model. Therefore, damage models generally yield mesh dependent results, and no convergent solution as for stable material behaviour (see Drucker's postulates in Sect. 6.1.1) of elasto-plasticity or viscoplasticity exists at mesh refinement. The calculated failure load may thus be "user dependent" [5] as it becomes arbitrarily small for $(\Delta x, \Delta y, \Delta z) \rightarrow 0$. This effect is often used as fundamental objection against damage mechanics in general. This argument ignores, however, that modelling of material softening is not only of practical relevance for predicting failure loads but that localisation of deformation and damage is also a real physical phenomenon.

A realistic reproduction of the material and structural behaviour requires the introduction of an additional material parameter, namely a characteristic microstructural length [51, 56] which is related to the size of the RVE or unit cell, Eq. (8.16). Non-local theories incorporating deformation or damage gradients in the constitutive equations provide theoretically sound realisations [64, 72]. They are difficult to implement in commercial FE codes, however. Regularisation by viscoplastic effects has also been applied [40]. A frequently used engineering approach is the introduction of the element height in the process zone as material parameter [51]. To avoid uproar of FE experts, some authors use the term "computational cells" [18, 20, 47, 70, 71] instead of finite elements to indicate their relation to RVEs. Some authors claim that the element size directly represents the mean distance of voids but in fact, the relation is determined by the dissipation energy density according to Eq. (8.16).

8.4 Continuum Damage Mechanics

Continuum damage mechanics (CDM) is a phenomenological theory which aims at unifying the constitutive description of damage in arbitrary materials. The basic idea is that internal defects like micro-voids, micro-cavities, micro-cracks cause deterioration of materials by reducing the load-bearing area of volume elements so

that instead of an area ΔA of an RVE orthogonal to the surface normal, $\mathbf{n}$, only an "effective" area

$$\Delta\tilde{A} = \Delta A - \Delta A_{\mathrm{D}} \tag{8.28}$$

is available for transmission of forces. The areal density of defects, i.e. micro-cracks or sections of micro-voids with the plane,

$$D_{(\mathbf{n})} = \frac{\Delta A_{\mathrm{D}}}{\Delta A}, \tag{8.29}$$

depends on the orientation, $\mathbf{n}$, of the section plane, in general. For isotropic damage, the defect density is independent of $\mathbf{n}$ and damage can be described by a scalar variable, D,

$$\Delta\tilde{A} = (1 - D)\Delta A \quad \text{with} \quad D = \frac{\Delta A_{\mathrm{D}}}{\Delta A}. \tag{8.30}$$

Anisotropic damage requires tensorial damage variables, either as 2nd rank tensor,

$$\tilde{n}_i \Delta\tilde{A} = \left(\delta_{ij} - D_{ij}\right) n_j \Delta A, \tag{8.31}$$

or 4th rank tensor,

$$m_i \tilde{n}_j \Delta\tilde{A} = \left(\delta_{ik}\delta_{jl} - D_{ijkl}\right) m_k n_l \Delta A, \tag{8.32}$$

having the symmetries $D_{ijkl} = D_{ijlk} = D_{jikl} = D_{klij}$. The latter is the most general (and most complex) case.

By means of the effective area, effective stresses are defined, namely .

$$\tilde{\sigma}_{ij} = \frac{\sigma_{ij}}{1 - D}. \tag{8.33}$$

as in Eq. (8.25) for isotropic damage and

$$\tilde{\sigma}_{ij} = \left(\delta_{ik}\delta_{jl} - D_{ijkl}\right)^{-1} \sigma_{kl} \tag{8.34}$$

for anisotropic damage with a 4th rank tensor. As $(\delta_{ik} - D_{ik})^{-1}\sigma_{kj}$ is not symmetric, the definition of respective stresses with a 2nd rank damage tensor requires symmetrisation,

$$\tilde{\sigma}_{ij} = \frac{1}{2}\left[(\delta_{ik} - D_{ik})^{-1}\sigma_{kj} + (\delta_{ki} - D_{ki})^{-1}\sigma_{kj}\right]. \tag{8.35}$$

CDM is based on effective stresses and the principle of strain equivalence postulating that the constitutive equations for a damaged material are obtained from the constitutive equations of the undamaged material by simply replacing the stress tensor by the effective stress tensor. Scalar or tensorial damage enters the respective equations as additional internal variable. Whereas total strains, ε_{ij}, and temperature, Θ, are observable state variables, internal variables are non-observable. In the framework of a thermodynamically consistent theory, all evolution equations are derived from a unified dissipation potential, $\Phi\left(\sigma_{ij}, \bar{\kappa}, \xi_{ij}, Y\left[\text{or } Y_{ijkl}\right]\right)$, which is a convex function of all state variables being work conjugate to $\left\{\varepsilon_{ij}^{\mathrm{p}}, \bar{\varepsilon}^{\mathrm{p}}, \alpha_{ij}, D\left[\text{or } D_{ijkl}\right]\right\}$, see Table 8.1. The internal variable, Y, which is conjugate to D, is sometimes called "energy density release rate", which is an energy per volume, not to be mistaken for Griffith' energy release rate, $\mathcal{G}$, which is an energy per area.

The dissipation potential is a generalisation of the flow potential in plasticity, Eq. (3.10), from which the associated flow rule, Eq. (3.12), has been derived. It ensures that that the total dissipation rate is positive or in other words, the Clausius-Duhem inequality,

$$\sigma_{ij}\dot{\varepsilon}_{ij}^{\mathrm{p}} - \bar{\kappa}\dot{\bar{\varepsilon}}^{\mathrm{p}} - \xi_{ij}\dot{\alpha}_{ij} + Y\dot{D}\left[\text{or } Y_{ijkl}\dot{D}_{ijkl}\right] \geq 0, \tag{8.36}$$

which is the local form of the second principle of thermodynamics, is met. Thus, a unified framework for dissipative processes of plasticity and damage is established,

$$\begin{aligned}
\dot{\varepsilon}_{ij}^{\mathrm{p}} &= -\dot{\lambda}_{\mathrm{p}} \frac{\partial \Phi}{\partial\left(-\sigma_{ij}\right)} = \dot{\lambda}_{\mathrm{p}} \frac{\partial \Phi}{\partial \sigma_{ij}} \\
\dot{\bar{\varepsilon}}^{\mathrm{p}} &= -\dot{\lambda}_{\mathrm{p}} \frac{\partial \Phi}{\partial \bar{\kappa}} \\
\dot{\alpha}_{ij} &= -\dot{\lambda}_{\mathrm{p}} \frac{\partial \Phi}{\partial \xi_{ij}} \\
\dot{D} &= -\dot{\lambda}_{\mathrm{p}} \frac{\partial \Phi}{\partial(-Y)} = \dot{\lambda}_{\mathrm{D}} \frac{\partial \Phi}{\partial Y} \quad \text{or} \quad \dot{D}_{ijkl} = \dot{\lambda}_{\mathrm{p}} \frac{\partial \Phi}{\partial Y_{ijkl}}.
\end{aligned} \tag{8.37}$$

Table 8.1 Work conjugate internal state variables

Phenomenon	Internal state variable	Conjugate variable
Plasticity	$\varepsilon_{ij}^{\mathrm{p}}$	$-\sigma_{ij}$
Isotropic hardening	$\bar{\varepsilon}^{\mathrm{p}}$	$\bar{\kappa}$
Kinematic hardening	α_{ij}	ξ_{ij}
Isotropic damage	D	$-Y$
Anisotropic damage	D_{ijkl}	$-Y_{ijkl}$

CDM provides a consistent framework, why it is favoured by theoreticians of engineering mechanics, but it cannot help with the problem how to establish the dissipation potential. Only detailed knowledge of micromechanics and damage mechanisms can accomplish this. For further details see Chap. 6 on cracking and fracture in Lemaitre [30] and Chap. 7 on damage mechanics in Lemaitre and Chaboche [31].

8.5 Parameter Identification

Material constants in classical constitutive theories like Young's modulus in elasticity or yield strength in plasticity, which can be directly measured in tensile tests, for instance, are traditionally regarded as genuine material "properties". A more present-day view, however, considers them as nothing more than parameters in some constitutive model which more or less approximately describes a specific material behaviour for a certain range of application. There is no Young's modulus outside Hooke's law of elasticity, no yield strength outside the von Mises theory, no creep exponent outside Norton's law. This view avoids fruitless discussions about an artificial discrimination between real material properties and "fit parameters".

The increasing number of parameters in complex constitutive equations raises the problem of their experimental identification, however, as they cannot be directly evaluated from measured data any more. Instead, hybrid methods are required by which tests are numerically simulated and the model parameters identified by a comparison between numerical and experimental results [9, 32]. Very often, this is still done by a trial-and-error method based on an optical assessment of coincidence of load-displacement curves, which is mostly not that bad if based on expert knowledge and experience. If the number of parameters is too large and their interaction unclear, numerical optimisation techniques, evolution strategies or neural networks are employed.

Let $\mathbf{R}(\mathbf{x},t)$ be the response of a structure in terms of measurable quantities to mechanical or thermal impact, $\mathbf{F}(\mathbf{x},t)$, where $\mathbf{x} \in \mathbb{G}$ denote the spatial coordinates of material points and t the time. The response of the respective model is given by a functional,

$$\mathbf{R}_{\mathrm{mod}}(\mathbf{x},t) = \mathcal{F}^{t}_{\tau=0}\{\mathbb{G},\mathbf{c},\mathbf{F}(\mathbf{x},\tau)\}, \tag{8.38}$$

in dependence on the geometry, $\mathbb{G}$, material parameters, $\mathbf{c}$, and loading history, $\mathbf{F}(\mathbf{x}, t)$. The functional, $\mathcal{F}$, is commonly represented by the numerical solution of the boundary value problem.

Equation (8.38) represents the "direct problem", where $\mathbb{G}$, $\mathbf{c}$, $\mathbf{F}$ are input variables, and $\mathbf{R}_{\mathrm{mod}}$ is the output. The structural response is given by a finite number of data at locations, $\mathbf{x}_i$ ($i = 1,\ldots,M$), and time steps, t_j ($j = 1,\ldots,K$). For fixed geometry and loading history and assuming that a unique solution as well as a method for obtaining it exist, the functional $\mathcal{F}$ reduces to a mapping,

$$\mathbf{c} \mapsto_{\mathbb{G},\mathbf{F}} \mathbf{R}_{\text{mod}}: \quad \mathbf{R}_{\text{mod}} = \mathcal{R}(\mathbf{c}), \tag{8.39}$$

with $\mathbf{c} \in \mathbb{C}$ and $\mathbf{R}_{\text{mod}} \in \mathbb{R}$ being elements of the sets of physically meaningful model parameters and structural responses, respectively.

Parameter identification is the corresponding "inverse problem", which consists in finding model parameters, $\mathbf{c}$, for a given, experimentally measured response $\mathbf{R}$,

$$\mathbf{R} \mapsto \mathbf{c}: \quad \mathbf{c} = \mathcal{R}^{-1}(\mathbf{R})\big|_{\mathbb{G},\mathbf{F}(\mathbf{x}_i,t_j)}. \tag{8.40}$$

This requires that the available information allows for a unique solution, namely that $\mathcal{R}^{-1}$ is unique and $\mathbf{R}$ is complete. In order to call $\mathbf{c}$ material parameters, $\mathcal{R}^{-1}$ has to be independent of $\mathbb{G}$ and $\mathbf{F}$ within a certain range of application. Nevertheless, specimen geometries and loading histories for determining material parameters of common constitutive equations of elasticity, plasticity, creep etc. are prescribed in test procedures and standards. Respective rules for advanced present-day constitutive models are still missing.

Methods of parameter identification are:

- Graphical best-fit curves, if material parameters can be directly related to recorded test data;
- Trial and error with optical check of coincidence between simulation results and measured data, a simple but often time consuming method;
- Numerical optimisation techniques minimising the difference between simulation and test data with respect to some target, error or quality function,

$$q(\mathbf{c}) = \|\mathbf{R}_{\text{mod}}(\mathbf{c}) - \mathbf{R}\| \to \min_{\mathbf{c}\in\mathbb{C}}, \tag{8.41}$$

  applying deterministic (e.g. gradient method [33]) or stochastic methods (Monte Carlo) or evolution strategies [48];

- Neural networks learning to recognise nonlinear relations by training, a concept derived from observations of information flux between biological neurons [11]

The objective is to determine a unique set of material parameters which can be applied to arbitrary components. There is no possibility of proving uniqueness, however, but only counter-evidence can be attained, if so. The application of optimisation algorithms does not per se guarantee an objective result, because a number of user dependent decisions are implied like choice of the error function, weighting of experiments, selection of involved parameters, etc. Parameter identification requires interdisciplinary expertise in modelling, material science and experimental techniques. Any blind trust in results of simulations and optimisations can be fatal.

References

1. Aurich D, Baer W, Häcker R, Klingbeil, D, Ohm K (1999): Analyse und Weiterentwicklung bruchmechanischer Versagenskonzepte, Schwerpunkt: Anwendung fortgeschrittener zähbruchmechanischer Konzepte; Bruchübergang, Abschlussbericht zum Vorhaben 1500 970 des Bundesministeriums für Bildung, Wissenschaft, Forschung und Technologie, Bundesanstalt für Materialforschung und—prüfung (BAM), Berlin
2. Benzerga AA, Leblond JB, Hassan A, van der Giessen E (2010) Ductile fracture by void growth to coalescence. Adv Appl Mech 44:169–305
3. Beremin FM (1981) Cavity formation from inclusion in ductile fracture of A 508 steel. Metall Trans A 12A:723–731
4. Beremin FM (1983) A local criterion for cleavage fracture of a nuclear pressure vessel steel. Metall Trans A 14A:2277–2287
5. Bernauer G, Brocks W (2002) Micro-mechanical modelling of ductile damage and tearing—Results of a European numerical round robin. Fatigue Fract Engng Mater Struct 25:363–384
6. Bernauer G, Brocks W, Schmitt W (1999) Modifications of the Beremin model for cleavage fracture in the transition region of a ferritic steel. Eng Fract Mech 64:305–325
7. Bridgman PW (1952) Studies in large plastic flow and fracture. McGraw-Hill
8. Brocks W, Klingbeil D, Künecke G, Sun, DZ (1995) Application of the Gurson model to ductile tearing resistance. In: Kirk M, Bakker A (eds) 2nd symposium on constraint effects, ASTM STP 1224, Philadelphia, pp 232–252
9. Brocks W, Steglich D (2007) Hybrid methods. In: Milne I, Ritchie RO, Karihaloo B (eds) Comprehensive structural integrity, vol 11. Elsevier, pp 107–136
10. Brocks W, Sun DZ, Hönig A (1995) Verification of the transferability of micromechanical parameters by cell model calculations for visco-plastic materials. Int J Plasticity 11:971–989
11. Bröse E, Löffler HU (2004) Artificial neural networks. In: Raabe D, Roters F, Barlat F, Cheng LQ (eds) Continuum scale simulation of engineering materials. Wiley-VCH, Weinheim, pp 185–199
12. Chen JH, Cao R (2015) Micromechanism of cleavage fracture of metals. Elsevier
13. Chu CC, Needleman A (1980) Void nucleation effects in biaxially stretched sheets. Trans ASME, J Eng Mater Technol 102:249–256
14. Curry DA, Knott JF (1978) Effects of microstructure on cleavage fracture stress in steel. Metal Sci 12:511–514
15. Curry DA, Knott JF (1979) Effects of microstructure on cleavage fracture toughness in mild steel. Metal Sci 13:341–345
16. Dahl W, Dormagen W (1983) Micromechanisms of crack initiation and crack propagation. In: Larsson LH (1983) Elastic-plastic fracture mechanics, Proceeding of 4th Advanced Seminar on Fracture Mechanics (Ispra, Italy), Springer, The Netherlands
17. ESIS P6-98 (1998) Procedure to measure and calculate material parameters for the local approach to fracture using notch tensile specimens. European Structural Integrity Society
18. Faleskog F, Gao X, Shih CF (1998) Cell model for nonlinear fracture analysis: I. Micromechanics calibration. Int J Fract 89:355–373
19. François D (2001) Brittle fracture. In: Lemaitre J (ed) Handbook of materials behavior, vol II. Failures of materials. Academic Press, London, pp 566–576
20. Gao X, Faleskog F, Shih CF (1998) Cell model for nonlinear fracture analysis: II. Fracture-process calibration and verification. Int J Fract 89:375–398
21. Gologanu M, Leblond JB, Devaux J (1993) Approximate models for ductile metals containing nonspherical voids—case of axisymmetric prolate ellipsoidal cavities. J Mech Phys Solids 41:1723–1754
22. Gologanu M, Leblond JB, Devaux J (1994) Approximate models for ductile metals containing nonspherical voids—case of axisymmetric oblate ellipsoidal cavities. J Eng Mater Tech 116:290–297

23. Gologanu M, Leblond JB, Perrin P, Devaux D (1995) Recent extensions of Gurson's model for porous ductile metals. In: Suquet P (ed) Continuum micromechanics. Springer, Berlin
24. Gurson AL (1977) Continuum theory of ductile rupture by void nucleation and growth: Part I —yield criteria and flow rules for porous ductile media. J Engng Mater Technol 99:2–15
25. Huang Y (1991) Accurate dilatation rates for spherical voids in triaxial stress fields. J Appl Mech, Trans ASME 58:1084–1086
26. Hild F (2001) Probabilistic approach to fracture: The Weibull model. In: Lemaitre J (ed) Handbook of materials behavior, vol II. Failures of materials. Academic Press, London, pp 558–562
27. Kim JK, Gao XS (2006) Modeling of ductile fracture: significance of void coalescence. Int J Solids Structures 43:6277–6293
28. Koplik J, Needleman A (1988) Void growth and coalescence in porous plastic solids. Int J Solids Structures 24:835–853
29. Landes JD, Schaffer DH (1980) Statistical characterisation of fracture in the transition region. ASTM STP 700. American Society for Testing and Materials, Philadelphia, pp 368–372
30. Lemaitre J (ed) (2001) Handbook of materials behavior, Vol. II, Failures of materials. Academic Press, London
31. Lemaitre J, Chaboche JL (1990) Mechanics of solid materials. Cambridge University Press, Cambridge
32. Mahnken R (2004) Identification of material parameters for constitutive equations. In: Stein E, de Borst R, Hughes TJR (eds) Encyclopedia of computational mechanics. Wiley, Chichester, p 637
33. Mahnken R, Stein E (1994) The parameter identification of viscoplastic models via finite-element-methods and gradient methods. Model Simul Mat Sci Eng 2:597–616
34. McClintock FA (1968) A criterion for ductile fracture by the growth of holes. Trans ASME, J Appl Mech 35:363–371
35. Mudry F (1987) A local approach to cleavage fracture. Nucl Eng Des 105:65–76
36. Nahshon K, Hutchinson JW (2008) Modification of the Gurson model for shear failure. Europ J Mechanics A/Solids 27:1–17
37. Needleman A, Tvergaard V (1984) An analysis of ductile rupture in notched bars. J Mech Phys Solids 32:461–490
38. Needleman A, Tvergaard V (1987) An analysis of ductile rupture at a crack tip. J Mech Phys Solids 35:151–183
39. Nemat-Nasser S, Hori M (1993) Micromechanics—overall properties of heterogeneous materials. North-Holland, Amsterdam
40. Niazi MS, Wisselink HH, Meinders T (2013) Viscoplastic regularization of local damage models: revisited. Comput Mech 51:203–216
41. Pardoen T, Hutchinson JW (2003) Micromechanics-based model for trends in toughness of ductile metals. Acta Mater 51:133–148
42. Pirondi A, Bonora N, Steglich D, Brocks W, Hellmann D (2006) Simulation of failure under cyclic plastic loading by damage models. Int J Plasticity 22:2146–2170
43. Rice JR, Tracey DM (1969) On the ductile enlargement of voids in triaxial stress fields. J Mech Phys Solids 17:201–217
44. Ritchie RO, Knott JF, Rice JR (1973) On the relationship between critical tensile stress and fracture toughness in mild steel. J Mech Phys Solids 21:395–410
45. Rousselier G (1987) Ductile fracture models and their potential in local approach of fracture. Nucl Eng Des 105:97–111
46. Rousselier G (2001) The Rousselier model for porous metal plasticity and ductile fracture. In: Lemaitre J (ed) Handbook of materials behavior, vol II, failures of materials, Academic Press, London, pp 436–445
47. Ruggieri C, Panontin TL, Dodds RH (1996) Numerical modeling of ductile crack growth in 3-D using computational cell elements. Int J Fract 82:67–95
48. Schwefel HP (1995) Evolution and optimum seeking. Wiley-Interscience Publ, New York
49. Siegele D (1989) 3D crack propagation using ADINA. Comp Struct 32:639–645

50. Siegmund T, Bernauer G, Brocks, W (1998) Two models of ductile fracture in contest: porous metal plasticity and cohesive elements. In: Brown MW, De los Rios ER, Miller KJ (eds) Proceeding of ECF 12, Sheffield, vol II, Engineering Materials Advisory Services Ltd, pp 933–938
51. Siegmund T, Brocks W (1998) Local fracture criteria: lengthscales and applications. J de Physique IV 8:349–356
52. Steglich D (2004) Structure damage simulation. In: Raabe D, Roters F, Barlat F, Cheng LQ (eds) Continuum scale simulation of engineering materials. Wiley-VCH, Weinheim, pp 817–826
53. Steglich D, Brocks W (1997) Micromechanical modelling of the behaviour of ductile materials including particles. Comput Mater Sci 9:7–17
54. Steglich D, Pirondi A, Bonora N, Brocks W (2005) Micromechanical modelling of cyclic plasticity incorporating damage. Int J Solids Struct 42:337–351
55. Steglich D, Brocks W, Heerens J, Pardoen T (2008) Anisotropic ductile fracture of Al 2024 alloys. Eng Fract Mech 12:3692–3706
56. Sun DZ, Hönig A (1994) Significance of the characteristic length for micromechanical modelling of ductile fracture. In: Aliabadi MH, Carpinteri A, Kalisky S, Cartwright DF (eds) Proceeding of 3rd international conference on localized damage. Computational Mechanics Publication, Southampton, pp 287–296
57. Sun DZ, Hönig A, Böhme W, Schmitt W (1994) Application of micromechanical models to the analysis of ductile fracture under dynamic loading. In: Erdogan F (ed) Fracture Mechanics, 25th Symposium, ASTM STP 1220. American Society for Testing and Materials, Philadelphia, pp 343–357
58. Sun DZ, Siegele D, Voss B, Schmitt W (1988) Application of local damage models to the numerical analysis of ductile rupture. Fatigue Fract Eng Mater Struct 12:201–212
59. Thomason PF (1985) A three-dimensional model for ductile fracture by the growth and coalescence of micro-voids. Acta Metall 33:1087–1095
60. Thomason PF (1990) Ductile fracture of metals. Pergamon Press, Oxford
61. Thomason PF (1998) A view on ductile-fracture modelling. Fatig Fract Engng Mat Struct 21:1105–1122
62. Tvergaard V (1982) On localization in ductile materials containing spherical voids. Int J Fracture 18:237–252
63. Tvergaard V, Needleman A (1984) Analysis of the cup-cone fracture in a round tensile bar. Acta Metall 32:157–169
64. Tvergaard V, Needleman A (1995) Effects of non-local damage in porous plastic solids. Int J of Solids Structures 32:1063–1077
65. Tvergaard V, Needleman A (2001) The modified Gurson model. In: Lemaitre J (ed) Handbook of materials behavior, vol II. Failures of Materials. Academic Press, London, pp 430–435
66. Watanabe J, Iwadate T, Tanaka Y, Yokobori T, Ando K (1987) Fracture toughness in the transition regime. Eng Fract Mech 28:589–600
67. Weibull W (1939) A statistical theory of the strength of materials. Ingeniørsvetenskapakademiens, Nandlinger no. 151, Stockholm
68. Weibull W (1939) The phenomenon of rupture in solids. Ingeniørsvetenskapakademiens, Nandlinger no. 153, Stockholm
69. Weibull W (1951) A statistical distribution function if wide applicability. J Appl Mech 81:293–297
70. Xia L, Shih FC (1995) Ductile crack growth: I. A numerical study using computational cells with microstructurally-based length scales conditions. J Mech Phys Solids 43:233–259
71. Xia L, Shih CF, Hutchinson JW (1995) A computational approach to ductile crack growth under large scale yielding. J Mech Phys Solids 43:389–413
72. Yuan H, Chen J, Krompholz K, Wittmann FH (2003) Investigations of size effects in tensile tests based on a nonlocal micro-mechanical damage model. Comp Mater Science 26:230–243
73. Zhang ZL, Thaulow C, Ødegård J (2000) A complete Gurson model approach for ductile fracture. Eng Fract Mech 155–168

Chapter 9
The Cohesive Model

Abstract A phenomenological approach which has found numerous applications for all kinds of decohesion and separation processes is based on Barenblatt's idea of a cohesive zone. The basic concept and numerical realisation in the framework of finite elements are described. A number of proposed traction-separation laws for various applications including mixed mode and the physical significance of the cohesive parameters are discussed. Recent approaches to relate decohesion laws to damage mechanics are critically reviewed. Examples of applications to the simulation of crack extension in thin panels and shells are presented.

Numerical simulation of crack extension can be simulated in FE models by various techniques [12]:

- Release of element nodes in the ligament according to a global "driving force" like J, CTOD, CTOA (Chap. 5);
- Constitutive equations of damage mechanics (Chap. 8);
- Cohesive (zone) models.

The cohesive model is a phenomenological approach of high flexibility, a low number of parameters compared to damage models, parameters which nevertheless allow for a plausible physical interpretation, and numerical stability also for large crack extension. Its most apparent purpose is modelling of bonded interfaces in composite materials, where the intermediate glue material is very thin and for all practical purposes may be considered to be of zero thickness [1]. But it has found applications for all kinds of decohesion and separation processes where the thickness of the process zone can be assumed as negligible and in particular in fracture mechanics, Fig. 9.1. The cohesive zone represents degradation and failure, the bulk material, i.e. continuum elements, deformation of the material.

The present chapter will focus on ductile fracture under quasi-static loading. A broader overview can be found in Brocks et al. [12].

W. Brocks, *Plasticity and Fracture*, Solid Mechanics and Its Applications 244,
DOI 10.1007/978-3-319-62752-6_9

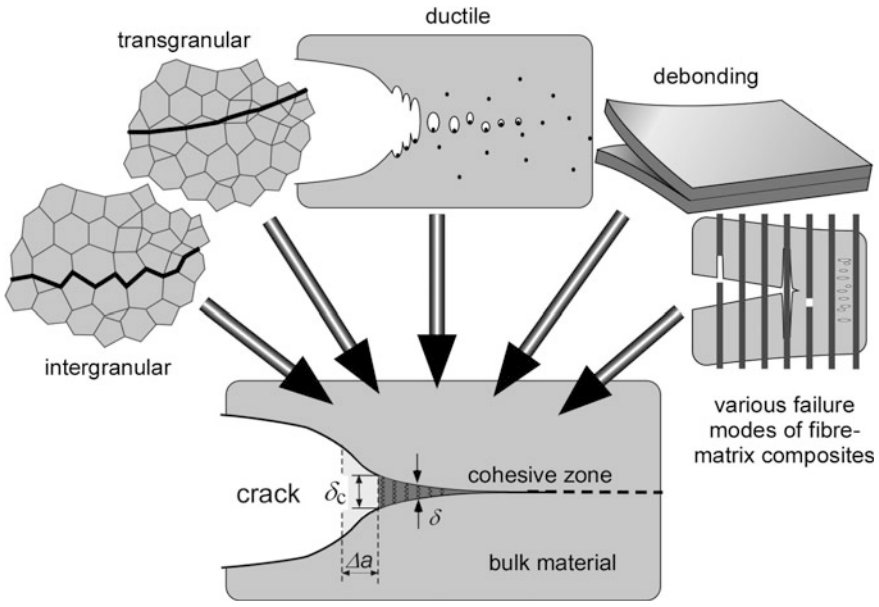

Fig. 9.1 Schematic of cohesive model and its applications

9.1 The Cohesive Zone

The idea of a cohesive zone at the crack tip to avoid non-physical singularities dates back to Barenblatt [4, 5] and Dugdale [22]. Two regions of the crack are distinguished, the stress-free crack faces and a process zone where cohesive stresses act, Fig. 4.6. Whereas Dugdale assumed that cohesive stresses equal the yield strength, R_0, which holds only for plane stress states and perfectly-plastic materials, Barenblatt assumed a stress distribution, $\sigma(x)$, at the crack tip which is specific to the material but independent of the loading. This stress distribution is not known, however, and cannot be measured, either. An application of this concept became possible with the advanced possibilities of numerical simulations.

The Barenblatt model has been modified by introducing a separation law, $\sigma(\delta)$, instead of $\sigma(x)$. Cohesive stresses do not depend on the distance to the crack tip but on the separation,

$$\boldsymbol{\delta} = [\mathbf{u}] = \mathbf{u}^+ - \mathbf{u}^-, \tag{9.1}$$

which is the vector of the displacement discontinuity in the process zone. This approach has been introduced by Hillerborg et al. [26] for concrete, where it is still known as the "fictitious crack model", and has become the basis of all modern realisations of the cohesive model in FEM. Cohesive stresses or tractions and separations are vectors, in general, $\boldsymbol{\sigma} = \{\sigma_n, \sigma_t, \sigma_s\}$, $\boldsymbol{\delta} = \{\delta_n, \delta_t, \delta_s\}$, with one

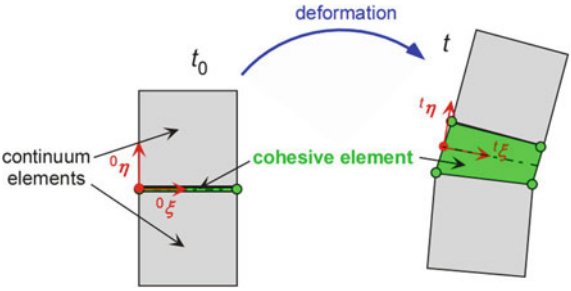

Fig. 9.2 Cohesive element at the boundaries of two neighbouring continuum elements in the undeformed state, $\{^0\xi, ^0\eta\}$, and deformed state, $\{^t\xi, ^t\eta\}$; $\xi \triangleq t$ for mode II separation, $\eta \triangleq n$ for mode I separation

normal component, σ_n, δ_n, corresponding to mode I, and two tangential components, σ_t, σ_s, δ_t, δ_s. For isotropic materials, the separation laws in t- and s-direction are identical so that only two separation laws remain. The process zone is modelled like an interface by surface or line elements of zero height located between two or three dimensional continuum elements in a co-rotating local coordinate system, Fig. 9.2.

This initially vanishing thickness is basic for cohesive elements. Introducing an artefact like a "*constitutive thickness*", which is "*usually different from the geometric thickness*" [1] is nonsensical.

As a result of material degradation, the initially collapsed corner nodes of the upper and lower surfaces of the cohesive element separate until the element completely loses its stiffness at some critical separation, δ_n^c, δ_t^c, respectively, so that the adjacent continuum elements are disjoined. The crack can only propagate along the element boundaries prescribed by the meshing. Additionally to the critical separations, the maximum tractions or cohesive strengths, σ_n^c, σ_t^c, are introduced as material parameters. The integration of the traction-separation laws,

$$\Gamma_n^c = \int_0^{\delta_n^c} \sigma_n(\delta_n)|_{\delta_n=0}\, d\delta_n \quad \text{or} \quad \Gamma_t^c = \int_0^{\delta_t^c} \sigma_t(\delta_t)|_{\delta_t=0}\, d\delta_t, \tag{9.2}$$

yields the mechanical work, which is dissipated in a cohesive element by the degradation process until final failure by normal or shear separation These separation energies can be used as material parameters alternatively to the critical separation. They represent energy release rates in Griffith's sense, Eqs. (2.11) and (5.24). Under the validity conditions of Eqs. (5.8)–(5.11), particularly the deformation theory of plasticity, the separation energy, Γ_n^c, equals Rice's J-integral at crack initiation for mode I. In incremental theory of plasticity,

$$\Gamma_n^c \le J_i, \tag{9.3}$$

holds for "real" materials.

9.2 Cohesive Laws

9.2.1 Shapes of Traction-Separation Laws

Different from constitutive equations in continuum mechanics, which establish relations between stresses and strains, cohesive laws are relations between stresses and displacements. This is a second fundamental feature like the zero thickness of the elements, and the two are interdependent. Abaqus [1] has to introduce a fictitious "constitutive thickness" since the cohesive laws are expressed in dependence on stresses and strains like the constitutive laws of continuum elements. This abandons fundamental advantages of cohesive elements compared to continuum elements, however, most notably their characteristic feature represented by Eq. (9.2) that the dissipated energy is not dependent on some element height as in damage mechanics, Eq. (8.16).

The shape of a cohesive law or traction-separation law (TSL) depends on the respective separation mechanism, and thus there is a diversity of approaches for traction-separation laws in the literature, see overviews by Brocks et al. [12] and Schwalbe et al. [49]. Their suitability to describe crack extension in a structure can be estimated by comparisons of macroscopic experimental and numerical data. For particular damage mechanisms, micromechanical simulations can be performed to conclude on the TSL. Unit cell calculations by Koplik and Needleman [28] or Siegmund and Brocks [51] as displayed in Fig. 8.6 show the typical damage behaviour due to void growth, which can be modelled by laws like those shown in Fig. 9.2b, c, f. Krull and Yuan [29] present analyses based on molecular dynamics which depict the behaviour due to atomic debonding, Fig. 9.3e as it was studied by Rose et al. [41]. Figure 9.3 compiles common cohesive laws of the literature, where $\sigma(\delta)$ stands for either $\sigma_n(\delta_n)$ or $\sigma_t(\delta_t)$. The interaction of the two modes is examined in Sect. 9.2.4.

Hillerborg et al. [26] used a simple linear softening law for describing crack growth in concrete, Fig. 9.3a,

$$\sigma = \sigma_c\left(1 - \frac{\delta}{\delta_c}\right), \quad \Gamma_c = \frac{1}{2}\sigma_c\delta_c. \tag{9.4}$$

It is generally suited for brittle, mineral materials.

The bilinear law of Bažant [6, 7], Fig. 9.3b,

$$\sigma = \sigma_c\begin{Bmatrix} 1 - \frac{\delta}{\delta_1} + \frac{\sigma_1}{\sigma_c}\frac{\delta}{\delta_1} & \text{for} & 0 \le \delta \le \delta_1 \\ \frac{\sigma_1}{\sigma_c}\left(1 - \frac{\delta - \delta_1}{\delta_c - \delta_1}\right) & \textit{for} & \delta_1 \le \delta \le \delta_c \end{Bmatrix}, \quad \Gamma_c = \frac{1}{2}\sigma_c\delta_c\left(\frac{\delta_1}{\delta_c} + \frac{\sigma_1}{\sigma_c}\right), \tag{9.5}$$

contains two additional shape parameters σ_1, δ_1, which increase the flexibility for describing different separation mechanisms. In its concave form, see solid curve

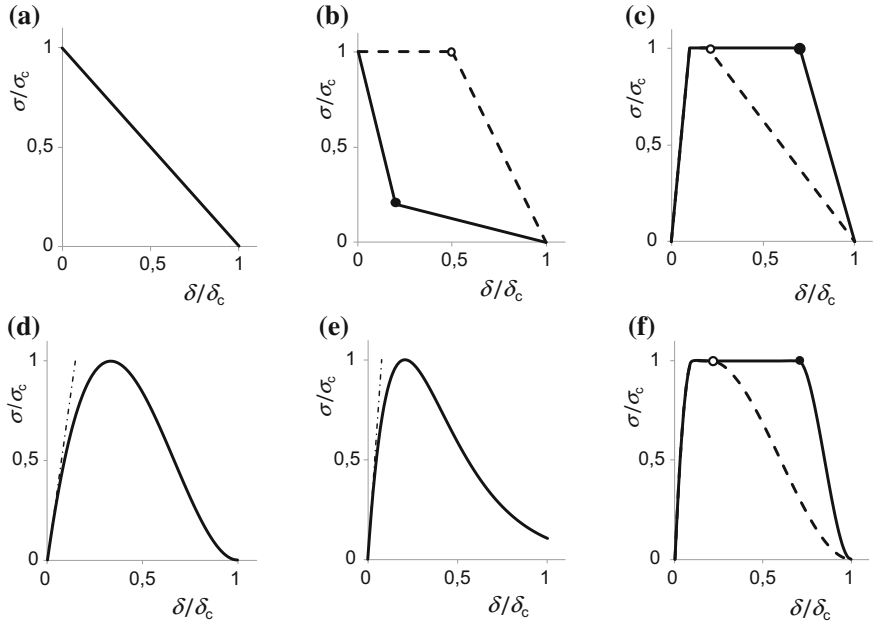

Fig. 9.3 Common cohesive laws: **a** linear [26]; **b** bilinear [6, 7]; **c** trilinear [59, 60]; **d** cubic [34]; **e** exponential [35]; **f** piecewise polynomial [42, 43]

with $\sigma_1 = 0.2\sigma_c$, $\delta_1 = 0.2\delta_c$, it is applied to concrete [6, 7, 31], in its convex form, see dashed curve with $\sigma_1 = \sigma_c$, $\delta_1 = 0.5\delta_c$, it can be used for ductile fracture due to void growth as in Fig. 8.6.

Though cohesive elements are not supposed to describe (elastic) deformation, numerical problems may arise for an infinite initial stiffness like in the TSLs of Hillerborg, Eq. (9.4) and Bažant, Eq. (9.5). That is why Tvergaard and Hutchinson [59, 60] introduced a trilinear TSL, Fig. 9.3c,

$$\sigma = \sigma_c \left\{ \begin{array}{ll} \frac{\delta}{\delta_0} & ;for\ \delta \le \delta_0 \\ 1 & ;for \quad \delta_0 \le \delta \le \delta_1 \\ \frac{\delta_c - \delta}{\delta_c - \delta_1} & ;for \quad \delta_1 \le \delta \le \delta_c \end{array} \right\}, \quad \Gamma_c = \frac{1}{2}\sigma_c \delta_c \left(1 - \frac{\delta_0}{\delta_c} + \frac{\delta_1}{\delta_c}\right), \tag{9.6}$$

having an initial compliance, $C_0 = \delta_0/\sigma_c$. This compliance has no physical meaning but only numerical significance and should be chosen as small as possible (Sect. 9.2.2). In Fig. 9.2c, the dashed curve represents $\delta_1 = 0.2\delta_c$, and the solid one $\delta_1 = 0.7\delta_c$. For $\delta_1 = \delta_0 \to 0$, the TSL approaches Hillerborg's Eq. (9.4) and describes a brittle behaviour. The "rectangular" TSL of Lin et al. [30] is obtained for $\delta_0 = 0$, and $\delta_1 = \delta_c$.

Needleman [34] introduced a 3rd order polynomial,

$$\sigma = \sigma_c \frac{27}{4}\frac{\delta}{\delta_c}\left(1-\frac{\delta}{\delta_c}\right)^2, \quad \Gamma_c = \frac{9}{16}\sigma_c\delta_c, \tag{9.7}$$

as cohesive law for mode I separation of ductile materials, Fig. 9.3d. It has been applied to a mode II problem, the debonding of fibres in a fibre reinforced metal, by Tvergaard [58].

The exponential TSL of Needleman [35], Fig. 9.3(e),

$$\sigma = \sigma_c \frac{16}{9}e^2\frac{\delta}{\delta_c}\exp\left(-\frac{16}{9}e\frac{\delta}{\delta_c}\right), \quad \Gamma_c = \frac{9}{16}\sigma_c\delta_c, \tag{9.8}$$

with $e = \exp(1)$, has been derived from an energy function of atomic binding forces by Rose et al. [41]. Different from the other cohesive laws, the cohesive stress does not vanish at δ_c but remains finite, $\sigma(\delta_c) = 0.105\sigma_c$. The separation energy is the same as for the cubic TSL in Eq. (9.7). It has been applied to brittle [62] as well as ductile materials [51].

Scheider [42, 43] suggested a piecewise polynomial, Fig. 9.3f,

$$\sigma = \sigma_c \begin{Bmatrix} 2\left(\frac{\delta}{\delta_0}\right) - \left(\frac{\delta}{\delta_0}\right)^2 & for & \delta \le \delta_0 \\ 1 & for & \delta_0 \le \delta \le \delta_1 \\ 2\left(\frac{\delta-\delta_1}{\delta_c-\delta_1}\right)^3 - 3\left(\frac{\delta-\delta_1}{\delta_c-\delta_1}\right)^2 + 1 & for & \delta_1 \le \delta \le \delta_c \end{Bmatrix}, \tag{9.9}$$
$$\Gamma_c = \tfrac{1}{2}\sigma_c\delta_c\left(1-\tfrac{2}{3}\tfrac{\delta_0}{\delta_c}+\tfrac{\delta_1}{\delta_c}\right)$$

which is similar to the TSL by Tvergaard and Hutchinson, Eq. (9.6), but differentiable in the transition points, δ_0, δ_1. The dashed curve represents $\delta_1 = 0.2\delta_c$, and the solid one $\delta_1 = 0.7\delta_c$, again. For $\delta_0 = \delta_1 = 0.33\delta_c$, it resembles Needleman's cubic law, its softening part being actually identical.

Abaqus [1] offers a basically different approach based on some "damage" concept (Sect. 9.2.5). The initial response of the cohesive element is assumed to be linear. Once an initiation criterion is met, material damage occurs according to a user-defined evolution law. Only two TSLs, $\sigma(\delta)$, are explicitly provided, namely linear softening as in Eq. (9.6) with $\delta_1 = \delta_0$, and exponential softening,

$$\sigma = \sigma_c \frac{\delta_0}{\delta}\left\{1-\frac{1-\exp[-\alpha(\delta-\delta_0)/(\delta_c-\delta_0)]}{1-\exp(-\alpha)}\right\}, \tag{9.10}$$

with α as an adjustable parameter. Alternatively, "damage evolution" can be defined tabularly resulting in a more or less meaningful TSL.

The choice of the cohesive law is on the user's responsibility. The ability to predict a specific separation process in terms of measurable macroscopic quantities like R-curves is the crucial decision criterion. As the shape of the TSL affects the

simulation results [45], model parameters as identified for a material are tied to the once chosen function, and transferability is ensured only for retaining this function in further simulations.

Cohesive parameters, like damage parameters, can be identified by numerical simulations of tests, primarily fracture mechanics tests, see general remarks in Sect. (8.5). Additional information can be found in Maier et al. [31], Brocks and Steglich [15], Brocks and Scheider [14].

9.2.2 Significance of Initial Compliance

Whereas the shape parameter δ_1 in the models of Tvergaard and Hutchinson, Eq. (9.6), and Scheider, Eq. (9.9), is specific for different separation mechanisms, the parameter δ_0 has only numerical significance. Since the deformation of the structure is determined by the constitutive equations of the bulk material, i.e. by the continuum elements, the initial compliance of cohesive elements,

$$C_0 = \left(\frac{d\delta}{d\sigma}\right)_{\delta=0}, \tag{9.11}$$

should be smaller than the compliance, h/E, of the continuum elements,

$$\frac{C_0 E}{h} \simeq \frac{\delta_0}{h}\frac{R_0}{\sigma_c}\frac{E}{R_0} < 1, \tag{9.12}$$

where E is Young's modulus and h is the (smallest) element height of the FE model. This can be realised by a sufficiently small δ_0/h. The "ideal" case of $\delta_0 = 0$ as (apparently) in the TSLs of Hillerborg, Eq. (9.4), and Bažant, Eq. (9.5), is not feasible as an infinite stiffness will spoil the global stiffness matrix of the structure in a deformation based FE scheme. Cohesive elements of too high compliance can produce numerical artefacts, particularly if a high number of cohesive elements is placed in the mesh. Deterrent examples can be found in the literature.

A problem arises with respect to the cubic and the exponential laws of Needlemen, Eqs. (9.7) and (9.8), because their initial compliances cannot be chosen independently but depend on δ_c/σ_c,

$$C_0 = \frac{\delta_c}{\sigma_c}\begin{cases} \frac{4}{27} = 0.148 & \text{cubic TSL} \\ \frac{9}{16e^2} = 0.076 & \text{exponential TSL} \end{cases}. \tag{9.13}$$

An example of a defective result due to the improper choice of a TSL has been obtained during simulations of cup-cone fracture of round tensile bars by Scheider and Brocks [44], Fig. 9.4. The whole necking section of the bar had to be meshed by triangular continuum elements with cohesive elements at all boundaries, Fig. 9.4a, in order to allow for crack bifurcation (Sect. 9.3.2). Physically

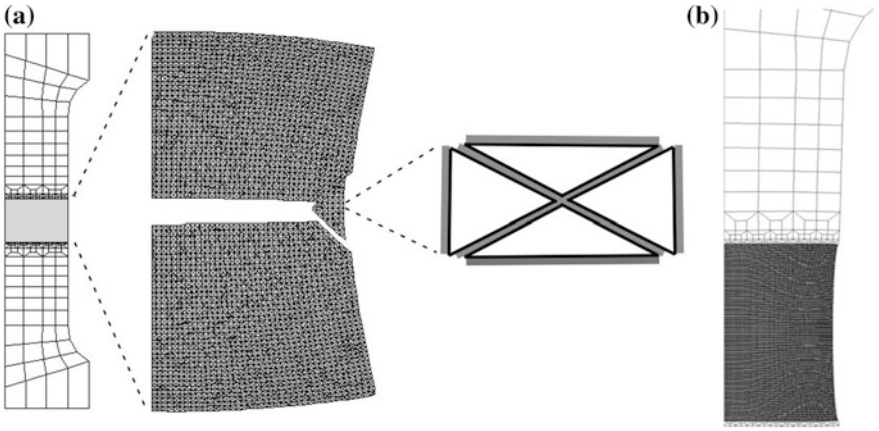

Fig. 9.4 Modelling of cup-cone fracture of a round tensile bar by cohesive elements: **a** FE mesh and deformed necking section with crack bifurcation [44]; **b** defective result due to high compliance of cohesive elements

meaningful results, Fig. 9.4a, were achieved with a mixed mode version of Scheider's TSL, Eq. (9.9). Applying the cubic TSL, Eq. (9.7) yielded a defective result, Fig. 8.4b: necking occurred prior to the load maximum due to shear separation and an additional elongation of 18% was simply due to normal separation of the cohesive elements.

Compliance issues are addressed in Elices et al. [23] and Song et al. [55].

9.2.3 *Unloading and Reloading*

The above TSLs have to be complemented by assumptions for unloading and reloading processes in mode I and II, Fig. 9.5.

Two limiting cases can be considered:

- Unloading, $\dot{\delta} < 0$, at point A occurs parallel to the initial slope of the TSL as in plasticity. A permanent separation remains at $\sigma = 0$. Reloading follows the same line up to point A and along $\sigma(\delta)$ from there on. For compressive normal stresses, $\sigma_n < 0$, the separation rate, $\dot{\delta}$, has to be zero. Numerical reasons require a finite, though small compliance however, Fig. 9.5a. Reversal shear stresses, $\sigma_t < 0$, follow the unloading line until point B, where the same absolute value as in point A is reached, $\sigma_t^{(B)} = -\sigma_t^{(A)}$. For continuing $\dot{\delta}_t < 0$, cohesive shear stresses decline to zero, Fig. 9.5b. This behaviour suits for modelling ductile damage and fracture.

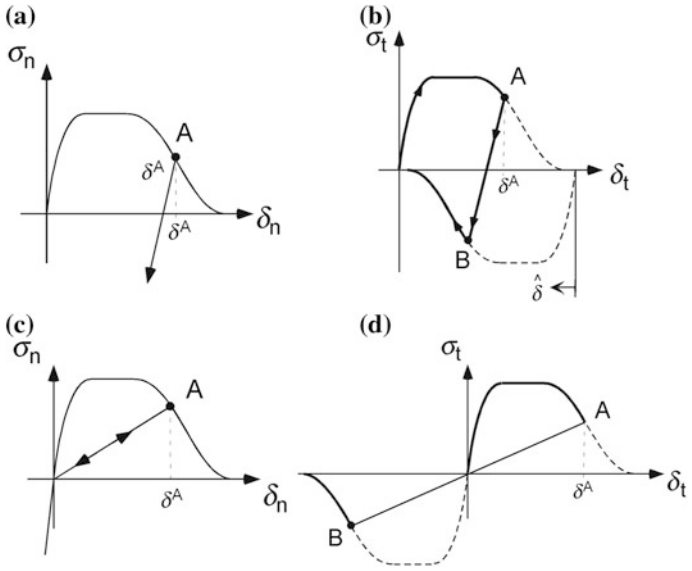

Fig. 9.5 Unloading and reloading of cohesive elements: **a**, **b** "ductile" unloading; **c**, **d** "brittle" unloading

- Unloading, $\dot{\delta} < 0$, at point A traces back to the origin of $\sigma(\delta)$, Fig. 9.5c, d, and reloading follows up the unloading line. There is no permanent separation at $\sigma = 0$. The material degradation manifests in an increase of the elastic compliance, C_0. This behaviour describes brittle damage processes. It is the only option available in Abaqus [1].

As and when required, combined models may be implemented.

9.2.4 Mixed Mode

The cup-cone fracture of a round tensile bar depicted in Fig. 9.4 and all cases of in-plane crack kinking [36] are examples of local mixed mode I + II conditions which require consideration of the interaction between normal and shear separation, $\sigma_n(\delta_n,\delta_t)$, $\sigma_t(\delta_t,\delta_n)$. Shear separation will reduce normal tractions and vice versa. Likewise, the out-of-plane slant fracture occurring in thin sheets [53] is a mode I + III situation. Note, that all these examples represent local mixed mode, where the global loading is still pure mode I.

As for the shapes of the TSL, Fig. 9.3, various approaches exist in the literature for the interaction between normal and shear separation. It may be modelled entirely phenomenologically,

$$\begin{aligned}\sigma_n(\delta_n,\delta_t) &= \sigma_n^c f(\delta_n) g(\delta_t)\\ \sigma_t(\delta_t,\delta_n) &= \sigma_t^c f(\delta_t) g(\delta_n)\end{aligned}, \tag{9.14}$$

with some user-defined interaction function $g(\delta)$ with $g(0) = 1$, $g(\delta_c) = 0$, and $f(\delta)$ being any of the functions, Eqs. (9.4–9.9), defined above. This approach requires four parameters, σ_n^c, δ_n^c, σ_t^c, δ_t^c, plus some user-defined parameters for $g(\delta)$, if necessary.

Camacho and Ortiz [16] introduced effective values for separation and traction, in which different weight is assigned to the components of the separation by a factor, β,

$$\delta_{eff} = \sqrt{\delta_n^2 + \beta\delta_t^2}. \tag{9.15}$$

As in Eq. (9.14), all cohesive laws presented in Sect. 9.2.1 can be applied to mixed-mode situations requiring three parameters, σ_c, δ_c, β.

Tvergaard [58] extended the cubic TSL, Eq. (9.7), to mixed mode by defining a potential resulting in

$$\sigma_{n,t} = \sigma_{n,t}^c \frac{27}{4}\frac{\delta_{n,t}}{\delta_{n,t}^c}\left(1 - \frac{\delta_{eff}}{\delta_n^c}\right)^2, \tag{9.16}$$

with the weighting factor, $\beta = \delta_n^c/\delta_t^c$. Four model parameters, σ_n^c, δ_n^c, σ_t^c, δ_t^c are required. A similar approach is used for the cohesive law of Tvergaard and Hutchinson [60], replacing δ in Eq. (9.9) by δ_{eff},

$$\begin{aligned}\sigma_n &= \sigma(\delta_{eff})\frac{\delta_n^c}{\delta_{eff}}\frac{\delta_n}{\delta_n^c}\\ \sigma_t &= \sigma(\delta_{eff})\frac{\delta_n^c}{\delta_{eff}}\frac{\delta_n^c}{\delta_t^c}\frac{\delta_t}{\delta_t^c}\end{aligned}. \tag{9.17}$$

It requires five parameters in total, namely $\sigma_n^c = \sigma_t^c = \sigma_c$, δ_n^c, δ_t^c and two shape parameters, δ_0, δ_1.

Xu and Needleman [62] extended the exponential cohesive law, Eq. (9.8), which has been derived from an energy function of atomic binding forces by Rose et al. [41], to combined normal and shear separation by an interaction parameter, $0 \le q \le 1$,

$$\begin{aligned}\sigma_n &= \sigma_c e\frac{\delta_n}{\delta_0}\exp\left(-\frac{\delta_n}{\delta_0}\right)\left\{\exp\left(-\frac{\delta_t}{\delta_0}\right)^2 + (1-q)\left[1 - \exp\left(-\frac{\delta_t}{\delta_0}\right)^2\right]\right\}\\ \sigma_t &= 2\sigma_c e\frac{\delta_t}{\delta_0}q\left(1 + \frac{\delta_n}{\delta_0}\right)\exp\left(-\frac{\delta_n}{\delta_0}\right)\exp\left(-\frac{\delta_t}{\delta_0}\right)^2\end{aligned}, \tag{9.18}$$

where δ_0 denotes the separation at maximum normal traction, $\sigma_n(\delta_0) = \sigma_c$.

Abaqus [1] offers several stress and strain criteria for the onset of softening in mixed mode, which are based on a respective maximum value or a quadratic

interaction function, and two options for describing "damage evolution" in terms of either tractions, σ_n, σ_t, σ_s, or energies, Γ_n^c, Γ_t^c, Γ_s^c, as defined by Eq. (9.2).

On the whole, the approaches to local mixed mode are manifold and a consistent background theory including rules for parameter identification does not appear as finally established. Mixed-mode laws are favourably deduced by introducing potentials [38] from which tractions are derived,

$$\boldsymbol{\sigma} = \frac{\partial \Phi_{\text{coh}}}{\partial \boldsymbol{\delta}}, \tag{9.19}$$

but, as in CDM, this cannot help with the problem how to establish the appropriate potential which reflects the specific separation process. Nevertheless, the fascination of a thermodynamically consistent unified framework as established for CDM has also caught the "cohesive community", and several attempts have been started to adopt the concept of damage to the formulation of cohesive laws [37].

9.2.5 Cohesive Laws and Damage

A scalar damage variable, D, which represents the overall damage in the material and evolves from 0 to 1 after the initiation of damage is introduced in combination with an elastic potential,

$$\Phi_{\text{coh}} = (1 - D)\frac{1}{2}\boldsymbol{\delta} \cdot \mathbf{K}_{\text{coh}} \cdot \boldsymbol{\delta}. \tag{9.20}$$

from which the traction separation law is derived according to Eq. (9.19),

$$\boldsymbol{\sigma} = (1 - D)\mathbf{K}_{\text{coh}} \cdot \boldsymbol{\delta}, \tag{9.21}$$

where $\mathbf{K}_{\text{coh}} = \mathbf{C}_0^{-1}$ is an "elastic" stiffness or inverse of compliance matrix of the cohesive element [2, 17, 33]. This concept is realised in Abaqus [1].

Assigning an elastic stiffness to cohesive elements is a fundamentally disparate concept to the basic idea of a cohesive zone representing material separation. The deformation of a material is described by constitutive equations of elasticity, plasticity, viscoplasticity etc. in the framework of continuum mechanics. It is decoupled from degradation and failure restricted to occur in some boundary layer or interface of negligible thickness. The concept of a cohesive interface realises the idea of a surface energy, γ, introduced by Griffith [25], see Sect. 2.1. Endowing this layer with deformation properties, whether they are elastic or plastic, is physically questionable.

Furthermore, the discussion in Sect. 9.2.2 has clarified that the initial compliance of a TSL, $C_0 = \delta_0/\sigma_c$, has no physical significance but plays, first and foremost, a numerical role. Thus, it may be chosen arbitrarily but should follow the condition of Eq. (9.12). As shown in Fig. 9.4b, a too high compliance may be detrimental. Since

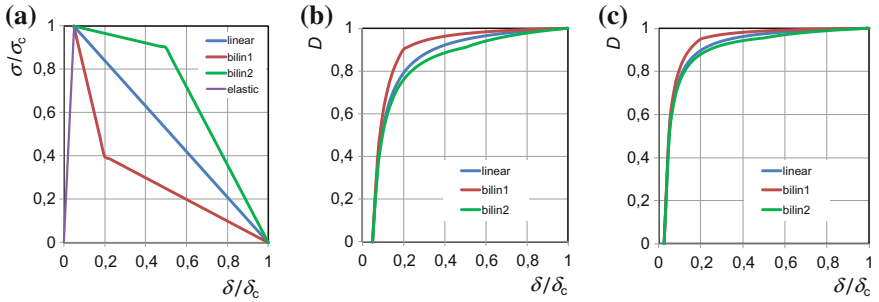

Fig. 9.6 Cohesive laws **a** and corresponding "damage" for **b** $\delta_0 = 0.05\ \delta_c$, **c** $\delta_0 = 0.025\ \delta_c$

C_0 has no physical meaning, "damage" D does not have any, either, because it is defined according to Eq. (9.21) as

$$D = 1 - \frac{\sigma(\delta)}{K_{\text{coh}}\delta} = 1 - \frac{\sigma(\delta)}{\sigma_c}\frac{\delta_0}{\delta}, \tag{9.21}$$

i.e. it depends on the choice of the fictitious numerical value, δ_0.

Figure 9.6 demonstrates the consequences. Three TSLs are chosen, one linear and two bilinear ones as in Fig. 9.3a, b with an initial "elastic" slope, δ_0, and the corresponding damage curves are calculated from Eq. (9.21) for $\delta_0 = 0.05\ \delta_c$. in Fig. 9.6b and $\delta_0 = 0.025\ \delta_c$. in Fig. 9.6c. The three curves $\sigma(\delta)$ display considerable qualitative differences as rather ductile (green curve) or rather brittle (red curve). Changing the initial slope from $0.05\ \delta_c$ to $0.025\ \delta_c$ does not change their typical shapes. The corresponding damage curves, $D(\delta)$, do not mirror the appearances of the TSLs at all. Even worse, they change quantitatively with smaller δ_0, and any differences between the three curves will completely vanish for $\delta_0 \to 0$. Obviously, "damage" has no physical meaning, and it is impossible to define a unique $D(\delta)$ curve (as required in Abaqus) to obtain a specific $\sigma(\delta)$ law.

Realising that it might not be a smart idea to define ductile damage with reference to a (fictitious) elastic compliance, some authors have proposed "elastic-plastic" cohesive laws [56, 61], but this does not remedy the conceptual defect of mixing continuum with cohesive properties. After all, it is not clear what the advantage of introducing a "damage" variable in a cohesive law could be.

9.2.6 *Triaxiality Dependence of Cohesive Parameters*

Whereas the damage models of Gurson and Rousselier account for the effect of hydrostatic stress on void growth, the cohesive parameters are considered as material parameters which do not depend on the stress state. This is an approximation and not fully correct, of course, as the results of respective cell model

calculations in Fig. 8.6 and the models of McClintock [32] and Rice and Tracey [39] indicate. The cohesive parameters depend on the triaxiality, Eq. (5.37), of the stress state. The cohesive strength increases and the separation energy decreases with increasing triaxiality, η, [43, 51] and both approach limiting values. This effect is known from macroscopic tests on smooth and notched round tensile bars in which the maximum load increases and the fracture strain decreases with increasing notch radius.

The dependencies $\sigma_c(\eta)$ and $\Gamma_c(\eta)$ can be incorporated in the TSL [3], if quantitatively known, but numerical simulations of crack growth under plane-strain conditions revealed that the predicted R-curves did not not significantly depend on whether or not the triaxiality effect has been considered. Actually, the separation energy supplies only a small contribution to the overall dissipated work, Eq. (5.74), namely less than 10% for C(T) specimens and just about 1% for M(T) specimens [9, 11]. The major contribution results from overall plasticity, which explains the geometry dependence of R-curves, Fig. 8.9. In addition, high values of triaxiality are reached at the crack tips of fracture specimens and thick-walled structures at which the dependence of cohesive parameters on triaxiality is minor, anyway.

The addressed dependence prohibits a transfer of the parameters from thick to thin-walled structures close to plane-stress conditions, however.

9.3 Applications

The phenomenological model of a cohesive zone is widely spread and has found diverse applications for different kind of materials and loading cases. Different from fracture mechanics but like damage models, it is not dependent on some assumed or existent initial crack. Its advantages compared to continuum damage models are the less number of model parameters and the numerical stability even for large crack extension. The two parameters of cohesive strength, σ_c, and separation energy, Γ_c, permit a physically plausible interpretation of fracture toughness with reference to micromechanical mechanisms of ductile damage [9, 51, 52].

The cohesive model is versatile and shows great promise for practical applications [19, 20, 47, 49]. It also allows for numerous advancements, a few of which will be addressed in Sect. 9.4.

Cohesive elements can be used in 3D, axisymmetric and 2D FE models, the latter in both plane strain and plane stress or in combination with shell elements. Mode I ductile crack extension perpendicular to the external loading in thick fracture specimens or plane components can be approximately simulated by plane-strain models. Figure 8.9 has demonstrated that both the Gurson model and the cohesive model can capture the geometry dependence of J_R-curves by discerning local dissipation due to material separation from overall plasticity according to Eq. (5.76). The respective simulations were performed under plane strain conditions and refer to side-grooved fracture specimens. Any dependence of cohesive parameters on triaxiality (Sect. 9.2.6) has been neglected.

9.3.1 Crack Extension in Thin Panels and Shells

Whereas the void-growth models of Gurson or Rousselier are not or less suited for low constraint conditions close to plane stress, the cohesive model fits also well for predicting crack growth in metal sheets, provided that the lateral reduction of thickness is taken into account. Otherwise, plastic collapse of the adjacent continuum elements according to Dugdale's model, Fig. 4.6b, might occur. The information on thickness reduction which is commonly not available in plane-stress or shell elements is calculated from the adjacent continuum elements and transmitted to the cohesive elements [46].

Transmitting the information on thickness reduction is one of two necessary provisions for the simulations. The second special effect of crack extension in metal sheets is the occurrence of slant fracture [8], i.e. tilting of the fracture surface out of the normal x, z-plane into a 45° orientation with respect to the loading, Fig. 9.7. The local mechanism is hence a mixed mode I and III separation. For predicting the crack extension in the ligament (x-direction) and the residual stiffness of the structure, a 2D model in plane stress will suffice. The respective cohesive parameters represent "effective" values, however, of a process which is a mixed-mode situation in reality.

With a thus modified cohesive zone model numerically stable simulations can be performed for large crack extensions. Validations can be found in Scheider et al. [48] who present simulations of crack extension based on CTOA and the cohesive model in various specimens made of aluminium sheet metal of 3 mm thickness and study the predictive capabilities. Cohesive parameters were determined from a C(T) specimen of width $W = 50$ mm and transferred to simulations of larger C(T) and M(T) specimens as well as a biaxially loaded centre cracked panel. Good coincidence between test data and simulations was found in all cases.

Figure 9.8 shows results obtained by students in a course at Politecnico di Milano [10] for a M(T) specimen of width $W = 150$ mm. The simulations were

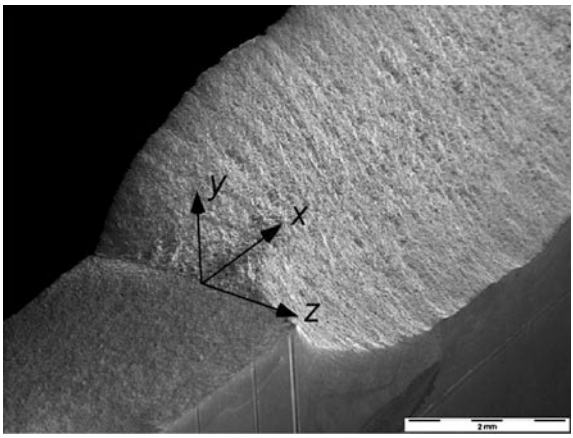

Fig. 9.7 Slant fracture of a thin panel

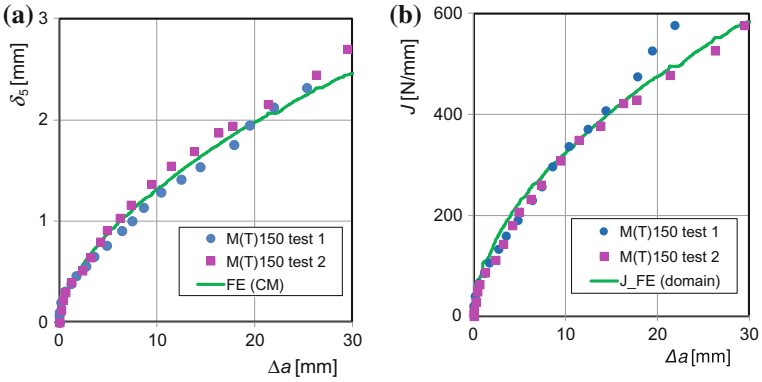

Fig. 9.8 Simulation of crack extension in a M(T) specimen of width $W = 150$ mm made of aluminium sheet metal, thickness 3 mm [10]: **a** CTOD R-curves, **b** J_R-curves

performed applying Scheider's model, Eq. (9.9), implemented as a user element in Abaqus [1]. The experimental data are taken from Scheider et al. [48].

Cornec et al. [20] present an analysis of the residual strength of a large scale fuselage structure with a two-bay crack, demonstrating the significance for safety assessments in the aircraft industry.

9.3.2 Crack Path Branching

A drawback of the cohesive model is that crack extension can only occur along element boundaries which are prescribed by the FE mesh. The analysis of cup-cone fracture presented in Fig. 9.4 demonstrated the high efforts to model crack paths, at least approximately, which are not known in advance. Extremely refined triangular meshes with interface elements have to be used in 2D models or tetrahedrons in 3D for simulations of slant fracture. Simulations for heterogeneous and quasi-brittle materials with arbitrary crack path evolution have been presented by Tijssens et al. [57], which allowed for the development of crack patterns with several short secondary cracks besides the main cracks. Comparably complex and elaborate simulations of crack path deviation at a material interface in a laser weld were performed by Nègre et al. [36]. Constitutive models of continuum damage are more advantageous for these kinds of problems as they do not have any preferable orientation of potential crack path bifurcation [8].

There is a number of practical problems, however, where the application of cohesive elements is convenient, because crack path branching is not completely arbitrary and only a limited number of possible crack paths exists. A matrix crack in a reinforced composite which approaches a fibre can continue in its original direction and break the fibre or it can change its path along the fibre direction causing decohesion of the fibre. A macroscopic correspondent is crack extension in

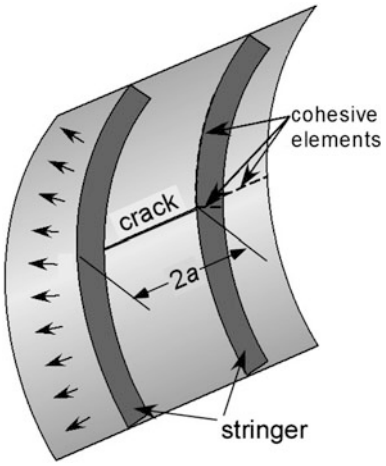

Fig. 9.9 One-bay crack in the model of an airplane fuselage under internal pressure, Brocks and Scheider [13]

a structure encountering a stiffener like a stringer in an airplane fuselage. The practical relevance of this problem became evident in an accident of a Boeing 737 during the Aloha Airline flight 243 in 1988 when parts of the upper shell were completely ripped off in flight, an event which had far-reaching effects on aviation safety policies and procedures. Brocks and Scheider [13] investigated a model of this configuration, Fig. 9.9, in a parametric study. The stiffened cylindrical shell under internal pressure contained an axial one-bay axial crack between two stringers. The crack was allowed to extend either in its original axial direction and cut the stringer or it could deviate in circumferential direction along the stringer. Cohesive elements were placed accordingly in axial direction in the skin, in the stringer and in circumferential direction between skin and stringer. In fact, the crack path changed in dependence on the stringer thickness. Beyond a certain thickness, the crack did not cut the stringer any more but deviated in circumferential direction as it had happened in the airplane accident mentioned above.

The change of the fracture mechanism affects the residual strength of the structure. Crack branching, which occurred in dependence in the stringer thickness in this example, will also occur due to potential variations of the bonding strength of welds. Respective effects that stringers peeled off the skin have been observed in tests. The cohesive model provides a convenient tool to describe respective phenomena and predict implications to the residual strength in this and comparable components [47].

9.4 Advancements

Publications on cohesive models for various kinds of materials, separation mechanisms and applications flood the market, and it is impossible to give any representative overview. Beside developments which extend the spectrum of

applications, considerations on fundamental physical principles [37] or damage based approaches boom. Whether the latter represent actual advancements remains questionable.

The present chapter on cohesive models has focussed on quasistatic separation processes, so far, described by equations of the type $\sigma(\delta)$. The cohesive parameters have been taken as material constants, mostly, but they may depend on external field variables. Providing the TSL with information on thickness reduction of the continuum elements in the crack ligament has proven as vital for simulations applying plane-stress and shell elements [46], and the dependence of cohesive parameters on the local stress triaxiality has been discussed in Sect. 9.2.6. Anvari et al. [3] studied dynamic ductile fracture of aluminium bars applying the cohesive model and had to consider strain rate effects. Based on unit cell calculations, the authors implemented the rate and triaxiality dependence of cohesive strength and separation energy.

Likewise, temperature or any other physical field variable can affect the cohesive properties and can be taken for modifying the parameters, provided the respective variable is available in the FE code and the effect can be quantified. An ambitious modelling of this kind has been presented by Falkenberg et al. [24] who investigated the effect of hydrogen embrittlement on ductile tearing resistance of steels with cohesive elements. It required to implement hydrogen diffusion into the FE code and to consider the effect of hydrogen concentration on both yield strength and cohesive strength. The author was able to capture the strong decrease of the crack growth resistance under hydrogen charging conditions at low displacement rates, which was observed in the respective tests.

Rate- and time-dependent fracture phenomena are of great interest for the fracture behaviour of polymers [64] and the simulation of adhesives. For metals, rate effects are relevant at high-temperature conditions or dynamic crack growth [63]. They can be captured implicitly by rate dependent parameters [3] or by specific cohesive laws, $\sigma\left(\delta, \dot{\delta}\right)$, which explicitly include the separation rate [18, 21, 54].

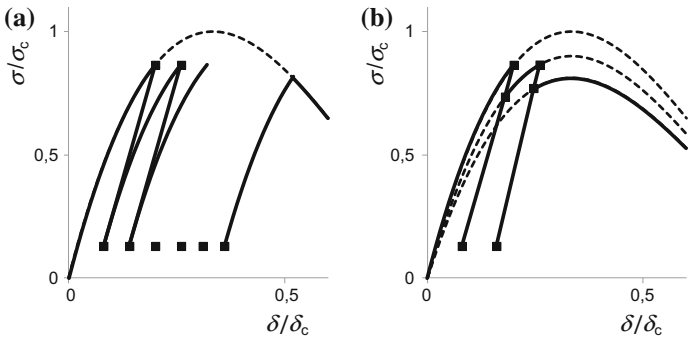

Fig. 9.10 Schematic of ratcheting effect due to cyclic plasticity: **a** varying slopes for unloading and reloading; **b** shape change of monotonic TSL

Applications of the cohesive model to crack extension under cyclic plastic deformations have become topical, recently. They require major modifications of the cohesive law. The monotonic TSL is a unique curve, unloading and reloading follow the same straight (elastic) line, Fig. 9.5, and do not result in any degradation or damage. Cyclic loading has to affect either the slope of reloading [50], Fig. 9.10a, or the shape of the monotonic TSL [27, 40], Fig. 9.10b. The latter may be described by a damage variable, $\sigma_c = \sigma_c^0(1 - D)$. Different from approaches like Eq. (9.21), D has a physical significance here describing the reduction of cohesive strength due to alternating plastic deformation. Evolution laws for D or the changes of the unloading/reloading slopes are required, which represent the actual challenge of modelling. Due to numerical time and effort cohesive models are less suited for large numbers of cycles.

References

1. Abaqus (2014) User's Manual, Version 6.12. Dassault Systèmes Simulia Corp, Providence, RI, USA
2. Allix O, Ladevéze P, Corigliano A (1995) Damage analysis of interlaminar fracture specimens. Compos Struct 31:61–74
3. Anvari M, Liu J, Thaulow C (2007) Dynamic ductile fracture in aluminum round bars: experiments and simulations. Int J Fract 143:317–332
4. Barenblatt GI (1959) The formation of equilibrium cracks during brittle fracture: general ideas and hypothesis, axially symmetric cracks. Appl Math Mech 23:623–636
5. Barenblatt GI (1962) The mathematical theory of equilibrium cracks in brittle fracture. Adv Appl Mech 7:55–129
6. Bažant ZP (1993) Current status and advances in the theory of creep and interaction with fracture. In: Bažant ZP, Carol I (eds) Proc. 5th Int. RILEM Symp on Creep and Shrinkage of Concrete, E & FN Spon, London and New York, pp 291–307
7. Bažant ZP (2003) Concrete fracture models: testing and practice. Eng Fract Mech 69:165–205
8. Besson J, Steglich D, Brocks W (2001) Modeling of crack growth in round bars and plane strain specimens. Int J Solids Struct 38:8259–8284
9. Brocks W (2005) Cohesive strength and separation energy as characteristic parameters of fracture toughness and their relation to micromechanics. Struct Integr Durab 1:233–243
10. Brocks W, Rabbolini S (2015) Computational fracture mechanics. Report Students Project, Dipartimento di Meccanica, Politecnico di Milano
11. Brocks W, Anuschewski A, Scheider I (2010) Ductile tearing resistance of metal sheets. Eng Fail Anal 17:607–616
12. Brocks W, Cornec A, Scheider I (2003) Computational aspects of nonlinear fracture mechanics. In: Milne I, Ritchie RO, Karihaloo B (eds) Comprehensive structural integrity, Vol. 3, Elsevier, pp 127–209
13. Brocks W, Scheider I (2008) Prediction of crack path bifurcation under quasi-static loading by the cohesive model. Struct Durab Health Monit 70:1–11
14. Brocks W, Scheider I (2010) Identification of material parameters for structural analyses. Struct Durab Health Monit 161:1–24
15. Brocks, W, Steglich, D (2007) Hybrid methods. In: Milne I, Ritchie RO, Karihaloo B (eds) Comprehensive structural integrity, Online Update Vol. 11, Elsevier, pp 107–136
16. Camacho GT, Ortiz M (1996) Computational modelling of impact damage in brittle materials. Int J Solids Struct 33:2899–2938

17. Camanho PP, Davila CG, de Moura MF (2003) Numerical simulation of mixed-mode progressive delamination in composite materials. J Compos Mater 37:1415–1438
18. Corigliano A, Ricci M (2001) Rate-dependent interface models: formulation and numerical applications. Int J Solids Struct 38:547–576
19. Cornec A, Scheider I, Schwalbe KH (2003) On the practical application of the cohesive model. Eng Fract Mech 70:1963–1987
20. Cornec A, Schönfeld W, Schwalbe KH, Scheider I (2009) Application of the cohesive model for predicting the residual strength of a large scale fuselage structure with a two-bay crack. Eng Fail Anal 16:2541–2558
21. Costanzo F, Walton JR (1997) A study of dynamic crack growth in elastic materials using a cohesive zone model. Int J Eng Sci 35:1085–1114
22. Dugdale DS (1960) Yielding of steel sheets containing slits. J Mech Phys Solids 8:100–104
23. Elices M, Guinea GV, Gómez J, Planas J (2002) The cohesive zone model: advantages, limitations and challenges. Eng Fract Mech 69:137–163
24. Falkenberg R, Brocks W, Dietzel W, Scheider I (2010) Modelling the effect of hydrogen on ductile tearing resistance of steels. Int J Mat Res 101:989–996
25. Griffith AA (1920) The phenomena of rupture and flow in solids. Philos Trans R Soc London A211:163–198
26. Hillerborg A, Modeer M, Petersson PE (1976) Analysis of crack formation and crack growth in concrete by means of fracture mechanics and finite elements. Cem Concr Res 6:773–778
27. Jha D, Banerjee A (2012) A cohesive model for fatigue failure in complex stress-states. Int J Fatigue 36:155–162
28. Koplik J, Needleman A (1988) Void growth and coalescence in porous plastic solids. Int J Solids Struct 24:835–853
29. Krull H, Yuan H (2011) Suggestions to the cohesive traction–separation law from atomistic simulations. Eng Fract Mech 78:525–533
30. Lin G, Cornec A, Schwalbe K-H (1998) Three-dimensional finite element simulation of crack extension in aluminium alloy 2024 FC. Fatigue Fract Eng Mater Struct 21:1159–1173
31. Maier G, Bocciarelli M, Bolzon G, Fedele R (2006) Inverse analyses in fracture mechanics. Int J Fract 138:47–73
32. McClintock FA (1968) A criterion for ductile fracture by the growth of holes. Trans ASME, J Appl Mech 35:363–371
33. Mosler J, Scheider I (2011) A thermodynamically and variationally consistent class of damage-type cohesive models. J Mech Phys Solids 59:1647–1668
34. Needleman (1987) A continuum model for void nucleation by inclusion debonding. J Appl Mech 54:525–531
35. Needleman A (1990) An analysis of decohesion along an imperfect interface. Int J Fract 42:21–40
36. Nègre P, Steglich D, Brocks W (2005) Crack extension at an interface: prediction of fracture toughness and simulation of crack path deviation. Int J Fract 134:209–229
37. Ottosen NS, Ristinmaa M, Mosler J (2015) Fundamental physical principles and cohesive zone models at finite displacements—limitations and possibilities. Int J Solids Struct 53:70–79
38. Park K, Paulino GH, Roesler JR (2009) A unified potential-based cohesive model of mixed-mode fracture. J Mech Phys Solids 57:891–908
39. Rice JR, Tracey DM (1969) On the ductile enlargement of voids in triaxial stress fields. J Mech Phys Solids 17:201–217
40. Roe RL, Siegmund T (2003) An irreversible cohesive zone model for interface fatigue crack growth simulation. Eng Fract Mech 70:209–232
41. Rose J, Ferrante J, Smith J (1981) Universal binding energy curves for metals and bimetallic interfaces. Phys Rev Lett 75:675–678
42. Scheider I (2001) Bruchmechanische Bewertung von Laserschweißverbindungen durch numerische Rißfortschrittsanalysen mit dem Kohäsivzonenmodell. Ph.D. thesis, Technical University Hamburg-Harburg, Report GKSS 2001/3, GKSS-Research Centre, Geesthacht, Germany

43. Scheider I (2009) Derivation of separation laws for cohesive models in the course of ductile fracture. Eng Fract Mech 76:1450–1459
44. Scheider I, Brocks W (2003) Simulation of cup-cone fracture using the cohesive model. Eng Fract Mech 70:1943–1961
45. Scheider I, Brocks W (2003) The effect of the traction separation law on the results of cohesive zone crack propagation analyses. Key Eng Mater 251–252:313–318
46. Scheider I, Brocks W (2003) Cohesive elements for thin-walled structures. Comput Mater Sci 37:101–109
47. Scheider I, Brocks W (2008) Residual strength prediction of a complex structure using crack extension analyses. Eng Fract Mech 75:4001–4017
48. Scheider I, Schödel M, Brocks W, Schönfeld W (2006) Crack propagation analysis with CTOA and cohesive model: Comparison and experimental validation. Eng Fract Mech 73:252–263
49. Schwalbe KH, Scheider I, Cornec A (2009): SIAM CM09 – The SIAM method for applying cohesive models to the damage behaviour of engineering materials and structures. Report GKSS 2009/1, GKSS-Reseach Centre, Geesthacht, Germany
50. Serebrinsky S, Ortiz M (2005) A hysteretic cohesive-law model of fatigue-crack nucleation. Scripta Mater 53:1193–1196
51. Siegmund T, Brocks W (1999) Prediction of the work of separation and implications to modeling. Int J Fract 99:97–116
52. Siegmund T, Brocks W (2000) The role of cohesive strength and separation energy for modeling of ductile fracture. In: Jerina KL, Paris PC (eds) Fatigue Fracture Mechanics, vol 30. ASTM STP 1360. American Society for Testing and Materials, Philadelphia, pp 139–151
53. Siegmund T, Brocks W, Heerens J, Tempus G, Zink W (1999) Modeling of crack growth in thin sheet aluminium. In: ASME Int. Mechanical Engineering Congress and Exposition: Recent Advances in Solids and Structures, ASME PVP 398, Nashville, pp 15–22
54. Siegmund T, Needleman A (1997) A numerical study of dynamic crack growth in elastic–viscoplastic solids. Int J Solids Struct 34:769–787
55. Song SH, Paulino Glaucio H, Buttlar GH (2006) A bilinear cohesive zone model tailored for fracture of asphalt concrete considering viscoelastic bulk material. Eng Fract Mech 73: 2829–2848
56. Su C, Wei YJ, Anand L (2004) An elastic-plastic interface constitutive model: Application to adhesive joints. Int J Plasticity 20:2063–2081
57. Tijssens A, van der Giessen E, Sluys LJ (2001) Modeling quasi-static fracture of heterogeneous materials with the cohesive surface methodology. In: Bathe KJ (ed) Computational Fluid and Solid Mechanics (1st MIT Conf), vol 1. Elsevier, Amsterdam and London, pp 509–512
58. Tvergaard V (1990) Effect of fibre debonding in a whisker-reinforced metal. Mater Sci Eng, A 190:203–213
59. Tvergaard V, Hutchinson JW (1992) The relation between crack growth resistance and fracture process parameters in elastic-plastic solids. J Mech Phys Solids 40:1377–1397
60. Tvergaard V, Hutchinson JW (1993) The influence of plasticity on mixed mode interface toughness. J Mech Phys Solids 41:1119–1135
61. Xu Q, Lu Z (2013) An elastic–plastic cohesive zone model for metal–ceramic interfaces at finite deformations. Int J Plasticity 41:147–164
62. Xu X, Needleman A (1994) Numerical simulations of fast crack growth in brittle solids. J Mech Phys Solids 42:1397–1434
63. Xu XP, Needleman A (1996) Numerical simulations of dynamic crack growth along an interface. Int J Fract 74:289–324
64. Xu DB, Hui CY, Kramer EJ, Creton C (1991) A micromechanical model of crack growth along polymer interfaces. Mech Mater 11:257–268

Index

W. Brocks, *Plasticity and Fracture*, Solid Mechanics and Its Applications 244,
DOI 10.1007/978-3-319-62752-6